



University  
of Glasgow

Sala, Bianca (2019) *Scanning transmission electron microscopy characterisation of carbide precipitates in steel*. PhD thesis.

<https://theses.gla.ac.uk/72470/>

Copyright and moral rights for this work are retained by the author

A copy can be downloaded for personal non-commercial research or study, without prior permission or charge

This work cannot be reproduced or quoted extensively from without first obtaining permission in writing from the author

The content must not be changed in any way or sold commercially in any format or medium without the formal permission of the author

When referring to this work, full bibliographic details including the author, title, awarding institution and date of the thesis must be given

Enlighten: Theses

<https://theses.gla.ac.uk/>  
[research-enlighten@glasgow.ac.uk](mailto:research-enlighten@glasgow.ac.uk)

# **Scanning transmission electron microscopy characterisation of carbide precipitates in steel**

**Bianca Sala**

Submitted in fulfilment of the requirements for the Degree of  
Doctor of Philosophy

School of Physics and Astronomy  
College of Science and Engineering  
University of Glasgow



May 2019



## Abstract

High strength micro-alloyed steels are used extensively in a number of industries such as car manufacturing. The properties of these steels, including their high strength, are caused in part by the formation of nanoscale precipitates during thermomechanical processing. In the case of the steels examined in the work reported in this thesis, the microalloying elements added to the steel were titanium, vanadium and niobium. During hot rolling, these combined with carbon and nitrogen to form stable carbides, nitrides and carbonitrides.

Many steel properties depend on the size, distribution and chemistry of these precipitates, which in turn depend on the exact thermomechanical processing steps used during manufacture. The overall aim of the project was to understand how the combination of Ti, V and Nb influences the properties of bainitic steels and characterise the precipitation at different stages during manufacture. Electron microscopy techniques have been used to characterise the distribution, size and chemistry of these precipitates. This involved two different approaches, both using electron energy loss spectroscopy (EELS). First, large areas of steels were mapped using low-loss EELS. This allowed us to identify areas rich in precipitates, image their distribution and obtain a measurement of their size distribution as absolute volume fractions. The results from this are presented in Chapter 4 of this thesis. To process this data and obtain results from precipitates smaller than 1nm in diameter, a method to analyse the low-loss datasets has been developed as part of this PhD. This is detailed in Chapter 3. Once areas containing precipitates had been found, some of these were picked for more in-depth quantitative chemical analysis using DualEELS. A series of results for different types of precipitates found in a range of steel samples is detailed in Chapter 6. Again, the method used to analyse these datasets was partly developed as part of this PhD and is described in Chapter 3. It uses a multiple linear least squares fitting approach where experimentally obtained cross-sections are fitted to the precipitate data. The results of this are then used to quantify the exact chemistry of the precipitates. The details of the measurement of these cross-sections, and the method used to obtain them, are presented in Chapter 5.

For the first time, we have been able to perform large area volumetric analysis coupled with detailed analysis of the chemistry of individual precipitates. This gave us the ability to track the precipitate formation resulting from the manufacturing process while while obtaining both a statistically significant overview and fine chemical detail. This has clear applications to the future of steel processing and other reactions involving precipitation or formation of nanoscale chemical inhomogeneity in materials.



## Declaration

This thesis is a record of the work carried out by myself in the Materials and Condensed Matter Physics group at the University of Glasgow between September 2015 and December 2018, under the supervision of Dr. Ian MacLaren, Prof. Alan J. Craven and Dr. Damien McGrouther. The work described here is my own, except for:

- The scripts written by Prof. Alan Craven, Mr. Robert Webster and Dr. Bernhard Schaffer as indicated in the text.
- Bulk steel specimens were manufactured by either the CRM Group or CEIT.
- VC and NbC bulk specimens were provided by Prof. Walter Lengauer from TU Wien.
- FIB samples from the PrecHiMn project discussed in the text were prepared by Dr. Joanna Bobynko as part of her PhD.

This thesis has not been previously submitted for a higher degree.

Parts of this work have been published in the following peer-reviewed papers:

- A. J. Craven *et al.*, *Microscopy & Microanalysis*, 24 [S1] (2018) 436-437
- A. J. Craven *et al.*, *Ultramicroscopy* 186 (2018) 66-81
- A. J. Craven *et al.*, *Ultramicroscopy* 170 (2016) 113-127

The following oral and/ or poster presentations have also been given at conferences:

- B. Sala *et al.*, Large area mapping for analysis of nanoscale carbonitride precipitates within the steel matrix, IMC19, Sydney, September 2018
- B. Sala *et al.*, Absolute chemical analysis of nanoscale carbide precipitates within steel matrices, IMC19, Sydney, September 2018
- B. Sala *et al.*, Large area mapping of precipitates within steel matrices, University of Glasgow PhD student conference, Glasgow, June 2018
- B. Sala *et al.*, Absolute quantification of nanoscale carbonitride precipitates in steel, MMC/EMAG, Manchester, July 2017

## Acknowledgements

I would like to express my gratitude to all those who supported me and contributed to this thesis. A special mention goes to my supervisor, Dr. Ian MacLaren, for his support throughout my academic career, from my undergraduate studies to this point, and for his guidance during my transition to become an independent researcher.

I am eternally grateful to Prof. Alan Craven for his constant advice, his willingness to help me with getting things down on paper, and his focus on the tiniest of detail in my analysis. I would also like to thank Robert Webster and Dr. Bernhard Schaffer for their scripting help. To Dr. Damien McGrouther, thanks for all your sample prep advice.

None of this work would have been possible without the amazing technical help available in the MCMP group. Many thanks to Dr. Sam McFadzean, Billy Smith and Colin How for the countless hours spent training me and helping me out each time I needed.

To my examiners, Dr. Yu Lung Chiu, Dr. Donald MacLaren and Dr. Amalio Fernandez-Pacheco – thank you for making my viva good fun and far less scary than I imagined it would be!

Thanks to Kirsty and Tom for being the best office mates anyone could possibly ask for – for the endless hugs, slices of cake, coffees and words of encouragement. Also, thanks to John for dragging me out climbing, laughing at me (with me!) and sharing the occasional, but much needed, bottle of wine.

A huge thank you also to David Keeble, Aurora Sicilia-Aguilar and Keith Wilcox in Dundee for trusting me to teach their undergraduate classes when I was straight out of thesis writing. Your faith in me means a lot.

Also, thanks to Dr. Elizabeth Adams for all her invaluable advice and for helping me rediscover my love of writing.

A huge thank you goes to my family. To my parents, Dan and Angela, for supporting me throughout my time in London and Glasgow in every possible way, I will be forever grateful. I hope that I can repay you one day for all the sacrifices you've made for me. To my grandparents for raising me, especially my grandad for patiently teaching me the name of every plant and animal I would come across! To my auntie Doina for being one of my best friends and always being there for me.

To Amanda and Tim, I cannot express how grateful I am for all your support. Whether in Cumbria or France, you've opened your home to me and patiently listened to all my problems until we inevitably ended up having a massive giggle at them.

To Sia, thank you for all the lunchtime chats and for listening to my complaints when it all got too much. To Dina, thanks for all the walks and for making our time with Pint of Science one of the most enjoyable parts of my PhD.

To my rhino children, Bertus, Qabid and Sanjay, thank you. You have no idea how much joy your antics brought into my life.

A special thanks goes to all the fluffy friends who've made my PhD that much more bearable. Pufi and Jessie, thank you for forcing me to take breaks by constantly napping on my laptop. Margaret and Bronwen, thank you for taking me out on walks and always being there for a snuggle. Costel, thank you for your endless trust. Katla and Mushu for their cuddles. Heather, Angus, Una, Ruadh, Zece, Snowy, Daisy and the entire bovine population of Scotland, thank you. And Hamish. None of this would have been possible without you. Long may you moo.

Finally, my heartfelt thanks go to Ruaraidh. Thank you for being my best friend for so many years.

## List of abbreviations

**3DAPT** – 3-Dimensional Atom Probe Tomography

**ADF** – Annular Dark Field

**APT** – Atom Probe Tomography

**BCC** – Body Centred Cubic

**BCT** – Body Centred Tetragonal

**BF** – Bright Field

**CCD** - Charged Coupled Device

**DualEELS** – Dual Electron Energy Loss Spectroscopy

**EDX** – Energy Dispersive X-ray Spectroscopy

**EELS** – Electron Energy Loss Spectroscopy

**EFTEM** – Energy Filtered Transmission Electron Microscopy

**ELNES** – Energy Loss Near Edge Structure

**EXELFS** – Extended Energy Loss Fine Structure

**FCC** – Face Centred Cubic

**FEG** – Field Emission Gun

**FIB** – Focused Ion Beam

**GIF** – Gatan Imaging Filter

**HAADF** – High Angle Annular Dark Field

**HSLA** – High Strength Low Alloy

**MLLS** – Multiple Linear Least Squares

**MSA** – Multivariate Statistical Analysis

**PCA** – Principal Component Analysis

**SEM** – Scanning Electron Microscope/ Microscopy

**SI** – Spectrum Image

**SNR** – Signal to Noise Ratio

**STEM** – Scanning Transmission Electron Microscope/ Microscopy

**TEM** – Transmission Electron Microscope/ Microscopy

**ZLP** – Zero-Loss Peak

# Contents

Abstract

Declaration

Acknowledgements

List of abbreviations

1. Introduction	17
1.1. Introduction to project	17
1.2. Structure of the thesis	18
1.3. Literature review: precipitation in steels	19
1.3.1. The Fe – C phase diagram	19
1.3.2. Different types of steel	21
1.3.3. Basics of alloying and the effects of precipitation on steels	22
1.3.4. Ti, V, and Nb carbide precipitation	23
1.3.5. Methods for imaging nanoscale precipitates in steels	25
1.4. Summary	31
2. Sample preparation and Instrumentation	32
2.1. Focused ion beam (FIB)	32
2.1.1. The FIB instrument	32
2.1.2. The FIB lift-out method	33
2.1.3. Differences between Ga and Xe ion beams	36
2.1.4. Needle sample preparation	36
2.2. Transmission electron microscopy (TEM)	38
2.2.1. The use of electrons for imaging	38
2.2.1.a) Electron sources	39
2.2.1. b) The condenser system	39
2.2.1. c) The objective lens	41
2.2.1. d) Post specimen lenses	42
2.2.1. e) Detectors and the charged coupled device (CCD)	42
2.3. Scanning transmission electron microscopy	42
2.3.1. Outline	42
2.3.2. STEM bright, annular dark and high angle annular dark field	43
2.3.3. Aberrations in the STEM and correction for them	43
2.3.3. a) Astigmatism	43
2.3.3. b) Spherical aberration	43
2.3.3. c) Chromatic aberration	45
2.4. Electron energy loss spectroscopy (EELS)	45
2.4.1. Outline	45

2.4.2.	The electron energy loss spectrum .....	47
2.4.2. a)	The zero-loss peak (ZLP).....	47
2.4.2. b)	The low-loss spectrum.....	47
2.4.2. c)	The high-loss spectrum.....	48
2.4.3.	Cross-sections for EELS interactions .....	50
2.4.4.	Spectrometers and the Gatan Imaging Filter (GIF).....	51
2.4.5.	Dual electron energy loss spectroscopy (DualEELS).....	52
2.4.6.	Spectrum imaging and the data cube.....	53
2.5.	Summary.....	53
3.	<b>EELS data processing</b> .....	55
3.1.	Basic DualEELS processing and noise reduction.....	57
3.1.1.	Linearisation.....	57
3.1.2.	Removing the background before the ZLP.....	58
3.1.3.	Aligning the spectrum images and correcting for the ZLP centring.....	58
3.1.4.	Volume extraction .....	59
3.1.5.	X-ray removal.....	59
3.1.6.	Principal component analysis (PCA).....	59
3.1.7.	Splicing and deconvolving.....	61
3.2.	Multiple linear least squares (MLLS) fitting .....	62
3.3.	Removing the matrix contribution.....	63
3.4.	Accurate quantification using MLLS fitting .....	65
3.5.	Factor rotations.....	68
3.6.	Processing large area low-loss maps .....	69
3.7.	Summary.....	71
4.	<b>Large area low-loss EELS mapping</b> .....	72
4.1.	Motivation.....	72
4.2.	Low-loss EFTEM and EELS mapping in principle and practice.....	73
4.3.	600°C tempering of a martensitic V-7, Nb-3, Ti-5 steel.....	75
4.3.1.	Data acquisition.....	77
4.3.2.	Precipitate size distribution as a function of tempering time .....	78
4.4.	Precipitate mapping in a Ti-10 Nb-3 steel.....	83
4.5.	Possible sources of systematic errors.....	86
4.6.	Summary.....	86
5.	<b>Accurate measurement of EELS differential cross-sections</b> .....	88
5.1.	Mean free path measurements.....	89
5.2.	Materials and experimental methods.....	90
5.3.	Data analysis.....	90
5.4.	Results .....	92
5.4.1.	TiC, TiN, VC and VN.....	92
5.4.2.	NbN and NbC.....	97
5.5.	Discussion.....	99
5.6.	Summary.....	101

<b>6. Accurate precipitate quantification using DualEELS</b>	102
6.1. The samples	103
6.1.1. Samples with (Ti,V)(C,N) precipitates	103
6.1.2. Samples with Nb containing precipitates	104
6.2. Data acquisition	104
6.3. Data analysis	104
6.3.1. Results for (Ti,V)(C,N) precipitates in a high-manganese steel	106
6.3.2. Results for (Nb,Ti)C precipitates in high manganese steel	112
6.3.3. Results for (Nb,Ti,V)C precipitates in CRM 60min tempered martensite steel	113
6.3.4. Large, manganese rich cementite particle	117
6.4. Summary	121
<b>7. Conclusions and Future work</b>	123
7.1. Thesis summary	123
7.2. Future work	125
<b>8. References</b>	128
<b>Appendix</b>	140
1. Script to characterise the non-linearity in spectrometer dispersion (by Dr. Bernhard Schaffer)	138
2. Script to measure and correct the spectrometer dispersion non-linearity (by Mr. Robert Webster)	153
3. Script to quantify the precipitates using their MLLS fit coefficient maps (by Prof. Alan J. Craven)	166

## List of figures

- Figure 1.1:** Diagram of two different cubic structures of steel, a) the body centred cubic structure of ferrite and b) the face centred cubic structure of austenite.....18
- Figure 1.2:** Schematic of the Fe – C phase diagram, showing the different types of equilibrium phases for steel. The steels discussed in this thesis have started in the austenite phase and have been cooled down towards ferrite, often quickly so as they would not form equilibrium phases.....19
- Figure 1.3:** The formation of an FCC carbide precipitate in austenite (FCC) and ferrite (BCC) showing the difference in shape between the two resulting precipitates. The green and orange spheres represent the steel matrix, the purple represents the metal in the precipitates and the black the carbon in the precipitates. Figure made by Dr. Ian MacLaren and used with permission.....22
- Figure 1.4:** Diagram showing the 3-window method for mapping elemental edges using EFTEM. The two pre-edge windows allow for the background to be extrapolated to the region under the edge and then subtracted from the total signal, leaving only the signal from the edge behind. Figure made by Dr. Ian MacLaren and used with permission.....25
- Figure 2.1:** Schematic diagram of a FIB – SEM instrument showing the main components, including the ion and electron columns and the position of a typical detector.....31
- Figure 2.2:** The FIB sample preparation process for a TEM cross-section with a) the protective platinum layer on the surface, b) the cross-section after side-trenches have been milled from the bulk, c) the J-cut to release the sample, d) the sample attached to the micromanipulator being moved towards the copper grid, e) top-down view of the sample being milled down to electron transparency and f) a side-view of the final thinned sample.....33
- Figure 2.3:** The sample being deposited on top of an annularly milled grid to be milled into a needle shape. ....35
- Figure 2.4:** a) Schematic diagram of the setup for convergent beam TEM showing the condenser lenses, spherical aberration corrector, objective lens, apertures and projection lenses and b) the principal planes including the object, back focal and image plane. ....39
- Figure 2.5:** Diagram of electron paths through a lens when affected by spherical aberration, with the rays furthest away from the optical axis being affected the most.....42
- Figure 2.6:** Diagram showing scattering events, with a) showing elastic scattering where the incoming electron interacts with the atomic nucleus, b) inelastic scattering off inner shell electrons where the incoming electron experiences Coulomb repulsion and c) inelastic scattering off outer shell electrons. In the inelastic scattering events the atomic electrons are excited to a higher energy level, shown by arrows in the diagrams.....44
- Figure 2.7:** The EEL spectrum of a (Ti, V) precipitate embedded in a high manganese steel matrix, showing the ZLP, the plasmon peaks and the core-loss edges on a logarithmic scale.....45
- Figure 2.8:** Diagram of a Gatan Imaging Filter (GIF) showing the entrance apertures, prism and entrance slit, together with the tuning and projection multipoles and the CCD.....50

<b>Figure 2.9:</b> A spectrum image data cube, with x and y representing the pixels scanned across and the third dimension, $\Delta E$ , representing the spectrum at each (x, y) pixel in the cube.	51
<b>Figure 3.1:</b> The as-acquired low-loss (blue) and high-loss (orange) spectra of a precipitate in a high-manganese steel, showing the range and intensity difference between the two. Due to the large intensity of the zero-loss peak, and the large difference in intensity between the low-loss and high-loss, the graph is plotted on a logarithmic scale. The high-loss has a longer acquisition time than the low-loss, hence the intensity difference where their energy losses overlap.	53
<b>Figure 3.2:</b> a) The misaligned ZLP before being aligned in energy loss and b) the large amount of noise in each channel of the as-acquired spectra.	54
<b>Figure 3.3:</b> The effects of dispersion non-linearity in DualEELS: a) Mismatch between the Si $L_{2,3}$ edge from $\text{SiO}_2$ appearing on the low-loss (red) and high-loss (blue) as acquired spectra, b) The error on each of the channels based on the ZLP position and c) Comparison between the position of a prominent feature on the low-loss and high-loss spectra after correcting for the dispersion nonlinearity.	55
<b>Figure 3.4:</b> Changes in the ZLP peak position when scanning the beam across the imaged area, with the ZLP moving by about $\pm 1.5\text{eV}$ across the scan.	57
<b>Figure 3.5:</b> Comparison between the pre- (blue) and post (orange) -PCA extracted spectra from the center of a (Ti, V) (C, N) precipitate. It is clear that the blue pre-PCA spectrum contains a lot more random noise than the orange post-PCA spectrum.	58
<b>Figure 3.6:</b> Improvements in the splice ratio of data when compared to the ideal (green) when it has been linearised (red) and when it has been linearised and had the stray background subtracted (black) as opposed to when it just had noise reduction applied (blue). The vertical axis shows the ratio between the high-loss acquisition time and the low-loss acquisition time, ie. the time ratio which in this example is 100. Ideally, the splice ratio would be the same as the time ratio, however the figure shows that this is not the case.	60
<b>Figure 3.7:</b> a): Extracted spectra showing the precipitate signal in blue with the spectrum obtained from the MLLS fit shown in red and the fit residuals showing in green and b) The cross-sections used in the MLLS fit to the precipitate signal (blue). (2016).	62
<b>Figure 3.8:</b> The results of the quantification in the case where the matrix was removed, followed by removal of the background shape.	63
<b>Figure 3.9:</b> Plots showing the distribution of VC, TiC, C from VC, N from VN and a-C in four (Ti, V)(C, N) precipitates in a high manganese steel.	64
<b>Figure 3.10:</b> a): Line profiles of equivalent thickness for each element in a (Ti,V,Nb) C precipitate and b): Values of x, y and $(1-x-v)$ metal coefficients in the $\text{Ti}_x\text{V}_v\text{Nb}_{(1-x-v)}\text{C}_y$ precipitate.	66
<b>Figure 3.11:</b> Procedure for quantifying precipitate statistics from a low-loss spectrum image: a) shows the spectrum image before PCA is applied. b) shows the PCA component map that shows the precipitates. This is summed with c), which shows the precipitate map as obtained from factor analysis. d) shows the sum of b) and c) after a mask has been applied to remove all matrix contributions and contains only the outline of the precipitates. e) shows the precipitates after being	

identified and analysed using the particle analysis software feature. f) shows the pre-PCA spectrum image (blue) and compares its shape with the shapes of the outputs from PCA (orange) and those of factor analysis (grey) showing that the outputs from factor analysis can be correlated back to the original spectrum while the outputs from PCA cannot.....68

**Figure 4.1:** Low-loss spectra extracted from both precipitates and the steel matrix, highlighting the difference between the two.....72

**Figure 4.2:** a) Map of a precipitate rich region in one of the steel samples discussed in this chapter (75 minutes tempering time), clearly showing that many of the precipitates have formed along lines and throughout the sample and b) annular dark field image of a large area of the steel showing individual grains and grain boundaries.....73

**Figure 4.3:** The thermal treatment applied to the Ti-5 Nb-3 V-7 steel series provided by CRM, with the final stage being the only one different for each of the samples in the series, with tempering at 600°C taking different amounts of time for each of the samples.....74

**Figure 4.4:** Measured hardness as a function of isothermal tempering time for the Ti-5 Nb-3 V-7 steel series tempered at 600°C for different amounts of time. The samples tempered for 45, 60, 75 and 90 minutes were picked for analysis.....75

**Figure 4.5:** Maps of 100nmx100nm precipitate rich areas in each of the four CRM samples analysed, with the 90min sample showing the most precipitates and the 45min sample showing very few by comparison.....76

**Figure 4.6:** Survey image showing a grain boundary (indicated by arrow) and precipitates having formed in the region (dark grey).....78

**Figure 4.7:** Composition maps for a series of precipitates formed along a manganese rich grain boundary.....78

**Figure 4.8:** The total number of precipitates identified in each diameter range, for each of the CRM samples from the tempered martensite series.....79

**Figure 4.9:** Comparison between the number of precipitates per unit volume in each diameter range for each of the four samples in the four CRM samples tempered at 600°C for different lengths of time.....80

**Figure 4.10:** The thermomechanical treatment applied to the steel of composition Ti-10 Nb-3 V-0.....82

**Figure 4.11:** ADF image of a lamella prepared from the CEIT steel, showing different grains and the boundaries between them.....82

**Figure 4.12:** Precipitate map of a 100nm × 100nm area in the Ti-10 Nb-3 steel.....83

**Figure 4.13:** The distribution of precipitates per unit volume in the CRM sample of base composition Ti-10 Nb-3 .....83

**Figure 5.1:** A large area low-magnification TEM image of an NbN needle shaped sample. Only the very top of the sample, where the needle is the thinnest, was used. ....87

**Figure 5.2:** Plots of  $(1/(I_0)_{xy}) (I^{E_{xy}}/\Delta E) (S^{xy}/T)$  versus  $n_M \lambda_B (t/\lambda)_{xy}$  for two values of energy in the TiC<sub>0.98</sub> dataset, with a) being at the energy of the Ti L<sub>3</sub> peak and b) being at an energy just before the onset of the Ti L<sub>2,3</sub> edge.....90

**Figure 5.3:** Comparison of the average experimental cross-sections, the scaled “experimental background” obtained from TiN<sub>0.88</sub> and the Hartree-Slater cross-sections for a) VC<sub>0.83</sub>, b) TiC<sub>0.98</sub>, c) VN<sub>0.97</sub> and d) TiN<sub>0.88</sub>.....91

**Figure 5.4:** a) The C-K edge compared to the shape of the background subtracted intensity from amorphous carbon, b) the N-K edge cross-section, c) the Ti-L cross-section and d) the V-L cross-section.....93

**Figure 5.5:** a) The VC<sub>0.83</sub> residuals on an expanded vertical scale, b) the ratio of the experimental non-metal cross-sections and their corresponding Hartree-Slater calculated cross-sections, as a function of energy loss above the edge threshold; the thin lines represent data before it was corrected to take into account the stoichiometry of the samples, with the thick lines being after the correction, c) the ratio of the experimental and Hartree-Slater cross-sections for the metals, with the thin lines being before and the thick lines being after correcting for full stoichiometry, and d) X/M (non-metal over metal) versus the window integration width  $\Delta$  for the stoichiometric standards; the thin lines again are the data before the correction; the lower group of plots have the integration window start at the threshold while the upper group of plots have the integration window start with an offset.....94

**Figure 5.6:** The experimental cross-section of the Nb-M<sub>4,5</sub> edge from NbN compared to the Hartree-Slater theoretical cross-section.....96

**Figure 5.7:** The experimental NbC cross-section used in quantifying all Nb containing precipitates during this research.....97

**Figure 6.1:** Maps for the fit coefficients for VC<sub>0.83</sub>, TiC<sub>0.98</sub>, C from VC<sub>0.83</sub>, N from VN<sub>0.97</sub> and amorphous carbon for the four precipitates analysed.....105

**Figure 6.2:** Contributions of the individual components to the overall fit for a region in the centre of precipitates 1 and 2. The matrix contributions are not shown as they are much larger than the other contributions and would make them less visible. Residuals are also shown.....106

**Figure 6.3:** Line profiles for the four elements through the center of the four precipitates, with the vertical scale for nitrogen being expanded due to the small amount of nitrogen present. The black lines are from MLLS fits done with thick and thin matrix shapes. The red and blue lines use spectra extracted from the surface and bulk rather than the matrix, with the red fit starting at 150eV and the blue one at 200eV.....108

**Figure 6.4:** Comparison of the thickness profiles for the four precipitates, with the purple line being the thickness from Ti+V, the orange line is the  $t/\lambda$  thickness after subtracting the matrix contribution and the green line also having the a-C contribution subtracted and not just the matrix contribution.....109

**Figure 6.5:** a) The elemental profiles of x, y, z and the X/M non-metal to metal ratio in Ti<sub>x</sub>Nb(1-x)CyNz and b) the equivalent thicknesses of Ti, Nb, C, N, Ti+Nb and C+N taken across the centre of the precipitate.....110

**Figure 6.6:** The survey image showing scanned area in the green box, the precipitates as darker areas in the matrix and the grain boundary direction indicated by the arrows.....111

**Figure 6.7:** Elemental maps of the precipitates and the grain boundary, obtained from fitting a background before the edges and integrating over a signal window over the edge. A precipitate rich in manganese is shown by the white arrow on the manganese map, and one of the precipitates found alongside the grain boundary is shown by the orange arrow on the vanadium map. .... 112

**Figure 6.8:** Maps of the MLLS fit coefficients for the standards for the (Ti, V, Nb) C precipitates. It shows the coefficients from the component shapes, the background shape as well as the thick and thin matrix shapes and the constant and step functions.....113

**Figure 6.9:** Extracted spectrum from the centre of the manganese rich precipitate in Figure 6.7, showing clear Ti and V edges but no conclusive N signal (marked with red where the N-K edge would be).....113

**Figure 6.10:** The equivalent thickness of carbon and each of the non-metals in one of the precipitates in the CRM steel tempered for 60min.....114

**Figure 6.11:** a) the equivalent thickness of each element in the precipitate and b) the values of x, v and 1-x-v in  $Ti_xV_vNb_{(1-x-v)}C_y$ ..... 115

**Fig 6.12:** Manganese map of the cementite particle dataset with the MnS precipitate discussed in this section indicated with an arrow, and a vanadium map indicating some plate-like precipitates ..... 116

**Figure 6.13:** MLLS coefficient maps for the fit on the cementite particle and the area surrounding it. The “top matrix” contribution is a spectrum extracted from the top half of the dataset with the “bottom matrix” is a spectrum extracted from the bottom half of the dataset  
117

**Figure 6.14:** The extracted spectrum from one of the MnS particles surrounding the cementite, showing the Mn and S edges.....118

**Figure 6.15:** Extracted spectrum from small plate-like precipitates, with the Ti and V edges marked and visible above the background signal (blue). The orange line represents the signal after a power-law background was extracted. ....119

# Chapter 1

## Introduction

### 1.1. Introduction to project

Over the last few decades, alloy steels have been used for a variety of industrial applications where high-strength is needed, such as in the automotive industry. One of the reasons they have an increased strength is the formation of nanoscale precipitates from the addition of microalloying metals such as niobium, titanium or vanadium [1]. During the hot rolling of steels, the microalloying elements combine with the carbon and nitrogen present in the steel solution to form stable carbide, nitride and carbonitride precipitates [2]. These precipitates stop or slow down the movement of dislocations or defects in the iron lattice, causing the material to harden. The size, structure and shape of the precipitates depend on the thermomechanical treatment the steel is subjected to, in addition to the precise chemistry of the steel [3].

Studies have been conducted to investigate how the properties of alloy steels can be influenced by the addition of transition metal alloys such as the ones mentioned above. Additionally, empirical models have been built with the aim to understand and control these precipitate sequences [4]. The effects of adding either niobium or vanadium to the steel solution have been investigated in detail. However, the addition of titanium has been investigated a lot less, with the same being true for combining all three metals. The few projects that have looked at titanium-alloyed steels have found that this leads to the formation of titanium nitride precipitates. These precipitates trap free nitrogen in the investigated steels, which improved their toughness. They have also been shown to strengthen low-carbon content bainitic steels. Similarly, vanadium is used to strengthen ferrite (the body centred cubic form of iron) through vanadium carbide precipitation, and niobium is used for controlling the grain growth of austenite (face centred cubic form of iron) by delaying its recrystallisation [5] [6]. Carbonitrides can start forming during the rolling of austenite, which leads to a significant increase in the strength of the alloyed steel. A more detailed literature review of the past research will be presented further into this chapter.

The properties of these alloyed steels are greatly influenced by small variations in the manufacturing process, such as uneven cooling rates or differences in temperature [7]. This can lead to large deviations from the desired properties, not just from one coil of steel to another, but also along the same strip of steel. As the steel is being strip processed in a rolling mill to create strips, it is important that the properties are constant throughout most of the strip, if not all of it. Some recommendations on alloy compositions that will be insensitive to such inevitable variations in processing conditions were considered essential by the steel industry. This is important as there is no control of the precipitation sequences along the whole length of the steel strip. With industry manufacturers needing consistent properties,

the non-uniform steel would fail quality control tests. This means that the strip needs to be scrapped and remelted, leading to large financial and environmental costs [8].

In order to investigate the properties of these microalloyed steels under different thermomechanical treatments, this project (“Control of precipitation sequences during hot rolling to improve product uniformity of titanium containing high strength steel”, or PreTiControl) was set up by the European Commission under the Research Fund for Coal and Steel (RFCS), in a consortium led by CRM in Belgium and including partners from Spain (CEIT), Germany (Thyssenkrupp), Belgium (CRM and OCAS) and the UK (Tata Steel and the University of Glasgow). It aimed to understand how the combination of titanium, niobium and vanadium influences the structure and properties of high titanium hot rolled bainitic steels while they are being manufactured. The structure of bainite, and other types of steel encountered during this project, will be explained later in this chapter. The influence of these elements on how austenite recrystallises and bainite undergoes phase transformations was investigated by a range of techniques as part of the overall project.

At the University of Glasgow, we have focused on analysing the distribution of precipitates within the steel matrix, measuring their size and accurately quantifying their chemistry. This was done using Electron Energy Loss Spectroscopy (EELS) in the Scanning Transmission Electron Microscope (STEM), which will be discussed in detail.

## **1.2. Structure of the thesis**

The research presented in this thesis revolves around acquiring electron energy loss spectroscopy (EELS) spectrum images under different acquisition conditions and analysing them to obtain information about precipitates within steel matrices. This includes large area distribution maps, particle size distribution or the accurate chemistry of precipitates. Investigations in these different areas will all be presented in this thesis, with comparisons being drawn between different types of steels.

The thesis will start with a brief discussion of the iron-carbon system and its different phases as related to this research, followed by a discussion of precipitation in steels and the effects of their formations on the steel properties. Different methods of imaging precipitation will be compared, and the gaps in the current research that will be filled by what is presented in this thesis will be identified.

Chapter 2 will begin with a discussion of focused ion beams (FIB) and the sample preparation techniques used in this thesis. The FIB lift-out methods used to prepare transmission electron microscopy (TEM) cross-sections as well as needle samples will be presented in detail. This will be followed by a discussion TEM, with an emphasis on scanning TEM (STEM) as it relates to this project. Electron Energy Loss Spectroscopy (EELS) data was acquired throughout the project, and the principles behind EELS, the spectrum components and the instrumentation are presented towards the end of Chapter 2.

Chapter 3 discusses how the EELS data acquired using the equipment described in Chapter 2 was processed and analysed. It begins by discussing the effects of dispersion non-linearity and why it needs to be corrected. It is then followed by a discussion of standard noise reducing steps; these involve removing noisy channels at the spectrum edges and reducing the volume of the data using Principal Component Analysis (PCA) by decomposing it and reconstructing using just the components that are rich in signal and mainly noise-free. Next, the methods used to quantify EELS data of precipitates are presented. This method development was started during a previous PhD project [9] and has been improved significantly during this research. Next, the steps used to measure the size distribution of precipitates in large area maps are described.

In Chapter 4, the large area low-loss mapping used to identify precipitates and measure their size distribution is introduced. This has been applied to two different types of steels. The first one was a tempered martensite series of steels of the same composition, provided by CRM, where we compared the precipitation of four samples tempered for different amounts of time. Next, a steel of different composition and thermal treatment, provided by CEIT in Spain, was analysed and briefly compared to the OCAS series. The distribution of the precipitates in each of the steels was calculated.

Chapter 5 introduces experimental core-loss EELS cross-sections for the constituents of the carbonitrides and demonstrates the need to use them in preference to theoretically calculated ones. The first part of the chapter discussed the TiC, TiN, VC and VN cross-sections and why it is essential to use experimental backgrounds rather than the usual power-law backgrounds. The second part of the chapter discusses the issues in calculating the NbN and NbC experimental cross-sections and presents some calculated data, while also discussing the uncertainties and possible future improvements. These cross-sections are then used for quantifying the chemistry of a few selected precipitates, with the results thereof being presented in Chapter 6. Results for both (Ti, V) and Nb steels are presented in detail.

Chapter 7 concludes the thesis by summarising what has been achieved and providing possible ways to take the research forward.

## **1.3. Literature review: precipitation in steels**

### **1.3.1. The Fe – C phase diagram**

Carbon steels represent one of the largest classes of alloys used in the world. At a basic level, steel is a mix of iron with a small amount of carbon (up to 2.1%). As the liquid iron-carbon solution cools down, three solid crystalline phases can usually be observed, depending on temperature, composition and cooling rates: body-centred cubic (BCC) ferrite or  $\alpha$ -iron (the basic structure is shown in Figure 1.1 a), face-centred cubic (FCC) austenite or  $\gamma$ -iron (the basic structure is shown in Figure 1.1 b), and cementite ( $\text{Fe}_3\text{C}$ ). Straining the BCC structure can lead to the formation of a body centred tetragonal one (BCT). Cementite can form when carbon is precipitated from solid solutions of ferrite or austenite, and is very stable once it has formed [3].

Ferrite and austenite form at different temperatures and compositions, with the equilibrium between the two phases and its temperature and carbon content dependence being altered by the addition of alloying elements or impurities from the original feedstock.

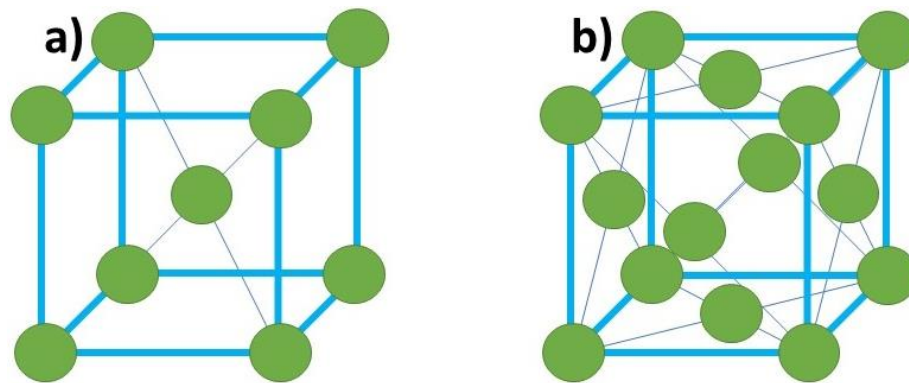


**Figure 1.1:** Diagram of two different cubic structures of steel, a) the body centred cubic structure of ferrite and b) the face centred cubic structure of austenite.

The equilibrium phases in the iron – carbon steel system are often shown on a phase diagram, where their dependence on composition (ie. carbon content) and temperature of the solution can be easily shown. A schematic phase diagram of the Fe – C system can be seen in Figure 1.2. The lines delimitating the individual phases on the diagram are known as phase boundaries. When one of these lines is crossed, either by altering the amount of carbon or by slowly changing the temperature of the solution (or both), a phase transformation occurs [10]. However, care must be taken when using phase diagrams as they only apply when the phases are in thermodynamic equilibrium. For example, a low-carbon steel can undergo the phase transformation from austenite to ferrite (and pearlite, to be briefly discussed in the following section) if the temperature is decreased slowly enough for the ferrite and cementite phases to have time to form. If the drop in temperature is much faster, it could result in the formation of metastable phases. The austenite structure allows for more carbon to be dissolved within it than ferrite does, and in the case of the slow cooling this extra carbon can diffuse. However, at fast cooling rates no significant diffusion of carbon has time to take place to form stable ferrite, so a metastable body centred tetragonal (BCT) structure that is supersaturated in carbon gets formed.

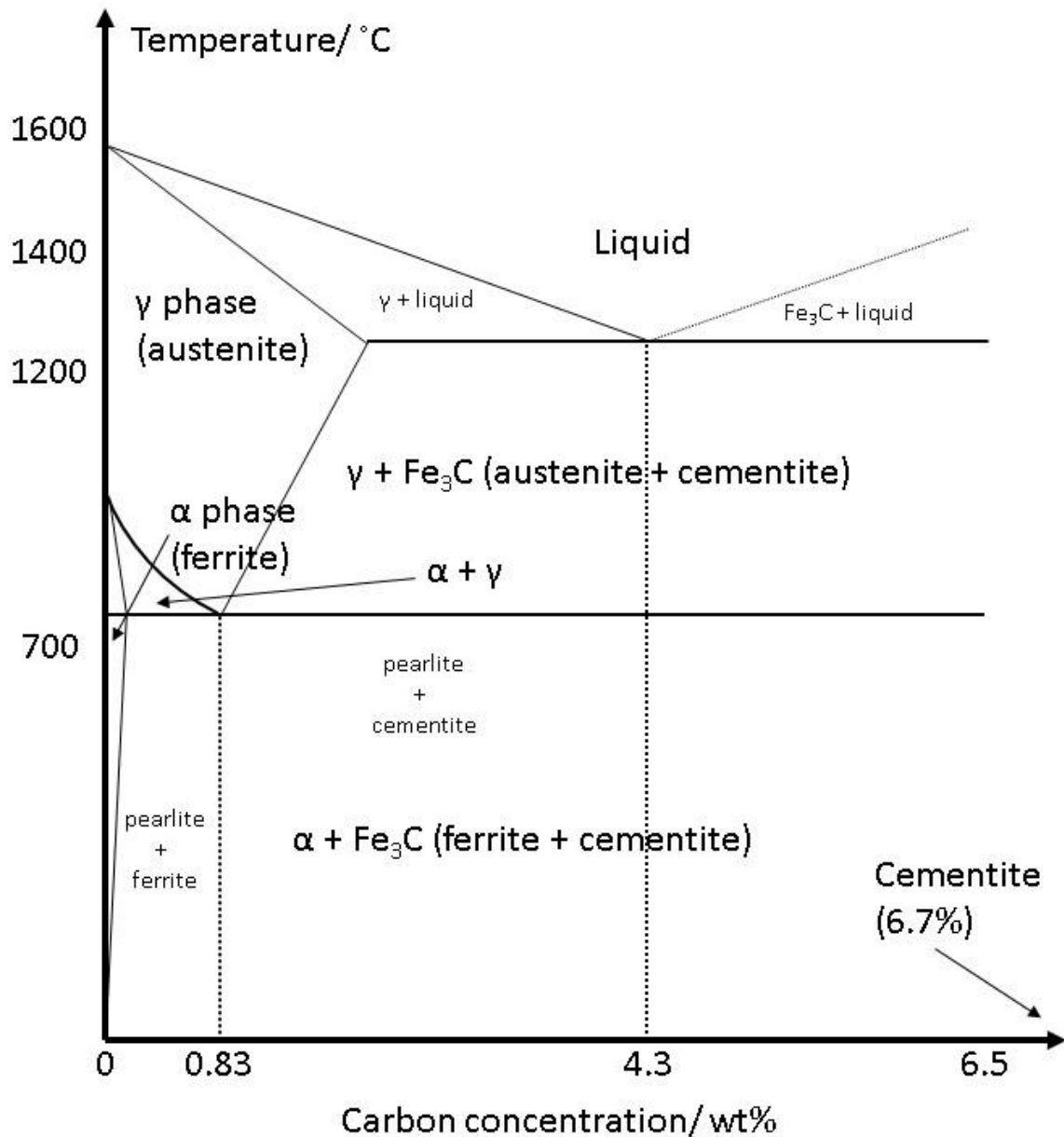


**Figure 1.2:** Schematic of the Fe – C phase diagram, showing the different types of equilibrium phases for steel. The steels discussed in this thesis have started in the austenite phase and have been cooled down towards ferrite, often quickly so as they would not form equilibrium phases.

### 1.3.2. Different types of steel

The carbon supersaturated BCC steel structure that was introduced at the end of the last subsection is known as martensite. This forms when the austenite solution, in the high temperature region of Figure 1.2, is cooled rapidly at a given rate so that a distorted ferrite structure can form. The excess carbon ends up distorting the BCC unit cell to form a tetragonal one. A martensitic steel series was studied as part of this PhD, with the results being presented in Chapter 4.

Another phase mentioned previously is pearlite, in reality a two-phase lamellar structure of ferrite and cementite [11]. When steel is cooled quickly and austenite decomposes at

temperatures below the range where pearlite forms but above those where martensite formation occurs, another metastable phase known as bainite forms. Bainite is formed of plate-shaped ferrite and carbides formed as a secondary reaction [12] [13].

There are more possible phases and microstructures, but these are the ones most relevant to this research so the other ones will not be discussed here. However, even from this short introduction to the different types of steel, it is clear that there is a complex range of phases as well as microstructure that can form in the Fe – C solution depending on the amount of carbon present, the temperature of the solution and the rates at which temperatures are changed.

The different phases can have vastly different properties, making iron – carbon alloys widespread in their applications. For example, high-strength sheet steels are used by the automotive industry to improve the safety of cars and reduce their overall weight, thus improving their fuel efficiency. For this application, dual-phase steels containing both ferrite and martensite have been used for their high strength and ductility [14]. The presence of retained austenite during the plastic deformation of forming sheets brings an increase in ductility and work hardening [15]. Work hardening refers simply to the strengthening of a metal as it undergoes a plastic deformation. While most common steels have a strength around 200MPa, dual-phase steels containing retained austenite have been found to have strengths of up to 2000MPa or a 10x increase in strength [14] meaning they are more resistant to being deformed from their original shape. This can be achieved by adding relatively small amounts of alloying elements. For this reason, high strength low alloy (HSLA) steels have been widely used and investigated due to their properties [16][17].

### **1.3.3. Basics of alloying and the effects of precipitation on steels**

HSLA steels contain small amounts of microalloying elements, mainly other transition metals such as titanium, to alter their properties. These metals will combine with the carbon in the matrix and other elements such as nitrogen to form precipitates, which alter the steel properties on a macroscopic scale.

Many of the properties of steels come from the fact that they are metals and so have metallic bonding. In metallic bonding, the conduction electrons are free to move around the material and are shared by the positively charged metal ions. This type of bonding leads to many of the well-known properties of metals. For example, the strength of the electrostatic attraction between the free electrons and the metal cations means that a lot of energy is required to overcome it, leading to high melting points.

While strong, metallic bonding is not particularly directional. This leads to metals forming close packed structures in which it is relatively easy for different parts of the crystal to move relative to each other. This causes dislocations to form and move through the metal, by a process called slip. However, if dislocations can form and move easily throughout a structure, it means that the structure is not particularly strong, but it is tough and resistant to brittle

and uncontrolled fracture. In the case of many types of steels, strength is an important property and as such, the movement of dislocations needs to be slowed down and suppressed. This would effectively make it much harder for part of a crystal to move with respect to another part of the same crystal.

There are different ways to increase the strength of a steel and slow down the movement of dislocations, with dispersion/precipitation hardening being one of the most important. Precipitation hardening by encouraging the formation of small carbonitride precipitates has been commonly used for many years to increase the strength of hot rolled microalloyed steels [18]. Some studies suggest that the strengthening effect is obtained when the precipitates start nucleating in ferrite during or after the steel undergoes a phase transformation, with precipitates having formed in austenite at high temperature before the phase transformation to ferrite negatively affecting the strength by using up the limited amount of microalloying elements in the solution available to form precipitates [18]. However, other studies suggest that precipitates that have formed in the high-temperature austenite phase immediately after the steel has been rolled can also contribute to the overall increase in strength of the steel [19]. Apart from being able to form both in the ferrite and austenite phases, the precipitates can also nucleate during the austenite to ferrite phase transition, when they form along the interface between the two phases as they co-exist in the solution, which is called interphase precipitation. However, the exact time in the manufacturing process when the precipitates form will lead to different distributions and will alter their effects on the steel properties [20][21]. In fact, interphase precipitation has been identified as a common mechanism in which carbonitrides form in micro-alloyed steel, with the particles forming rapidly as the austenite – ferrite interphase boundary moves through the solid solution [22].

Strengthening the material by impeding dislocation motion is best achieved by the formation of many small precipitates. However, the microalloying elements can also form much larger particles, for example large cementite structures. The larger precipitates can also control the possible size of austenite grains by suppressing the movement of grain boundaries, and thus restricting grain growth, or by functioning as nucleation points for recrystallisation of grains in high temperature annealing after heavy deformation.

#### **1.3.4. Ti, V and Nb carbide precipitation**

As it has been briefly touched upon at the beginning of this chapter, there is a relatively large body of work investigating the precipitation behaviour of microalloying transition metals such as vanadium and niobium, and the influence this has on the steel properties. There is a smaller amount of published research on the effects of titanium, with the consequence that its effects on mechanical properties are less well understood. Furthermore, even less is known about combining titanium with vanadium and/or niobium. All normally combine with the carbon in the steel matrix, forming transition metal carbide precipitates [23]. These metal carbides have high hardness and melting points while not being particularly chemically reactive [24]. Additionally, the transition metals added as microalloying elements can also form nitrides

when they remove any nitrogen from the matrix (although this may be rather little in Al-containing steels, as this forms AlN at an early stage in the processing). Manganese sulphides have been observed during this project as well, in which case the manganese traps some of the sulphur impurities that would make the steel more brittle [25] [26]. All these precipitates tend to have an FCC rock-salt structure [27], which when forming in BCC ferrite will stop them from becoming circular (as when forming in FCC austenite) but will instead be plate-like. Their formation in both ferrite and austenite is shown in Figure 1.3, with orange and green showing atoms in the steel matrix and purple showing the metals in the precipitate. The small black circles represent the carbon atoms in the precipitate.

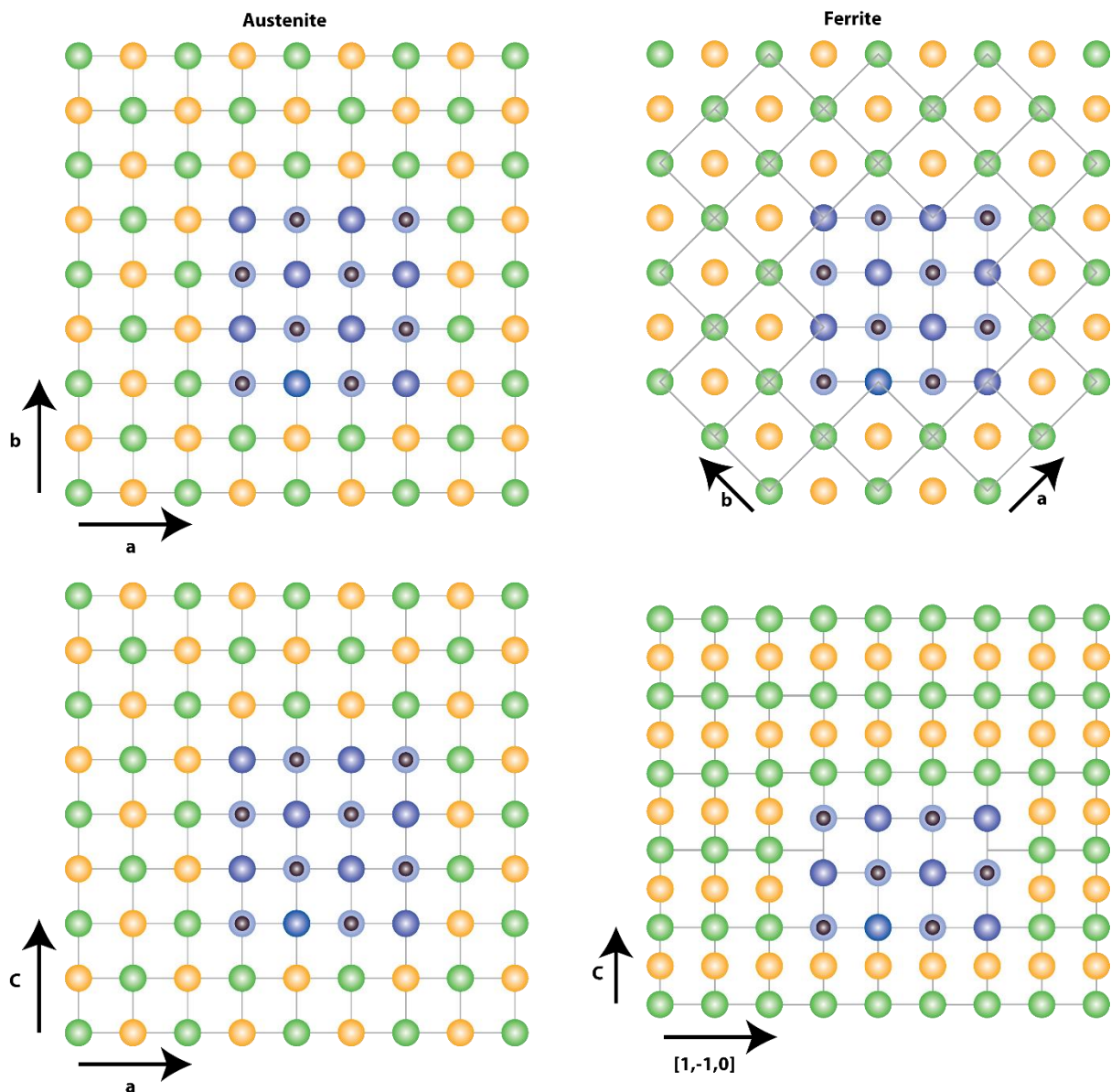


**Figure 1.3:** The formation of an FCC carbide precipitate in austenite (FCC) and ferrite (BCC) showing the difference in shape between the two resulting precipitates. The green and orange spheres represent the steel matrix, the purple represents the metal in the precipitates and the black the carbon in the precipitates. Figure made by Dr. Ian MacLaren and used with permission.

When the precipitates form in austenite, there is no difference in structure between the matrix and the precipitates that would stop the precipitates from forming along both the x and y directions. However, when they form in ferrite, the difference in structure between the FCC precipitate and the BCC matrix means that it is easier for the precipitate to expand its diameter along one axis than it is along the other one. This is because, along one axis, the lattice parameters of the matrix and the precipitate match so growth is easy. However, along the other axis they do not so precipitate growth along that axis causes a lot of strain hence requiring a large amount of energy which is why the precipitate is not growing along that direction. This causes the precipitates to form as plates rather than spheres, following the Baker - Nutting orientation relationship [28].

A comprehensive literature review conducted by Klinkenberg *et al.* [29] on the formation of NbC precipitates in microalloyed steel suggested that the final rolling and cooling conditions play a strong influence in the formation of the precipitates in either ferrite or at the  $\gamma$ - $\alpha$  interphase during phase transformations. One of the processing conditions found to be favouring the formation of NbC precipitates in ferrite is slow cooling from about 900°C with isothermal holding at 600°C or more and rapid cooling rates. Air cooling seemed to promote the formation of interphase precipitates. The precipitation of strain-induced NbC can be delayed by the addition of Ti [30]. This was suggested to be due to reduced supersaturation of Nb which is caused by stable (Ti, Nb) (C, N) remaining undissolved by reheating processes, which then act as nucleation sites for (Nb, Ti) C.

### **1.3.5. Methods for imaging nanoscale precipitates in steels**

Over the years, a few different methods to image steel precipitates have been developed, each having advantages and disadvantages.

Scanning Electron Microscopy, or SEM, can image large areas but can only provide information about the surface layers of a sample. It also cannot provide any information about nanoscale precipitates within the sample, only about large precipitates at the scale of several tens of nm, or larger. One of the first uses of a scanning electron microscope (SEM) to study the precipitation of steels comes from 1957 when Wilson used it to image carbides and nitrides in a steel at different stages in the tempering process [31].

Regular Transmission Electron Microscopy (TEM) studies of thin foils using diffraction contrast also allow us to image large areas with very good resolution. However, there are many sources of contrast and no chemical information is available. Early developments in TEM made the imaging of large cementite particles possible [32]. Precipitates with sizes of about 20nm in diameter were routinely seen in the 1970s, however it was strongly suspected that much smaller precipitates, of only a few nm in diameter, were forming in the steel matrix as well. However, these were not easy to find with the imaging capabilities of the time and it was only later that advances in microscope manufacture and analytical techniques made their analysis routine [33]. For example, rows of precipitates were seen in Nb-microalloyed steels isothermally held for a short time (10s) at temperatures between 650°C and 750°C by

Okamoto *et al.* [34]. The spacing between the planar rows of precipitates was observed to increase with increasing isothermal holding temperature, however it was suggested that the spacing between the rows of precipitates is likely to be affected by other conditions as well. Some irregularly spaced precipitates also formed alongside grain boundaries. When the hardness was measured with respect to holding temperature, it was seen to first increase until reaching a maximum, and then start to decrease with further increases in temperature. Charleux *et al.* [35] also looked at the interaction between precipitate strengthening and dislocation hardening in a Nb/Ti HSLA steel using diffraction contrast TEM. Very fine (about 1nm) Nb/ Ti needle shaped precipitates have been identified as causing strengthening, with their nucleation and growth happening mainly on ferrite dislocations. Additionally, large TiN precipitates (approximately 1 $\mu$ m in diameter) were found, together with grain boundary precipitates (about 10nm in diameter). Furthermore, Ray *et al.* [36] was able to study the precipitation in low carbon steel thin films and conclude that the addition of alloying elements had a significant impact on how, when and where the precipitates form within the steel.

Another TEM imaging technique uses extraction replicas, where the steel matrix is partially dissolved, the surface coated with a suitable material, and the precipitates and coating are extracted from the steel by further dissolution. This material is often carbon, but aluminium or copper can be used as well [37]. For example, it was used in making grain-size measurements of low-carbon high-strength steels with Ti, Nb and V added as microalloyed elements [38]. Grain sizes between 1 $\mu$ m and 5 $\mu$ m were observed in four different types of steel. Again, using extraction replicas one can cover large areas and a large number of precipitates can be extracted this way. However, all the microstructural context from the steel is lost when the matrix is dissolved, there is always the possibility that the smallest precipitates are dissolved and not extracted, and that the stoichiometry of precipitates is changed during the extraction process. Additionally, as the matrix is completely removed, volume fractions for the precipitates cannot be obtained.

Energy dispersive X-ray spectrometers available on commercial TEMs made some qualitative and quantitative chemical analysis possible [39]. Until recently, it has mainly been restricted to point analysis, and the signal to noise ratio (SNR) is usually low. While some quantification for heavier elements can be done, it is very difficult to quantify for carbon and nitrogen as they are light elements producing low energy X-rays that are easily reabsorbed in the sample [40]. In the area of steel precipitation, Craven *et al.* [41] looked at the precipitation of titanium and niobium in aluminium containing HSLA steels and concluded that TiN tends to form the cores of (Ti, Nb) (C, N) complex precipitates. The cooling rate applied to the steel during manufacturing affected the ratio of Nb to Ti in the precipitate cores, with the ratio being consistently smaller in the cores than overall in the steel. The cores were surrounded by a phase forming at lower temperatures, with varying compositions such as Nb (C, N), NbC and (Nb, Ti) C. However, they have also used EELS, described later, to study the structure of these precipitates. These are the types of precipitates that have been expected in the work presented in this thesis. This segregation of Ti and Nb was also noticed by Poths *et al.* [42] in

microalloyed plate steel, with a stable TiN centre forming surrounded by Nb carbonitrides. Reheating the steels at different temperatures suggested a decrease in the Nb content as the temperatures are increased. These results were also confirmed using a different method, this time EFTEM, which will be explained later.

At roughly the same time in the 1970s and 1980s as X-ray systems started being routinely used, electron energy loss spectroscopy (EELS) was introduced. In EELS, the amount of energy electrons lose when interacting with certain parts of the sample is measured. Initially, only EELS point analysis was possible with serial spectrometers, with the acquisition of a full spectrum taking a long amount of time [43].

By recreating an image from the electrons that have passed through the slit, a map showing where in the sample they have come from could be created. This is the main result of Energy Filtered TEM, introduced in the 1990s [44]. In EFTEM, the electrons being detected are first filtered so only those within a narrow range of energy losses are allowed to reach the detector and form the image [45]. A common method used to create EFTEM images is the three-window method, where a narrow energy window is recorded to span the edge of interest, with two background windows before the edge being recorded as well. A background in the area of the edge is then extrapolated from the two background windows and subtracted, leaving only the signal from the edge. This is then used to create a map showing the position of the imaged element within the mapped area [46]. The three windows and the background extrapolation are shown schematically in Figure 1.4, with the pre-edge backgrounds in blue, the extrapolated background shown in green and the signal used in mapping shown in orange.

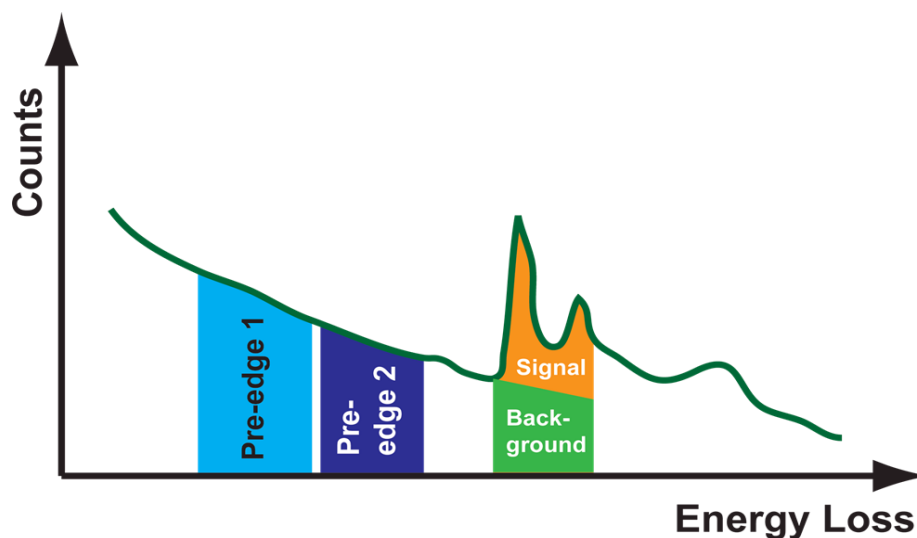


**Figure 1.4:** Diagram showing the 3-window method for mapping elemental edges using EFTEM. The two pre-edge windows allow for the background to be extrapolated to the region under the edge and then subtracted from the total signal, leaving only the signal from the edge behind. Figure made by Dr. Ian MacLaren and used with permission.

EFTEM allowed the imaging of carbon and nitrogen distributions alongside those of the metals [47]. Large areas can be mapped and the precipitates are left within the matrix, meaning that

the relationship between precipitates and the microstructure is preserved. However, faint signals from small precipitates are often hard to detect, with different sources of contrast contributing to the final image. This makes it incredibly difficult to quantify the chemical composition of particles using EFTEM. EFTEM has been used to quantify precipitate size distributions in a creep resistant 9% chromium steel used in fossil fuel power plants by mapping the chromium and vanadium edges [48]. Precipitates of the type  $M_{23}C_6$  and MX, where M represents one of the metals and X a non-metal, have been identified, with the first type having diameters in the 50-100nm range and the second type being much smaller, with most precipitates identified being between 10 and 30nm in diameter. However, it was assumed that the selected areas were representative of the entire steel structure, which was later shown not to be the case, suggesting that mapping larger areas at the same or better resolution would be necessary. Hofer et al. [49] quantified the precipitates in a 10% chromium steel using EFTEM and made a distinction between the different types of precipitates that form in the steel and the thermomechanical conditions that favoured their formation.

The next key development was the introduction of parallel spectrometers, also in the 1990s. These spectrometers use a scintillator able to turn the signal from incoming electrons into photons, and a detector (such as a CCD) sensitive to the position of the incoming photons. Parallel spectrometers have the advantage of being much faster than serial ones in acquiring data. There are a few things that differentiate parallel EELS from EFTEM, one of the main ones being reported by Krivanek et al. in 1995 [50] being the role of the objective lens in imaging. In EFTEM, the objective lens forms the images with the inelastically scattered electrons within the narrow energy window as defined by the slit, with the illumination being set to parallel rather than a small convergent beam [51]. These differences in the energy of electrons means that chromatic aberrations in the objective lens can have an important role in reducing the resolution. On the other hand, in STEM the objective lens focuses the almost monochromatic electron beam into a small probe that is then scanned across the sample, with the inelastically scattered electrons then being collected without further imaging by lenses that could introduce important chromatic aberrations. Aberrations decrease the resolution that can be attained when using EFTEM, and as an increase in collection angle can lead to further increase in the effect of aberrations, it also limits the amount of signal that can be collected in EFTEM. In current microscopes, EFTEM raises the microscope voltage so that energy loss electrons pass through the post-specimen lenses in an identical way to the zero-loss electrons in a bright field image. While EFTEM has been used extensively to map the position of precipitates within steels before, as well as to obtain information about their chemical composition, the limited resolution and collection efficiency that can be achieved means that the smallest precipitates might not be imaged effectively.

Unlike most of the methods introduced so far, EELS is best suited to analysis of smaller sample areas of the order of less than  $1\mu\text{m}$ . This has advantages over EFTEM in that it allows better spatial resolution, lower detection limits, and is less affected by crystallographic contrast. It

is also potentially much more quantitative and with care and good SNR data, allows for carbon and nitrogen analysis.

EELS mapping has now become more automatic, with the next major improvement being the introduction of EELS spectrum imaging (SI). This allows for the acquisition of spectra from each pixel of the mapped area, thus building a three dimensional dataset [52]. In 2010s, DualEELS was introduced, allowing for near-simultaneous acquisition of the full energy-loss spectrum, whereas before it was only possible to collect either just the electrons with small energy losses or those with large ones [53]. The introduction of DualEELS made the quantification of electron energy loss data much more straightforward by allowing the collection of a full spectrum using the same experimental parameters.

When it comes to using EELS to quantify the composition of precipitates, the usual method was to fit a background before an edge of interest and a signal window over the edge and integrate it, as described by Egerton [54]. However, this method depends on the choices of windows made by the user and is not very accurate, as will be discussed in detail in Chapters 3 and 6 in this thesis. A different method makes use of theoretically calculated cross-sections for the edges to be quantified and fits them using a multiple linear least squares (MLLS) fitting approach. There are different methods of calculating these theoretical cross-sections, such as the older hydrogenic model and the Hartree-Slater one [55]. The method has been used with hydrogenic cross-sections, for example, by Allison et al. [56] in an attempt to quantify the stoichiometry of vanadium carbide, one of the precipitates expected to be found in this research. However, the stoichiometry calculated using an MLLS fit with hydrogenic cross-sections was a lot less than the known one obtained by chemical analysis, suggesting that theoretical cross-sections are not the best way of accurately determining composition.

A procedure using “reference spectra” and MLLS with well-known formulas can be used for quantification as well, as it has been described by Courtois et al. [57] when studying the C/Nb and N/Nb ratios in nano-precipitates formed in ferrite treated under different conditions. After analysing a total number of 90 precipitates coming from three different steel samples, they identified precipitates as small as 3nm in diameter. Due to poor signal to noise ratio they were not been able to quantify precipitates smaller than about 6nm. However, this work did prove the presence of nitrogen in precipitates and was able to distinguish between carbides, nitrides and carbonitrides.

While STEM-EELS provides a way to accurately quantify particles inside a matrix, another useful alternative is atom probe tomography (APT). For this, a needle shaped specimen is needed and is placed under high voltage in a vacuum chamber. Small impulses are applied on top of the high voltage, which cause the ejection of individual atoms. Essentially, ions from its surface are evaporated and detected at the end of the cryo chamber some distance away. The time of flight of these ions depends on their mass to charge ratio, which gives access to chemical information and the ability to create a 3D map of the sample area [58] [59].

The sampled volumes when using APT are even smaller than that available with EELS, but APT is significantly better for detecting small amounts of elements, since a very high fraction of the evaporated ions are detected and quantified. Small amounts of carbon in the matrix can be detected, so the early formation of precipitates and carbon diffusion along boundaries can be imaged. However, the volume statistics are poor due to the limited volume being sampled, but the technique complements EELS particularly well.

Early studies were able to reconstruct the sample in one dimension, such as a study by Thuvander et al. [60] that looked at the composition of a range of metal carbides. However, limitations in the detectors meant that many events where multiple ions were coming from adjacent sites in the sample were not detected properly, leading to lower carbon concentrations than what was expected from the known stoichiometry. As carbon is one of the main components in precipitates, this was a major issue with APT at the time.

As it is now possible to reconstruct the data in three dimensions (3DAPT), the distribution of precipitates within the steel matrix can be obtained more accurately. Nohrer et al. [61] combined 3DAPT and TEM to investigate the precipitation of vanadium in ferrite and austenite after a series of thermo-mechanical treatments. Precipitates were not found in the austenite; however, two types were seen to have formed in the ferrite. Interphase precipitates, forming at the boundaries between different phases of the steel, were found to contain vanadium, carbon and manganese while precipitates distributed randomly throughout the ferrite matrix contained vanadium, carbon and nitrogen but no manganese. In this case TEM was used to distinguish between areas of ferrite and martensite in the steel, with diffraction patterns showing spots from both the ferrite and from some of the vanadium-rich precipitates. Kapoor et al. [62] has used both STEM and APT to study (Nb,Ti)C and (Nb,Ti)(C,N) precipitates in HSLA steels and found the amount of niobium decreasing as the precipitate size increased. However, in some cases the whole precipitate could not be captured using APT, and most precipitates captured were larger than the ones we have identified using our STEM-EELS method. In some cases, large discrepancies in the carbon content of enriched regions in bainite measured by APT and by other methods such as X-ray diffraction (XRD) have been reported (Rememteria *et al.* 2017) [63], with the APT consistently reporting smaller concentrations of carbon than XRD. APT alone does not allow for the complete identification of such carbon rich regions, and other forms of analytical electron microscopy are often needed to reveal the nature of the phases being imaged. For very small concentrations, the minimum concentration of carbon that could have been detected in the matrix was limited by the sources of background signal. While these can be corrected for, the procedure could introduce further errors. On the other hand, the STEM-EELS method used in this thesis was able to identify very small concentrations of a given element (errors of  $\pm$  few atoms across the diameter of a precipitate) in matrices of over 100nm in thickness.

While both APT and STEM are useful techniques on their own, analysing the same steels using both techniques can provide a lot more information. This has been suggested before by

Craven et al. [64] when also investigating vanadium precipitates in micro-alloyed steels using APT and EELS. Combining both methods reduces or even eliminates the disadvantages of each individual technique. For example, STEM can give information about the microstructure of steel, such as the size of grains, while APT cannot. Similarly, the ability to map in 3D is not available in STEM but is an integral part of 3DAPT.

#### **1.4. Summary**

The aim of this European Commission funded project was to study the precipitation of titanium in conjunction with niobium and vanadium in industrial steels.

While many methods of imaging precipitates do exist, they all have disadvantages. SEM can image large areas but can only provide surface information. Diffraction contrast TEM images large areas of thin foils at high resolution but the many sources of contrast make distinguishing precipitates difficult and there is no chemical information. By comparison, finding precipitates is much easier when using extraction replicas, however the matrix is dissolved during the extraction process meaning that the relationship between precipitates and the microstructure is lost.

Early developments in EELS and EFTEM allowed for better resolution and chemical mapping when imaging precipitates. Further developments, such as EELS spectrum imaging and then DualEELS, made accurate quantification possible. The sample volumes that can be imaged with EELS are much smaller than, for example, the volumes that can be imaged using diffraction contrast TEM, but small precipitates can be easily detected, and their composition investigated.

Even smaller sample volumes are imaged when using 3DAPT, however the technique allows for small amounts of elements to be detected which means precipitates can be imaged just as they form. This technique works particularly well when combined with EELS spectrum imaging.

At the University of Glasgow, we have used EELS to measure the distribution, size and chemistry of these precipitates. The size and distribution were measured using low-loss EELS over large areas of the steel matrix. Once precipitates were identified, some were selected for accurate chemical analysis using DualEELS. Significant progress has been achieved during this research with both techniques, especially with the data analysis required. The next chapter will discuss how the steel samples were prepared to allow imaging in the STEM, the basic layout of a TEM and introduce the main technique used for imaging, EELS.

## Chapter 2

### Sample preparation and Instrumentation

In order to be able to analyse the chemical structure and distribution of precipitates within a steel matrix using scanning transmission electron microscopy (STEM), the steels need to first be prepared as thin (<100nm) cross-section samples. These are often fabricated using focused ion beam (FIB) techniques, particularly the FIB lift-out method, which has been used for the preparation of each cross-section (lamella) sample used during this PhD. Some samples had to be prepared as needle specimens for electron energy loss spectroscopy (EELS) experimental cross-section analysis. Once prepared, the samples were imaged and analysed using EELS in a JEOL transmission electron microscope (TEM) operated in scanning mode. This has been possible thanks to the many advances in electron microscope instrumentation, particularly aberration correction and Dual EELS.

This chapter begins by introducing the FIB microscope and describing a standard lift-out method in detail. During the course of the PhD research it became possible to prepare cross-section samples using both a xenon beam FIB in addition to the more long-standing gallium beam FIB, and the key differences between the two instruments are presented. The method used for the preparation of needle shaped samples is described. Following this, a description of the standard TEM is given and followed by a discussion of scanning transmission electron microscopy (STEM). Finally, EELS is presented in detail, including the hardware used as well as the many features in an EEL spectrum.

#### 2.1. Focused ion beam (FIB)

##### 2.1.1. The FIB instrument

FIBs, and especially systems combining FIB and scanning electron microscopy (SEM), have gained popularity in the last decades due to their ability to both prepare site-specific samples and image them at the same time. A major advantage is the fact that they can be used to prepare cross-sections from a large variety of materials. [65]

The FIB-SEM instrument consists of a vacuum system and chamber, an ion source, an ion column, an electron source, an electron column, a movable stage that the sample is placed up on and a range of detectors. The ion source is usually a liquid metal, most commonly gallium [66], but more recently noble gases such as xenon as well [67][68]. Figure 2.1 shows a diagram of the basic FIB - SEM instrument with the components mentioned above. In the case of the microscopes used during this PhD, the Helios Xenon Plasma FIB and the Nova Gallium FIB, both manufactured by FEI (now Thermo Fisher Scientific), the ion column is at an angle of 52° to the electron column, which is perpendicular to the sample stage as can be seen from the diagram in Figure 2.1. This means that for the ion beam to be perpendicular to the sample and mill straight down it, the stage has to be tilted at an angle of 52°.

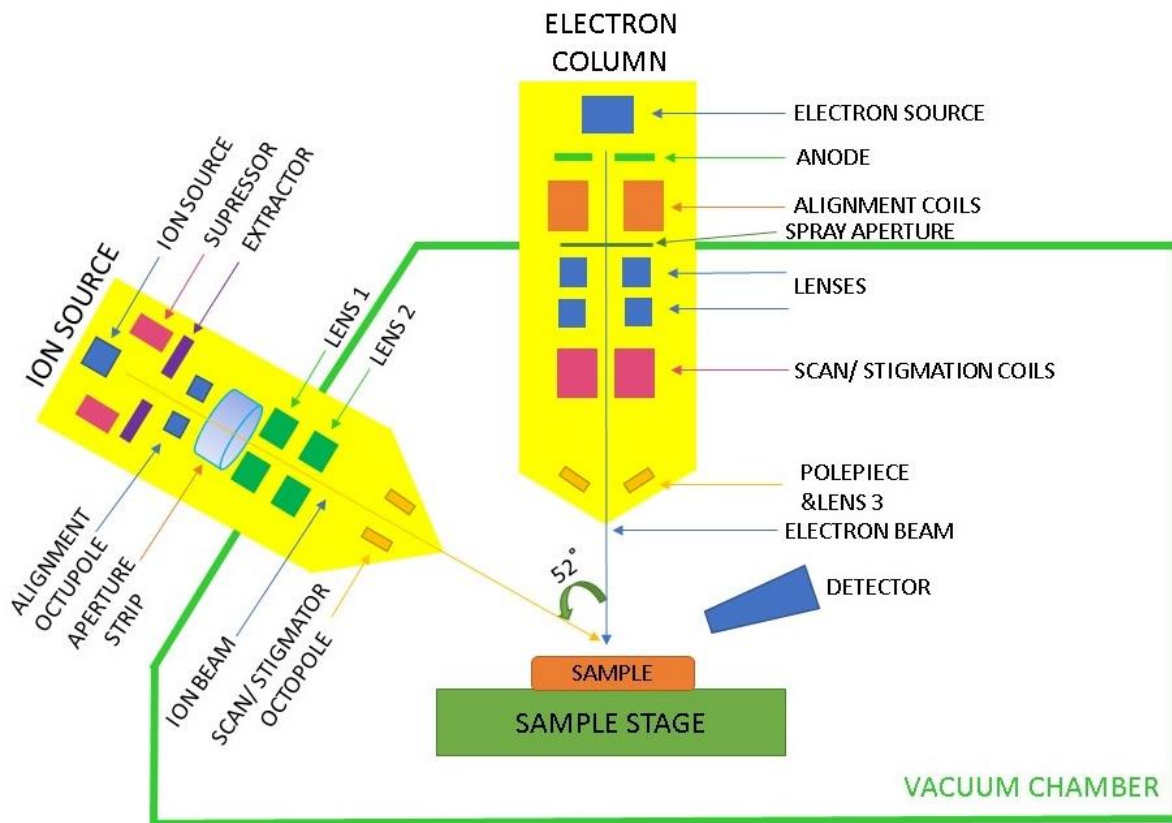


**Figure 2.1:** Schematic diagram of a FIB – SEM instrument showing the main components, including the ion and electron columns and the position of a typical detector.

Most FIBs accelerate the ions in the beam to energies of up to 30keV. The ion beam can sputter (remove) atoms from the surface of the sample in a process known as milling. Focus is performed by an objective lens (labelled Lens 1 in Figure 2.1) found in the ion column with a further condenser lens (labelled Lens 2) forming the beam. The lenses in the ion column of a FIB are electrostatic rather than magnetic, as ions are much heavier than electrons, hence much harder to move and steer using magnetic lenses. A moving set of apertures located before the electrostatic lenses can be selected from the user interface. These are used to select from a range of available ion currents. Available currents usually vary from a few pA to a few nA, with higher beam currents being available on xenon noble gas instruments up to  $\mu\text{A}$  [69]. A gas injector is used for injecting the platinum for deposition of the sample surface.

### 2.1.2. The FIB lift-out method

The lift-out approach was originally proposed by Overwijk *et al.* [70] and involves cutting a cross-section of the material using different milling patterns, currents and tilt angles, using a micromanipulator to lift the section from the bulk and then attaching it to a grid where it is thinned down. Most of the milling is done with 30keV beam energy, with just the final steps being done at lower beam energies of 5keV and 2keV to remove the surface damage caused by the high energy beam. The beam current usually ranges between a few pA to a few nA. By tilting the stage at different tilting angles different faces of the sample can be exposed to the

beam so the sample can be thinned from different directions. The beam currents are progressively reduced as the sample gets thinner [71]. The sample must be electron transparent to be used in for STEM-EELS data acquisition. During this PhD, EELS data was acquired using a 200keV beam of electrons, and in this case the sample had to be 100nm or less in thickness to minimise the number of multiple scattering events the electrons from the beam would undergo when going through the sample.

The exact milling steps have been optimised to apply to the steel samples made during this PhD with the Helios Xenon PFIB. Once a suitable part of the sample has been identified, a protective layer of platinum and carbon is deposited on top. First a small amount of Pt of about 500nm in thickness is deposited using the electron beam, then a thicker one (about 3 $\mu$ m thick) is deposited using the ion beam. The platinum layer deposited on the surface is shown in Figure 2.2a). The reason for this is that electron deposited Pt will form smaller metal particles in the layer, making the milling steps undertaken later smoother [72]. Trenches are then cut lengthwise on each side of the sample in a series of three steps, with the resulting cross-section shown in Figure 2.2b). Using the nomenclature used in the FEI user interface software and the parameters adapted for using the FEI Helios instrument with the Xe beam, the steps are described below:

1. With the ion beam perpendicular to the sample (stage tilt angle of 52°) and a Regular Cross-Section milling pattern (mills a staircase shaped pattern), large trenches are cut on each side of the lamella using high beam currents (59nA) with a 30keV beam. This beam has a diameter of about 2.4 $\mu$ m, so the patterns were placed away from the cross-section to avoid milling into it.
2. Still maintaining a stage tilt of 52°, rectangle patterns are now milled on both sides of the sample. The same beam voltage is used, but the current is decreased to 16nA, with the beam having a smaller diameter than before.
3. Lastly, a Cleaning Cross-Section pattern (slowly scans a rectangular pattern towards one side) is used. The beam current is decreased again to 9nA, making its diameter even smaller. Here the ion beam is not perpendicular to the sample anymore but instead has a 2° angle to each of the sample surfaces (in practice, 50° and 54° stage tilts are used).

Next, the sample is separated from the bulk. First, side trenches are milled deep below the lamella to avoid damage to the sample. Next, a “J-shaped” cut is made, composed of three rectangles on the sides of the lamella, which leaves it attached to the bulk in only one place, as shown in Figure 2.2c).

A micromanipulator needle is then attached to the free side of the cross-section using platinum, and the entire section is then milled free from the bulk. The micromanipulator and sample are lifted away from the bulk, with the sample then being attached to a copper grid using platinum deposition before being thinned down. Figure 2.2d) shows the sample and the micromanipulator (bottom of the image), together with the grid.

Once the sample is attached to the grid it can be thinned. As the lifted cross-section is  $> 1\mu\text{m}$  thick, a beam of 30keV and high currents (59nA) were used in the initial steps. This was done to mill most of the material away quickly to speed up the process. The beam currents are progressively reduced, to 15nA and then 6nA. For uniform thinning, milling is done from both sides. This is achieved by tilting the sample  $\pm 2^\circ$  relative to the ion column. Long samples can have progressively smaller sections thinned as the beam current is decreased, with only the far end of the cross-section being milled to the final thickness. This is shown in Figure 2.2e) in top-down view and Figure 2.2f) in side-view with respect to the ion beam. The last section is the thinnest and the bright layer at the top of the image represents the protective platinum layer that was left on the sample.

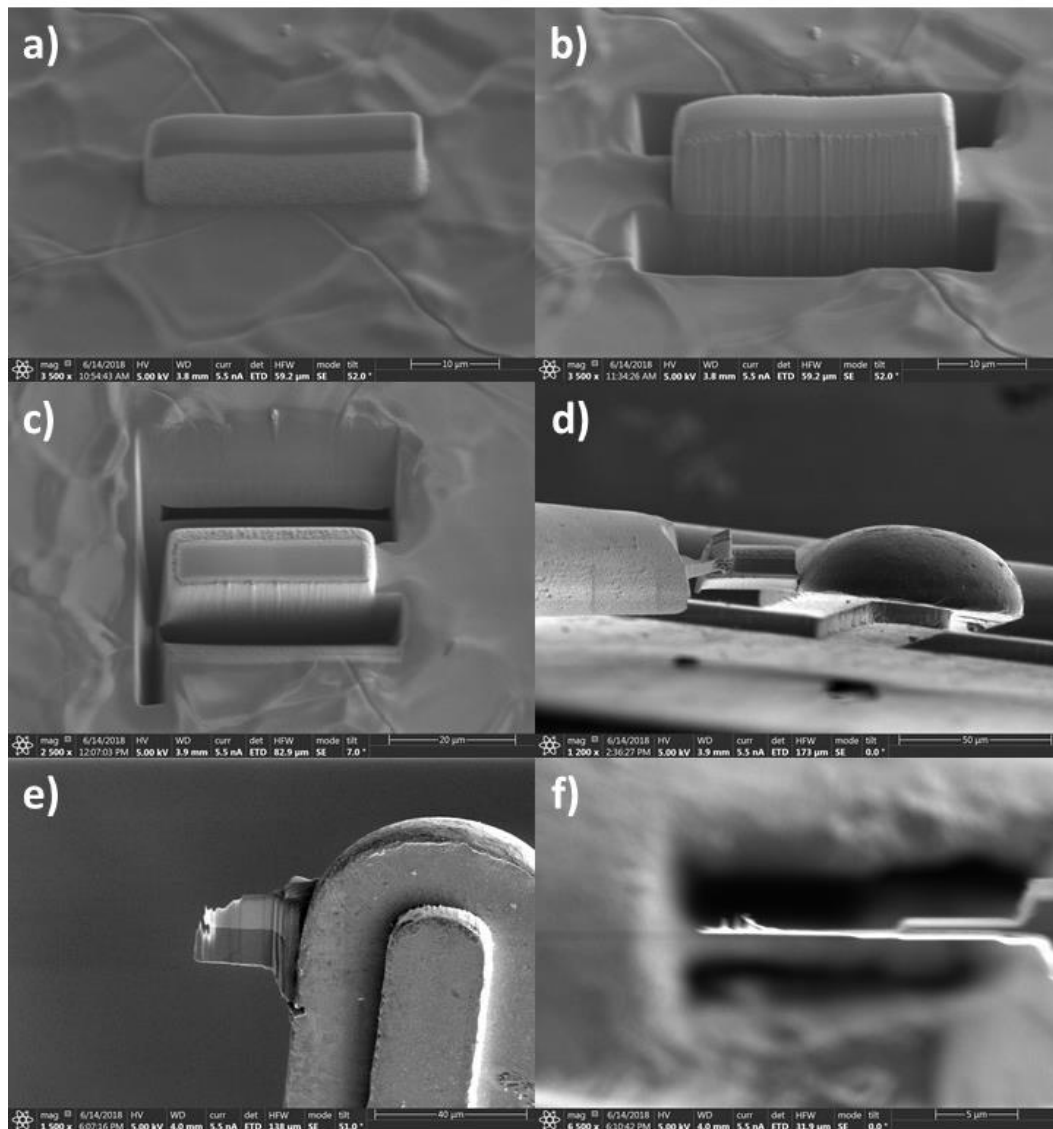


**Figure 2.2:** The FIB sample preparation process for a TEM cross-section with a) the protective platinum layer on the surface, b) the cross-section after side-trenches have been milled from the bulk, c) the J-cut to release the sample, d) the sample attached to the micromanipulator being moved towards the copper grid, e) top-down view of the sample being milled down to electron transparency and f) a side-view of the final thinned sample.

Ion beam milling introduces damage to the samples by surface amorphization, and ion implantation can be a problem, especially in the case of Ga<sup>+</sup> FIBs [73]. This is minimised by depositing a sacrificial layer of platinum at the beginning to protect the sample surface but is not fully avoided. Therefore, for the final preparation steps the sample is cleaned using low-energy ion beams to reduce the surface damage and contamination induced by the previous steps [74]. This is done for short times using 5keV and 2keV ion beams with the sample at  $\pm 1^\circ$  to the ion column.

### **2.1.3. Differences between Ga and Xe ion beams**

There are many differences between using xenon plasma beams as compared to using gallium beams. In many cases and material systems such as semiconductors, gallium implantation and the damage to the sample are major drawbacks. The use of a Xe<sup>+</sup> beam means that gallium implantation would not be an issue [75]. Additionally, with gallium there is the possibility of chemical interactions with the sample being milled [76]. With xenon being a noble gas, this is not a possibility making noble gas beams a particularly attractive alternative in the case of gallium sensitive materials [69].

The range of currents available differs greatly between the two types of beams, with a large range from a few pA to a few  $\mu$ A available when using a plasma FIB. By comparison, a typical Gallium liquid metal ion source (LMIS) FIB has a much smaller range of available beam currents, usually from around 1pA to a few tens of nA. In the case of xenon plasma FIBs, when sufficient demagnification is available in the ion column, sub-25nm spot sizes are achievable with a beam energy of 30keV and a beam current of 1pA. At large beam currents, above 50nA, the energy spread is such that the source exhibits higher beam current densities than the LMIS-FIB [77] [78].

When using low-currents, the resolution of the Ga FIB is superior to that of the Xe FIB, however the situation is reversed at high currents. This is simply due to the form of the ion source, with the gallium source being a fine tip while the plasma source is a cavity with a larger diameter exit aperture [69]. The large currents available when using a Xe FIB mean that much faster bulk milling is possible, so preparing large structures is much more time effective [79]. However, when milling with low currents, the Ga FIB produces more precisely defined structures due to the better resolution as it has a smaller diameter beam.

### **2.1.4. Needle sample preparation**

Needle shaped samples were produced for calibration purposes, as explained in Chapter 6. The shape was chosen as a conical sample provides a range of thicknesses over its length; rotating the sample by 90° to acquire an HAADF image after acquiring a spectrum image provides a direct measure of the thickness of the material in the spectrum image. The needle sample has to taper to less than 100nm diameter, and manufacturing one with a perfectly

circular cross-section given these requirements is difficult. The preparation method has been adapted from the one used by Miller *et al.* [80] to prepare atom probe specimens.

The initial preparation stages are the same as when preparing a cross-section sample using the FIB [81]. A protective layer of platinum is deposited on the surface, followed by a section of the sample being lifted out and deposited onto a TEM grid. However, instead of depositing the section on the side of the TEM holder, it is deposited on top of the holder as shown in Figure 2.3. Figure 2.3 shows the copper holder after it was annularly milled to have a rough circular shape first. This is the case as it was noticed that the sample deposits onto the holder better this way.

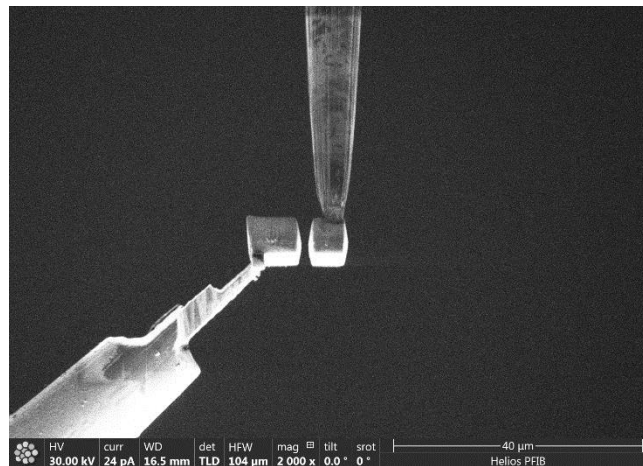


**Figure 2.3:** The sample being deposited on top of an annularly milled grid to be milled into a needle shape.

Once the lifted section is deposited, an annular milling pattern was used to produce a sharp needle. The initial outer diameter of the annular pattern is selected to be slightly larger than the cross-section of the specimen being prepared. The inner diameter and the milling current are then progressively reduced to get the desired diameter of the needle. While it is usually suggested (from discussions with FEI application specialists) that the outer diameter is kept at the same diameter throughout the sample preparation to minimise misalignments due to small amounts of sample drift, it was found that decreasing it in incremental steps along with the inner diameter is much more time efficient and does not affect the final sample. However, care must be taken to not move the pattern during or in-between milling steps and to keep it centred on the centre of the needle being milled. Once a suitable diameter is reached, the sample is cleaned with a low energy beam similar to cross-section samples.

The end radius of the specimen tends to be a few nm smaller than the final inner diameter of the pattern due to the beam tails. Here a significant difference was noticed between using a Gallium beam versus a Xenon beam. At the low currents required for the final annular milling stages, the diameter of the Xenon beam is much larger than that of the Gallium beam, making it more difficult to maintain the cylindrical shape of the sample while reaching an appropriate diameter.

Obtaining a thin enough needle sample from the materials needed for this research has been a challenge, but the following have been found to help during preparation:

- milling the top of the copper TEM grid into a rough circular post not much larger than the section lifted from the bulk makes it much easier to attach the sample to the post before starting the annular milling
- the sample is milled height-wise and lost very quickly once the platinum layer disappears, so adding a thicker sacrificial layer (approx. 10 microns thick) has helped with decreasing the needle diameter at which the sample starts getting milled away
- increasing the carbon content of the sacrificial platinum layer makes it much harder to mill it away, so adjusting the flow of carbon from 2% to about 5% has helped.

Sample selection is important as well. Ideally, the sample should have a fairly high density throughout. Some of the initial samples used for needle preparation in this research contained many voids within the material, which meant that the needle would fail at a void somewhere. A different bulk material was obtained, and the one containing voids was only used for preparing TEM lamellas.

## 2.2. Transmission electron microscopy (TEM)

### 2.2.1. The use of electrons for imaging

The resolution of light or electron microscopes is limited by the wavelength of the radiation used in imaging, be it or photons electrons. This resolution limit  $R$  is given by the Abbe diffraction limit, where  $NA$  is the numerical aperture of the microscope and  $\lambda$  is the wavelength of the light used:

$$R = \frac{\lambda}{2NA} \quad (2.1)$$

Assuming a typical wavelength of light of 500nm, the maximum resolution that can be achieved given the Abbe limit is of 250nm. To achieve higher resolutions, radiation with smaller wavelengths needs to be used for imaging.

In 1925, Louis de Broglie postulated that electrons behave as both a particle and a wave, with a wavelength significantly smaller than that of visible light [45]. The idea of using electrons in a microscope was proposed not long after, with Knoll and Ruska first using the term in a paper in 1932 [82]. While heavier particles such as ions would, in principle, have even smaller wavelengths, electrons have the advantage of being easy to produce and light enough to steer and focus easily using magnetic fields.

Electron microscopes surpassed the resolution of light microscopes a year later [45]. They have continued to be optimised ever since, with resolutions of  $<2\text{\AA}$  with 200kV electrons being achieved without aberration correction. In modern, aberration-corrected TEMs, a

resolution of a few tens of picometers is possible, making atomic resolution routinely accessible.

The basic outline of a transmission electron microscope consists of a source of electrons, a condenser system, a sample, an objective lens, projector lenses and finally a system to detect the transmitted electrons.

### **2.2.1. a) Electron sources**

There are two types of electron sources that are bright enough to be used in an electron microscope: thermionic and field-emission. Thermionic sources can be tungsten filaments or more commonly now, lanthanum hexaboride ( $\text{LaB}_6$ ) crystals [83]. These sources produce electrons when they are heated. Field emitters are sharp tungsten needles and produce electrons when a large potential is applied between them and an anode. Schottky emitters combine the two by using both heat and field emission. The sources are part of what is called an “electron gun”.

As the research presented in this thesis was done using a TEM with a cold field emission gun (FEG), this will be the only type of source presented in more detail in this sub-section. A cold FEG consists of a sharp tungsten tip followed by two anodes. The tip needs to be sharp in order to enhance the applied electric field at the tip up to the point where electrons tunnel out.

For field emission to be possible, the surface of the tungsten tip needs to be free of any contamination or oxides, so the gun must be operated under ultra-high vacuum conditions. In this case the gun is operated at room temperature, hence the name “cold FEG” [84].

This gun provides a narrow beam, however, there are instabilities in the emission and the extracted current does decrease with time. Contamination on the gun builds up due to the large electrostatic field in the gun area, with a negatively charged gun and a positively charged cathode. Any molecules present in the area will be ionised, with the positive ion attaching itself to the negatively charged electron source, thus contaminating it. Thus, the tip must be “flashed” regularly (by heating briefly with the extraction voltage turned off) during use to prevent contamination built-up.

### **2.2.1. b) The condenser system**

The condenser system consists of two condenser lenses, C1 and C2, as well as shift-and-tilt coils above and below the condenser.

The condenser system controls the illumination of the sample, with the gun cross-over at the condenser acting as a source for the illumination system. The position of the C1 cross-over, as seen in Figure 2.4a), depends on how strong the C1 lens is, with the job of the C1 lens being to further de-magnify the beam coming out of the gun. The position of this cross-over point then affects the size of the probe that the C2 lens can form, which then transfers the de-

magnified beam further down the column. A weak C1 lens will allow more current passing towards the C2 lens, however, will give less source demagnification leading to a larger probe diameter. Increasing the strength of the C1 lens will lead to less current passing towards C2, however it will cause more demagnification thus leading to a finer probe. The size of the C2 lens aperture determines how convergent the beam hitting the specimen is. A measure of this is the convergence angle  $\alpha$ .

The standard mode for operating in STEM involves a convergent beam being scanned across the sample, which is illustrated schematically in Figure 2.4a). Using the upper polepiece of the objective lens as a third condenser lens gives large convergence angles  $\alpha$  with the smallest possible probe.

Above the C1 lens there are two gun-shift and -tilt coils which align the gun with the C1 lens. Below the C2 lens there are beam tilt and shift coils, which align the beam coming out of the C2 lens with the rest of the electron microscope column and towards the objective lens. For simplicity these have not been shown on the diagram in Figure 2.4.

In the JEOL ARM200 microscope used in this research, there is an aberration corrector between the C2 and C3 lenses. This is shown as a single component in Figure 2.4a) for simplicity but is composed of a series of elements. This will be described in more detail in Section 2.3.3.

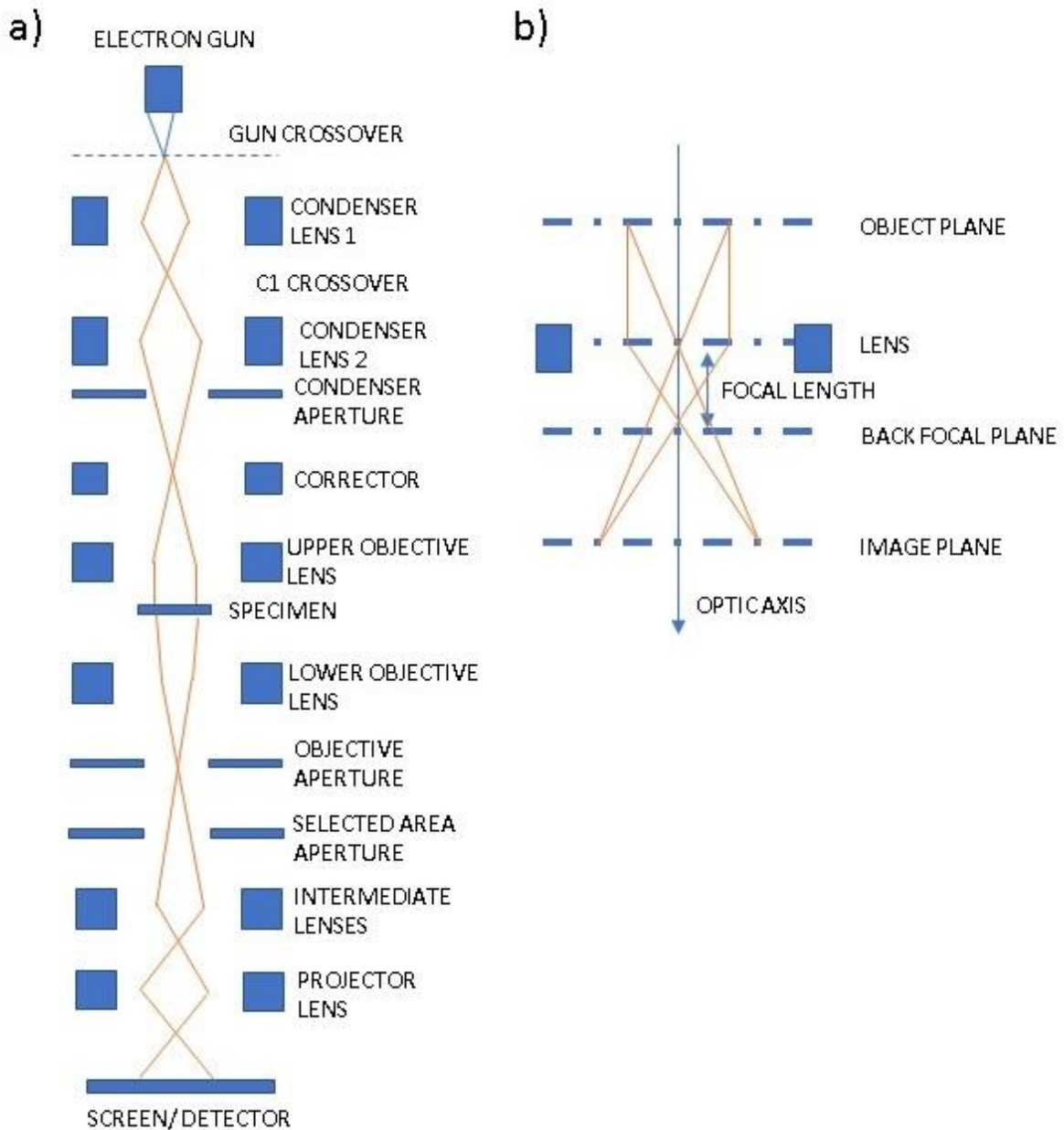


**Figure 2.4:** a) Schematic diagram of the setup for convergent beam TEM showing the condenser lenses, spherical aberration corrector, objective lens, apertures and projection lenses and b) the principal planes including the object, back focal and image plane.

### 2.2.1. c) The objective lens

The objective lens focuses the electrons leaving the sample, forming the first magnified image of the specimen. Once the electrons have interacted with the sample, those who have left the object plane in the same direction are focused in the back focal, thus producing a diffraction pattern. The back focal plane and imaging plane are shown schematically in Figure 2.4 b)

In order to project an image on the detector, the object plane has to be the image plane of the objective lens. This is achieved by adjusting the first post-specimen lens.

The objective lens is significantly stronger than all the other lenses in a TEM. Usually, the upper and lower polepieces are separated, meaning that both the specimen and an aperture can be inserted between the polepieces into the centre of the objective lens.

#### **2.2.1. d) Post specimen lenses**

The post-specimen projector lenses magnify and project the image of the sample or its diffraction pattern onto the detector. Together they form the projection system as shown schematically in Figure 2.4a), where it includes the intermediate lens and the projector lens. The coupling between the TEM system and the EELS system is provided by these post-specimen lenses, the programming of which has been optimised for specific applications in the case of the Glasgow JEOL ARM200F used in this research.

#### **2.2.1. e) Detectors and the charged coupled device (CCD)**

Charged coupled devices (CCDs) are one of the most common methods used to readout the signals available from a TEM. CCDs are made of arrays of many pixels which are individual capacitors isolated from each other. The pixels accumulate charge generated by the incoming electrons proportionally to the numbers of electrons hitting a given pixel. At their most basic, CCDs convert light into charge. However, the radiation source in this case is electrons, meaning that a scintillator must convert the incoming electrons into light first. In order to create an image, the arrays need to be read. This is done by transferring the charge serially from each pixel in the array into the output at the edge of the chip. Once all the pixels have been emptied of charge the CCD array can be exposed again and a new image recorded. Often, the detection limits and the amplifier noise levels of the CCD is what limits the data. For the high-loss spectrum where the number of counts is small, larger integration times are needed to get an appropriate signal to noise ratio because of the noise intrinsic in the CCD recording and readout.

### **2.3. Scanning transmission electron microscopy (STEM)**

#### **2.3.1. Outline**

In STEM, a focused electron beam is scanned across the sample in a raster pattern similar to that of a scanning electron microscope, however in the case of STEM it is the transmitted electrons (or other signals) that are detected. Moving the beam in a raster pattern to scan is achieved by adjusting the scan coils. In the case of STEM, the objective lens is used to focus the beam. The size of the beam, limited by diffraction and aberrations of the objective lens, is the main limiting factor of resolution in the STEM.

One of the main advantages STEM has over TEM is that in STEM it is possible to use signals which cannot be spatially correlated in the TEM. Examples of these signals are secondary

electrons, high-angle incoherently-scattered electrons, characteristic X-rays and, perhaps most importantly for the research presented in this thesis, energy loss electrons.

### **2.3.2. STEM bright, annular dark and high angle annular dark field**

In STEM, the transmitted electrons are collected using annular detectors. Three annular detectors are routinely used for image formation in a STEM: the bright field detector, placed on the optic axis, the annular dark field detector and the high angle annular dark field (HAADF) detector.

The ADF detector images the electrons that have been scattered by small or medium angles. The HAADF detector then detects the electrons that have been scattered at high angles and incoherently. This detection is highly sensitive to the type of atoms the electrons in the beam have interacted with, with heavier atoms appearing as brighter and easier to detect. Thus, the main form of contrast is Z-contrast [85], although some diffraction and channelling effects also contribute [86].

While acquiring EELS data, only the ADF and HAADF detectors are used as the BF detector would sit in the beam path of the transmitted electrons.

### **2.3.3. Aberrations in the STEM and correction for them**

#### **2.3.3. a) Astigmatism**

Astigmatism occurs when electrons travel through a non-uniform magnetic field as they travel around the optic axis in a spiral path. This can occur, for example, because the lens polepieces are not perfectly symmetric, thus distorting the image formed. Further distortion occurs due to the lenses having inhomogeneities in their microstructure, the apertures introduced not being perfectly centred around the optic axis, or contaminant particles on the aperture edges charging and thus deflecting the beam. Astigmatism can be seen as streaking in an image, which changes when passing through focus. An image streaking in the X direction will change to streaking in the Y direction when passing through focus from an under-focussed to an over-focussed image. At perfect focus the streaking is not visible, but the image will not be as sharp as a non-astigmatic image.

Astigmatism is easily corrected using stigmators, which are small octupole lenses that introduce a compensating field to balance out the inhomogeneities introduced by the main microscope lenses. There are stigmators for the condenser lens in the illumination system, and in the imaging system for the objective lens.

#### **2.3.3. b) Spherical aberration**

The most significant aberration in electron lenses is spherical aberration, which occurs due to the lens field behaving differently for on- and off-axis rays. This is explained schematically in Figure 2.6, showing that the further away from the optic axis an electron is, the stronger its

path is bent towards the axis. This causes the image of a point to not be a point, but instead a central high intensity region surrounded by a halo of decreasing intensity.

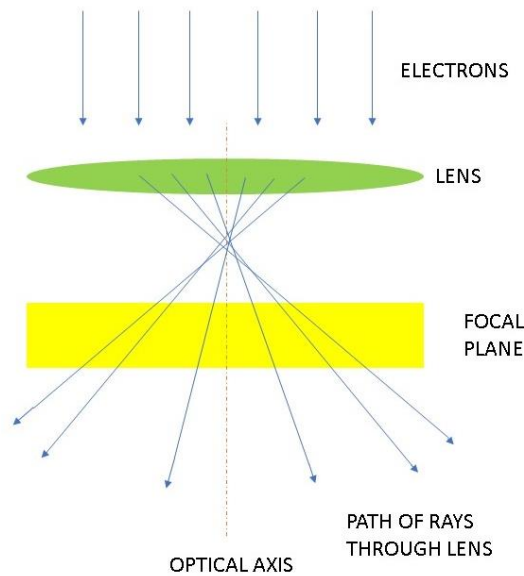


**Figure 2.5:** Diagram of electron paths through a lens when affected by spherical aberration, with the rays furthest away from the optical axis being affected the most.

Spherical aberration is an inevitable property of all electron lenses, as they are all round lenses with positive focal length. This means that all electron microscopes having only cylindrical lenses will have positive spherical aberration [87]. Careful microscope and lens design can minimise its effects, but never completely eliminate them.

Spherical aberration in the objective lens degrades the details that can be resolved in a TEM image, and all the following lenses in the column magnify the aberrations introduced by it. In a STEM, spherical aberration in the condenser lenses limits the size of the probe that can be formed while having the most current.

While spherical aberration can now be corrected for, it still limits the resolution of most TEMs. Spherical aberration correctors are non-cylindrical, multipole lenses that produce negative spherical aberration in certain directions where a diverging effect is created. A combination of two or more multipole lenses can negate the effects of positive spherical aberration introduced by the cylindrical electron lenses. A spherical aberration corrector compensates for the spread of a point image into a disk by making the off-axis beams converge to a point rather than a disk in the image plane. The correction is achieved by a computer-controlled set of quadrupoles and octupoles or a set of hexapoles.

In terms of the research presented in this thesis, the microscope used uses a Rose-Haider hexapole design to correct for the spherical aberration and other low order aberrations such as astigmatism, at the expense of higher order aberrations [88]. Having aberration correction means that larger convergence angles  $\alpha$  can be used. Without aberration correction the maximum convergence angle that could be achieved is approximately 10mrad while still being

able to use small spot sizes [40], however with the correction convergence angles of 36mrad have been used in this research. This leads to an increase in the available electron intensity that can be used, as it leads to an approximately three times greater angle of incidence hence resolution up to three times smaller as calculated using the Abbe criterion. While not used in the research presented in this thesis, atomic resolution is easily achievable with aberration correction. However, spherical aberration correction has been incredibly useful in the case of the EELS data acquisition for this research. A three times greater angle of incidence leads to nine times as much intensity from the tip useable in the beam, making the acquisition of spectroscopy data almost one order of magnitude faster. This has been useful when acquiring high signal to noise ratio data using EELS. While not used in this research, the same would be true for energy dispersive X-ray (EDX) data acquisition.

#### **2.3.4. c) Chromatic aberration**

Chromatic aberration occurs due to the fact that electrons of different energies have different focal points in a lens, with lower energy electrons being focused more strongly.

Especially for lower voltages, chromatic aberrations can seriously limit the resolution of a microscope in the probe formation. However, chromatic aberration is significantly reduced when using an electron source with a small energy spread, such as a cold FEG which is used in this case and is not believed to be the limiting factor at 200 kV accelerating voltage.

### **2.4. Electron energy loss spectroscopy (EELS)**

#### **2.4.1. Outline**

Electron energy loss spectroscopy, or EELS, is an analytical STEM technique that measures changes in the kinetic energy of initially almost monochromatic electrons after they have interacted with a thin sample. These interactions are governed by Coulomb forces and result in the scattering of some of the electrons, either elastically (in which case there is a very small amount of energy exchanged) or inelastically (in which case a significant amount of energy is transferred from the incoming electrons to the atoms in the sample). When electrons are scattered elastically, the interaction follows Bragg's law,

$$n\lambda = 2d\sin\theta, \quad (2.2)$$

where  $n$  is an integer,  $\lambda$  is the wavelength of the electrons,  $d$  is the distance between atom planes within the sample and  $\theta$  represents the angle at which the electrons in the incoming beam are scattered at after the interaction. In most materials, the electrostatic field of the nucleus decreases further away from the centre of the atom meaning that the incoming electrons will experience a smaller electrostatic field the further away from the nucleus they travel. Most of the electrons will follow such a path and their scattering angles will be small (typically between 0-10°). In crystals, the intensity of the scattered electrons will reach a peak at angles which are related to the spacing between atomic planes in the material which leads

to what is known as diffraction [45]. A diagram of elastic scattering interactions and the path the incoming electrons take near atoms is shown in Figure 2.6a). Inelastic scattering can occur when the incoming electrons interact with either the inner-shell electrons of the atom or the outer-shell ones. Both these interactions are important when discussing EELS and are described schematically in Figures 2.6b) and 2.6c) respectively.

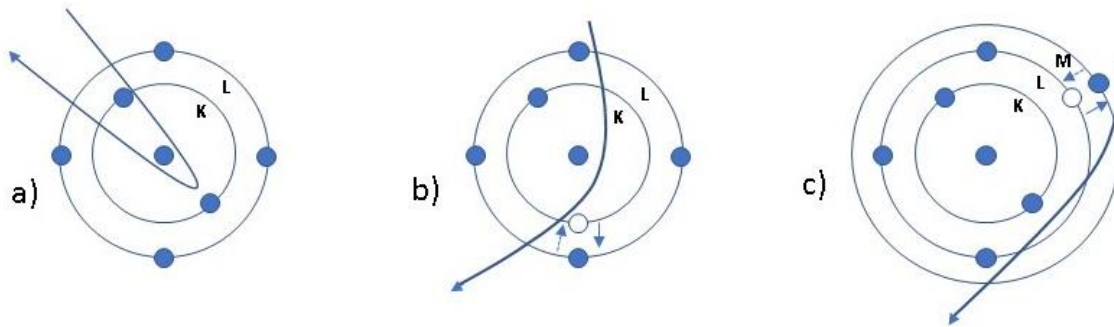


**Figure 2.6:** Diagram showing scattering events, with a) showing elastic scattering where the incoming electron interacts with the atomic nucleus, b) inelastic scattering off inner shell electrons where the incoming electron experiences Coulomb repulsion and c) inelastic scattering off outer shell electrons. In the inelastic scattering events the atomic electrons are excited to a higher energy level, shown by arrows in the diagrams.

When the incoming beam interacts with inner shell electrons, it loses a large amount of energy that is absorbed by the inner shell electron. The inner shell electron then gets promoted into an unoccupied state above the Fermi level of the material, while the incoming electron has lost an amount of energy equal to the one absorbed by the inner shell electron. The amount of energy lost is characteristic to the elements the incoming electrons interacted with and are used in EELS to extract compositional information. In the case of outer shell electrons, the interactions can be considered to involve many atoms in the sample rather than just one. The incoming electron beam will excite these shared electrons and create plasma resonances known as plasmons. These interactions are important in EELS as well.

These interactions mean that a wealth of information is available at different energy losses. It is not just chemical information that can be obtained by EELS, but also details on the bonding between separate chemical elements, surface structure and more. The typical energy loss-spectrum contains a low-loss region and a high-loss region. The low-loss region extends out to roughly a few tens of electron volts. The most intense peak in this region occurs at 0eV and is therefore called the zero-loss peak (ZLP). It represents the electrons that have undergone no inelastic scattering, and hence no significant energy loss. The energy lost by elastic scattering interactions with the atomic nuclei is too small to be measured without a specialist monochromated microscope and high stability, high dispersion spectrometer [89]. The ZLP has a measurable width, which is due to a combination of the energy spread of the electron source and the MTF (modulation transfer function, representing the response in spatial frequency) of the detector in the spectrometer [90]. This is typically between 2eV and

a few meV. The other features in the low-loss spectrum occur due to inelastic scattering, either by the conduction or the valence electrons. A prominent peak in this region is due to plasmon resonances of such weakly bound electrons. Some of the ionisation edges also occur in this region – they are the result of inelastic scattering from inner-shell electrons. Such ionisation edges occur throughout the high-loss spectrum as well, their onset energy being a characteristic of the chemical element on which electrons were scattered from.

## 2.4.2. The electron energy loss spectrum

### 2.4.2. a) The zero-loss peak (ZLP)

The predominant feature in an EEL spectrum of a thin specimen is the zero-loss peak, or ZLP, shown in Figure 2.7 as the most intense feature.

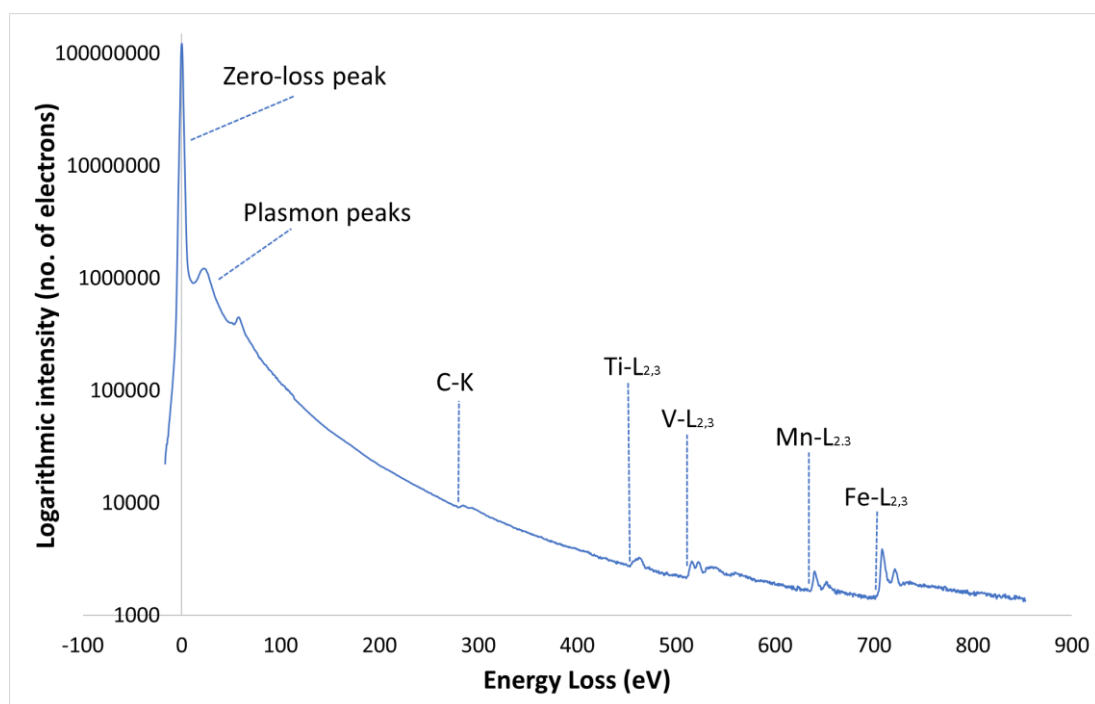


**Figure 2.7:** The EEL spectrum of a (Ti, V) precipitate embedded in a high manganese steel matrix, showing the ZLP, the plasmon peaks and the core-loss edges on a logarithmic scale.

The ZLP also contains electrons that have energy losses below the resolution limit of the spectrometer and those due to the energy spread of the electron source. Electrons having scattered from phonons (collective vibrational excitations of atoms in a lattice) are included in this – this is also called thermal diffuse scattering. These contributions produce a tail on the positive (energy-loss) side of the ZLP, with the negative side having a smaller tail that is mainly due to the point spread function of the spectrometer electronics.

### 2.4.2. b) The low-loss spectrum

After the ZLP, the next major peaks are those caused by plasmons. These are found in the low-loss spectrum, seen as the still intense but slightly smaller peaks on Figure 2.7, in between

the ZLP and an arbitrary cut-off of about 50eV. Here, the electrons from the beam have interacted with those of the conduction and valence bands causing longitudinal oscillations of valence electrons. The electrons in the valence and conduction bands control many of the electronic properties of the sample.

At least one strong plasmon peak can be found in all but the thinnest of specimens, with the intensity of the plasmon peak being correlated to the thickness of the sample. Additionally, there is a shift in the plasmon peak position based on composition, so the position of these peaks can be used in compositional analysis. Williams and Carter [45] describe the use of this method to study magnesium and aluminium alloys, where the plasmons are sharp Gaussian shaped peaks. These are three dimensional bulk plasmons, however two-dimensional surface, one-dimensional edge plasmons and even zero-dimensional corner plasmons can also be excited in a sample [91].

However, quantitative analysis using this method does have limitations regarding how accurate it can get, and core-loss EELS, discussed later in this chapter, is preferred.

The shapes of the plasmons provide useful information for distinguishing specific chemical phases. This can be understood by considering the free electron theory of metals, with plasmon oscillations being treated as a harmonic oscillation of the “electron sea” against the fixed ionic cores of the metals. The energy of the harmonic oscillation is then related to the effective mass of the charge carriers and the electron gas density, which depend on the properties of the material. This means that the position of the plasmon peak changes due to small changes in the material properties, such as lattice parameter changes, or changes in the number of free electrons per atom as a function of alloying.

Another thing the low-loss spectrum is useful for is locally determining the dielectric function of samples. For this, the spectrum up to about 20eV energy loss is used. A single scattering spectrum is needed for this; however, Fourier deconvolution methods are readily available in the Gatan Digital Micrograph software package and can be used to remove the effects of plural scattering. Differences in the plasmon shapes and in the dielectric functions of different materials are used in this research to distinguish between precipitates and the matrix surrounding them and will be discussed in more detail in the chapter dedicated to low-loss mapping.

#### **2.4.2. c) The high-loss spectrum**

Found after the 50eV energy-loss cut-off, the high-loss spectrum contains the core-loss or ionisation edges on a rapidly decreasing plural scattering background. These edges are a result of inelastic interactions with inner shell electrons. During the process, a core-shell electron (from K, L, M... shells) interacting with the electron beam gains enough energy to move into a vacant state above the Fermi level. The beam electron loses the energy needed to eject a core-shell electron from the sample, and this energy loss is what gets detected. The

energy required for this process is characteristic for the atom involved, so the signal detected is a direct source of compositional information.

The edges are named after the atomic shell where the ionisation event occurs, for example the C-K edge represents events resulting in the promotion of an electron from the K-shell of a carbon atom. Because the K-shell electrons are the closest to the nucleus, they require the most energy to be ejected and the K-edges appear at the highest energy losses in the EEL spectrum for any given atom. The heavier an element is the larger the energy-loss at which the K-edge appears. These K-edges have low cross-sections and the intensity of the edge is low. For this reason, L- and M- edges are more usually used for heavier elements. Another reason for this is the fact that the spectral intensity decreases with increasing energy loss.

Because a large amount of energy is needed for inner shell ionisations, the cross-sections are fairly small with the mean free path of electrons for such interactions being relatively large. Cross-section and mean free path calculations will be discussed in detail in the chapter discussing the quantification of precipitates using DualEELS.

The edges appear as a sharp rise at the energy-loss needed for ionisation, which then decreases slowly towards the background. The decreasing background is due to electrons that have undergone random plural scattering events when travelling through the sample. The shape and location of the core-loss edges in a precipitate embedded in a high-manganese steel matrix are shown in Figure 2.7, together with the ZLP and the plasmon peaks. A logarithmic scale is used in the figure due to the large intensity difference between the low-loss and core-loss parts of the spectrum.

The edges can also show more complicated, finer structure. Less than about 50eV after the edge onset, fine structure oscillations are present due to bonding effects and are termed energy-loss near-edge structure, or ELNES. At energies greater than 50eV and extending for up to several hundreds of eV after the edge, small intensity oscillations are present due to diffraction effects from the atoms surrounding the atom undergoing an ionisation event. These are called extended energy-loss fine structure, or EXELFS, and can disturb the backgrounds out to at least 200eV after the edges they are connected to. EXELFS have been a reason for using experimental backgrounds rather than theoretically calculated power law or first order log polynomial backgrounds when quantifying precipitates in this research, as will be discussed in Chapter 6. Low-loss structure can also be present in the ionisation edges, which is a result of electrons undergoing plural scattering and losing energy via ionisation events as well as losing some energy to plasmon interactions. These effects significantly complicate the shape of ionisation edges, but also provide a large amount of information. For example, the low-loss structure and ELNES provide information on bonding. For example, the Si edge shape in pure Si is different from the edge shape in SiO<sub>2</sub>, and the C-K ELNES is different between different transition metal carbides with the rock-salt structure [92].

One of the most important examples of ELNES are the white lines present as intense, sharp peaks on some of the ionisation edges [93]. The  $L_{2,3}$  edges of the transition metals and the  $M_{4,5}$  edges of the rare-earth elements show white lines. An example relevant to the research presented in this thesis is that of the Fe L edge, where the  $L_2$  and  $L_3$  edges are white lines. These lines arise because the  $d$  shell of Fe has several unfilled states per atom just above the Fermi level, so the electrons are excited into these well-defined empty states rather than into the continuum of states at higher energy.

### 2.4.3. Cross-sections for EELS interactions

The cross-section,  $\sigma$ , is a measure of how likely a scattering event is to happen when an incident electron strikes an atom within the sample. The cross-sections depend on the energy of the electron beam, and all the possible interactions have their own cross-sections that are proportional to the probability of the interaction happening. For an EELS edge, the following relationship holds true:

$$I = I_0 N \sigma, \quad (2.3)$$

where  $I$  is the intensity of the edge,  $I_0$  is the intensity of the ZLP,  $N$  is the number of atoms per unit volume and  $\sigma$  is the cross-section.

The formula assumes that the electron has only undergone one scattering event, however it is often the case that an electron will undergo more than one scattering event. This is known as plural (or multiple) scattering and becomes a significant issue when the specimens are not sufficiently thin. In these cases, the energy loss spectrum is a convolution of the single scattering distribution and the low-loss spectrum, with the shape of the low-loss spectrum being dependent on the sample thickness [94]. A deconvolution approach is then needed to separate the two and obtain a single scattering distribution.

Once deconvolution has been applied and a single scattering distribution obtained, the following relationship applies:

$$I = \int \frac{dI}{dE} dE = N I_0 \int \frac{d\sigma}{dE} dE = N \sigma I_0, \quad (2.4)$$

where  $N$  is the number of atoms per unit area of the specimen,  $I_0$  is the integrated zero loss intensity,  $\frac{dI}{dE}$  is the spectrum intensity divided by the channel width,  $I$  is  $\frac{dI}{dE}$  integrated over an appropriate energy window and  $\sigma$  is the partial cross-section obtained by integrating the differential cross-section,  $\frac{d\sigma}{dE}$  over the same energy window. This means that  $N$  can be determined if  $\frac{d\sigma}{dE}$  is known. Knowing  $N$  is vital for quantifying DualEELS data of the precipitates, which is why determining the experimental cross-section has been an integral part of this PhD. The results from calculating the experimental cross-sections of TiN, TiC, VC and VN will be discussed in Chapter 5 and have also been published in Craven *et al.* [95].

#### 2.4.4. Spectrometers and the Gatan Imaging Filter (GIF)

In order to analyse the amount of energy lost by electrons upon interacting inelastically with atoms in the sample, a spectrometer is needed. The main component of a spectrometer is a magnetic prism which disperses electrons according to their kinetic energies, and as such according to the amount of energy they have lost during interactions with the sample. The amount they are deflected by, or the radius of curvature  $R$  of their path if it were a complete circle, is given by the following formula:

$$R = \frac{\gamma m}{eB} v, \quad (2.5)$$

where  $m$  is the rest mass of an electron,  $v$  is the speed it is travelling with in the  $z$  direction in a magnetic field  $B$  pointing in the  $y$  direction, perpendicular to the direction of the beam.  $\gamma$  is the Lorentz factor given by:

$$\gamma = \frac{1}{\sqrt{1 - \frac{v^2}{c^2}}} \quad (2.6)$$

As the equation above shows, each electron in the magnetic field will be deflected onto a slightly different path based on its velocity. The smaller the velocity, the smaller the amount of deflection the electrons experience. Of course, the smaller the velocity when entering the spectrometer, the more energy the electrons have lost when interacting with the sample. Therefore, these electrons will depart the magnetic prism with a larger deflection angle than those which have not lost as much energy during the interaction.

There are in-column and post-column imaging filters and spectrometers, but the one used in this research is the Gatan Imaging Filter, or GIF. This is a post-column filter allowing for both energy filtering and spectroscopy. The magnetic prism here bends the electron beam through  $90^\circ$ , with the electrons being dispersed on a vertical line based on their energy as described above. The electrons that have the most energy, ie. the ZLP and plasmon electrons, experience the least amount of bending and appear at the bottom of the vertical distribution. Core-loss electrons, having lost the most energy, are bent the most and appear at the top of the vertical distribution.

A rough diagram of the GIF is shown in Figure 2.8, showing the magnetic prism and the path of electrons bending when it travels through it towards the projection system and the CCD detector. A fuller description of the workings of such spectrometers is given in Section 2.4.4.

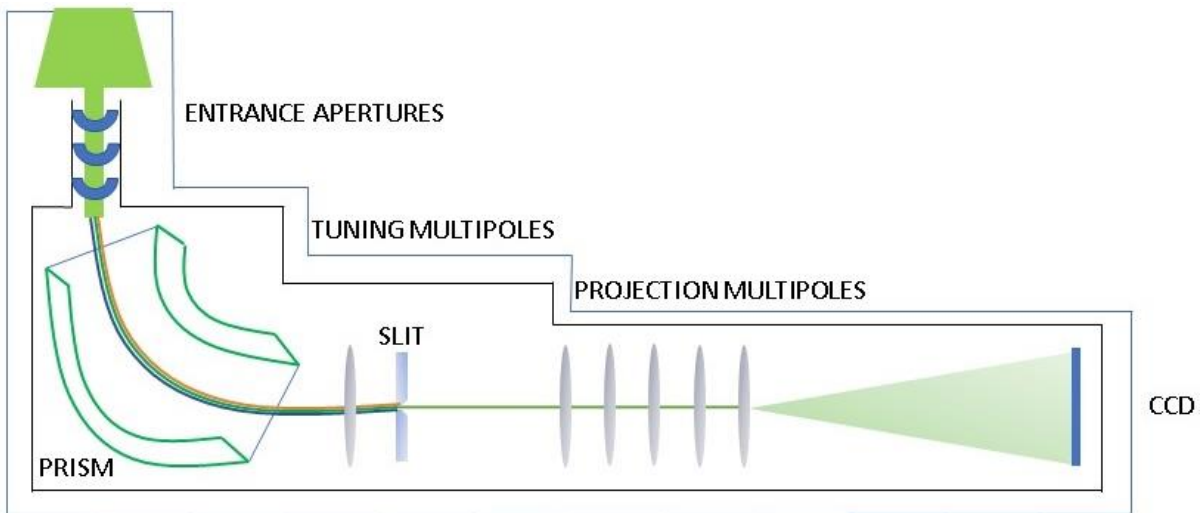


**Figure 2.8:** Diagram of a Gatan Imaging Filter (GIF) showing the entrance apertures, prism and entrance slit, together with the tuning and projection multipoles and the CCD.

#### 2.4.5. Dual electron energy loss spectroscopy (DualEELS)

With DualEELS, both the low-loss and the high-loss spectra can be collected near-simultaneously at each pixel in a spectrum image. This is done using a fast electrostatic shutter (or fast beam switch) with a microsecond response time incorporated in the spectrometer. [53] Once the more intense low-loss spectrum has been acquired at a specific pixel, the electrostatic shutter deflects the beam to a different area of the CCD and then the high-loss spectrum can be acquired. The two can then be recorded under the same optical conditions, but with the high-loss spectrum taking longer to acquire due to its much smaller intensity. Using the DualEELS method to record data in this way overcomes the limited dynamic range of the CCD detector which limits the range of intensities that can be imaged at the same time.

In this research, the GIF Quantum electron spectrometer was used. It has a 2kV field of view at an accelerating voltage of 200kV and a maximum acquisition rate of 1000 spectra per second and allows for the acquisition of low- and core- loss spectra up to 2kV apart, as described in Gubbens et al 2010 [96]. The high-speed detector, together with the electrostatic shutter, can take full advantage of the high beam current available on the JEOL ARM. Two apertures are available for spectroscopy, a 5mm one and a 2.5mm one, both allowing for the high collection angles needed in order to do high resolution EELS analysis. In this research, only the 2.5mm aperture was used giving a spectrometer acceptance angle of 36mrad.

Having both the low-loss and the core-loss spectra acquired under the same conditions is what makes the accurate quantification discussed in this thesis possible. Recording the ZLP allows for the normalisation of the core-loss edges and having acquired a low-loss spectrum allows for the removal of plural scattering from the spectrum. These are important steps in

quantifying a specimen. The data processing method used for DualEELS spectrum images will be described in detail in the next chapter.

#### 2.4.6. Spectrum imaging and the data cube

The EELS information is gathered in the form of a spectrum image. This is a data cube with two of the cube axes corresponding to spatial information while the third dimension being the energy loss spectrum, as can be seen in Figure 2.9. In order to do this, the beam is scanned across the sample and the spectrum collected at each  $(x, y)$  pixel. Thus, each  $(x, y)$  pixel position has an associated spectrum in the dataset. The method was first proposed in 1989 by Jeanguillaume and Colliex [52].

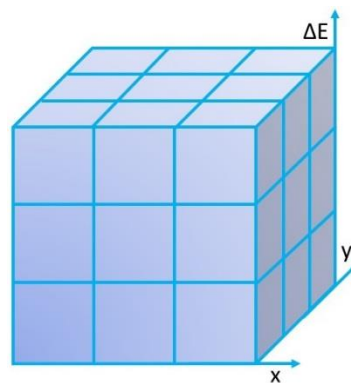


**Figure 2.9:** A spectrum image data cube, with  $x$  and  $y$  representing the pixels scanned across and the third dimension,  $\Delta E$ , representing the spectrum at each  $(x, y)$  pixel in the cube.

To record spectrum images, the beam is scanned across the sample in a raster pattern and a spectrum is recorded at each pixel of the scan area, thus forming the data cube. Having the entire spectrum collected and stored at each point allows for spectral processing to be applied to every pixel in the resulting spectrum image in a consistent manner, and to allow both mapping and statistical evaluation of the data.

The data cube can be analysed to produce maps correlating the species present in the sample with their location within the scanned area. The results of mapping can be significantly improved when the volume of the data cube is reduced by removing noise, which is routinely done by applying statistical methods such as Principal Component Analysis which will be discussed in detail in the next chapter.

## 2.5. Summary

Focused ion beam (FIB) microscopes have become commonly used in the preparation of samples for analysis in the transmission electron microscope (TEM) thanks to their ability to prepare site-selected thin specimens. Lamellae of <100nm in thickness were prepared using a standard lift-out method, some using a gallium liquid metal ion beam and some using a xenon plasma beam. Needle shaped specimens have been prepared using a modified method for making atom probe tips for use in mean free path calculations.

TEM and scanning TEM (STEM) make use of high-energy electron beams and their interactions with samples to obtain information about the structure and chemistry of materials. Condenser lenses shape the beam and direct it towards the specimen, with the objective lens then focusing the beam after it has interacted with the sample and providing the first magnified image of the specimen, which is then further magnified by the projection system before reaching the detector. All lenses have aberrations, including astigmatism, chromatic and spherical aberration. The use of aberration correctors in STEM has enabled us to use large currents for high spatial resolution analytical microscopy.

Having a spectrometer coupled to a STEM enabled us to obtain electron energy loss spectroscopy (EELS) data, where signals from scattered electrons are detected and used for mapping the chemistry of samples with sub-nanometre resolution. The EEL spectrum contains a variety of signals depending on the amount of energy lost by the beam electrons. The zero-loss peak (ZLP) arises due to electrons that have lost no energy in their interactions with the sample, the low-loss part of the spectrum contains the plasmon peaks due to collective oscillations of the valence electrons in the sample, with the high-loss spectrum containing the core-loss edges specific to each element, which arise due to inelastic scattering of the beam electrons.

DualEELS allows for the collection of high-loss and low-loss spectra near simultaneously under the same experimental conditions, meaning that more details of the sample can be extracted from having access to the full energy-loss spectrum. Having the low-loss spectrum and the ZLP means that the volume of the sample can be calculated, and the overall spectrum can be deconvolved to remove the effects of plural scattering and obtain a single scattering energy-loss distribution. This allows for not just qualitative chemical mapping, but also makes accurate chemical quantification of specimens possible.

Accurate chemical quantification requires a specific series of data processing steps, which will be described in detail in the next chapter. Some examples will be provided to illustrate the individual processing steps, with a more detailed discussion of the results provided in further chapters.

## Chapter 3

### EELS data processing

As was discussed in Chapter 2, DualEELS data is collected as a 3D data cube, with two of the dimensions being  $x$  and  $y$  to create a map, and the third dimension being energy loss at each of the pixels in the 2D map. The as-recorded data contains a large amount of experimental noise, as well as systematic errors such as non-linearities in the spectrometer dispersion. The low-loss and high-loss datasets are collected near-simultaneously as separate spectrum images in DualEELS mode, with extracted spectra from a single pixel in each being shown in Figure 3.1 below. The sample used to acquire this example data was a high manganese steel with additions of titanium and vanadium. The figure shows the full energy loss range over which the data has been acquired, as well as the differences in intensity between the two parts of the spectrum. The data can be displayed either in channels as imaged on the CCD, or in eV. The relationship between the two is given by the spectrometer dispersion, expressed in eV per channel. The data used in this research was collected at a dispersion of 0.5eV/channel.

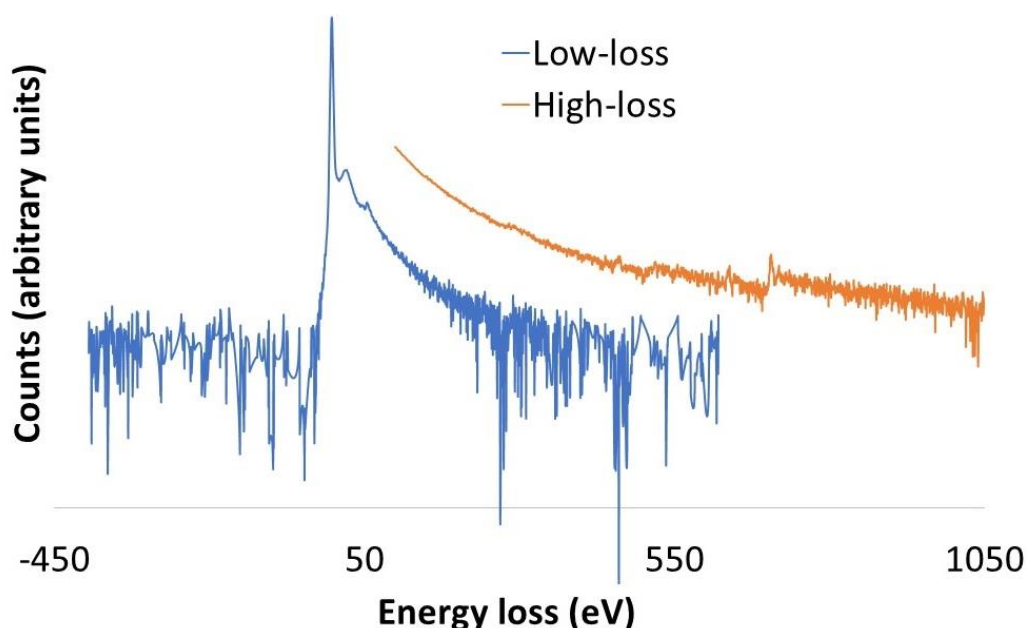


**Figure 3.1:** The as-acquired low-loss (blue) and high-loss (orange) spectra of a precipitate in a high-manganese steel, showing the range and intensity difference between the two. Due to the large intensity of the zero-loss peak, and the large difference in intensity between the low-loss and high-loss, the graph is plotted on a logarithmic scale. The high-loss has a longer acquisition time than the low-loss, hence the intensity difference where their energy losses overlap.

Figure 3.2 a) shows the ZLP not being centred on zero. The ZLP shifts across a spectrum image due to projection effects from the way the beam is scanned across the sample and is something that requires correcting during processing. Figure 3.2 b) shows the two spectra at high energy losses, with the spectrum acquired for the low-loss shown in blue and the high-

loss in orange. The low-loss is only required to include energies up to about 150eV for the processing done in this research, so its energy range is cropped above that energy loss early on in the processing. At these higher energies, the low-loss spectrum is mainly noise, and cropping that area out reduces some of it early on and stops some from filtering through the future steps into the final spectrum image to be analysed. A large amount of noise present is clearly visible in both spectra, with some of the core-loss edges being difficult to distinguish from the noise, especially in the case of the V-L and O-K edges which are also close together in energy loss.

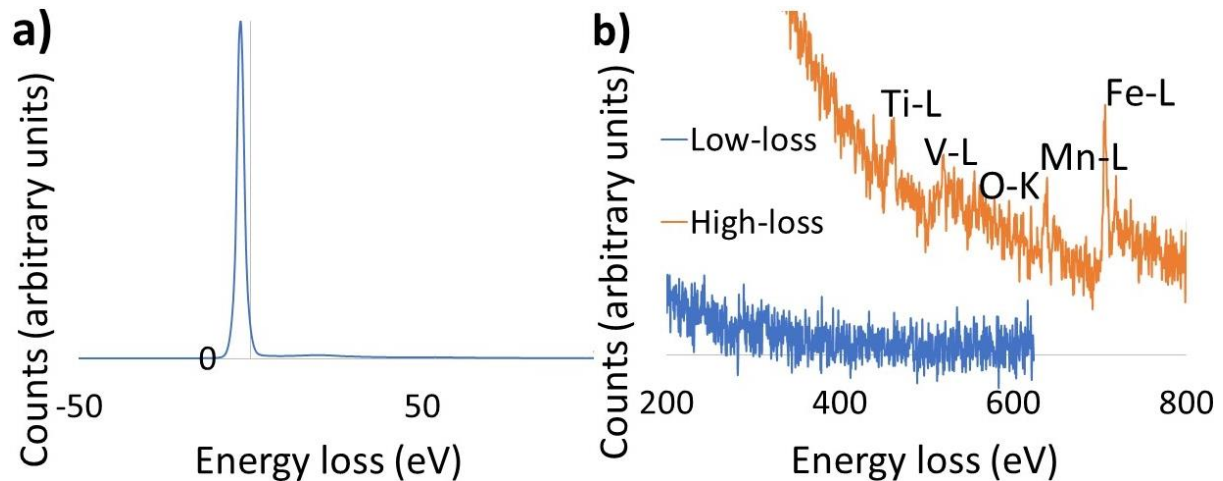


**Figure 3.2:** a) The misaligned ZLP before being aligned in energy loss and b) the large amount of noise in each channel of the as-acquired spectra.

There is a step in both the low-loss and the high-loss spectra which corresponds to the middle of the CCD (channel 1024), where the two different halves of the CCD are joined together. This step is difficult to see in the as-recorded data due to the high levels of noise present but becomes visible much more easily once the data has been pre-processed.

As such, before being able to extract any useful information from the collected spectrum images, the data needs to be processed to reduce its volume and the amount of noise present, and to consider the errors due to the experimental setup. This has been done through a series of steps, with the basic processing such as removing plural scattering being described in Bobynko *et al.* [97]. Other steps, such as the correction for dispersion non-linearity, have been developed as part of this project.

This chapter will cover all the processing steps used to process the data into a form where it can be used for precipitate analysis and quantification, and then discuss how the data is analysed.

### 3.1. Basic DualEELS processing and noise reduction

#### 3.1.1. Linearisation

When the low-loss and high-loss datasets were recorded, the two were not perfectly aligned in energy at the point where they are supposed to meet (the splice point, which will be described in more detail in subsection 3.1.7). This can be seen in Figure 3.3 a), showing the low-loss spectrum of SiO<sub>2</sub>, where the Si L<sub>2,3</sub> edge appearing just after 100eV energy loss and the Si L<sub>1</sub> edge at about 150eV should appear at the same energy in both the low-loss and the high-loss spectra. However, there is a visible misalignment between the two. This mismatch would affect every further step in the processing described in this chapter, so it was the first thing that needed to be dealt with in the as-acquired data.

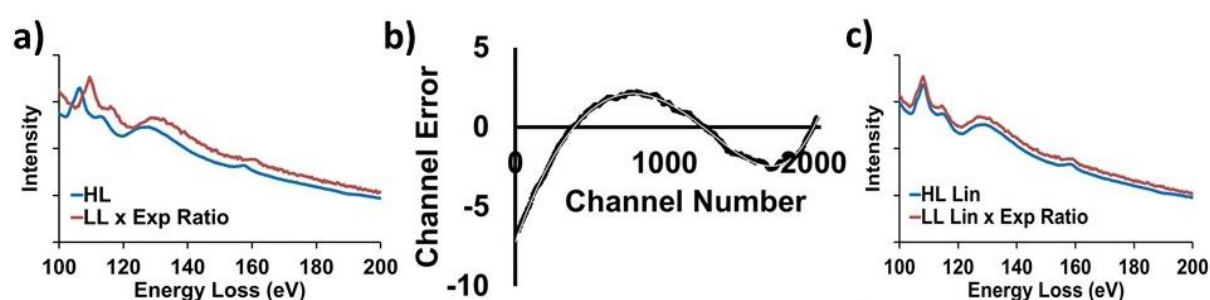


**Figure 3.3:** The effects of dispersion non-linearity in DualEELS: a) Mismatch between the Si L<sub>2,3</sub> edge from SiO<sub>2</sub> appearing on the low-loss (red) and high-loss (blue) as acquired spectra, b) The error on each of the channels based on the ZLP position and c) Comparison between the position of a prominent feature on the low-loss and high-loss spectra after correcting for the dispersion nonlinearity.

The mismatch occurred due to the energy scale in the spectrometer not being linear. The energy loss linearity had to be characterised first, and then corrected for before any other processing steps could be applied. The non-linearity was characterised using a script from B. Schaffer (Gatan) which scans the ZLP across the spectrometer using accurately known voltage shifts on the drift tube. The script is shown in Appendix 1 at the end of this thesis, with permission from the author.

A second script was used to analyse the results of the non-linearity characterisation and measure the peak position, which varied with spectrometer dispersion linearity. This script was provided by Mr. Robert Webster at the University of Glasgow and is shown in Appendix 2 with permission from the author. The script works by locating the position of the maximum intensity pixel throughout the full ZLP scan across the spectrometer and collating all these maxima into a single image. A gaussian is fitted to each peak to avoid the jitter on the ZLP, and this is then used to find the centre. The positions of these maxima are then compared to the ideal reference positions where the ZLP was expected to be, and the deviations calculated.

In the case of the SiO<sub>2</sub> sample discussed here, these deviations can be seen in Figure 3.3 b) and are fitted by a polynomial. This smooth polynomial fit is then used to correct the original as-acquired spectrum images. When the low-loss and high-loss spectra were compared again after linearization (Figure 3.3 c)), the mismatch in the peak position was not present anymore, suggesting that the dispersion non-linearity was successfully corrected for.

### **3.1.2. Removing the background before the ZLP**

While the high-loss is acquired, the ZLP and some of the low-loss are in the beam trap. Any part of the low-loss outside of the beam trap could give rise to a stray background. Especially when the energy shift between the low-loss and the high-loss spectra is not large enough, we end up with this stray signal in the form of an extra background before the ZLP (also known as bleed through). For all datasets acquired, care has been taken to choose appropriate energy shifts to minimise this problem as much as possible, however several channels before the ZLP have had to be removed every time. This has been done by fitting a routine power law background before the onset of the ZLP and removing it from the spectrum image. Another advantage in removing this background comes from the decrease in the data volume to be processed in the next steps. Particularly when doing principal component analysis (PCA), as described in detail in Section 3.1.6., the decrease in volume decreases processing time and the number of possible errors this step could introduce in the analysis.

### **3.1.3. Aligning the spectrum images and correcting for the ZLP centring**

Instrumental instabilities in the microscope and spectrometer can shift the zero-loss away from 0eV. Additionally, the ZLP drifts as a function of position in the spectrum image due to projection effects, as can be seen in Figures 3.2 and 3.4 where different colours indicate different ZLP position resulting from the scan.

In order to correct for these, the “Align SI by peak” function in Digital Micrograph™ is used to centre the ZLP to zero and remove the drift from pixel to pixel. Since the low-loss and core-loss data have been acquired at the same time, the software transfers the ZLP alignment to the high-loss spectrum as well using the map of the ZLP peak shift, as shown in Figure 3.4 with the position of the ZLP oscillating between -1.5eV and +1.5eV in this particular dataset (a CRM steel tempered for 90 minutes, details about which will be given in the next chapter).

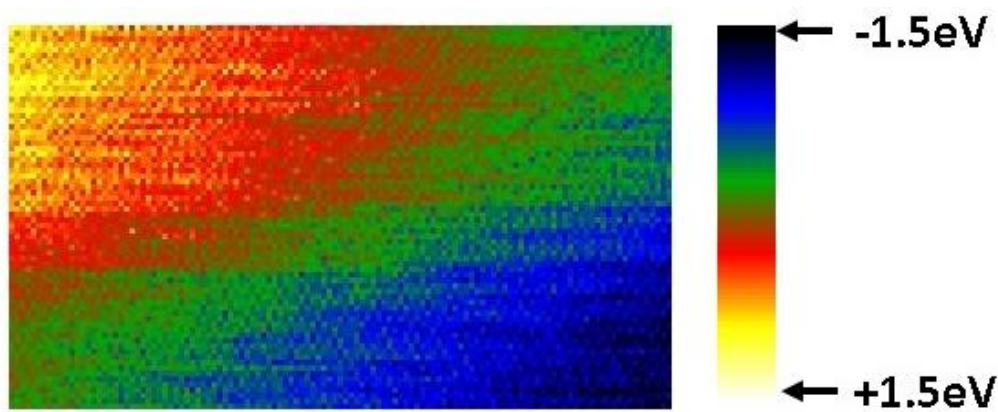


**Figure 3.4:** Changes in the ZLP peak position when scanning the beam across the imaged area, with the ZLP moving by about  $\pm 1.5\text{eV}$  across the scan.

### 3.1.4. Volume extraction

Using the “Volume” → “Extract volume” function in Digital Micrograph™, the spectrum can be cropped to exclude channels at each end. There is a loss of detection efficiency at the ends of the spectra caused by shadowing of the electron beam by the spectrometer aperture, so the higher energy loss end of the low-loss spectrum was removed keeping only enough of the spectrum to allow an accurate splicing, which will be discussed further in this chapter. Additionally, the highest core-loss edge used was the Fe  $L_{2,3}$  edge at an energy loss around 700eV. This means that the region after 800eV could be removed from the spectrum. Extracting only the volume that is useful also means that further steps are easier and take less processing power due to the smaller size of the spectrum images.

### 3.1.5. X-ray removal

Sometimes, large energy spikes can be found at some pixels in the spectrum images. These may be caused by electrons hitting internal parts of the spectrometer and exciting X-rays that strike the CCD and have little or no connection to the sample. They can be removed using the “Volume” → “Remove X-rays” tool in Digital Micrograph™. This checks each image plane of a dataset for spikes which lie more than a user selected number of standard deviations away from the median of the spectrum area they are found in. When found, they are replaced with the median intensity value. For all the spectrum images analysed as part of this project, a number of 5 standard deviations was used. This removed all the X-rays spikes from the data while keeping the processing time short enough even for large datasets. This, and the steps described above, has been described by Bobynko *et al.* [97] in 2015 as well as in Bobynko’s PhD thesis [9], where the method was also applied to steels.

### 3.1.6. Principal component analysis (PCA)

Principal component analysis (PCA) is the step that removes by far the most amount of noise from the spectrum images and has been used at other stages in this research as well. A Multivariate Statistical Analysis (MSA) plug-in for Digital Micrograph developed by Lucas *et al.*

has been used in this research [98]. MSA is a family of techniques used in a wide variety of fields to analyse large datasets containing many known and unknown variables. Of these techniques, PCA is one of the most common and well-known, with its aim being to reduce the dimensionality of a large dataset by describing it with the minimum number of variables possible without losing any relevant information [99]. In the case of an EEL spectrum, this essentially means that the original spectrum image ends up being described by a small number of useful spectral components with a large number of noise-containing components being discarded.

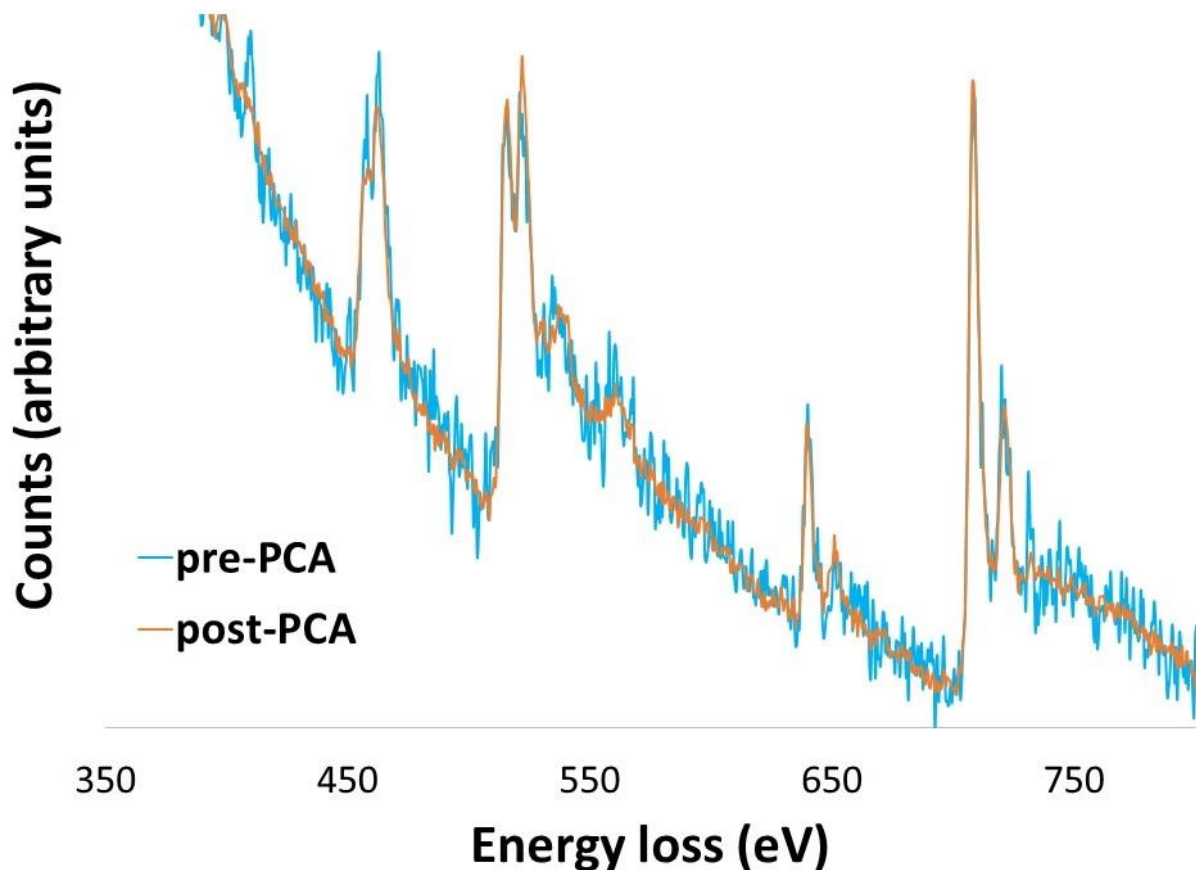


**Figure 3.5:** Comparison between the pre- (blue) and post (orange) -PCA extracted spectra from the center of a (Ti, V) (C, N) precipitate. It is clear that the blue pre-PCA spectrum contains a lot more random noise than the orange post-PCA spectrum.

This is achieved by treating the original spectrum image as a matrix. Then, the two spatial dimensions ( $x,y$ ) are stored in the matrix columns, while the spectrum associated with each ( $x,y$ ) pixel is stored in the rows. The PCA decomposition will then produce two-dimensional maps called “scores” and one-dimensional spectra called “loadings”. While difficult to interpret directly, differences between different PCA outputs are usually easy to notice. If there is a large difference between two consecutive outputs, they are very likely to represent real signals, while very similar consecutive ones are likely to be random noise. This provides a way of reconstructing back the data without the noise components.

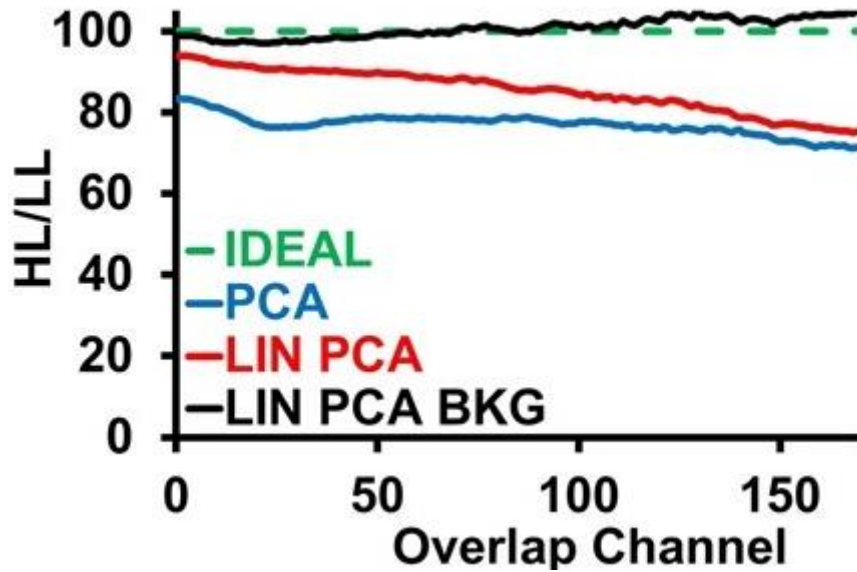
However, care must be taken when using PCA as it can introduce artefacts and bias in the reconstructed data, especially when too few components are used in the reconstruction leading to some of the weaker components being missed [100] [101].

Figure 3.5 shows the effect of PCA on the spectrum extracted from a small number of pixels (in this case four pixels) in the center of a (Ti, V) (C, N) precipitate. The blue spectrum was extracted from the spectrum image processed up to after the X-ray removal step, with the orange spectrum being extracted from the PCA reconstructed spectrum image. It can be easily seen that the PCA reconstructed spectrum has a significantly reduced level of random noise when compared to the non-PCA processed spectrum.

### **3.1.7. Splicing and deconvolving**

To further analyse a dataset, the low-loss and high-loss spectra need to be spliced together into a single spectrum image. If the spectrometer bleed-through described in section 3.1.1. is not removed, there can be issues such as steps in the spliced spectrum image in the region of the splice point. The low-loss and high-loss data have different acquisition times as has been discussed. This means the spectra will have different intensities at the splice point, with the high-loss having higher intensity than the low-loss there. When splicing, the two are scaled to the same intensity with the difference in intensity being given by the splice ratio. This intensity difference can be seen in Figure 3.1, and the splicing was done at approximately 100eV energy loss. An overlap of 20 channels (20eV) across the two spectra was used to calculate the splice ratio. This varies across the dataset, with the splice map showing the splice ratio at each (x, y) pixel in the spectrum image. Ideally, the splice ratio at each point will be the same as the time ratio, i.e. the difference in intensity between the low-loss and high-loss spectra at the splice point is the same as the difference in acquisition times between the two. However, this is not usually the case and small pixel to pixel variations were expected. However, we have often noticed big differences between the two, especially in the case of the Nb cross-section data. Figure 3.6 shows this, as well as the improvement in agreement after the corrections described so far in this chapter have been applied. The agreement is better after the non-linearity in the dispersion is corrected for, with further improvement when the stray signal from spectrometer bleed-through is removed as well. These corrections have to be applied together with PCA for noise reduction, as described above in section 3.1.6.

Fourier-logarithmic deconvolution is used to remove plural scattering. This removes the effect on the shape of the low-loss from changes in the specimen thickness, carbon contamination or composition. It also ensures that the steps described further in the chapter can be performed, as it makes the use of standard spectra taken under different experimental conditions possible as long as they have also been deconvolved.



**Figure 3.6:** Improvements in the splice ratio of data when compared to the ideal (green) when it has been linearised (red) and when it has been linearised and had the stray background subtracted (black) as opposed to when it just had noise reduction applied (blue). The vertical axis shows the ratio between the high-loss acquisition time and the low-loss acquisition time, ie. the time ratio which in this example is 100. Ideally, the splice ratio would be the same as the time ratio, however the figure shows that this is not the case.

For the research presented in this thesis, the spectra analysed need to be the result of a single scattering distribution. However, the transmitted electrons can scatter more than once depending on the thickness of the sample so the spectrum obtained is the result of a multiple scattering distribution. The effects of these scattering events need to be removed to obtain a spectrum due to single scattering events only. This step uses Fourier transforms and is based on the assumption that plural scattering will follow Poisson statistics. The single scattering distribution,  $I(E)$ , is found using the following formula:

$$i(v) = z(v) \ln \left[ \frac{i(v)}{z(v)} \right], \quad (3.1)$$

where  $i(v)$  is the Fourier transform of the recorded spectrum from the ZLP to beyond the last core-loss edge of interest and  $z(v)$  represents the ZLP [102] [103].

Care must, of course, be taken to avoid any negative counts in the spectrum as this will lead to artefacts in the deconvolution. These negative counts can often be found before the ZLP after the bleed through signal has been removed, giving another reason to eliminate the signal in that region using volume extraction.

### 3.2. Multiple linear least squares (MLLS) fitting

Multiple linear least squares fitting is a fingerprinting method which requires a pre-existing set of standard spectra for the elements or phases present in the sample. It then creates a

model where the original spectrum image is treated as a linear combination of the standard spectra. The model is then fitted to the original spectrum image by adjusting the coefficients of the linear terms to minimise the squared deviation between model and original. MLLS fitting is an excellent method of separating overlapping edges and complicated fine structure [104]. The best fit is often obtained by trial and error, changing which standard shapes are included, with the residual spectrum image constantly being compared against the original and MLLS fit spectrum images to see where the fit is not accurate. The best fits were always obtained when every single contribution to the data was included in the fit, including thin and thick matrix spectra and constants due to small inaccuracies in the dark current subtraction.

Apart from spectrum images for the fit and the fit residuals, the algorithm also returns maps for the fitting coefficients of each of the standard spectra used in the fit. These show the weighting factors for the standard spectra. If the standard spectra are differential cross-sections, as is the case here, it is possible to convert these weighting factors into absolute quantities and a discussion on how to do this will follow in this chapter in Section 3.4.

### 3.3. Removing the matrix contribution

Removing the matrix contributions from the analysed spectrum images has been an important step in the early stages of this PhD research when analysing some of the high manganese steel precipitates. However, issues with fitting backgrounds before edges meant that the method did not produce the most accurate results. This means that it has not been used when processing any of the data presented in this thesis, so it will be briefly introduced and will not be described in a lot of detail here. The method used originally was the same as the one described in Bobynko *et al.* (2015) [97]. A spectrum from an area of only matrix would be extracted and scaled to every pixel in the spectrum image, then subtracted from the original spectrum image leaving nothing but the precipitate. The subtraction was done using a custom-built script.

The result of this subtraction is a spectrum image for the precipitate only. The background would be subtracted and an MLLS fit would be done using predetermined experimental cross-sections. The results of such a fit for a (Ti, V)(C, N) precipitate in a high manganese steel, together with the original spectrum and the residuals to the fit can be seen in Figure 3.7a). The blue line represents the original precipitate spectrum, with the red line being the spectrum from the MLLS fit using standard shapes. The difference between the original and the fit is given by the residuals, which are shown in the figure in green. When away from the edges, the residuals are fairly evenly distributed around zero suggesting a good fit. However, a slight increase in the residuals can be seen in the area of the C-K and the V-L edges, showing that the fit could be further improved in the region of those edges. Figure 3.7b) shows all the cross-section contributions to the final fit shown in Figure 3.7a). When looking at the V-L edge, the graph shows that both the VN (green) and the VC (black) cross-sections contribute to the MLLS fit in that area. The VN cross-section also has a significant contribution to the N-K edge. It is noted that a cross-section for nitrogen, extracted from the VN one, was also used in the

to fit over the nitrogen edge. This is shown in pink on the graph, and it can be seen that the contribution from it is negative. The negative contribution suggests that the precipitate contains less nitrogen than the binary nitride standard used in the MLLS fit.

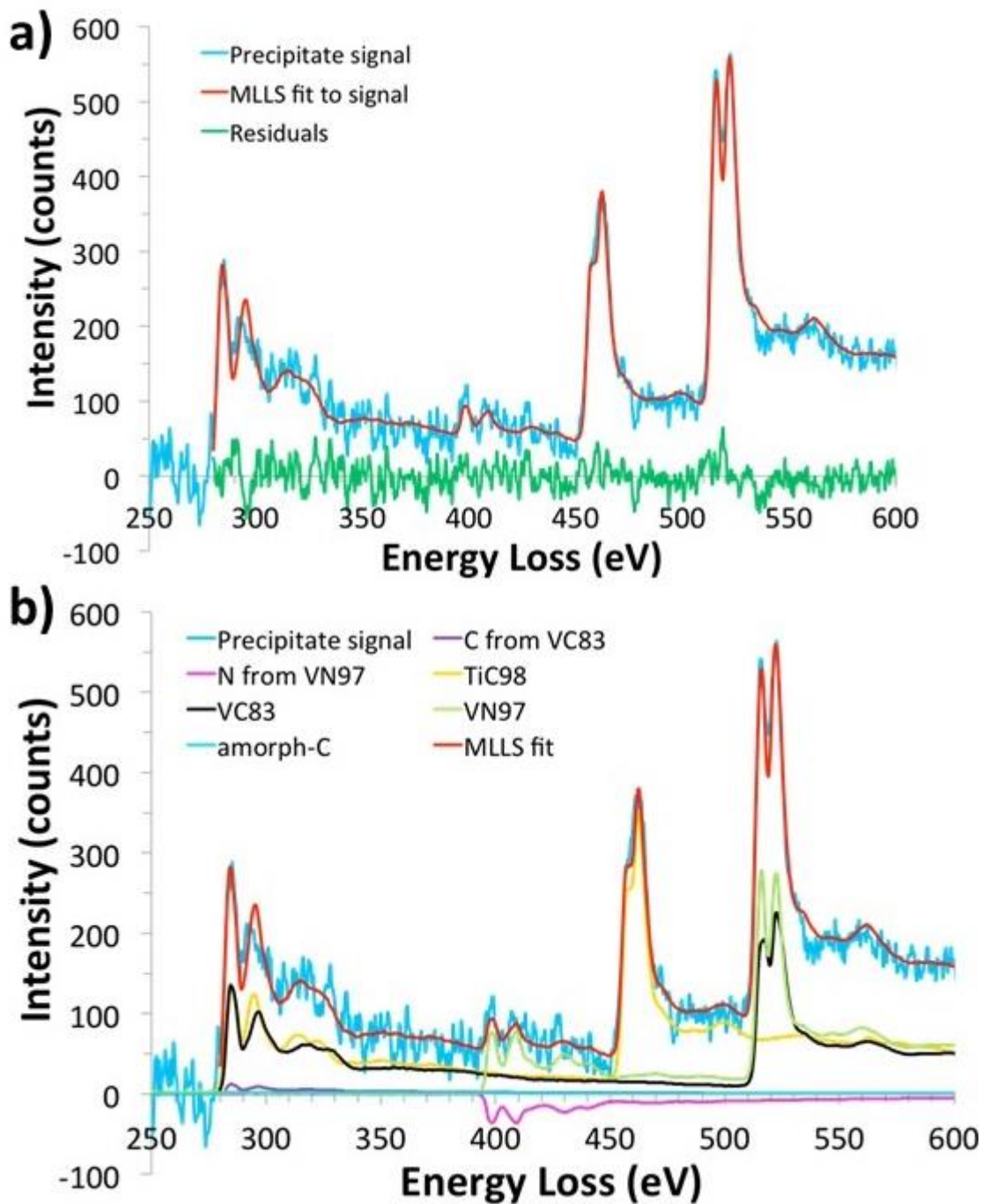


**Figure 3.7a):** Extracted spectra showing the precipitate signal in blue with the spectrum obtained from the MLLS fit shown in red and the fit residuals showing in green and b) The cross-sections used in the MLLS fit to the precipitate signal (blue). Image first published in Craven et al. (2016)[95].

While the results of this MLLS fit show fairly evenly distributed residuals in areas away from the edge, it was hoped that the elemental edges could be fitted better and that the residuals could be further minimised. A major issue with the fit presented here is the background

subtraction. The effects of EXELFS extend to about 200eV after their edge, meaning that the background is affected over large regions making it deviate from a power law. It was then decided that the background should not be removed prior to performing the MLLS fit anymore.

### 3.4. Accurate quantification using MLLS fitting

Using the fit coefficient maps obtained from MLLS fitting, together with scripts doing basic calculations, allows us to accurately quantify the chemistry of the identified precipitates. First, the data is processed up to obtaining a deconvolved spectrum image as explained in Section 3.1. The standard method of quantification after that point would be to fit a standard power law background under the edges to be quantified [54]. However, the position of the background and signal windows, together with their widths, have a significant effect on the results of the quantification and are dependent on user choice. Additionally, the method depends on theoretical cross-sections which are known to deviate significantly from the experimental ones. Therefore, it was decided not to use this method. The differences between experimental and theoretical cross-sections are discussed in detail in Chapter 5 of this thesis, with a detailed discussion of quantification being given in Chapter 6.

The method used initially in this research, and described in the previous section, was to remove the matrix and then remove the background from the precipitate signal before the MLLS fit and running the quantification script.

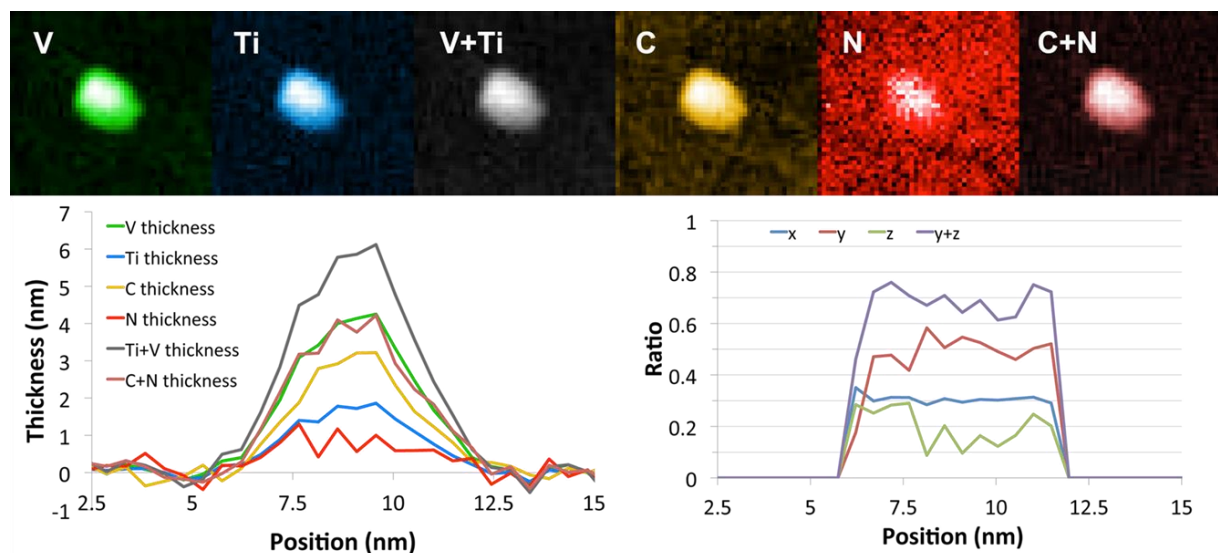


**Figure 3.8:** The results of the quantification in the case where the matrix was removed, followed by removal of the background shape.

However, the results of the quantification have been greatly improved by not removing either the matrix or the background shape. Instead, the MLLS fit is done directly on the deconvolved spectrum image. The procedure is described in detail in Craven *et al.* (2018) [105].

The usual high-quality binary nitride and carbide spectra are used in the MLLS fit, together with shapes for the C-K and N-K edges. These two edges had to have the background removed in order to be calculated, so the background shape used in obtaining them is also included as a standard in the MLLS fitting routine. The background shape used is an experimental shape extracted from a  $\text{TiN}_{0.88}$  spectrum. Additionally, thin and thick matrix shapes extracted from areas where there are no precipitates are used to take into account the matrix signal and thickness variations in the imaged area. A shape for amorphous carbon is also used to remove any surface contamination from the quantification.

Some additional shapes can be included in the MLLS fit to further reduce the residuals. These are not related to the sample, but to the experimental setup itself. A step function to account for slight differences in the response from the different halves of the CCD was included. To take into account potential small errors due to the dark current subtraction being automatically performed at the end of each spectrum image acquisition, a further shape being equal to 1 at each energy loss value was included. An example of the elemental fitting coefficients from the full MLLS fit on four (Ti, V) (C, N) precipitates is shown in Figure 3.9. The results will be discussed in detail in Chapter 6 and have been published in [105].

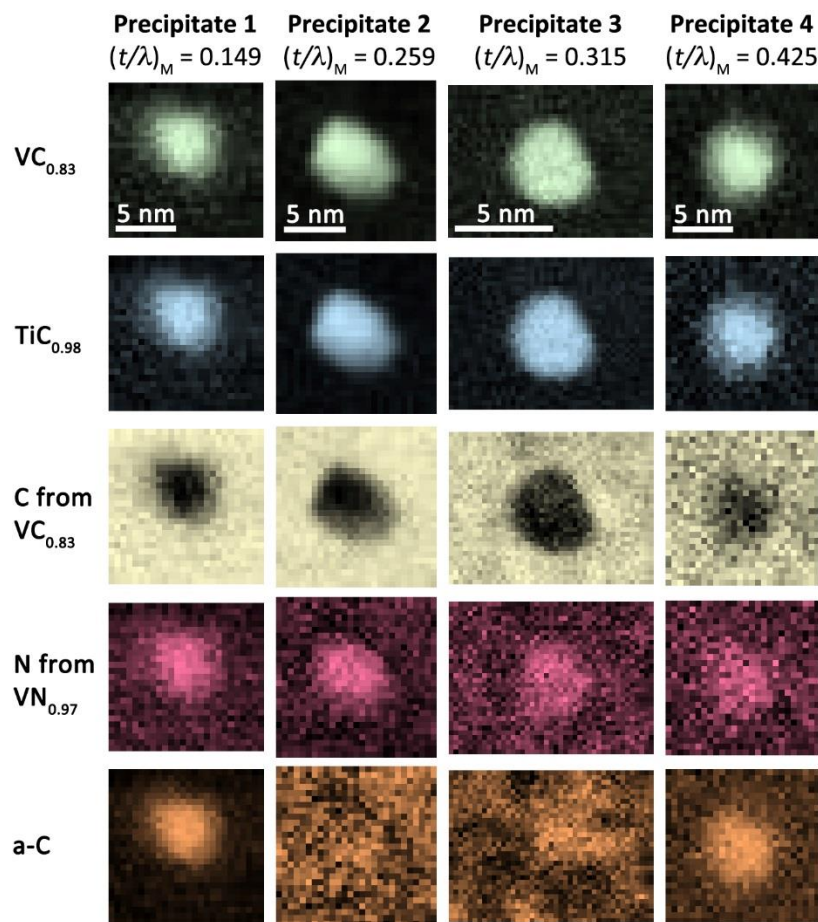


**Figure 3.9:** Plots showing the distribution of VC, TiC, C from VC, N from VN and a-C in four (Ti, V)(C, N) precipitates in a high manganese steel. Image first published in Craven et al. (2018) [105].

The MLLS fit coefficients are then used in the quantification script (written mainly by Prof. Alan Craven and copied in Appendix 3 for the full version to quantify Ti, V and Nb, with permission) together with the map of the zero-loss peak intensity at every pixel, the splice ratio map, the lattice parameter of the precipitate (will be slightly different depending on the exact composition) and some experimental parameters such as acquisition times. The script does the following:

1. Sum the individual elemental fit coefficients (such as TiC or C from VC) to create a mask of the precipitate. Use this mask to remove the matrix from the dataset and leave just the precipitate to be dealt with.
2. Calculate the coefficients for the individual metals, for example  $V = VC + VN$ . Then calculate the total amount of metal as  $Ti + V + Nb$ .
3. The number of metal atoms per unit area is calculated by dividing the total amount of metals calculated in Step 2 by the ZLP intensity (this normalises the data and takes thickness effects away), the  $\frac{\text{time ratio}}{\text{splice ratio}}$  (takes out any differences left between the two) and then by dispersion (in eV/ channel as cross-section is given in barns/eV). Finally, a conversion factor is applied to move from barns to nm.
4. The thickness of the precipitate in unit cells is calculated by dividing the number of atoms per unit area by the number of atoms/nm<sup>3</sup> in the cell (i.e. 4 for an FCC cell / the cube of the lattice parameter  $a$ ). This can then be multiplied by the unit cell dimension,  $a$ , to obtain a total metal thickness in nm.
5. The process is repeated for the non-metals in the precipitate.
6. Individual profiles for each element can be calculated in the exact same way by starting the process from Step 3 using for example Ti instead of  $Ti + V + Nb$  to give an equivalent thickness for Ti.
7. Elemental ratios are calculated by dividing each metal by the total amount of metals, i.e.  $x$  in  $Ti_xV_{(1-x)}C_yN_z$  is Ti thickness divided by total metal thickness. The same is true for non-metals.
8. The rest of the script deals with setting tags and saving data rather than calculations.

The script produces compositional maps showing the position and relative concentration of different chemical elements in the precipitate. Line profiles can be easily drawn on these maps, which will provide the equivalent thickness of each element in the precipitate. Such line profiles are drawn through the center of a (Ti,V,Nb)C precipitate from steels produced by CRM in Belgium for this project are shown in Figure 3.10.

From Figure 3.11 a), the equivalent thickness of the individual elements in the precipitate can be seen. There is about twice as much vanadium as titanium, with the thickness of carbon being only slightly less than the total amount of metal in half of the precipitate and slightly more in the other half. No amount of nitrogen was detected, and as such we can confidently say that the precipitate was a metal carbide.

Figure 3.11 b) shows the quantities of titanium, vanadium and niobium (assuming  $Ti + V + Nb = 1$ ) across the precipitate. The relative amount of titanium can be deduced from the figure to be about 0.3 from the total amount of metal, with vanadium being about 0.5 and niobium about 0.2. This suggests that the precipitate has the approximate chemical formula  $(Ti_{0.3}V_{0.5}Nb_{0.2})_y C_x$ . The flat profile of  $x$  means that the amount of titanium is constant throughout the precipitate, with some segregation between vanadium and niobium being possible based on the shapes of the profiles.

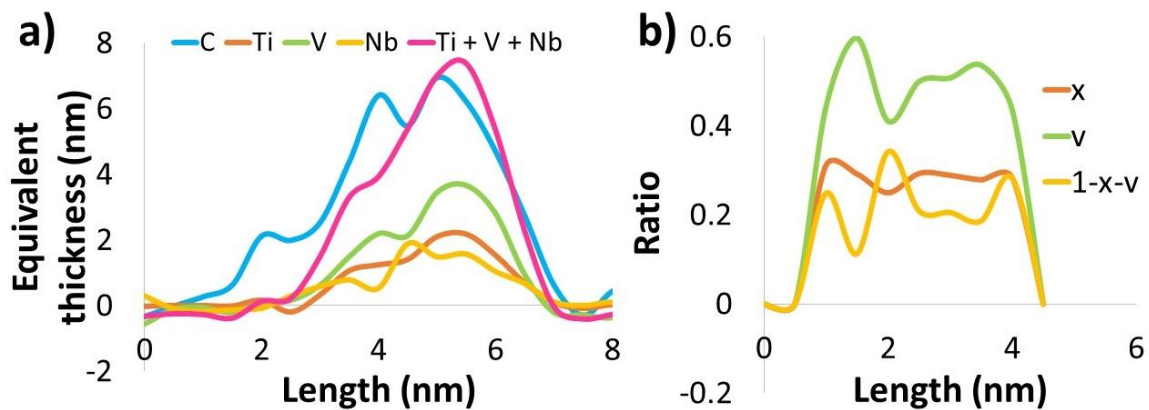


**Figure 3.10** a): Line profiles of equivalent thickness for each element in a  $(Ti, V, Nb)_y C_x$  precipitate and b): Values of  $x$ ,  $y$  and  $(1-x-v)$  metal coefficients in the  $Ti_x V_v Nb_{(1-x-v)} C_y$  precipitate.

More results from this method will be discussed in detail in the chapter dedicated solely to the quantification of precipitates using DualEELS.

### 3.5. Factor rotations

Factor rotation is another function available in the Multivariate Statistical Analysis plug-in for Digital Micrograph, with the function of maximising the variance of either the spectral or the special factors i.e. to enhance the contrast of one domain [98]. Factor analysis makes the interpretation of data easier, especially with the scores and loadings resulting from PCA having no direct physical meaning. As opposed to PCA, factor analysis provides easier-to-interpret results which are elemental spectra correlated to respective abundance maps. An example of such a spectral result is shown in Figure 3.11 f), with the spectral factor shown in grey and the original extracted spectrum shown in blue. While their intensity is different, the main features are present in both and can be interpreted. This is not the case with individual spectral components, an example of which is shown in orange in Figure 3.11 f).

Factor analysis was used when processing large area maps of small precipitates, as it worked well in separating the faint signals from the precipitates from the rest of the matrix. This made masking easier. The processing steps taken to analyse large area maps are described in section 3.6. below.

### 3.6. Processing large area low-loss maps

Low-loss EELS mapping has been used for a number of years in identifying different chemical phases present in a sample [106]. The method, and a review of research in which it has been used in the past can be found in Chapter 4 of this thesis as Chapter 3 mainly deals with the processing of acquired data. Due to the shortened acquisition times required for low-loss EELS in comparison to high-loss EELS or DualEELS, mapping can be done much faster, thus allowing the imaging of much larger areas.

Large area low-loss mapping has been used extensively to identify precipitates and calculate their distribution. As only the low-loss data is acquired here, splicing as described in Section 3.1.6. has not been used. Apart from that, most of the steps, from aligning the ZLP to noise reduction using PCA, are used. In the low-loss spectrum, features such as the iron and manganese plasmons, and Ti, V and Nb M-edges are used to differentiate between precipitates and the matrix.

Once PCA has been done, there are two methods to extract a map showing the precipitates. One way is to do an MLLS fit on spectra using standards from well understood binary nitrides and carbides, together with standards for the matrix, with the resulting fitting coefficients representing maps of the precipitates. This has been explained in the context of accurate quantification in Section 3.4. The other method is to use PCA and factor analysis, where the components showing the precipitates can be used straight away as maps. During this research the second method has been used more often. The resulting maps from the PCA component showing the precipitates are then summed with the map showing the precipitates best from the factor analysis. This enhances the precipitates and reduce the signal to noise ratio in the final map to be used.

Once a precipitate map has been obtained, data processing and particle analysis can be applied following a series of steps. These steps will reveal the outline of the precipitates and provide measurements such as diameter, and hence precipitate volume under the assumption that the precipitates are spherical. While most precipitates can be assumed to be spherical, some of them are not and this could lead to uncertainties which will be discussed in Chapter 4. This method for extracting the outlines of precipitates and their diameters is outlined in Figure 3.11. This shows the original pre-processed spectrum image which has undergone all the steps up to and including PCA reconstruction (a), followed by the map obtained from PCA components (b) and factor rotations (c). b) and c) are then summed to produce a cleared, less noisy map of the precipitates. This is then masked using a custom script to produce a binary map, as shown in d), where the precipitates are represented with 1 count and the matrix by 0 counts. This essentially produces a map of the precipitate outlines. The particle analysis plug-in for Digital Micrograph is then used to identify the precipitates based on their outline and measures a range of statistics for them including their circular diameter. This can then be used to calculate the volume of the precipitates under the assumption that they are spherical. f) shows the original spectrum, and how it compares with

the outputs of PCA and factor analysis. The results from PCA cannot be correlated back to a real signal and have been magnified significantly to be visible. The results from factor analysis are much easier to correlate to real signals in the sample and can be interpreted as spectral signal.

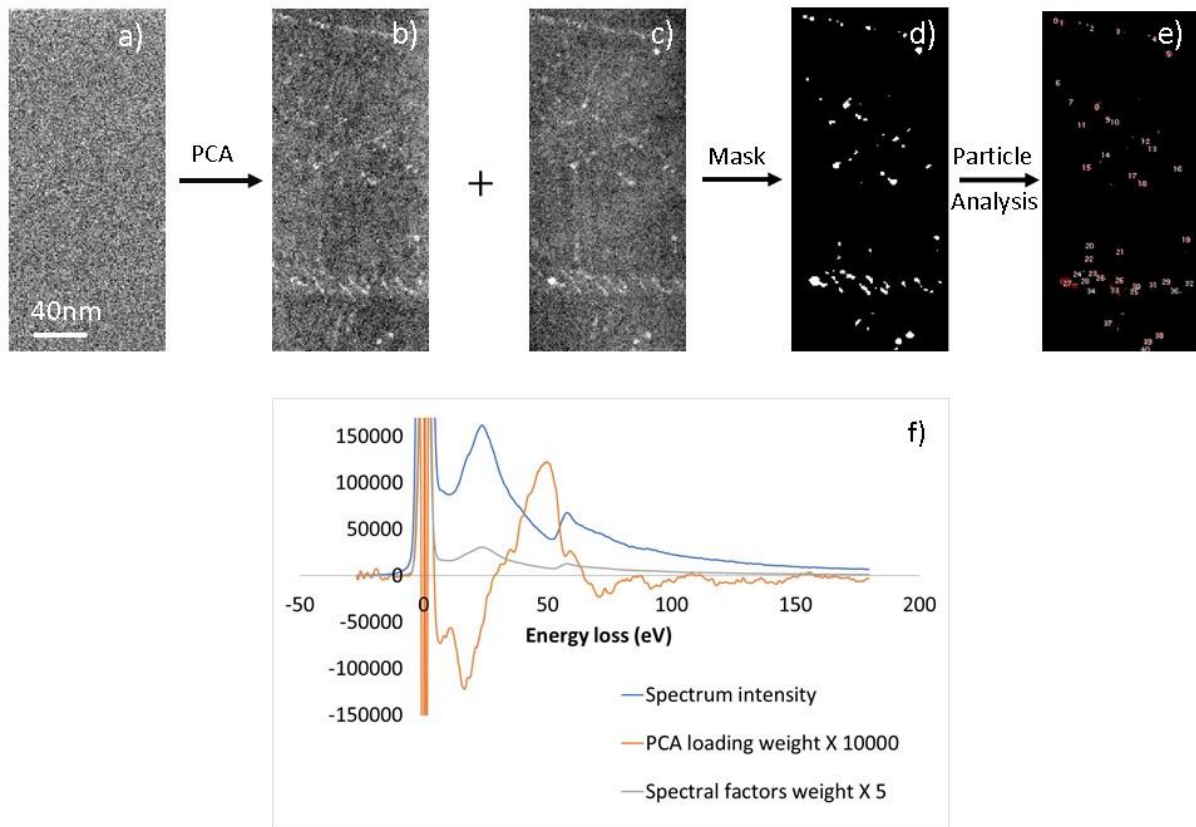


**Figure 3.11:** Procedure for quantifying precipitate statistics from a low-loss spectrum image: a) shows the spectrum image before PCA is applied. b) shows the PCA component map that shows the precipitates. This is summed with c), which shows the precipitate map as obtained from factor analysis. d) shows the sum of b) and c) after a mask has been applied to remove all matrix contributions and contains only the outline of the precipitates. e) shows the precipitates after being identified and analysed using the particle analysis software feature. f) shows the pre-PCA spectrum image (blue) and compares its shape with the shapes of the outputs from PCA (orange) and those of factor analysis (grey) showing that the outputs from factor analysis can be correlated back to the original spectrum while the outputs from PCA cannot.

The final step in the processing is to normalise the particle size distribution to be expressed in terms of particles per unit volume. The x and y dimensions of the datasets, and hence the scanned area, are known for each dataset. As the data acquired is the low-loss spectrum image, the thickness of the scanned area can again be easily obtained from the  $t/\lambda$  function in Digital Micrograph and from knowing the mean free path  $\lambda$  of electrons in the iron matrix. The volume of the matrix can easily be obtained using the formula for the volume of a cuboid.

Dividing the distribution of precipitates by this volume will provide a normalised particle distribution.

### **3.7. Summary**

The raw data that has been collected using DualEELS contains a large amount of random noise, as well as systematic errors due to the microscope and spectrometer. Before any useful information about the composition and distribution of precipitates in the acquired steel data can be obtained, the raw data must be processed and analysed. The initial processing deals with reducing both the volume of the datasets and the amount of noise within them present using methods such as Principal Component Analysis. This is then followed by removing plural scattering within the specimen from the datasets using a Fourier-log deconvolution method. The final analysis steps extract the precipitate information from the data, whether it is their distribution and size from the low-loss maps, or their accurate chemical composition from the MLLS fitting of DualEELS data.

The results of using these techniques on different EELS spectrum image datasets from a range of different steels from the project will be presented in the following chapters. Firstly, Chapter 4 will concentrate on the low-loss mapping of precipitate distributions and using this to measure their size distribution and analyse where in the matrix they form. Chapter 5 will discuss how experimental cross-sections are obtained for a range of binary carbides and nitrides used to accurately quantify precipitates. Quantification results are presented in detail in Chapter 6, with a range of precipitates from different samples being discussed.

## CHAPTER 4

### Large area low-loss EELS mapping

As reviewed above in Section 1.3, the mechanical properties of microalloyed steels are critically dependent on the size and distribution of nanoscale precipitates. This depends on the alloying element content, and upon the thermomechanical treatment schedule. Thus, mapping nanoscale precipitate distributions in such steels over large enough areas to gain statistically significant results is critical to understanding the processing-performance relationship in such steels. This chapter discusses how large enough volumes of steel can be mapped using low-loss EELS to identify the precipitates and measure their size distribution. This is then used to study two different sets of steels originating from within the PreTiControl project. Firstly, we study a martensitic Ti-5 Nb-3 V-7 steel tempered at 600°C for different amounts of time and follow the precipitation evolution, as well as looking qualitatively at precipitate composition in larger precipitates in this steel. Then, the precipitate distribution in a Ti-10 Nb-3 V-0 sample tempered at 600°C is determined and compared with the first steel.

#### 4.1. Motivation

Hardness is an important property of steels, and one way of influencing the hardness is with the formation of small precipitates, as discussed in Chapter 1. Hence, understanding the formation of precipitates and the conditions that influence their formation is important. Ideally, their relationship with the steel matrix would be investigated as well. However, while extremely important, analysing the distribution of the precipitates while they are still embedded in the steel matrix is a challenging task. Methods of analysing precipitates do exist, but they often involve chemically extracting the precipitates from the matrix, especially using the carbon replica extraction technique [107]. This, whilst it can provide extremely useful information, has a lot of drawbacks, such as:

- the matrix is dissolved in the process, so the relationship between the precipitates and the matrix and their distribution within it are lost;
- the smallest precipitates might not be extracted at all, so we cannot obtain any information about them;
- the precipitate composition may be altered during their extraction, making accurate quantification impossible [108].

3D atom probe tomography would solve many of the issues associated with carbon replica extraction, analysing precipitates that are left in the matrix. However, the amount of sample analysed is very limited, which is a disadvantage when trying to analyse a large number of precipitates over a large sample volume [109]. Additionally, some of the ion species are difficult to identify due to peak overlaps, such as the peak at a mass to charge ratio of 28 being

representative of both  $^{14}\text{N}_2^+$  and  $^{56}\text{Fe}^{2+}$  ions. When atom probe tomography results of vanadium precipitates in steel were compared to results for the same sample obtained by carbon replica extraction, there was a  $>1$  ratio of Fe/ V in the precipitate cores. As the precipitates would not contain iron, especially not in such large quantities, these results were likely due to aberrations in the ion trajectories leaving the specimen. These aberrations led to a large reduction in lateral spatial resolution [64].

Energy filtered transmission electron microscopy can produce maps of large areas of the steel and identify the position and size of precipitates as well as a qualitative assessment of the elements present. However, it is not possible to quantitatively determine their chemical composition, with the minimum diameter of detectable particles being larger for EFTEM than for EELS [110]. Additionally, the spatial resolution available in EFTEM is diffraction limited at  $\sim 1\text{nm}$ , which is larger than many of the particles expected to have formed in the steels discussed here. The signal to noise ratio (SNR) for particles with diameters of the order of only a few nm is poor in EFTEM, further limiting the achievable resolution [50]. As such, a better method had to be developed that would image many precipitates that are still embedded in the matrix and measure their distribution over large areas while also allowing the composition of a select few precipitates to be accurately quantified with minimal changes to the experimental setup.

## 4.2. Low-loss EFTEM and EELS mapping in principle and practice

Warbichler et al. used EFTEM to identify precipitates and grain boundary phases in a ferritic-martensitic steel with 10% chromium added [111]. The Fe-L<sub>2,3</sub> edge was used for imaging, with the small precipitates identified using the absence of iron in their composition. Due to the position of the C-K edge at just under 300eV and that of the N-K edge at 400eV, they overlapped with the broad, delayed M<sub>4,5</sub> edges of niobium and molybdenum making it difficult to obtain maps of carbon and nitrogen, let alone trying to quantify them. Hättestrand and Andrén used EFTEM to evaluate the size distribution of precipitates in a 9% chromium steel aged isothermally at 600°C and 650°C [112]. Among other precipitates and phases, VN and M<sub>23</sub>C<sub>6</sub> precipitates were identified, with their rough volume fraction in the sample being estimated by assuming they are spherical and from knowing the average thickness of the sample from thickness maps obtained from the unfiltered images and a zero-loss image. Of the VN precipitates found, many had diameters much larger than 10nm while most of the M<sub>23</sub>C<sub>6</sub> particles had diameters of 50nm or more. By comparison, many of the precipitates we were interested in had diameters of 1nm or even smaller, so a different method was needed to image them.

The earliest studies to have used low-loss EELS to differentiate between different phases and components have investigated different phases in polymer compounds, such as a study by Hunt *et al.* in 1995 [106]. To differentiate between the polymer phases a window was used to select a specific low-loss peak for one organic molecule, and the intensity inside integrated to give a map, whilst excluding peaks corresponding to the other molecules. By selecting

different window positions, different molecules could be mapped. EFTEM can also be used in a similar way, with the narrow slit being placed so that the low-loss spectral features corresponding to certain polymer compounds are mapped while those corresponding to different compounds are not. This technique was used for example by Linares et al. in 2009 [113] to dielectric polymers and some inorganic compounds such as aluminium phosphate. The differences in the EEL spectra corresponded to areas of a given composition imaged using EFTEM. Similarly, Valadares *et al.* [114] investigated aggregates made from polymers and inorganic particles such as silica and aluminium phosphate, this time also using EFTEM together with low-loss EELS. Differences between the low-loss EEL spectra of different regions were visible and correlated back to compositional maps of carbon and phosphorus obtained by EFTEM. More recently, Annand *et al.* used EELS and the differences in the shape of low-loss spectra to differentiate between different phases in oxidized Zircalloy-4 material to map the oxide-metal interface [115].

The low-loss mapping method takes advantage of the difference in electronic band structure and low-lying atomic states between the different phases, which leads to differences in the dielectric function. As the shape of the low-loss spectrum in the plasmon region depends partly on the dielectric function of the material, there is an energy window where the shape of the low-loss spectra differs between the different phases. This can be seen in Figure 4.1, where spectra taken from this PhD research shows the low-loss spectra of precipitates when compared to that of the steel matrix, with the energy range where the two differ significantly highlighted. Using a background before that region (typically a first order log-polynomial rather than a power law is used in the plasmon region) and integrating over the window where the low-loss shapes are different will quickly reveal a map of the precipitates. Extracting a spectrum from one of these and using it in an MLLS fit over that region together with a shape from the matrix, will produce a good quality map such as the one in Figure 4.2, showing the position of small precipitates throughout the imaged area.

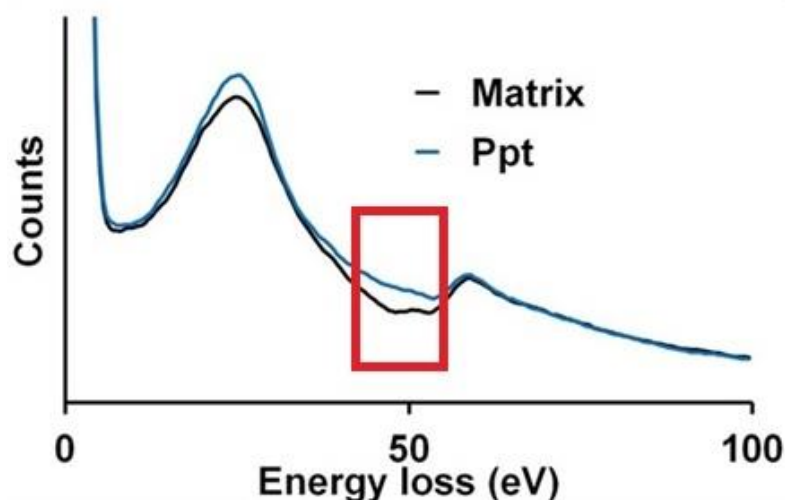


**Figure 4.1:** Low-loss spectra extracted from both precipitates and the steel matrix, highlighting the difference between the two.

The region highlighted in the red box in Figure 4.1 contains the metal (Ti, V, Nb) M-edges as well as plasmons from iron and manganese. As the matrix contains iron and manganese and the precipitates contain Ti, V and Nb, this causes the difference between the matrix and precipitate extracted spectra as seen in Figure 4.1.

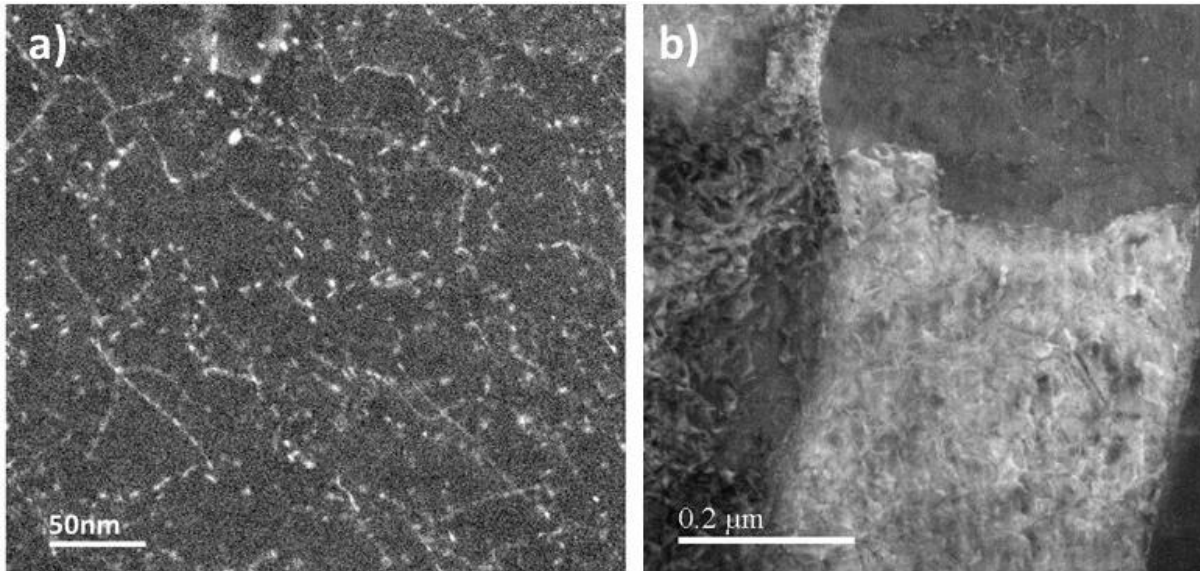


**Figure 4.2:** a) Map of a precipitate rich region in one of the steel samples discussed in this chapter (75 minutes tempering time), clearly showing that many of the precipitates have formed along lines and throughout the sample and b) annular dark field image of a large area of the steel showing individual grains and grain boundaries.

### 4.3. 600°C tempering of a martensitic V-7, Nb-3, Ti-5 steel

The samples have been provided by CRM and are part of a tempering series of a martensitic steel. The steel composition is 0.06 wt.% carbon, 1.8 wt.% manganese, 0.03 wt.% niobium, 0.05 wt.% titanium, 0.07 wt.% vanadium, 0.005 wt.% nitrogen, 0.03 wt.% aluminium, 0.02 wt.% phosphorus and 0.002 wt.% sulphur, with the rest being iron.

The samples have undergone two different heating, holding and quenching cycles before being tempered at 600°C, as detailed in Figure 4.3. For both cycles they were rapidly heated, being held at 1000°C for one minute during the first cycle, and at 1250°C for 10 minutes during the second cycle. The rapid cooling ensures that the carbon from the original austenite steel cannot escape solid solution, thus remaining trapped in a distorted martensite structure. After this sequence of steps, the steels were tempered at 600°C for different amounts of time, followed by a final rapid quench to preserve the resulting structure, with the hardness being measured for each tempering time. Large precipitates were believed to have formed in the early stages of the processing steps when the steel solution was kept at high temperatures. During the tempering cycle at the end is when the small precipitates were expected to form in the case of these steels.

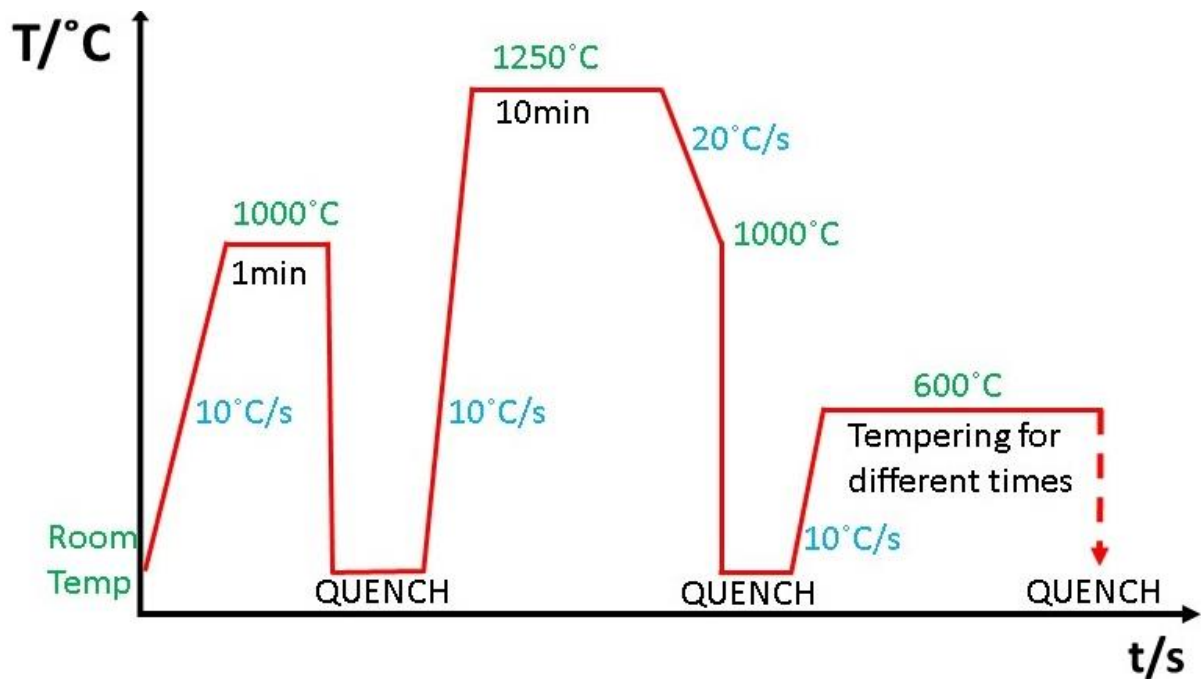


**Figure 4.3:** The thermal treatment applied to the Ti-5 Nb-3 V-7 steel series provided by CRM, with the final stage being the only one different for each of the samples in the series, with tempering at 600°C taking different amounts of time for each of the samples.

The hardness was measured with respect to the isothermal tempering time, with the maximum hardness being measured in the sample tempered for 60 minutes, as can be seen on the graph in Figure 4.4. There was a progressive increase in hardness between a tempering time of 15 minutes and 60 minutes, with the hardness decreasing again for the samples tempered for 75 and 90 minutes. To investigate the precipitation across the tempering series and relate it to hardness, samples to either side of maximum hardness have been prepared and analysed. With the precipitation in the samples tempered for 15 and 30 minutes expected to be minimal, those samples were not analysed. As such, the precipitation has been mapped and the size distribution measured for the four samples tempered for 45, 60, 75 and 90 minutes respectively.

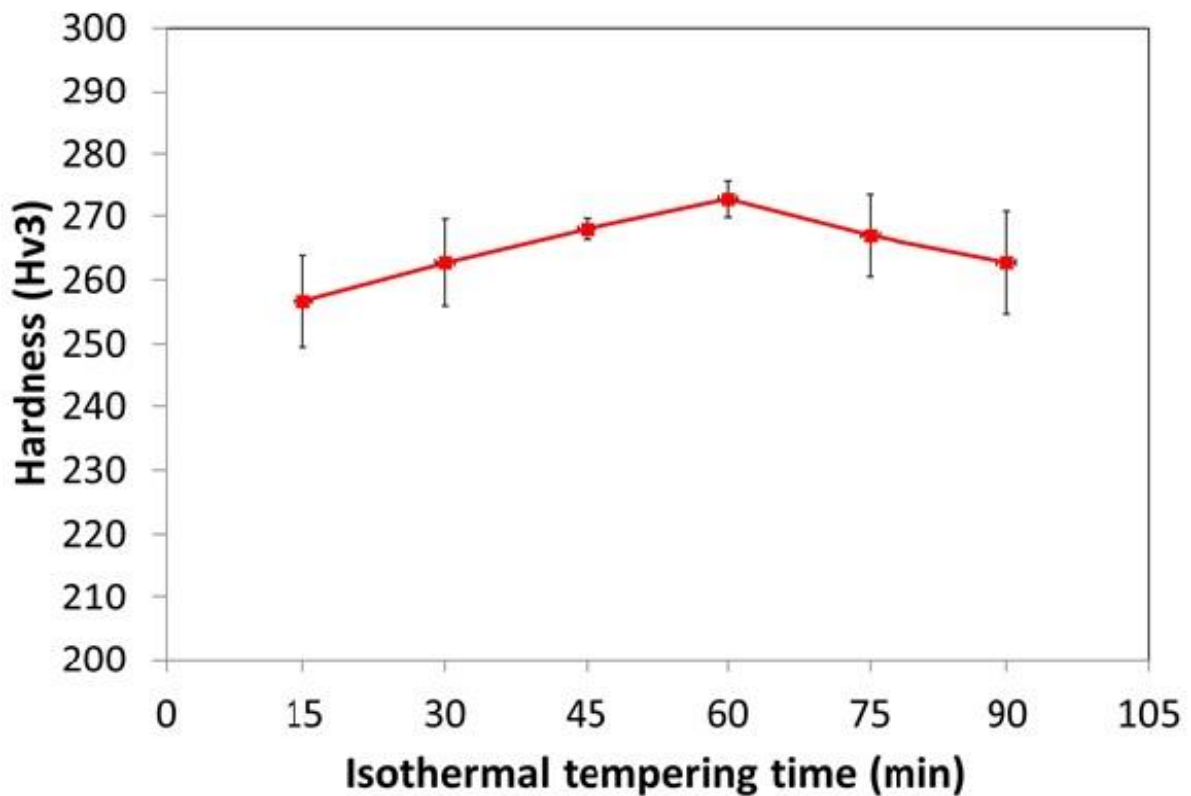


**Figure 4.4:** Measured hardness as a function of isothermal tempering time for the Ti-5 Nb-3 V-7 steel series tempered at 600°C for different amounts of time. The samples tempered for 45, 60, 75 and 90 minutes were picked for analysis.

#### 4.3.1. Data acquisition

The four samples analysed have been prepared using the FIB lift-out technique described in Chapter 2 of this thesis. Low-loss EELS data has been acquired using the aberration corrected JEOL ARM200CF electron microscope equipped with a cold field emission gun and a Gatan Quantum ER EELS spectrometer with DualEELS capability. It was operated with an emission current of 14.6 $\mu$ A, giving a probe current of approximately 3000pA. The typical probe semi-convergence angle was 29mrad, and the Glasgow-specific post-specimen lens setup giving a spectrometer collection semi-angle of 36mrad.

The exposure time for acquiring the low-loss spectrum image was 0.0001s per pixel, having been chosen to ensure a long enough exposure time to give an appropriate signal to noise ratio but low enough to not saturate the detector. To identify the smallest precipitates, step sizes used were of the order of 1nm or smaller.

Once areas rich in precipitates had been identified, DualEELS data of selected precipitates and matrix structures was collected for chemical analysis. Further details of the analysis methodology will be given in Chapter 6, although some results are given below.

#### 4.3.2. Precipitate size distribution as a function of tempering time

The data was processed as described in Chapter 3, and the sizes of precipitates have been measured using the Particle Analysis plug-in for Digital Micrograph. Often, if precipitates were close together (for example having formed along a grain boundary) the algorithm would identify them as just one larger particle. In this case user intervention was required, and the total diameter found by the algorithm would be divided by the number of precipitates identified.

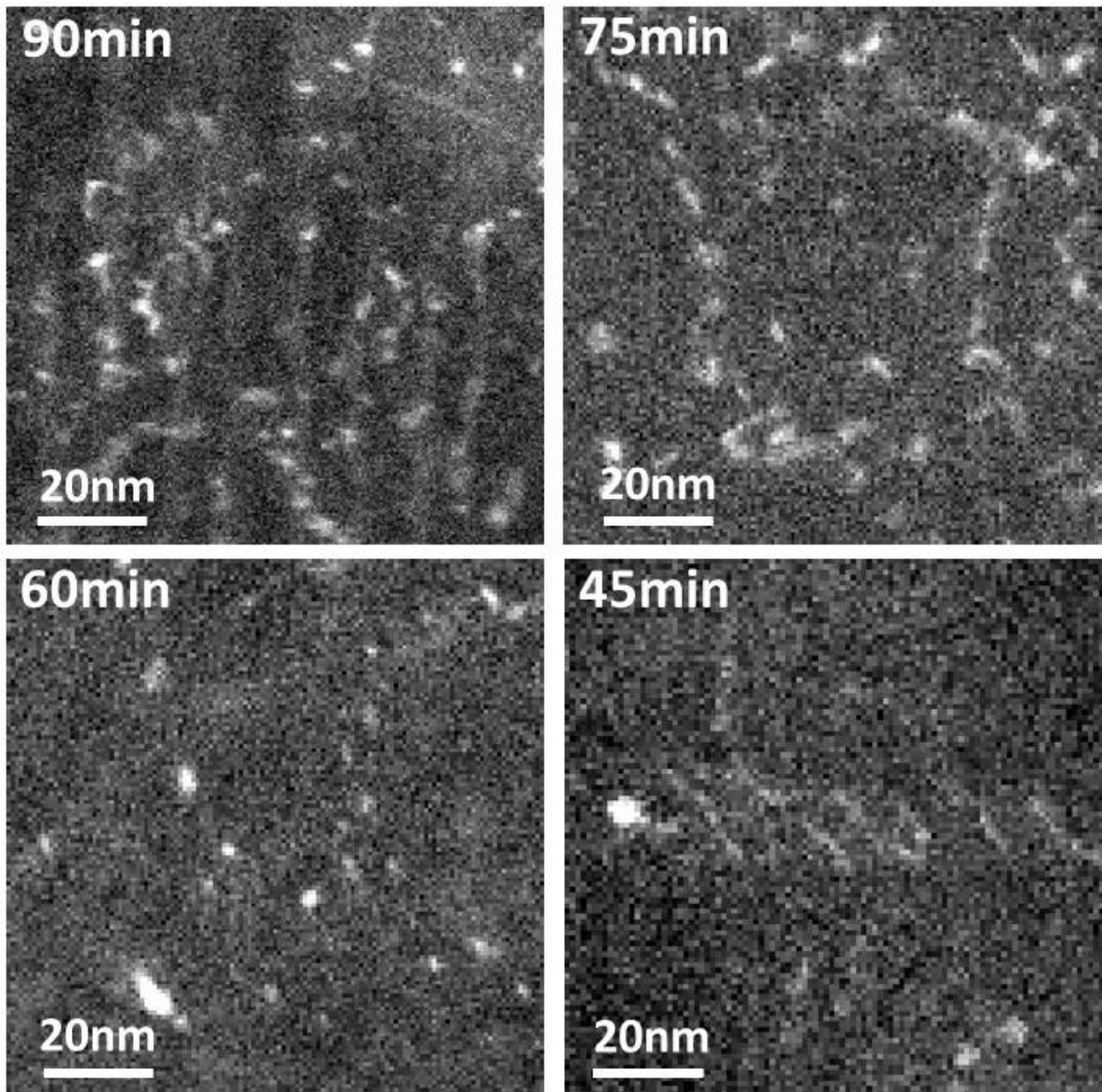


**Figure 4.5:** Maps of 100nmx100nm precipitate rich areas in each of the four CRM samples analysed, with the 90min sample showing the most precipitates and the 45min sample showing very few by comparison.

Examples of the analysed areas in each of the four steels are presented in Figure 4.5, illustrating the differences in precipitation between the samples. The maps cover areas of

100nm × 100nm (in total areas covering a few  $\mu\text{m}^2$  were imaged for each of the samples) of the steel and maps are in good agreement with the combined histograms in Figure 4.9, showing a decrease in the number of precipitates per imaged area from the 90 minutes tempered sample to the 75 and 60 minutes samples. The concentration of very small precipitates decreases as well, which can be seen when comparing between the maps for the 90 minutes and the 75 minutes tempered sample. There are significantly fewer precipitates in the 60 minutes tempered sample, especially precipitates under 2nm in diameter. The sample tempered for 45 minutes had by far the smallest numbers of precipitates mapped overall, and areas of a similar size to those of the other three samples could not be found to contain precipitates. The precipitation in this sample is very inhomogeneous and occurs mainly on grain boundaries that are likely to have been in the steel from the previous austenite phase prior to quenching into martensite. This can be seen on the map, with a few large precipitates being visible. The map also shown areas where smaller precipitates could have formed alongside lines, but this precipitation is restricted to the centre of the imaged area and is very inhomogeneous. Additionally, these precipitates are overall of larger diameters than most precipitates found in the other samples. This suggests that they have formed in austenite at high temperature, and not during the tempering process.

Larger precipitates have often been identified alongside grain boundaries or previous grain boundaries that appears to have been displaced later in the processing cycle. A series of precipitates formed alongside a grain boundary that has later been displaced was found in the sample tempered for 60 minutes. The survey image can be seen in Figure 4.6, with arrows pointing to the direction of the grain boundary. The precipitates can be seen as darker areas, originally running from the top of the image downwards alongside the boundary. They then turn towards the right, where the boundary would have been before being displaced towards the left in the survey image. The green box around the precipitates and some of the boundary represents the area that has been mapped using EELS. MLLS fitting of the low-loss data suggested that the particles are metal carbides, however accurate quantification of the low-loss area was not possible yet due to a lack of suitable cross-sections for all the edges present. However, even with low integration times, DualEELS provides enough signal in the high-loss spectrum to make a qualitative estimate of the composition of these precipitates. Elemental maps of the precipitates and grain boundary in the 60 minutes tempered sample discussed above are shown in Figure 4.7. The maps were created by using a simple power law background before the respective edges and integrating the signal over the edge. While this is not the ideal background for accurate quantification and an experimental one would be preferable, the noise level in the data made only a qualitative investigation possible. All the precipitates are metal carbides as suggested by the MLLS fit on the low-loss data, with high concentrations of titanium and vanadium. There is some evidence of niobium, however, due to the Nb-M edge being at low energy losses in an area dominated by strong EXELFS from the other metal M-edges, putting an accurate background before it is problematic. No evidence

of nitrogen was found in these precipitates. The grain boundary is manganese rich, with some of the precipitates having an increase in the manganese content as well.

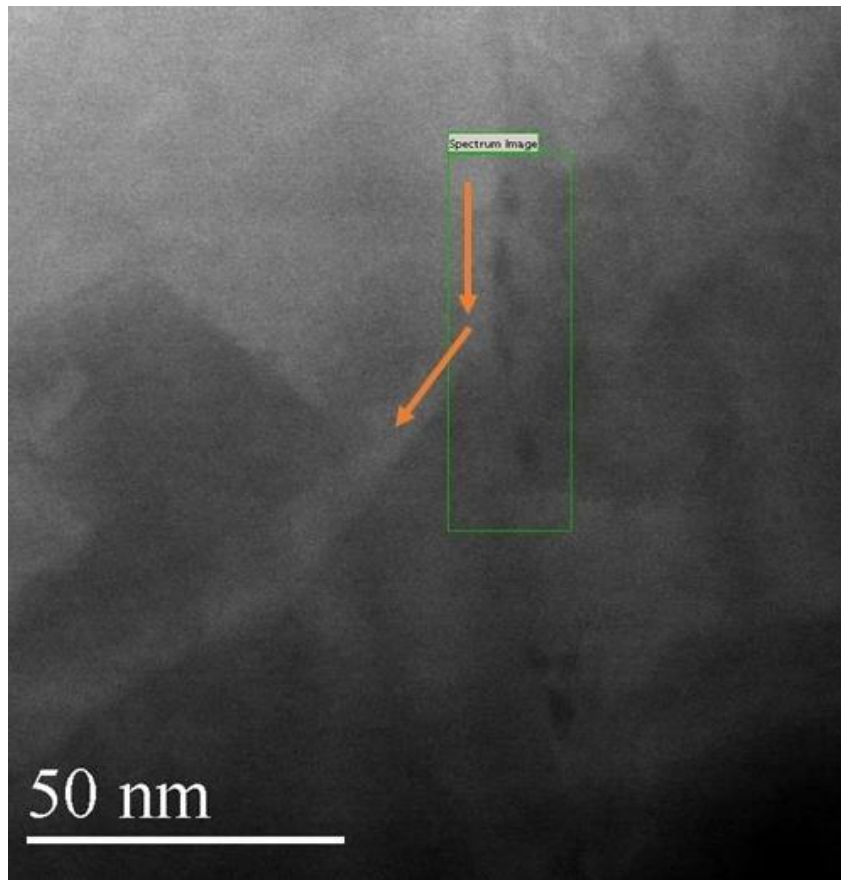


**Figure 4.6:** Survey image showing a grain boundary (indicated by arrow) and precipitates having formed in the region (dark grey).

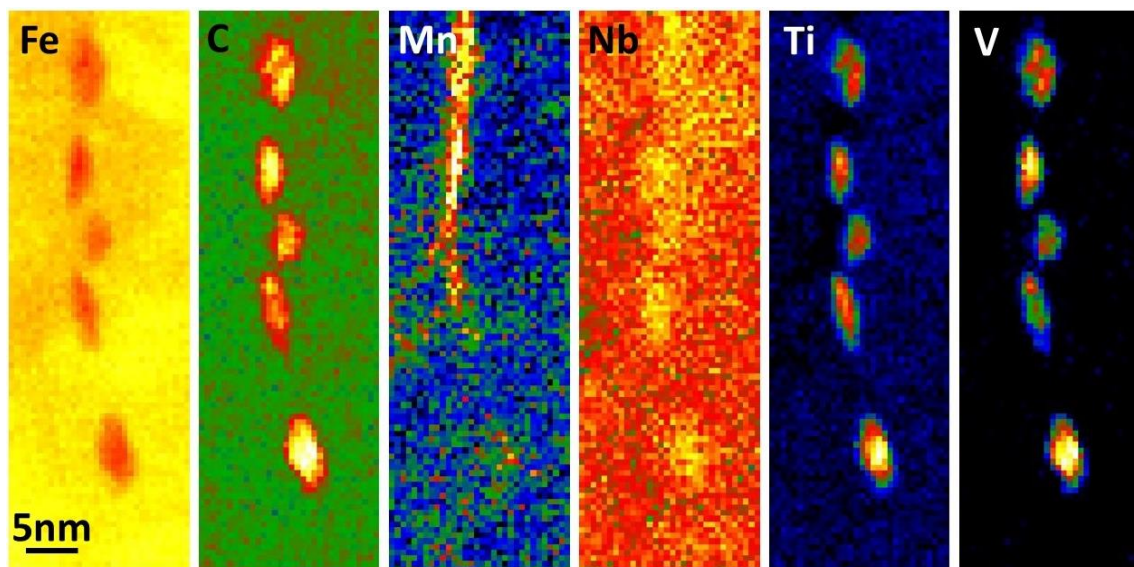


**Figure 4.7:** Composition maps for a series of precipitates formed along a manganese rich grain boundary.

Metal carbides and nitrides have a rock-salt structure, meaning that the precipitates will have a face centred cubic structure. However, they are formed in martensite, which has the ferritic body centred cubic structure. Thus, the formation of precipitates in this steel may follow a Baker – Nutting orientation relationship with respect to the ferrite matrix, forming as fine plate-like particles. These have been observed extensively in the past, for example by Yen *et al.*, in the case of titanium carbides forming in a titanium bearing steel [116]. This was clearly observed in the steels studied here, and an example of this will be discussed in detail in Chapter 6. There, the diffuse precipitates appearing larger are seen face-on, with the intense precipitates that appear small and elongated being seen edge-on.

For each sample in the CRM provided steels (tempering times 54, 60, 75 and 90 minutes), a few areas were imaged to identify precipitates. Examples of the imaged areas for each of the samples can be seen in Figure 4.8.

The precipitates were identified after the datasets have been processed as described earlier in Chapter 3 of this thesis. Their sizes were measured and the number of precipitates in each of the diameter ranges has been calculated. The results can be seen in Figure 4.8, showing the number of precipitates identified for each sample in each diameter range. For each of the samples, most of the precipitates are under 4nm in diameter. Their size distribution follows the same shape for each of the samples, with most of the precipitates being small and only a small number of precipitates identified having diameters above 8nm.

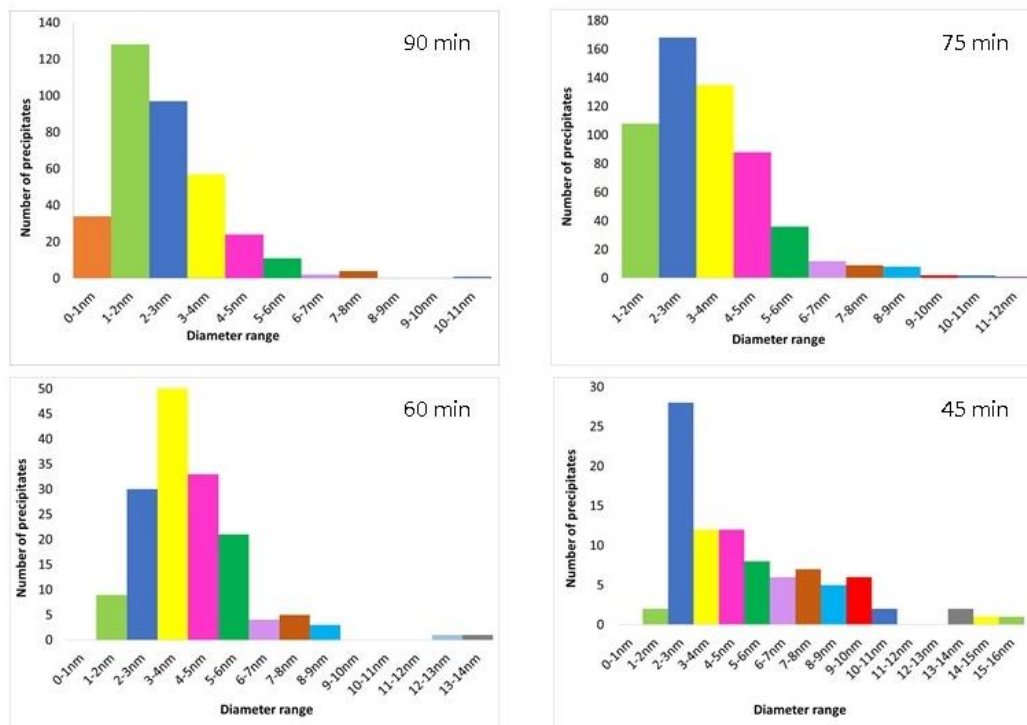


**Figure 4.8:** The total number of precipitates identified in each diameter range, for each of the CRM samples from the tempered martensite series.

Whilst the plots of Figure 4.8 provide a useful insight into the size of the precipitates and their relative abundance, they do not provide an absolute measure of the precipitate distribution or allow for comparisons between the samples as the total areas and volumes imaged are not exactly equal. However, the low-loss EELS spectrum also allows thickness determination in terms of the mean free path  $\lambda$  [117]. Thus, the thickness of matrix in the area imaged may be determined, provide  $\lambda$  is known, and thus the total volume of the matrix analysed may be determined. Dividing the precipitate distributions of Figure 4.8 by the total volume of matrix imaged gives the precipitate distribution per unit volume. This is shown in Figure 4.9 for all four samples, using total analysed volumes of approximately  $0.01\mu\text{m}^3$  for the samples tempered at 90, 75 and 50 minutes, with the distributions combined onto the same histogram. There are really two stories combined here. Firstly, all samples have similar distributions of 3-6 nm precipitates. These precipitates may have been formed earlier in the processing at higher temperatures and were unaffected by  $600^\circ\text{C}$  tempering. Secondly, the concentration of small precipitates  $< 3$  nm increases strongly with increasing tempering time, suggesting that the nucleation and growth of the small precipitates is the main story here. There is one anomaly in that the sample tempered for 45 minutes appears to have a larger number of precipitates in the 2-3nm diameter range than expected – which may indicate some local inhomogeneities (and the total volume of material analysed for 45 min was smaller than for the others – in this case it was approximately  $0.001\mu\text{m}^3$ ). This sample also had a larger number of large precipitates than all other samples. The probable reason for their high concentration is that the larger precipitates were formed on grain boundaries at much higher temperature, and they are at a low concentration overall, but one TEM sample caught a high concentration area containing a precipitate-decorated boundary.

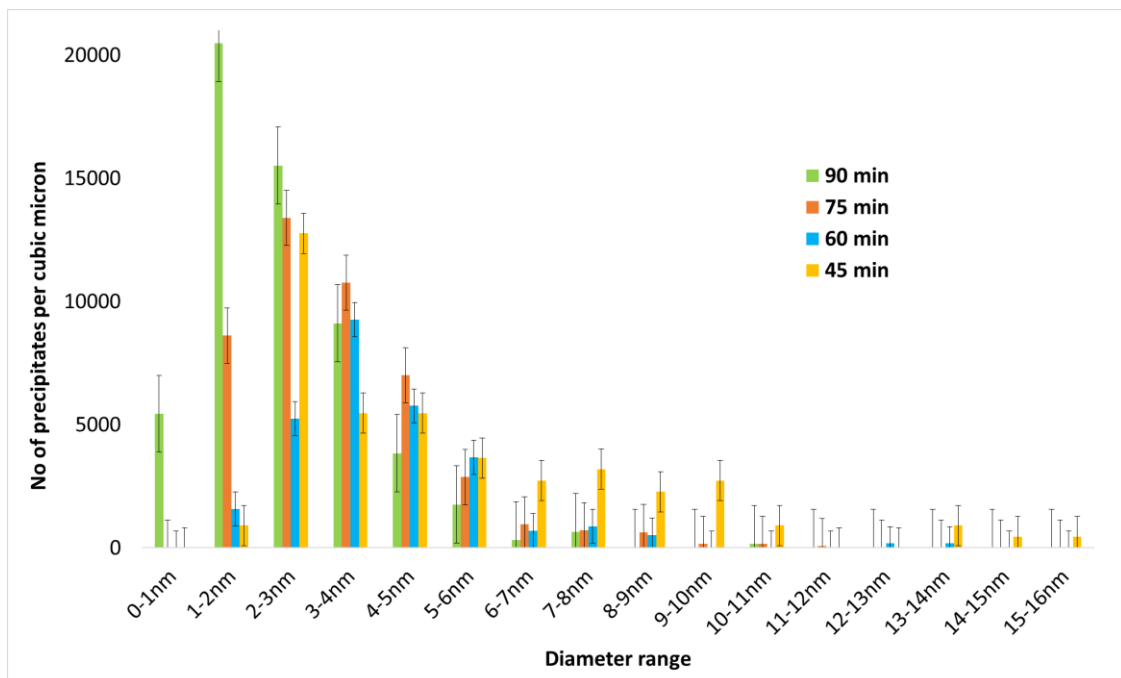


**Figure 4.9:** Comparison between the number of precipitates per unit volume in each diameter range for each of the four CRM samples tempered at  $600^\circ\text{C}$  for different lengths of time.

At the higher temperatures at the beginning of the processing cycle as seen in Figure 4.3, the formation of precipitates of larger diameters is expected. These were usually found to have formed around pre-existing defects and irregularities in the steel microstructure, such as grain boundaries. These larger precipitates have a significant manganese content on top of the large vanadium and titanium carbide contributions, as seen in Figure 4.8. No significant nitrogen content has been detected, with little evidence of a small amount of niobium potentially present in the precipitates.

At the end of the thermal processing cycle, the steel was tempered at lower temperatures for different amounts of time. It was during this tempering process that the smaller precipitates have started forming throughout the individual grains. Some of these precipitates appear to be very faint and circular, while others appear very elliptical and show up bright when mapped. This could be evidence that these precipitates being plate-like, quite likely following a Baker – Nutting orientation relationship. The faint, circular ones would in this case be observed top-down while the bright, elliptical ones would have been imaged edge-on. They are face centred cubic, rock-salt structures that have tried to form inside a body centred cubic matrix. The difference in structure meant that it was easier to expand in diameter in one axis than in another, thus forming plate-like structures and not spheres. Since the precipitate diameter distributions are calculated based on the assumption that all precipitates are spherical, this could introduce an error in the size distribution of small precipitates.

Comparing the precipitates distributions in Figure 4.9 to the hardness plot in Figure 4.4, an initial increase in hardness with an increasing tempering time (from 45 minutes tempering time to 60 minutes tempering time) can be seen. However, the precipitate number was highest in the steel tempered at 90 minutes, where the precipitates were also the smallest. This discrepancy between the number of small precipitates and the steel hardness is not commonly seen. There are many reasons why this could be the case here, and from discussions with the project partners it was suggested that the initial increase in hardness is due to the nucleation of small precipitates and the subsequent increase in dispersion hardening. However, the overall decrease in hardness for tempering times higher than 60 minutes could be due to the loss of titanium and vanadium from the solid solution into the formation of more and more precipitates and a loss of solid solution hardening. Other suggested reasons for the discrepancy could be to do with changes in grain size or microstructure heterogeneity.

#### 4.4. Precipitate mapping in a Ti-10 Nb-3 steel

In addition to comparing samples of the same composition that have undergone different thermal treatment, we have analysed a sample having a different composition. This sample was provided by CEIT in Spain and contains more titanium than the CRM series but does not have any added vanadium. The composition of this steel in weight percentages is 0.06 wt.% carbon, 1.8 wt.% manganese, 0.03 wt.% niobium, 0.10 wt.% titanium, 0 wt.% vanadium, 0.005 wt.% nitrogen, 0.03 wt.% aluminium, 0.02 wt.% phosphorus and 0.002 wt.% sulphur, with the

rest being iron. This sample has undergone two cooling stages as can be seen in Figure 4.10: a quick cooling stage from 900°C to 600°C, and then a cooling at a much slower rate down to 200°C before being quenched to room temperature to trap the formed microstructure.

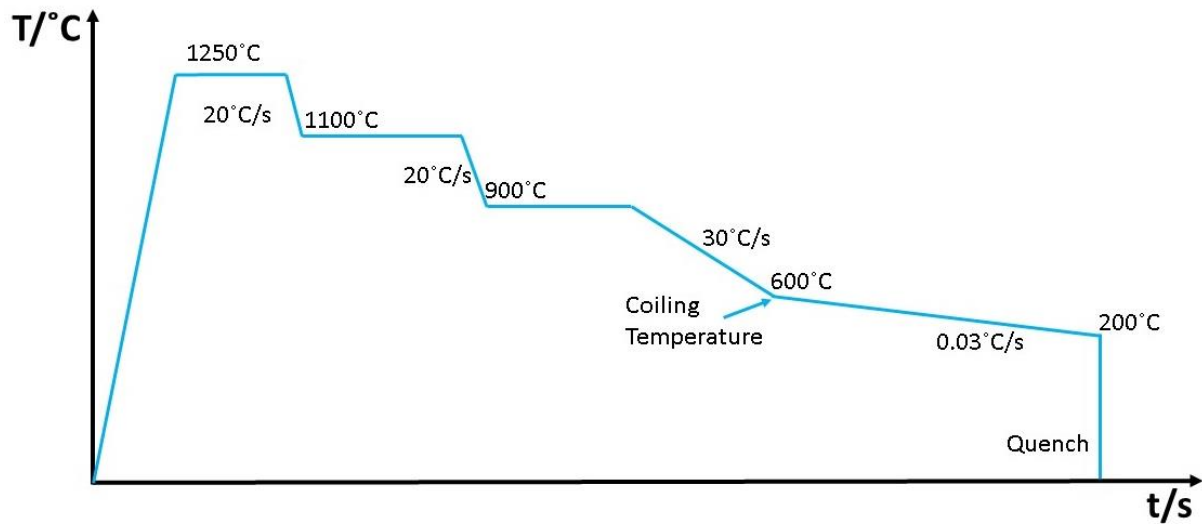


**Figure 4.10:** The thermomechanical treatment applied to the steel of composition Ti-10 Nb-3 V-0.

This steel was prepared in the same way using the FIB lift-out technique, with the STEM-EELS data being collected using the same microscope settings and parameters as in the case of the CRM samples. An ADF image of the steel lamella, with different grains visible, can be seen in Figure 4.11 with a much smaller area of the steel, this time 100nm × 100nm, being shown in Figure 4.12 with some precipitates visible.

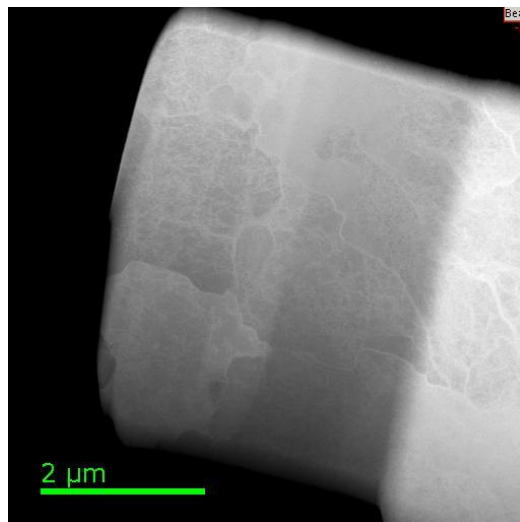


**Figure 4.11:** ADF image of a lamella prepared from the CEIT steel, showing different grains and the boundaries between them.

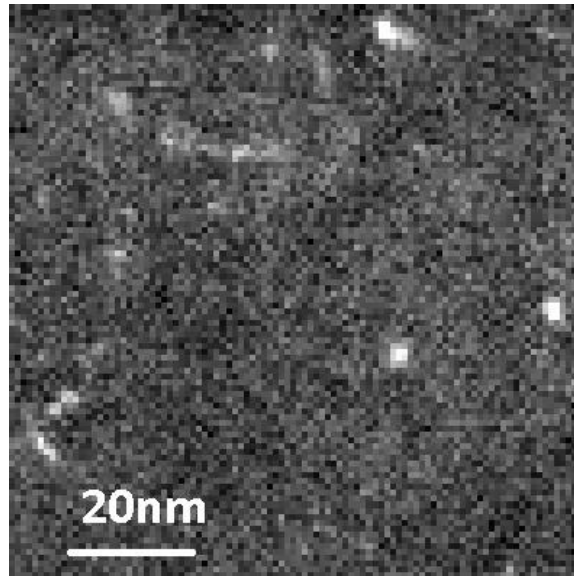


**Figure 4.12:** Precipitate map of a 100nm × 100nm area in the Ti-10 Nb-3 steel.

The data was analysed in the same way, and the number of precipitates per unit volume and their diameters are shown in Figure 4.12 below. A much smaller volume was imaged for this steel than for the ones in the tempered martensite series, with only a 0.003 $\mu\text{m}^3$  having been imaged. This was due to the sample being slightly damaged during the FIB milling.

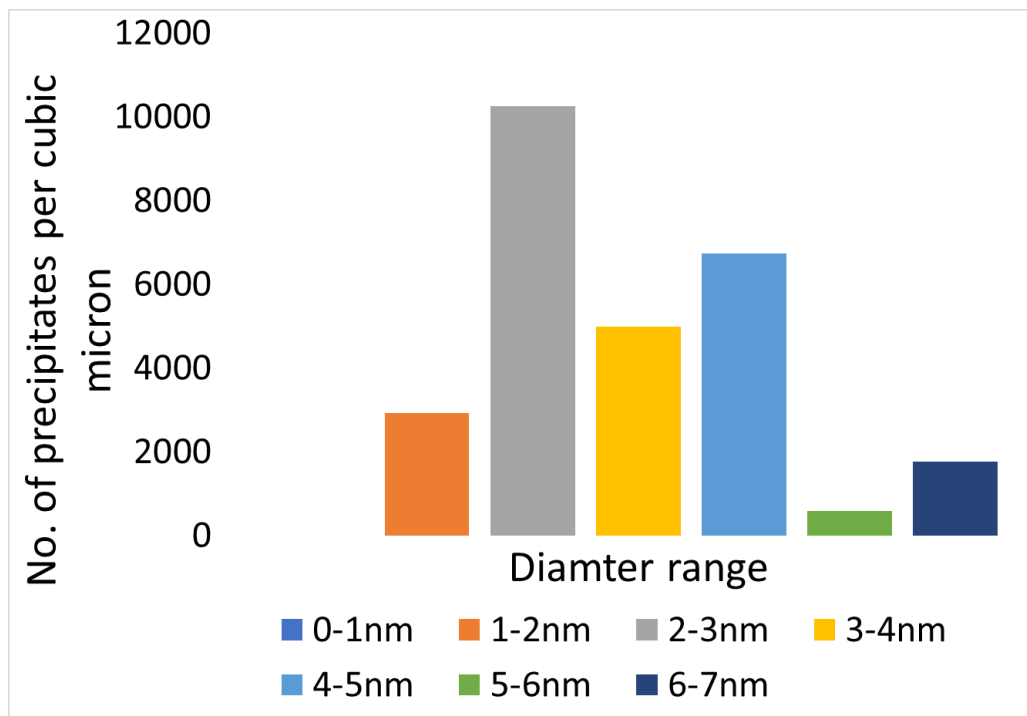


**Figure 4.13:** The distribution of precipitates per unit volume in the CRM sample of base composition Ti-10 Nb-3

Compared to the steels containing vanadium but less titanium, the diameter range of these precipitates is smaller. In this case there are no precipitates having diameters below 1nm in

diameter, and no precipitates with diameters larger than 7nm have been found. The histogram agrees with the map in Figure 4.11, where most of the precipitates are roughly the same size with extremes in diameters not being visible in this case. In this case it is possible that the nucleation of small precipitate has stopped earlier in the processing cycle, hence the lack of precipitates with diameters less than 1nm and the relatively small number of particles with diameters in the 1-2nm range, which were abundant in the tempered martensite steels.

#### **4.5. Possible sources of systematic errors**

A note on the errors on the size distribution needs to be made here. The error bars in Figure 4.6 are from  $\sqrt{N}$ , with N being the number of precipitates in each of the diameter ranges. However, there are several other errors introduced by the analysis procedure. As it can be seen from the area maps in Figure 4.7, precipitates often form close to one another and along pre-existing structures in the matrix. Often when this was the case, the masking script and Particle Analysis plug-in would identify multiple close precipitates as just one. When this was the case, the diameters identified were manually divided by the number of precipitates identified together. This assumes that they all have the same diameters, which might not be the case. They are also assumed to be spherical, which again is not always the case as plate-like precipitates have been identified throughout the samples. Another possible source of error in the analysis is again due to how the precipitates are masked and identified. It has been noticed that the very small precipitates are often identified as smaller than they are while the large precipitates, especially if surrounded by a thicker, brighter region of matrix, are identified as being larger than their actual diameter. In terms of the size distribution of precipitates, this means that the very small diameter precipitates could be slightly larger than measured while the largest ones could be slightly smaller. This has been noticed for each of the samples and datasets analysed as part of this research. This does not, however, change the shape of the distribution. None of the issues discussed here affect the overall shape of the size distribution and they only affect a small number of precipitates (the largest number of affected precipitates was about 10 in a dataset where over 100 have been identified in total).

#### **4.6. Summary**

The precipitate distribution of four steels belonging to a tempered martensite series was measured using low-loss EELS mapping. The four steels had been processed identically until the tempering stage, where they were held at 600°C for 90, 75, 60 and 45 minutes respectively.

The distribution of precipitate sizes is as was expected from discussion with the project partners, with more small precipitates nucleating the longer the steel spends being tempered at 600°C. The formation of small precipitates influences the hardness of the steel, with an increase in the number of precipitates leading to an increase in the hardness of the steel. However, the peak hardness is achieved when the sample is tempered for 60 minutes and

then decreases for the 75 and 90 minutes tempered samples. This is due to martensite softening as tempering time increases. Additionally, the formation of precipitates removed alloying elements such as titanium and vanadium from the matrix, leading to further softening of the matrix. As such, the overall hardness of the steel is a result of hardening due to the formation of small precipitates during tempering, and of softening due to both carbon and transition element precipitation [118]. Precipitation initially increases the strength before the softening effects become dominant with increasing tempering time.

While it was possible to measure the size distribution of precipitates formed in steel before, the methods available would either remove the matrix and potentially alter the chemistry of precipitates, or only analyse small volumes of matrix and be unsuitable of large area characterisation. The work presented in this chapter eliminated both of those issues, by mapping large areas of the sample over short time intervals and providing the opportunity to analyse particles while still embedded in the matrix. Particles as small as 1nm in diameter can be detected effectively, with small plate-like particles detected in multiple orientations.

Large area low-loss mapping allows for not just the identification of precipitates and measurements of their size and distribution, but also for an initial qualitative analysis of their composition. Once the precipitates have been identified, it is also easy and quick to switch from acquiring just the low-loss data to DualEELS acquisition, making chemical analysis much more time efficient than previous methods such as EFTEM, which require more changes in the microscope and acquisition settings. An in-depth analysis of the composition of some selected precipitates will be presented in Chapter 6. First, more details required for quantification, such as obtaining experimental cross-sections, will be discussed in Chapter 5.

## Chapter 5

### Accurate measurement of EELS differential cross-sections

Acquiring DualEELS data means that we have access to the complete energy range of the spectrum, including the zero-loss intensity. In addition to removal of plural scattering by Fourier logarithmic deconvolution, which has been discussed in Chapter 3, this allows the edge intensities to be normalised and for the local thickness to be determined [119].

Historically, much of EELS quantitative analysis has been done using theoretically calculated differential cross-sections. There are two models that are routinely used to calculate the cross-sections; these are the hydrogenic and the Hartree-Slater models [120] [121]. The calculations are based on isolated atoms and do not consider the contributions of neighbouring atoms present in a solid. As such, they do not contain any information of the energy loss near edge structure (ELNES) or the extended energy loss fine structure (EXELF). As discussed in Chapter 2 of this thesis, both ELNES and EXELF provide important information about the materials studied. The theoretical calculations also do not include the white lines present in the core-loss edges of transition metals, although a method for including them has been proposed [122].

Additionally, even with DualEELS the energy loss range available during a single data acquisition is limited. The core-loss edges that can be used in quantification vary with atomic number. For light elements such as carbon, the K edge can be used successfully however, the heavier the atomic mass of an element, the higher the energy-loss at which its K edge is located in the high-loss spectrum. The accuracy of the calculated cross-sections varies depending on the type of edge. For K edges, the calculated cross-sections are accurate to within a few percent [123]. However, this accuracy was thought to decrease significantly in the case of L and M edges, thus making the quantification of heavier elements, where only these edges are available, far less accurate. In the case of the  $L_{2,3}$  edges, the error on the calculated cross-section was thought to be approximately 15%, with the  $M_{4,5}$  edges having even greater errors. However, more recent calculations show the theoretical and experimental cross-sections for L-edges to match quite closely after the edge. In the case of M-edges, they also match about 200eV after the edge however the mismatch in the edge area is still significant. A further error is introduced by the fact that these edges have white lines [123]. These theoretical cross-sections are used widely, for example in the quantification routines available in Digital Micrograph.

The approach used here to quantify the composition of specimens has been to use experimentally obtained cross-sections from well-understood binary carbides and nitrides. The DualEELS data from the carbides and nitrides was acquired under the same experimental conditions as the spectrum imaging of precipitates [124].

There are two important issues that need to be addressed before accurate experimental cross-sections can be obtained. The first has been briefly presented in Chapter 2 when discussing FIB sample preparation methods and is to do with the fact that milling with ion beams can change the material and create a surface layer of different composition to the rest of the material. This is minimised as much as possible during sample preparation, and the surface layer contribution to the spectrum image is tackled by taking spectrum images over a range of thicknesses and assuming that the surface layer is of constant thickness. This allowed us to use a least squares fitting method to extract the bulk behaviour [125].

The second issue is that the absolute thickness of the samples must be accurately determined. The value of  $t/\lambda$  is obtained from the low-loss spectrum, and if an accurate value of  $\lambda$  is available then the local thickness can be calculated. For the research carried out in this PhD, the mean free path,  $\lambda$ , has been calculated for TiC. This has been done using a needle shaped sample of TiC and will be discussed in detail in this chapter. The mean free paths for TiN, VC, VN, and later NbN and NbC, have been calculated by using the results from TiC to scale the parametrisation of experimental data by Iakoubovskii et al. [126]. This parametrisation scales the mean free path as a function of the material density.

### 5.1. Mean free path measurements

For mean free path measurements, needle-shaped samples like the NbN needle shown in Figure 5.1 were used. For the cross-sections calculated and used in this research, a needle-shaped sample of TiC was used to calculate the mean free path. The sample was made before the start of this project, as part of a different PhD [127].

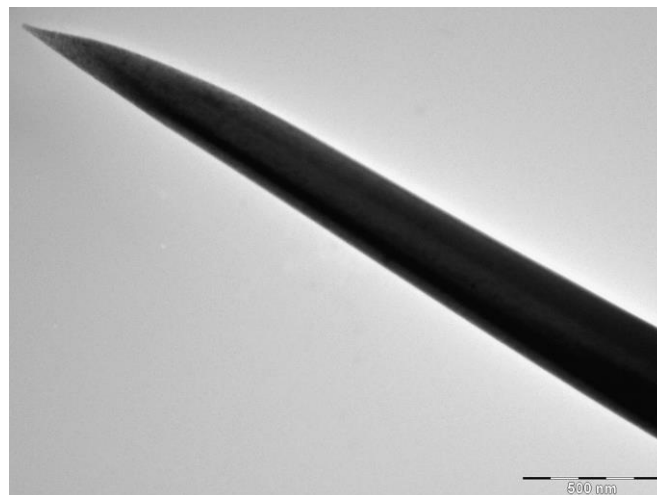


**Figure 5.1:** A large area low-magnification TEM image of an NbN needle shaped sample. Only the very top of the sample, where the needle is the thinnest, was used.

A method was used which made a direct measurement of the thickness of the needle sample during the experiment when the spectrum images to measure  $t/\lambda$  were taken. With the sample in a tomography sample holder, a spectrum image was taken at a given degree of tilt.

The sample was then tilted by 90° and a HAADF image taken at that orientation. The width of the HAADF image represents the thickness of the needle, which was then matched directly to the  $t/\lambda$  obtained from the low-loss spectrum image. As a needle shaped sample has a range of thicknesses, the effects of any surface layers on its surface could be removed.

## 5.2. Materials and experimental methods

Initially, solid polycrystalline ceramic specimens of TiC, TiN, VC and VN were used as standards for determining the absolute differential cross-sections. Later during the PhD, NbN and NbC cross-sections were determined as well following the same method. The stoichiometry of the samples was the following: TiC<sub>0.98</sub>, TiN<sub>0.88</sub>, VC<sub>0.83</sub>, VN<sub>0.97</sub>, NbC<sub>0.95</sub> and NbN<sub>0.988</sub>.

The standard samples for cross-section calculations were prepared using the FIB lift-out method described extensively in Chapter 2, with the needle shaped sample being prepared by the modified method from Miller et al. described in the same chapter [128]. As described before, FIB preparation involves the deposition of platinum layers to protect the sample surface during milling. An organometallic precursor is used here, which means that carbon contamination on the surface can be an issue. It was especially important to minimise it, as the precipitates we were interested in quantifying had carbon as a key element. To minimise contamination, the samples were baked in a Gatan PIPS system and then plasma cleaned in an argon-oxygen plasma using a Fischione Plasma Cleaner before being imaged in the microscope.

All spectrum images were recorded using our aberration corrected JEOL ARM200CF operated at 200keV with a cold field emission gun as the electron source. For recording the spectrum images, a Gatan GIF Quantum ER energy filter with fast DualEELS capability was used. A convergence half-angle of 29mrad was used. The spot size is approximately 1Å, with probe currents in the range of 180pA to 400pA. High EELS collection efficiency was ensured by using a collection semi-angle of 36mrad. The dispersion used was 0.5eV per channel.

## 5.3. Data analysis

After being recorded, the spectrum images were analysed as described in Chapter 3, following all the steps to reduce volume and noise, splice the low-loss and high-loss spectra together and then remove plural scattering using Fourier log deconvolution.

The method for acquiring the data was outlined above and involves the use of a spectrum image recorded at one needle orientation with an HAADF image recorded after the needle has been rotated by 90° around its axis. From the SI, a  $t/\lambda$  map can be obtained and a profile of  $t/\lambda$  can be taken along the axial direction. From the corresponding HAADF image, a profile of the needle thickness,  $t$ , can also easily be obtained across the same direction. Ideally, overlaying the two and taking the ratio would give another line profile with a constant value of  $\lambda$ , the mean free path. However, several issues had to be dealt with before obtaining a value of  $\lambda$  for TiC. All samples exposed to the atmosphere form a contamination layer on the

surface, and the FIB prepared needle was no different. However, in this case the surface layer was of a constant thickness along the needle.

The pixel size in the spectrum image (used to measure  $t/\lambda$ ) is larger than the pixel size in the HAADF image used to measure the thickness  $t$ . Of course, the two are also recorded at different specimen orientations. This leads to uncertainties in the axial position alignment of the two, as well as a mismatch in the position of the sampling points for the two sets of images. Linear plots of  $t$  and  $t/\lambda$  would make obtaining  $\lambda$  easy to obtain by taking the gradient of the plots and would remove the effects of constant surface layers or axial position offsets. In practice, this needle shaped sample was slightly blunted towards the tip. This made the line profiles across the images discussed earlier vary approximately as the square root of the axial position. In other cases, with different shaped needles this could be different. In the case of the data discussed here, the most stable results had been obtained by plotting  $t^2$  against  $(t/\lambda)^2$  and taking the gradient. This led to straight lines that were insensitive to the offset of the axial positions and, continuing the assumption that the surface layer is constant, the relationship between  $t$  and  $t/\lambda$  was expressed as a straight line of gradient  $m$  and intercept  $c$ , where the mean free path of the material was extracted from.

The value of the experimental mean free path for  $\text{TiC}_{0.98}$  was found to be  $103.6 \pm 0.5 \text{ nm}$ . The predicted mean free path for  $\text{TiC}_{0.98}$  is  $127 \text{ nm}$ .

The Iakoubovskii parametrisation was used to extrapolate the mean free path obtained from the TiC needle to the other standards. The density of the material, the number of atoms per unit volume are needed for this. They were obtained using the lattice parameter of each of the samples, which in turn were calculated using Vegard's Law to interpolate the data given by Goldschmidt [129]. The following experimental mean free paths were calculated for the Ti and V standards:  $103.5 \pm 0.5$  for  $\text{TiC}_{0.98}$ ,  $99.7 \pm 0.5$  for  $\text{VC}_{0.83}$ ,  $101.7 \pm 0.5$  for  $\text{TiN}_{0.88}$  and  $98.1 \pm 0.5$  for  $\text{VN}_{0.97}$ .

The value of the cross-section at each individual energy loss is found using a least squares fit to take the gradient of a plot of

$$\left( \frac{1}{(I_0)_{xy}} \right) \left( \frac{I_{xy}(E)}{\Delta E} \right) \left( \frac{S_{xy}}{T} \right) \text{ versus } n_M \lambda_B \left( \frac{t}{\lambda} \right)_{xy}. \quad (5.1)$$

$\lambda_B$  is the experimental mean free path calculated previously and  $n_M$  is the number of atoms per unit volume.  $I_{xy}(E)$  is the intensity of the  $xy$  pixel at a given energy loss  $E$ . The plot was done for every  $xy$  pixel. Maps of the splice ratio, zero-loss intensity and relative thickness are also required for this calculation, so is the corresponding  $xy$  pixel in them. These are labelled as  $S_{xy}$ ,  $(I_0)_{xy}$  and  $(t/\lambda)_{xy}$ , respectively.  $\Delta E$  is the energy width of the channels in the spectrum, which in the case of this research was always  $0.5 \text{ eV/ch}$ .  $T$  is the time ratio, ie. the ratio between the acquisition times for the high-loss and the low-loss spectrum.  $S_{xy}/T$  replaces the splice ratio that was used to splice the spectra with the time ratio, thus giving an

appropriate scaling between the intensities of the core-loss and the low-loss spectra. This was needed because, while ideally the splice ratio would be equal to the time ratio, this was not the case and there was a difference between the two.

The fits were performed using a custom-built script in Digital Micrograph which generated a spreadsheet of values of the points, fit values and deviations for each energy loss in the spectrum. Plots of the differential cross-section and the corresponding errors from the least squares fit are also produced. These can then be transferred into Microsoft Excel for their accuracy to be easily investigated. Figure 5.2 shows two of the plots for the  $\text{TiC}_{0.98}$  lamella, taken at a fixed energy over the entire needle to cover the whole thickness range. Figure 2a contains the data at the energy of the Ti-L<sub>3</sub> edge which has a high intensity. The data in figure 2b is from just before the Ti-L<sub>2,3</sub> edge in an area of low intensity. From the deviation plots, it is clear that the data follows a very good straight line.

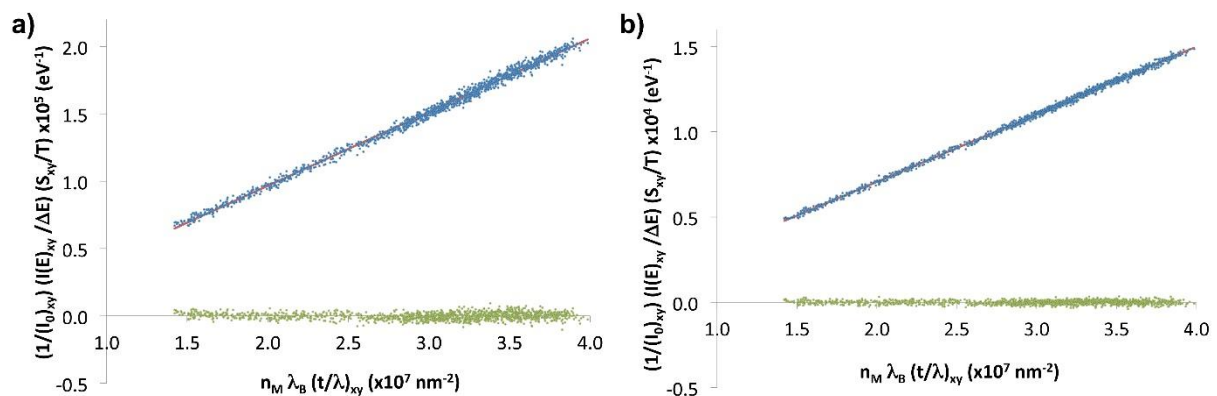


**Figure 5.2:** Plots of  $\left(\frac{1}{(I_0)_{xy}}\right) \left(\frac{IE_{xy}}{\Delta E}\right) \left(\frac{S_{xy}}{T}\right)$  versus  $n_M \lambda_B \left(\frac{t}{\lambda}\right)_{xy}$  for two values of energy in the  $\text{TiC}_{0.98}$  dataset, with a) being at the energy of the Ti L<sub>3</sub> peak and b) being at an energy just before the onset of the Ti L<sub>2,3</sub> edge. Image first published in [95].

The straight-line relationship on the graph calculating the cross-section at each given energy is only true provided that  $t/\lambda$  is between 0.2 and 0.8. At lower thicknesses, it is possible that surface effects become too significant. At much larger thicknesses the deconvolution procedure was seen fail as well. It is not clear why this is the case, but it could be due to too many plural scattering events.

## 5.4. Results

### 5.4.1. TiC, TiN, VC and VN

To obtain cross-sections for individual elements, the backgrounds must be removed from the original spectrum, and the edges separated. However, this is challenging as there are perturbations in the shape of the background, for example from extended energy loss fine structure (EXELF). The traditional way of extracting backgrounds involves fitting an  $Ae^{-r}$  power-law background shape before an edge and subtracting it from the total spectrum.

However, due to these perturbations, fitting a power law background before a non-metal edge will give an extrapolated background that is highly sensitive to the size of the background fitting window used and its energy range, thus leading to inconsistent results.

Other background fitting methods for our binary carbides and nitrides are available, for example modelling the experimental cross-section as the sum of a power law background and scaled Hartree-Slater metal and non-metal cross-sections. However, these too are sensitive to fitting windows used and thus can lead to inconsistent results.

For the cross-sections calculated here, a different approach was adopted. The overall shape in the four standards is very similar. In the two Ti containing standards, the deviation from a power law background was the smallest. In  $\text{TiN}_{0.88}$ , the background reaches the highest energy loss before encountering a non-metal edge. As such,  $\text{TiN}_{0.88}$  was used to extract an “experimental background shape” by fitting a power law background with a window 20eV wide before the N-K edge. Suitably scaled, this experimental background shape was used with all four standards discussed here.

Figure 5.3 shows the calculated average cross-sections for the four standards (black) together with the scaled backgrounds (green). The Hartree-Slater cross-sections added to the scaled background are also shown (orange for the non-metal cross-sections, red for the metal + non-metal ones). The non-metal cross-sections have been scaled by the stoichiometry, for example 0.83 for  $\text{VC}_{0.83}$ . The deviation between the experimental cross-section (black) and the theoretical one obtained by summing the two Hartree-Slater cross-sections to the background (red) are also shown in blue.

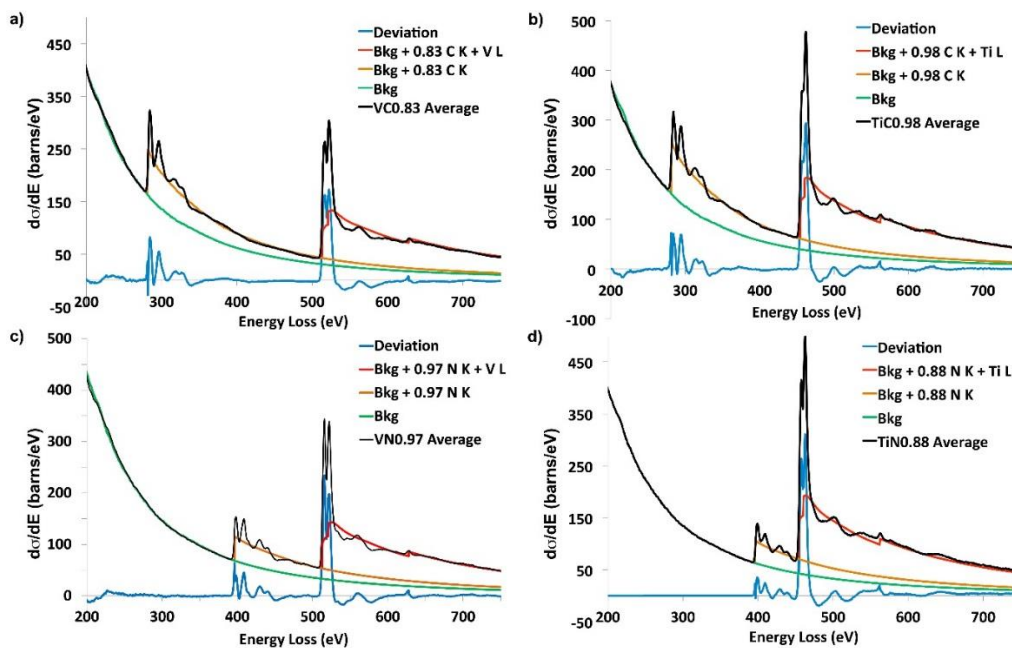


**Figure 5.3:** Comparison of the average experimental cross-sections, the scaled “experimental background” obtained from  $\text{TiN}_{0.88}$  and the Hartree-Slater cross-sections for a)  $\text{VC}_{0.83}$ , b)  $\text{TiC}_{0.98}$ , c)  $\text{VN}_{0.97}$  and d)  $\text{TiN}_{0.88}$ . Image first published in [95].

Our “experimental background shape” fits the data very well. Below about 300eV, the deviations are similar between the TiC, VC and VN samples. There is no such deviation for TiN because its background was used for the other three samples. There are some noticeable deviations at low energies between the experimental background shape and the experimental cross-section. These are likely to be due to the EXELFS from the strong M edges of the metals at about 40-50eV energy loss. The deviations differ between the four standards as the shapes of the EXELFS are controlled by both the threshold energies of the edges as well as by the lattice parameter of the material.

From this point, it is possible to extract the cross-sections for the individual metal and non-metal edges. The non-metal cross-sections can be corrected to values corresponding to full stoichiometry, and the pairs of cross-sections can be compared. This comparison is made in Figure 5.4. For the non-metals, the cross-sections at higher energy losses are extrapolated using the Hartree-Slater cross-section. As such, that region is not shown on the diagrams. The ELNES for the non-metals (carbon and nitrogen) is similar in shape and intensity, which was expected as the compounds investigated have very similar crystal structures. However, the lattice parameters of the compounds differ, which is why the energies at which the features are present in the spectra differ.

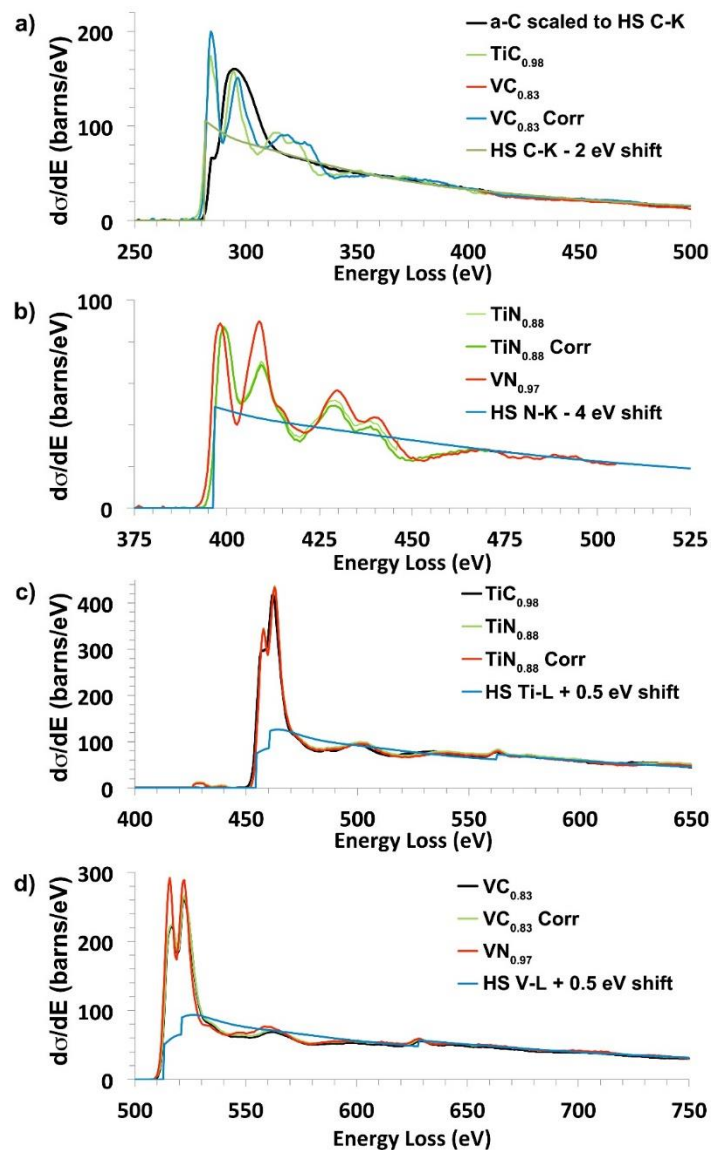
Figure 5.4a) shows the C-K edge cross-section, with the shape of the C-K edge obtained from a thin amorphous carbon film also shown for comparison. The amorphous carbon shape has not been calculated as a cross-section but is simply shown as a background subtracted edge from the single scattering distribution. It has been scaled to the Hartree-Slater cross-section in the region from 350eV to 500eV.

Figure 5.4b) shows the experimental N-K edge cross-section. The thin green line shows the result of splicing the experimental N-K cross-section from  $\text{TiN}_{0.88}$  to the Hartree-Slater cross-section immediately in front of the Ti-L<sub>2,3</sub> edge. This creates a sharp step, due to a large dip in the ELNES at that point.

Figures 5.4c) and d) show the experimental cross-sections for the two metal edges. All match their corresponding theoretical Hartree-Slater cross-sections very well at high-energy losses, well above the non-metal threshold. However, they are below the Hartree-Slater cross-sections in the region just after the non-metal threshold.

Despite the small mismatches at certain energies, our approach of using experimentally extracted backgrounds to separate the individual cross-sections gave excellent results, with quality of the fits is further explored in Figure 5.5. Figure 5.5 a) looks into more detail at the residuals of the fit for  $\text{VC}_{0.83}$ . The vertical scale has been expanded. The thin line shows how the residuals are negative for 100eV before the V L-edge and after approximately 100eV higher than its threshold. This suggests that there is a small problem in the background fitting for the  $\text{VC}_{0.83}$  sample which must be corrected for. The thick line shows the residuals after a minor correction to the background fitting.

Figure 5.5b) shows the ratio between the experimental and the Hartree-Slater cross-sections for the non-metal edges, with Figure 5.5c) showing the same ratio for the metal edges. Calculating the ratio between the experimental and the theoretical cross-sections is another way of assessing their agreement, with the ratio being 1 everywhere if the two match perfectly. In both Figures 5.5b) and c) the ratios are plotted as a function of the energy above the edge threshold. For carbon and nitrogen, the plots are terminated at the onset of the metal edge. The thin lines are the values of the ratio before corrections are applied to the  $\text{VC}_{0.83}$  and  $\text{TiN}_{0.88}$  cross-sections. These corrections will be discussed below, and the results after the corrections are applied are shown in thick lines.



**Figure 5.4:** a) The C-K edge compared to the shape of the background subtracted intensity from amorphous carbon, b) the N-K edge cross-section, c) the Ti-L cross-section and d) the V-L cross-section. Image first published in [95].

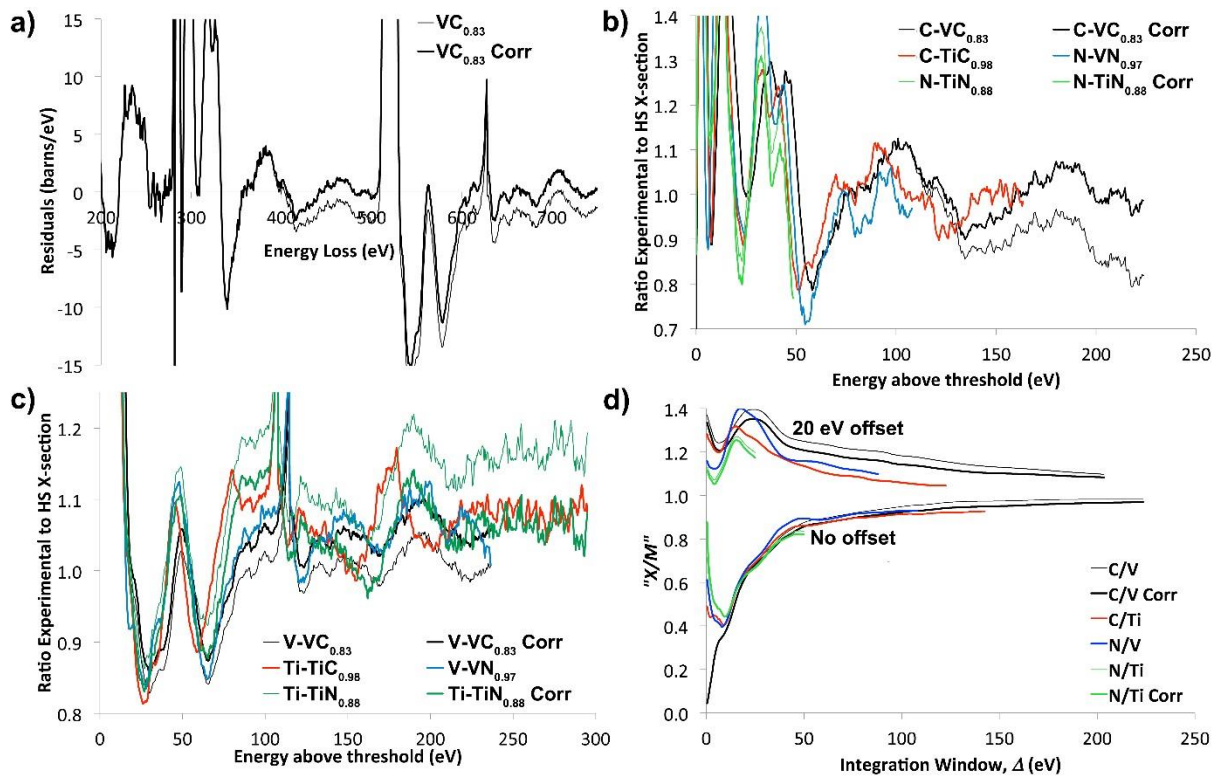


**Figure 5.5:** a) The  $VC_{0.83}$  residuals on an expanded vertical scale, b) the ratio of the experimental non-metal cross-sections and their corresponding Hartree-Slater calculated cross-sections, as a function of energy loss above the edge threshold; the thin lines represent data before it was corrected to take into account the stoichiometry of the samples, with the thick lines being after the correction, c) the ratio of the experimental and Hartree-Slater cross-sections for the metals, with the thin lines being before and the thick lines being after correcting for full stoichiometry, and d)  $X/M$  (non-metal over metal) versus the window integration width  $\Delta$  for the stoichiometric standards; the thin lines again are the data before the correction; the lower group of plots have the integration window start at the threshold while the upper group of plots have the integration window start with an offset of 20eV. Image first published in [95].

At low energies above the edge threshold, the ratios vary a lot around 1. This is due to the very strong ELNES present on the edges. However, when looking at the overlay between the different ratios when plotted against energy above threshold, the different lines follow each other incredibly well. This confirms that the ELNES is very similar between the different edges.

However, the plots show some deviations from the ideal background fitting we were hoping for. In Figure 5.5 b), the line for the uncorrected C-K edge data extracted from  $VC_{0.83}$  (thin grey line) displays a consistent drop at higher energy losses above the threshold. As was discussed before, if the theoretical and experimental cross-sections matched perfectly we would have expected the ratio to be a constant value of 1. However, we would still have expected a constant value ratio if either the stoichiometry or the ideal ratio between the experimental and Hartree-Slater cross-sections differed from unity.

In Figure 5.5c), looking at the ratio of the experimental and Hartree-Slater cross-sections for the metals, it can be seen that the thin grey line for the uncorrected V-L edge in  $VC_{0.83}$  lies below the lines for the Ti-L in  $TiC_{0.98}$  and V-L in  $VN_{0.97}$ . This suggests background fitting problems for this standard.

As has been discussed at the beginning of this chapter and throughout this thesis, these cross-sections are needed for accurately quantifying carbonitride precipitates within steel matrices. This means that errors in background fitting and cross-section extraction will lead to errors in the final quantification results. One way to assess the implications for quantification is to look at the non-metal to metal ratio,  $X/M$ . This has been obtained using the traditional quantification process using a background fitting window before an edge and is shown schematically in Figure 5.5d). The sum of the experimental cross-section over an energy window,  $\Delta$ , is divided by the sum of the Hartree-Slater cross-sections over the same energy window. Then, a ratio of a value for a non-metal and a metal is taken. The  $X/M$  values as a function of  $\Delta$  can be seen in Figure 5.5d), where the maximum value of  $\Delta$  for each compound being set when the window reaches the metal edge threshold. The bottom set of data has the integration window starting at the threshold. The top set has the integration window starting 20eV above the threshold.

The bottom set of lines, obtained with no offset, group together well for integration windows wider than 20eV. They do show good consistency, however the effects of ELNES are still visible as expected. The line for the uncorrected  $VC_{0.83}$  is, however, a little high. All the lines increase steadily towards one as the integration window width increases. However, in the case of  $VC_{0.83}$ , the line is still rising even when the integration window reaches 220eV, and still does not reach unity. When the 20eV offset is used before starting the integration, the lines spread out a lot more and are significantly less close together than without using the offset. The values of the non-metal to metal ratios are also greater than unity in this case. More of the ELNES could be excluded by increasing the offset, however that would exclude more of the high-energy loss signal which is the one that is least susceptible to background errors. Increasing the offset would also severely limit the possible window width. This diagram clearly shows the issues with the background fitting involved in the traditional quantification method, as it is extremely susceptible to the width and position of the integration window. These large inconsistencies arising from small changes in the size or position of the integration window would lead to large errors in the final results of the quantification. This clearly shows the need for accurate experimental cross-sections, and the correction for stoichiometry greatly improves their accuracy. The correction applied to the experimental cross-sections will be covered in the discussion section of this chapter.

#### **5.4.2. NbN and NbC**

The cross-sections for NbN and NbC have been calculated using the same method as described for Ti and V nitrides and carbides in the previous sub-section. Niobium is significantly heavier than both titanium and vanadium, and ideally a mean free path would

have been measured for it using a needle shaped sample from either NbN or NbC. However, due to the quality of the bulk materials available, a thin enough needle that had a wide enough thickness range was not possible to make. The same mean free path from the TiC needle had to be used to calculate them for the niobium standards using the Iakoubovskii parametrisation.

Due to the position of the Nb-M<sub>4,5</sub> edge, fitting a power law background before the edge is even more problematic than in the case of the titanium and vanadium cross-sections. The niobium edge is also very close to the carbon and nitrogen edges, making separating them difficult. Again, the experimental background obtained from TiN<sub>0.88</sub> has been used. Figure 5.6 shows the experimental cross-section of NbN with a TiN<sub>0.88</sub> background when compared to the theoretical Hartree-Slater cross-section for the Nb-M<sub>4,5</sub> edge that is used in Digital Micrograph.

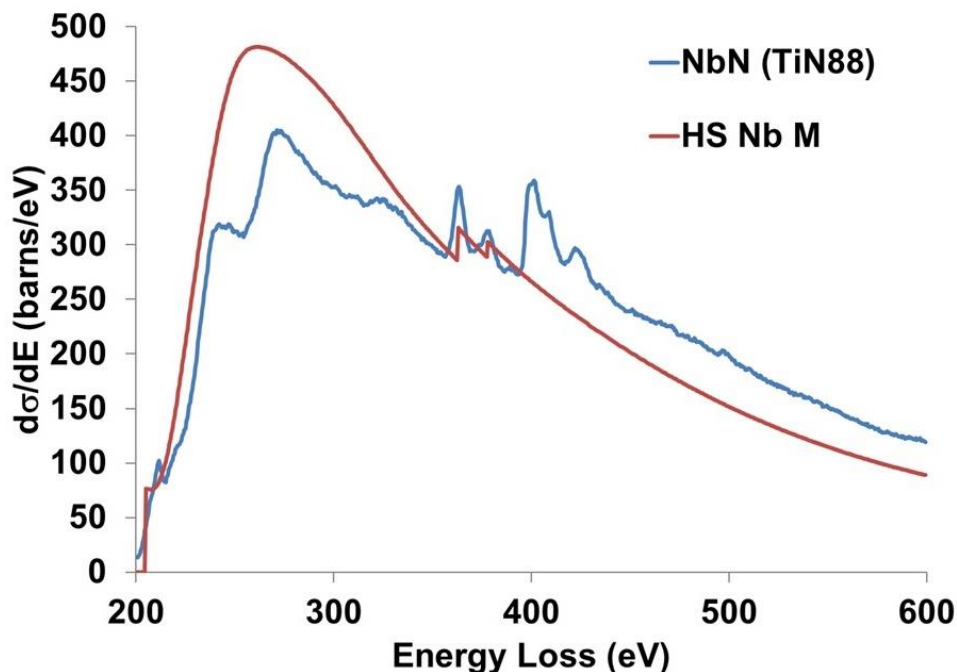


**Figure 5.6:** The experimental cross-section of the Nb-M<sub>4,5</sub> edge from NbN compared to the Hartree-Slater theoretical cross-section.

The Hartree-Slater cross-section has a significantly higher intensity than the experimental ones, and the structure of the edge is far more complicated than the theoretical model would suggest. Again, this shows the importance of using experimentally calculated cross-sections when trying to accurately quantify the composition of samples. Using the Hartree-Slater cross-section in quantification would lead to a composition that would suggest too small a niobium concentration.

Due to issues in the acquisition process, as described in Chapter 3, the cross-section data was acquired again after the results in Figure 5.6 were produced. The cross-section obtained from NbC in this case is shown in Figure 5.7 and is the one that was used in quantifying the

precipitates found in the PreTiControl steels discussed in Chapter 6. The feature just after 200eV was originally thought to be Zr contamination, however it is present in all Nb samples we have looked at which is why we believe it is a real feature of the Nb cross-section. However, at the time of writing this the feature is not understood.

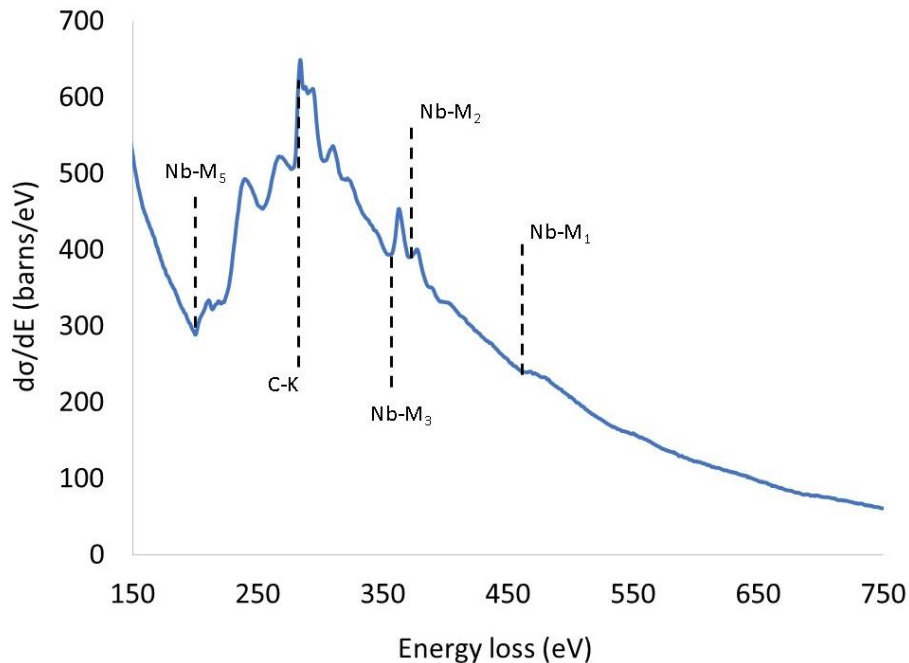


**Figure 5.7:** The experimental NbC cross-section used in quantifying all Nb containing precipitates during this research.

## 5.5. Discussion

The background subtraction has proved to be problematic in the case of all the cross-sections calculated here, so a correction was applied using the constrained background fitting model. The value of  $r$  in the  $Ae^{-r}$  power-law extrapolated section of our “experimental background shape” was adjusted to improve the fits for the  $VC_{0.83}$  and  $TiN_{0.88}$  data. This resulted in the shapes in the thick lines presented in the figures shown in the results sections. Studying the figures of the cross-sections and comparing the corrected and non-corrected shapes, the change in  $VC_{0.83}$  is incredibly small but the change in  $TiN_{0.88}$  is much more significant. When looking at the deviations in the  $VC_{0.83}$  cross-section, correcting the exponential factor  $r$  from 2.81 up to 3.05 brings the deviations much closer to zero both before and after the V-L edge threshold. The ratios between the corrected experimental and the Hartree-Slater cross-sections for  $VC_{0.83}$  agree significantly better with the ratios from  $TiC_{0.98}$  and  $VN_{0.97}$ . The non-metal to metal ratio,  $X/M$ , is lowered slightly for the set where no offset was used, leading to a slightly improved agreement.

For  $TiN_{0.88}$ ,  $r$  has been decreased from 2.81 to 2.41. There is a limited energy range available for the N cross-section, so an assessment on the improvement there is difficult to make. Due to this limited energy range available for the N-K edge and the difficulty to demonstrate an

improvement in it, it is also difficult to justify correcting the value of  $r$ . The correction is easier to justify in the case of  $\text{VC}_{0.83}$ , as both edges are corrected at the same time. Nevertheless, the consistency between the results was improved by applying this correction, even if it is not entirely clear why the extracted “experimental background shape” had to be corrected in the first place.

A discussion on the many possible systematic errors when calculating experimental mean free paths and then cross-sections is needed. The  $\text{TiN}_{0.88}$ ,  $\text{TiC}_{0.98}$ ,  $\text{VN}_{0.97}$  and  $\text{NbN}_{0.988}$  standards were supplied with measured stoichiometries. However, no errors on the measurements were provided but in other works they have been measured to be of maximum 0.1% [130]. For the VC sample no stoichiometry was provided beyond the information that it has a high carbon content. Selected area diffraction suggested the material is  $\text{V}_6\text{C}_5$ , which has carbon concentration values between 0.77 and 0.85 [131]. The lowest carbon concentrations only occur at very low processing temperatures, which was not the case here. The most likely stoichiometry was considered to be 0.83, with an uncertainty of  $\pm 0.02$ . Similarly, for the NbC standard we were not provided with an accurate stoichiometry but a measure of the composition in weight percentages was given. Calculating the stoichiometry from there led to a result of  $\text{NbC}_{0.95}$ .

There are no significant errors that have been introduced by contamination during sample preparation using FIB, and care has been taken to minimise surface damage as described in Chapter 2 of this thesis. Additionally, the samples were cleaned in the PIPS and the plasma cleaner prior to being loaded into the microscope to minimise further contamination, as explained in the data acquisition section of this chapter.

Not having needle shapes specimens for each of the standards and using the TiC mean free path and corrected Iakoubovskii parametrisation, multiplying by 80% [126] to calculate mean free paths for the other samples could prove to be a source of error. However, the consistency between the Ti and V carbide and nitride standards suggests that, at least in their case, the error is not significant.

By far the largest source of error is due to background fitting and removing the edges. As has been discussed before, using a power law background was not suitable. Before the non-metal edges, there was a large deviation from the standard power law background due to the EXELFS from the lower energy loss metal M-edges. Additionally, power law background fitting windows are selected by the user, with both the width and the starting point being open to interpretations. This could have led to further inconsistencies between different samples, or even data from the same sample that had been processed at different times. For the cross-sections calculated in the research presented here, care has been taken to obtain a suitable “experimental background shape” extracted from the  $\text{TiN}_{0.88}$  cross-section. The fitting errors due to the background shape have been considerably reduced when using the experimental shape rather than a power law. However, the experimental background shape had to be slightly modified for some of the standards to improve the fitting even further. It is not clear

why this was the case, however the corrected shapes have been kept and used in quantification as the fit was better and the consistency between the different cross-sections was improved.

## 5.6. Summary

The experimental cross-sections were calculated for  $\text{TiC}_{0.98}$ ,  $\text{TiN}_{0.88}$ ,  $\text{VC}_{0.83}$  and  $\text{VN}_{0.97}$  standards, using an “experimental background shape” obtained from the TiN spectrum. The results from these were published in 2016 [2]. The experimental backgrounds had to be corrected for some of the samples to improve the fitting. The results are significantly better than the theoretically calculated Hartree-Slater cross-sections, especially in the case of the metal L or M edges.

Ideally, the method used to calculate the cross-sections for our Ti and V carbides and nitrides could be extended to a wide range of other materials and EELS edges. This requires in the first place that a well-characterised sample from a well-understood material can be prepared. A suitable, repeatable background removal procedure needs to be found, and the core-loss edges need to be sufficiently spaced apart to be separated. For lower energy loss EELS edges this becomes considerably more difficult. The tail of the plasmon peak will lead to significantly more complex backgrounds, and the area also has a lot of overlapping edges. For example, trying to get accurate cross-sections from the Ti or V  $M_{2,3}$  edges for use in quantification would be extremely challenging. These low-lying edges complicate backgrounds further out to higher energy losses as well with their EXELFS, as has been discussed before in this chapter. This extends the “difficult” region to at least 200eV energy loss, making the Nb  $M_{4,5}$  edge in Figures 5.6 and 5.7 at 205eV incredibly difficult to obtain an experimental cross-section for and making background subtraction for it much trickier. This meant that obtaining the experimental cross-sections for NbN and NbC was significantly harder than for the other four standards. This was further complicated by the non-linearity in the spectrometer dispersion as well as by the stray scattering before the ZLP, which was later corrected for in processing as described earlier in this thesis.

The experimental cross-sections have been calculated to be later used in accurately quantifying the chemistry of metal carbonitride precipitates within a steel matrix. The results from this precipitate quantification will be discussed in Chapter 6.

## Chapter 6

### Accurate precipitate quantification using DualEELS

The observation and chemical characterisation of fine scale precipitates has been performed for several years using electron microscopy, with scanning transmission electron microscopy (STEM) studies being performed both of carbon replica extractions and focused ion beam (FIB) prepared cross-sections with the precipitates still embedded in the matrix. As has been previously discussed in the context of mapping and obtaining statistics from large numbers of precipitates, carbon replica extraction has a number of issues that could make accurate quantification impossible [132][133]. By using FIB cross-sections instead of carbon replicas in our STEM experiments, we have been able to investigate the structural context of the precipitation (such as their formation on grain boundaries or dislocations) alongside their accurate chemical composition. To quantify the chemistry of the precipitates found in the steel, the method initially developed by Bobynko et al. (2015) and described in detail in their PhD thesis [9] was significantly improved [97]. The method involves separating signals belonging to the matrix from those belonging to the precipitates. Initially this was done by subtracting the matrix contribution from the deconvolved spectrum image to obtain a spectrum image of the precipitate alone, as discussed in Chapter 3 of this thesis. However, results were significantly improved when the matrix was not subtracted but was instead treated as another contribution in a multiple linear least squares (MLLS) fit.

The challenge of any quantification technique is to quantify the data with high accuracy and sensitivity. The traditional quantification method, described by Egerton, involves fitting a power law background before an edge of interest, extrapolating the background and then subtracting it [119]. This is the same background fitting method described when discussing cross-sections in the previous chapter. The extracted signal is then integrated over a window with a typical width of 50-100eV. The signal is divided by the integral over the same window of a theoretically calculated cross-section [121]. The results can be normalised to give absolute numbers of atoms per unit area using the zero-loss peak (ZLP) intensity, if the ZLP is available as in the case of all the data discussed in this thesis. If the ZLP intensity is not available, only relative amounts of each element present in the composition can be determined.

As has been discussed in Chapter 5 of this thesis, when considering the issues with theoretically calculated cross-sections, these are in many cases very different from the experimental cross-sections, especially close to the edge onset. So by using a theoretically calculated cross-section in a quantification procedure, whether calculated using the hydrogenic model or the Hartree-Slater model, can lead to large errors in the quantification results [95]. When it comes to extracting each individual edge, if two edges are close to each other the fine structure of the lower energy loss edge will perturb the background for the higher energy loss edge, making accurate signal extraction impossible. Even for edges that

are widely spaced, the EXELFS from lower lying edges can perturb the background of higher energy edges more than 200eV apart in energy loss. This has been discussed at length in the cross-sections chapter as well as in the paper calculating the cross-sections of Ti and V carbides and nitrides [95].

Our approach is to use the standard cross-sections presented in the previous chapter together with standards extracted for the steel matrix to perform an MLLS fit to the steel spectrum. The fit provides a series of coefficient maps for each of the standards used, which can then be converted into concentration maps for the individual elements present in the precipitate using simple mathematics implemented in a custom-built script for Digital Micrograph.

In the first instance we have applied the method we developed to a series of (Ti, V) (C, N) precipitates formed inside a high manganese steel matrix (up to 20% Mn by weight). The results and details of the method have been published in Craven et al. [134]. They will be discussed in detail in this chapter. Niobium-containing precipitates have been analysed as well, however the larger uncertainties for the cross-section for the Nb edges [Section 5.4.2.] made those results slightly less accurate. The method used for quantification will be described in more detail than in the data analysis chapter (Chapter 3 Section 3.4).

In order to quantify these precipitates, a few things had to be dealt with. First of all, the bulk and surface contributions arising from the matrix had to be removed. This was done by treating each one of them as an individual signal to be included in the MLLS fit. Secondly, a successful background removal technique had to be found. Again, rather than using a power law shape, the “experimental background shape” from the  $\text{TiN}_{0.88}$  standard was used. To fit the transition metal carbonitride shapes, cross-sections from the binary carbides and nitrides as calculated in Chapter 5 were used (TiN, TiC, VN, VC, NbN and NbC). Then, there were differences in stoichiometry between the standards and the precipitates, and between each of the precipitates themselves. Finally, allowances had to be made for the data and the acquisition procedures not being perfect and potentially leading to small glitches in the spectrum or similar.

## **6.1. The samples**

All the samples have been prepared as FIB cross-sections using the FIB lift-out method discussed in Chapter 2 of this thesis. To minimise the amount of carbon that could have grown under the electron beam, the samples and the sample rods were cleaned for a few minutes in an argon-oxygen plasma cleaner.

### ***6.1.1. Samples with (Ti, V) (C, N) precipitates***

The steel containing these precipitates was provided by Thyssen Krupp Steel Europe in Germany as part of the PreCHiMn project and prepared as a FIB cross-section. It was a high manganese steel of base composition in weight percentages of 19.7% manganese, 1.50% aluminium, 0.58% carbon with an addition of 0.19% vanadium. There were traces of niobium,

titanium and nitrogen from the original feedstock, with the weight percentages being 0.002% niobium, 0.006% titanium and 0.008% nitrogen. The rest was iron. The steel was held at 850°C for 100 seconds, which was expected to give precipitates in the range of 5-10nm in diameter.

### **6.1.2. Samples with Nb containing precipitates**

For the analysis of Nb containing precipitates, more than one sample was used. The technique was first tested on another sample provided by Thyssen Krupp as part of the PreHiMn project. This sample had the following composition in terms of weight percentages: 20.3% manganese, 1.20% aluminium, 0.63% carbon, 0.001% vanadium, 0.11% niobium, 0.007% titanium and 0.003% nitrogen, with the rest being iron. This time, the sample was held at 900°C for the same time of 100 seconds.

Once the technique was established, samples from the current project, PreTiControl, were analysed, where the precipitates were expected to be smaller and thus more challenging to analyse. These were the same samples discussed in Chapter 4 in the context of large area low loss mapping to identify precipitates. They have been provided by CRM in Belgium and were expected to contain precipitates with all three metals in their composition. The steels from the current project were expected to have much smaller precipitates with a more complex chemistry than the ones from the PreHiMn project.

## **6.2. Data acquisition**

Areas containing precipitates suitable for DualEELS mapping have been identified using the large area low-loss maps discussed previously in Chapter 4. All the spectrum images have been recorded using the JEOL ARM200cF operated at 200keV and equipped with both a cold field emission gun and a probe corrector. A Gatan Quantum ER spectrometer with fast DualEELS capability was used to record both the low-loss and high-loss spectra at the same time. They were recorded using the Digital Micrograph software, with the scans under the control of the DigiScan-2 hardware. For all the spectrum images recorded during this work, a convergence semi-angle of 29mrad and a collection semi-angle of 36mrad were used. The spot size was approximately 1-2Å, with the probe currents being in the range of 180pA to 400pA. The dispersion used was always 0.5eV per channel.

## **6.3. Data analysis**

The datasets were processed to give single scattering distributions after Fourier-log deconvolution, as described in the data analysis chapter of this thesis.

In the original method, the matrix contribution was “extracted” from the deconvolved spectrum image to leave the precipitate spectrum image behind. This was done on the assumption that there is no iron in the precipitate, and that the matrix did not contain any titanium, vanadium or niobium. However, it was later found that this process did not deal properly with all the surface layers present, as iron oxide was found on the surface. While the

iron contribution was removed by the matrix subtraction, contributions from the O-K edge were not removed and had the potential to interfere with the quantification. Thus, a different approach was required, and it was decided to use two different average matrix spectra from regions of the spectrum image having significantly different values of  $t/\lambda$ . These two matrix spectra were taken from the thinnest and thickest regions of the imaged area. As they would represent a linear combination of the signals from the bulk of the matrix and the surface layers, they were used in the MLLS fit to help with separating the two.

Another challenge in quantifying EELS data is dealing with the backgrounds underneath the core-loss edges. The background from the matrix has significant deviations from the standard power law shape traditionally used in such analyses. These deviations are due to EXELFS from lower lying edges and would lead to considerable errors if the background from the standards and the steel data were to be removed before attempting quantification. Due to this issue, it was decided to do the MLLS fit on steel data that had been deconvolved but not background subtracted. Additionally, the titanium, vanadium and niobium standards did not have their backgrounds subtracted either. However, the carbon and nitrogen standard shapes were needed in the fit as well to account for changes in stoichiometry between the precipitates and the standards. To obtain those edge shapes, background subtraction is necessary. To allow for these two standards to be used with the background subtracted, the background shaped used in the subtraction (that obtained from the  $\text{TiN}_{0.88}$  standard) had to be included in the MLLS fit as well.

In addition to the spectral components mentioned above, three more components were included in the MLLS fits. The first one was the deconvolved, background subtracted C-K edge from a thin film of amorphous carbon. This was needed because, when fitting to some of the precipitates, the ELNES on the C-K edge fitted poorly when using only the  $\text{VC}_{0.83}$  and  $\text{TiC}_{0.98}$  experimental cross-sections. The shape of the residuals in the area indicated the presence of amorphous carbon on the sample surfaces.

The other two components were included to deal with minor artefacts found in the spectrum as a result of the dark current subtraction. One was a constant, set to 1, used to take account of slight errors in the overall dark current levels subtracted from various datasets. When not included, the fit was found to be either slightly higher or slightly lower with respect to the data than was expected. The other component was included to take into account the differences in the dark current subtraction between the two halves of the CCD detector when the high-loss spectrum was recorded. This difference resulted in an intensity step in the middle channel of the original high-loss spectrum, with the step having a different intensity from pixel to pixel. The effect was remediated using a step function as a standard shape in the MLLS fit, that was set to zero up until the channel where the step occurred and unity at all the channels after.

In summary, the cross-section used in the MLLS fit for precipitates were:

- Shapes extracted from thick and thin regions of the matrix
- Binary experimental cross-sections from VC, TiC and NbC as they were the largest contributions to the precipitate diameters. Nitrides were not included as there was very little evidence of significant nitrogen content in the precipitates.
- The background-subtracted, stoichiometric experimental cross-sections for the C-K and N-K edges. These allow for changes in stoichiometry between the standard samples and the precipitates.
- The TiN88 experimental background shape used to extract the C-K and N-K cross-sections, to provide the missing background shape for these two cross-sections.
- A C-K edge from amorphous carbon to consider its possible presence in some of the precipitates imaged.
- The constant and step functions to deal with artefacts in the dark current subtraction.

These are all the different shapes that have been used in the MLLS fit. More functions could have been used, however the improvement in the accuracy of the fit or the difference made to the final quantification result were minimal when these different fits were tried.

Rounding errors were observed in the fitting results. These were due to the fitting routine in Digital Micrograph requiring all components to be of roughly the same magnitude. To avoid the rounding errors, the fitting components that provide only shapes rather than absolute values were scaled so that their magnitudes were similar to those of the shapes providing absolute values.

### **6.3.1. Results for (Ti, V) (C, N) precipitates in a high-manganese steel**

The MLLS fit as described above was applied to four different precipitates from the PrechiMn project steels, each in different matrix thicknesses varying in  $t/\lambda$  from 0.149 to 0.425. The results of the MLLS fit are fit coefficient maps (one for each of the shapes used in the fit), with the ones carrying elemental information being shown in Figure 6.1. Additionally, the fit results also include a map of the sum of the square deviations for the fit at each pixel and two SIs, one of the fit to the spectrum at each pixel and one of the corresponding residuals (deviations of the data from the fit). The fit coefficients represent the contribution of the corresponding component of the spectrum intensity divided by its differential cross-section.

In Figure 6.1, for all the coefficient maps apart from C from VC<sub>0.83</sub>, dark means a coefficient close to zero. In the case of the C from VC<sub>0.83</sub> map, the coefficient in the area of the precipitates is negative, with the bright area surrounding them representing a coefficient close to zero. The precipitates can be clearly seen on the TiC<sub>0.98</sub> and VC<sub>0.83</sub> coefficient maps. The negative coefficient maps for C from VC<sub>0.83</sub> are negative in the areas of the precipitates are showing that all the precipitates have less carbon in their composition than the linear combination of the two binary standards, TiC and VC.

The maps of N from  $VN_{0.97}$  show a clear nitrogen contribution in the precipitates but are much noisier than the other maps. In the case of Precipitate 1 and Precipitate 4, there is a significant amorphous carbon contribution in the areas of the precipitate. In the case of Precipitates 2 and 3, the a-C contribution to the fit coefficient maps does not correlate to the position of the precipitates.

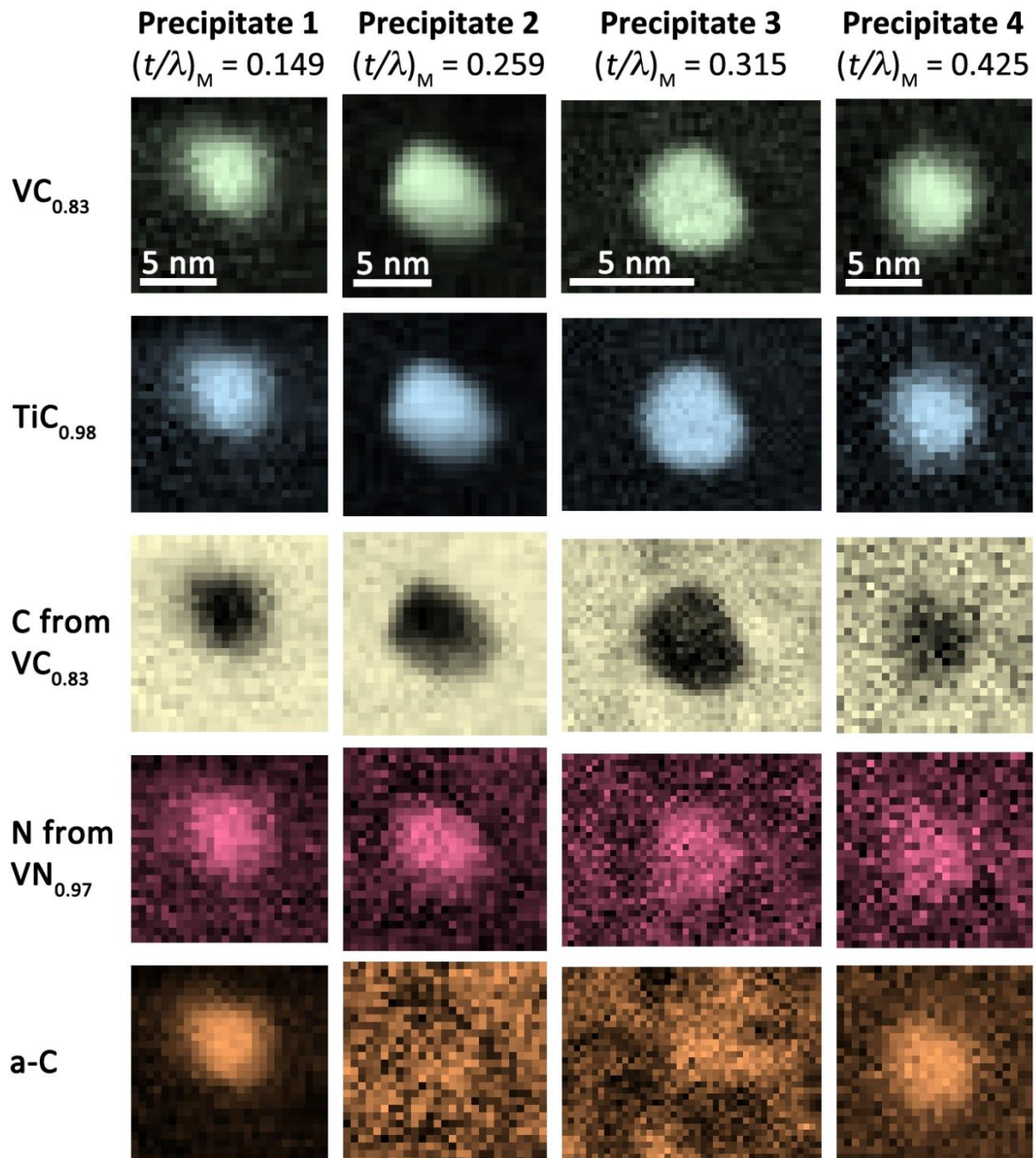


**Figure 6.1:** Maps for the fit coefficients for  $VC_{0.83}$ ,  $TiC_{0.98}$ , C from  $VC_{0.83}$ , N from  $VN_{0.97}$  and amorphous carbon for the four precipitates analysed. Figure first published in [134].

When looking only at the fit coefficient maps, it is difficult to quantitatively understand their individual contributions to the data. Figure 6.2 compares the contributions summed over 6x6 pixels in the centre of precipitates 1 and 2 from Figure 6.1. The contributions from the matrix are significantly larger than all the other contributions, so they have not been included in the figure to make sure that the small contributions are visible.

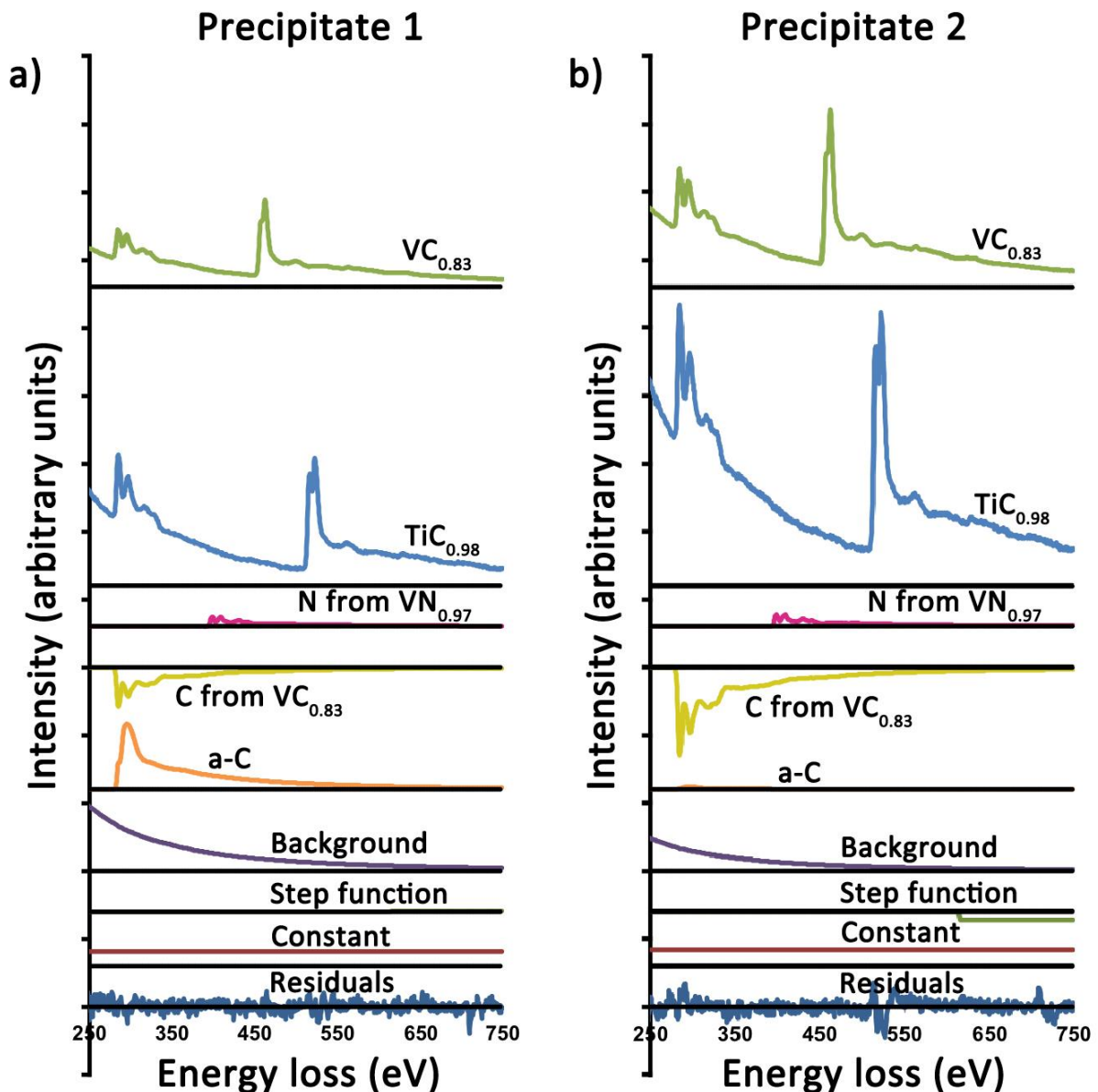


**Figure 6.2:** Contributions of the individual components to the overall fit for a region in the centre of precipitates 1 and 2. The matrix contributions are not shown as they are much larger than the other contributions and would make them less visible. Residuals are also shown. Figure first published in [134].

The contributions from the precipitate components such as TiC and VC are significantly smaller in Precipitate 1 than they are in Precipitate 2. However, the opposite is true for the contribution of amorphous carbon to the overall data, with its contribution for Precipitate 2

being at the same level as the residuals whereas it is significantly larger than the residuals for Precipitate 1.

It is possible to obtain further information on the precipitates as their four components are characterised by the fit coefficients for the binary carbides and those for the background subtracted C and N standards ie.  $b(\text{VC}_{0.83})$ ,  $b(\text{TiC}_{0.98})$ ,  $b\text{C}$  and  $b\text{N}$ . These fit coefficients are the contribution of the corresponding component of the spectrum intensity divided by its differential cross-section. As such, the TiC and VC fit coefficients are proportional to the number of Ti and V atoms per unit area respectively, with their sum being proportional to the total number of metal atoms.

Similar to the case for Ti and V,  $b\text{N}$  is proportional to the number of nitrogen atoms per unit area. As the amount of carbon in the precipitates is smaller than the combination of carbon from the two binary standards, the proportionality relationship for carbon is more complicated. In this case, it is the sum  $(0.83b \text{VC}_{0.83} + 0.98b \text{TiC}_{0.98} + b\text{C})$  that is proportional to the number of atoms per unit area. The values of  $x$ ,  $y$  and  $z$  in  $\text{Ti}_x\text{V}_{(1-x)}\text{C}_y\text{N}_z$  can be found pixel by pixel, for example the amount of titanium in the precipitate is given by

$$x = \frac{b\text{TiC}}{b\text{VC} + b\text{TiC}} \quad (6.1)$$

All the precipitates of interest here are carbides and nitrides and are expected to have a cubic rock salt structure. Once their composition was determined as described above, their lattice parameter can be interpolated from already published data such as that of Goldschmidt [27]. This means that the number of metal sub-lattice points per unit volume can be found, which is equal to the number of non-metal sub-lattice points in this case. Assuming that all the metal sites are occupied, the thickness of the precipitates can be calculated from  $b\text{TiC} + b\text{VC}$  together with the values for the ZLP obtained from the low-loss spectrum image and the channel width, which in this case is 0.5eV. The partial thicknesses, as explained in Chapter 3 Section 3.4) for each of the four elements in the precipitates was calculated as well. The results of this are shown in Figure 6.3 which plots one-pixel wide line profiles through the centre of each of the precipitates.

There are three different profiles for each of the contributions in each precipitate. The black lines represent the profiles when the MLLS fit was done over the region between 150eV and 750eV using extracted spectra from thin and thick regions of the matrix (extracted spectra from regions where the steel matrix in the thinnest and the thickest, respectively) that have been extracted from the deconvolved spectrum image. The red and blue lines use surface and bulk shapes instead of thin and thick matrix shapes in the MLLS fit, with the red line having the fit starting at 150eV and extending up to 750eV and the blue line having the fit start at 200eV and extending up to 750eV. This was done because the fit in the region right after the start was poor when it was started at 150eV but was significantly improved by starting it at 200eV. Figure 6.3 shows that there isn't much difference in the Ti and V contributions to the precipitates when comparing the three different fits. This is not the case with the non-metals,

with Precipitate 3 having different calculated carbon thicknesses in the precipitate area between the different fits. In the case of the nitrogen thickness, precipitates 2, 3 and 4 are all affected by the differences in calculated thicknesses when using the different fits. However, outside of the precipitate areas, the fit using thin and thick matrix shapes is close to zero suggesting the most accuracy. Due to the more limited fitting region to obtain a good quality fit when using bulk (iron and manganese) and surface contributions (such as iron oxide), the fit using thin and thick matrix shapes is the one that was used in further calculations.

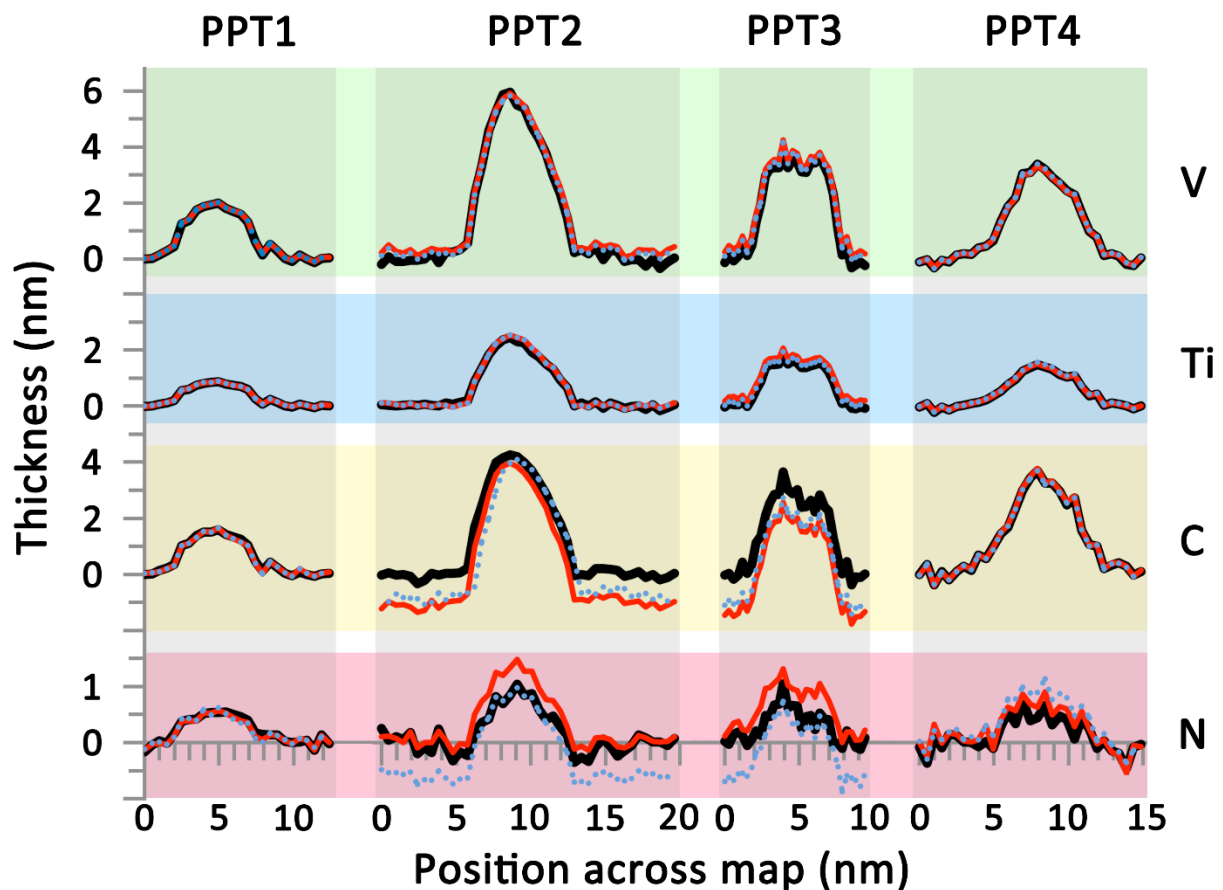


**Figure 6.3:** Line profiles for the four elements through the center of the four precipitates, with the vertical scale for nitrogen being expanded due to the small amount of nitrogen present. The black lines are from MLLS fits done with thick and thin matrix shapes. The red and blue lines use spectra extracted from the surface and bulk rather than the matrix, with the red fit starting at 150eV and the blue one at 200eV. Figure first published in [134].

The shapes for all elements are fairly similar for all precipitates, suggesting that their composition is homogenous and there is no evidence of segregation between the centre of the precipitates and an outer shell of different composition. The errors in the quantification here are fairly small, estimated to be of the order of +/- 3-4 atoms across. These are due to the errors in calculating the cross-sections with the experimental background, and potential instabilities in the results of the MLLS fitting of the precipitates.

When it comes to calculating the projected thickness of the precipitates, one way of doing that is by adding the partial thicknesses from Ti and V. Another way is to measure the values of  $t/\lambda$  from the deconvolved SI, after the matrix and the a-C contributions have been subtracted, thus leaving behind only the precipitate. By knowing the mean free path  $\lambda$  (the same that was used in calculating cross-sections), the thickness can be calculated [126].

The calculated thicknesses for the four precipitates are shown in Figure 6.4, with the purple lines showing the thickness obtained from summing the partial Ti + V metal thicknesses. The orange line represents the calculated thickness from  $t/\lambda$  after only the matrix contribution was subtracted, with the green line representing the thickness from  $t/\lambda$  after both the matrix and the a-C contributions have been subtracted. The thickness profiles have been taken through the center of the precipitates.

The thicknesses from summing the Ti and V partial thicknesses are consistently smaller than both thicknesses obtained from  $t/\lambda$  for all four precipitates analysed, with the maximum difference being of about 1.5nm. This was irrespective of the precipitate thickness but did drop to zero outside the precipitates into the matrix. We do not have a definite answer as to what causes this difference between the thicknesses obtained using the two methods. One possibility could be that there was a slight error in the removal of the surface oxide contribution.

When looking at the two thicknesses obtained from  $t/\lambda$ , Precipitate 2 shows no change between the two sets. This was also the precipitate that had no visible a-C contribution to the MLLS fit in the region of the precipitate. Precipitates 1 and 4 show decreases in thickness which were expected as these two precipitates show clear a-C signals in the areas of the precipitates. Precipitate 3 shows such a decrease in one half of the precipitate but not in the other half. This half of the precipitate profile corresponds to the top part of the a-C fit coefficient map, which shows some contribution from amorphous carbon but is not necessarily directly correlated to the position of Precipitate 3. However, the small differences in thickness obtained when subtracting the amorphous carbon contribution suggests that there is only a small amount of a-C on the lamella.

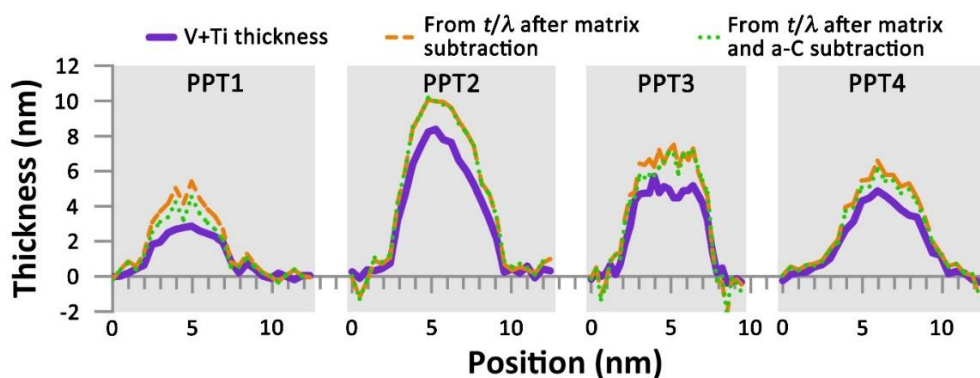


**Figure 6.4:** Comparison of the thickness profiles for the four precipitates, with the purple line being the thickness from Ti+V, the orange line is the  $t/\lambda$  thickness after subtracting the matrix contribution.

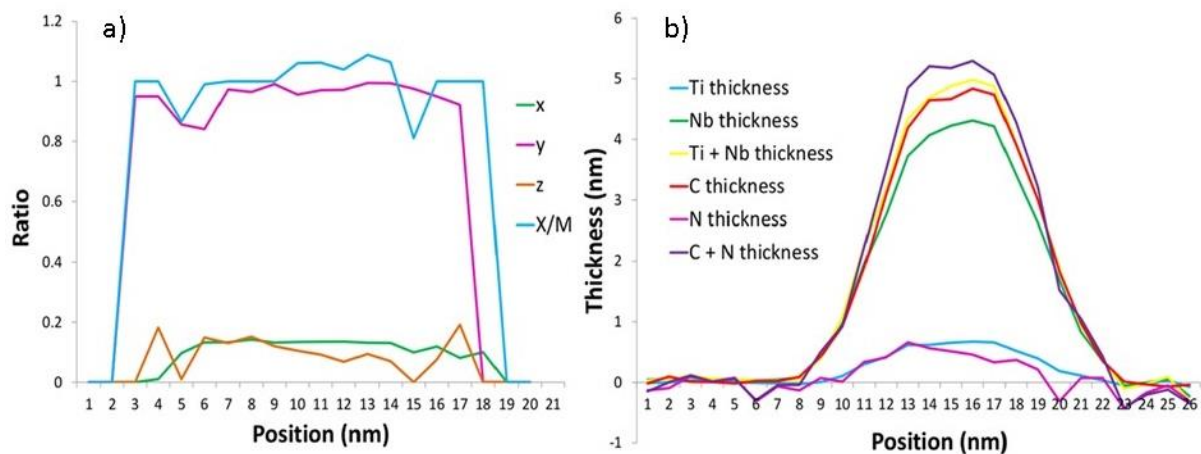
and the green line also having the a-C contribution subtracted and not just the matrix contribution.

Figure first published in Craven et al. (2018) [134]

### 6.3.2. Results for (Nb, Ti)C precipitates in TKSE high manganese steel

The Nb quantification and cross-sections were first tested on a high manganese steel provided by ThyssenKrupp as detailed in Section 6.1.2 of this chapter.

When calculating the cross-sections for NbC and NbN, there were questions on how to best fit backgrounds before the Nb  $M_{4,5}$  edge as well as on how to separate the C-K or N-K edges from the Nb. At that point it was decided to leave the backgrounds in the cross-sections and not try to subtract them from the precipitate spectrum images either. After that point, the quantification worked in exactly the same way as for the (Ti,V)(C,N) precipitates. The quantification results for one of the precipitates can be seen in Figure 6.5.



**Figure 6.5:** a) The elemental profiles of  $x$ ,  $y$ ,  $z$  and the  $X/M$  non-metal to metal ratio in  $Ti_xNb_{(1-x)}C_yN_z$  and b) the equivalent thicknesses of  $Ti$ ,  $Nb$ ,  $C$ ,  $N$ ,  $Ti+Nb$  and  $C+N$  taken across the centre of the precipitate.

On the equivalent thickness plot, it can be seen that there is very little nitrogen and titanium in the precipitate, almost down to the level of noise. However, there is a large amount of carbon and niobium, suggesting that the precipitate is indeed a niobium carbide rather than a carbonitride. There is a little more carbon than niobium, so the precipitate is close to stoichiometry but not exactly a 1:1 ratio. This is consistent with the ratio of non-metal to metal  $X/M$  (blue line in ratio graph) which is very close to 1 and at points slightly above. The profiles of  $Ti$  (green) and  $N$  (orange) are below 0.2, with the  $N$  plot being much noisier than  $Ti$  plot. On average, all the ratios including the  $X/M$  ratio are fairly flat suggesting there is no segregation between the different elements in the precipitate.

### 6.3.3. Results for (Nb, Ti, V) C precipitates in CRM 60min tempered martensite steel

Carbide precipitates containing a mix of Nb, Ti and V have been found in the steel tempered for 60 minutes as part of the CRM tempered martensite series that was introduced in Chapter 4 when discussing large area mapping using low-loss EELS.

The series of precipitates was found to have formed alongside a grain boundary, which can be seen in Figure 6.6 with the arrows pointing to the direction of the boundary through the steel. The boundary originally moves downwards through the scanned area with the precipitates being alongside it. At some point during the steel processing, it is possible that the boundary has moved towards the left. The precipitates continue along the right on what may have been the original direction of the grain boundary when the precipitates formed at higher temperature. This possibly happened in austenite rather than the later martensitic phase after cooling. The precipitates are relatively large, and their formation alongside a grain boundary was likely due to faster diffusion of carbon and transition metals in boundaries when compared to the bulk of the matrix.

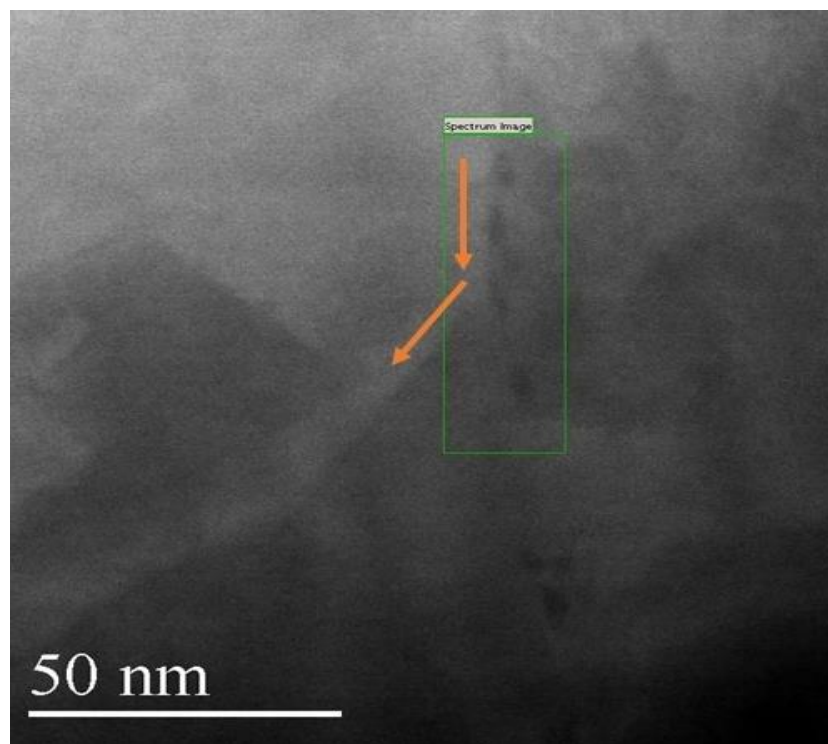


**Figure 6.6:** The survey image showing scanned area in the green box, the precipitates as darker areas in the matrix and the grain boundary direction indicated by the arrows.

A qualitative assessment of the composition of the precipitates and the grain boundary was obtained by fitting a background before each of the edges and integrating a short signal window over the edge. The maps obtained thereby can be seen in Figure 6.7, with yellow and white suggesting a larger concentration of the element mapped. There is clear decrease in the iron concentration in the area of the precipitates, and a large increase in Ti, V and C, suggesting that the precipitates are metal carbides. The Mn map revealed that the grain

boundary is manganese rich, with the largest precipitate (shown by the white arrow on the manganese map) potentially containing some manganese as well. Due to the position of the Nb-M edge at low energy losses, as shown in Figure 5.7, fitting a background before the edge does not fit well just before the onset of the edge and better fitting techniques are needed. Some differences between the intensity of the map for Ti and V in the areas of the precipitates can be seen, suggesting some possible segregation into a core/ shell structure. This has been seen in steel precipitates before, with for example Craven *et al.* [135] finding TiN cores at the centres of (Ti, Nb) (C, N) precipitates, which were probably the nucleation seeds for larger precipitates [136].

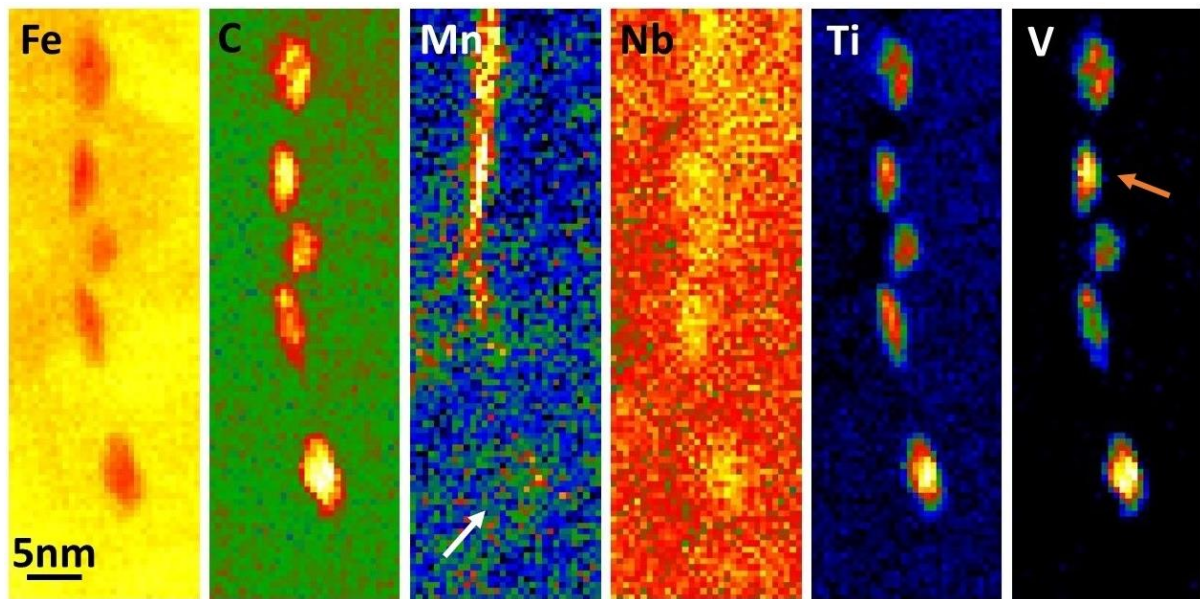


**Figure 6.7:** Elemental maps of the precipitates and the grain boundary, obtained from fitting a background before the edges and integrating over a signal window over the edge. A precipitate rich in manganese is shown by the white arrow on the manganese map, and one of the precipitates found alongside the grain boundary is shown by the orange arrow on the vanadium map.

Better quality DualEELS data was obtained later, and an MLLS fitting approach was used to obtain a more accurate composition for the precipitates. Additionally, by that point a correction for the dispersion non-linearity was available and as such it was applied, as described at the beginning of Chapter 3. The MLLS fit was done in the region between 150eV and 750eV, with all the standard shapes included in the fit for the composition of the (Ti, V) (C, N) precipitate discussed in the previous section (6.3.1.) plus the standard shape for NbC to account for the presence of Nb in this steel. The results of the MLLS fit are again maps of fit coefficients, with the ones representing elemental shapes being shown in Figure 6.8. For the TiC, VC and NbC coefficient maps, the bright areas represent a positive fitting coefficient and the dark areas represent coefficients near zero.

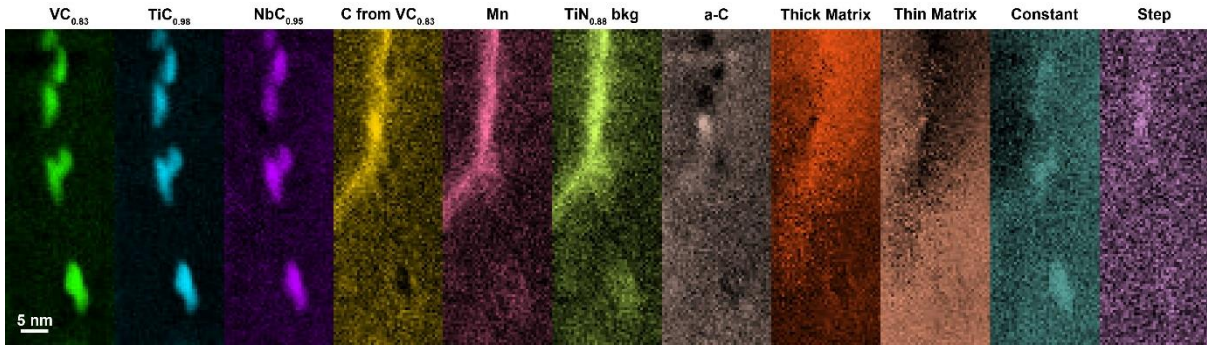


**Figure 6.8:** Maps of the MLLS fit coefficients for the standards for the (Ti, V, Nb) C precipitates. It shows the coefficients from the component shapes, the background shape as well as the thick and thin matrix shapes and the constant and step functions.

The map for elemental C extracted from VC shows a positive coefficient in the area of the grain boundary, suggesting that the boundary has more carbon in its composition than the surrounding matrix. The coefficient is slightly negative in the area of the precipitates, suggesting that the carbon content in the precipitates is again smaller than the linear combination of the binary standards. The nitrogen map shows a decrease in the fitting coefficient in the areas of the boundary and the precipitates; however, the decrease is small when compared to the coefficient in the matrix areas. This could suggest there is little nitrogen content in the precipitates, which was expected from the base composition of the steel and the precipitate spectra. However, both the results of the quantification routine shown in Figure 6.10 for the manganese rich precipitate (shown by the white arrow on Figure 6.7) and the extracted spectrum from an area in the centre of the precipitate (shown in Figure 6.9) do not show any signal in the area of the N-K edge.

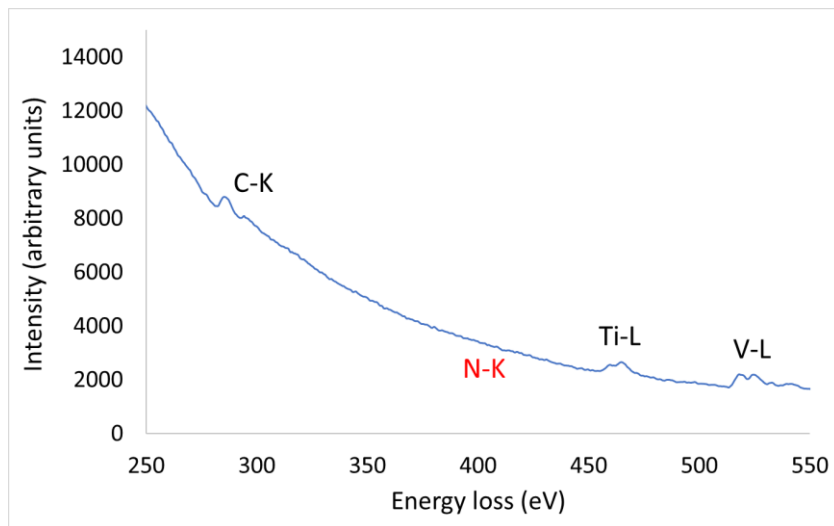


**Figure 6.9:** Extracted spectrum from the centre of the manganese rich precipitate in Figure 6.7, showing clear Ti and V edges but no conclusive N signal (marked with red where the N-K edge would be).

There is an increase in the amorphous carbon coefficient in a small area of the a-C map, which could point towards some build-up of contamination on the lamella during the data acquisition. As before, the equivalent thicknesses for each of the elements can be calculated from the MLLS fitting coefficient maps, with the results for the rightmost precipitate being shown in Figure 6.10.

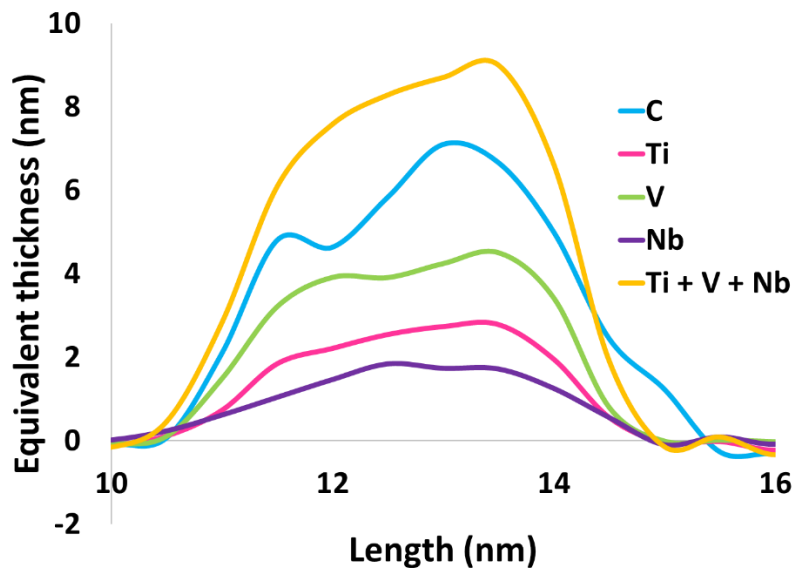


**Figure 6.10:** The equivalent thickness of carbon and each of the non-metals in one of the precipitates in the CRM steel tempered for 60min.

The equivalent thicknesses have been taken from line profiles through the center of the precipitate. The N equivalent thickness was not included in the plot as there is no evidence of nitrogen anywhere in the precipitate, and the script results showed a negative nitrogen thickness. This suggested that the N-K edge shape should not have been included in the MLLS fit, so another fit was done. The fit coefficient maps for the composition related shapes looked the same as those shown in Figure 6.10, showing that there was no nitrogen in the precipitates. The same calculations were performed using the script as before, with the equivalent thicknesses of the elements in the precipitate being the same as those presented in Figure 6.10 and thus are not reproduced.

The precipitate is approximate 5nm in length and the thickness calculated from summing the individual equivalent thicknesses of the metals is approximate 8nm, suggesting the precipitate is roughly elliptical. There seems to be an overall increase in thickness in one half of the precipitate when compared to the other half. While the niobium thickness appears to be constant throughout the center of the precipitate, the titanium and vanadium content do not appear so and are correlated with the increase in thickness in one half of the precipitate. When dividing the equivalent thickness of Ti by that of Nb and averaging the result across a 20-pixel line profile, such evidence of segregation between the elements was not visible in this precipitate.

One of the precipitates (second from the top, shown by the orange arrow on the vanadium map on Figure 6.7) that is still alongside the grain boundary even after it has been displaced has had the equivalent cross-section shape. The results are shown in Figure 6.11, with both the equivalent thicknesses of the elements being shown and the ratio of each of the metals in the over precipitate composition.

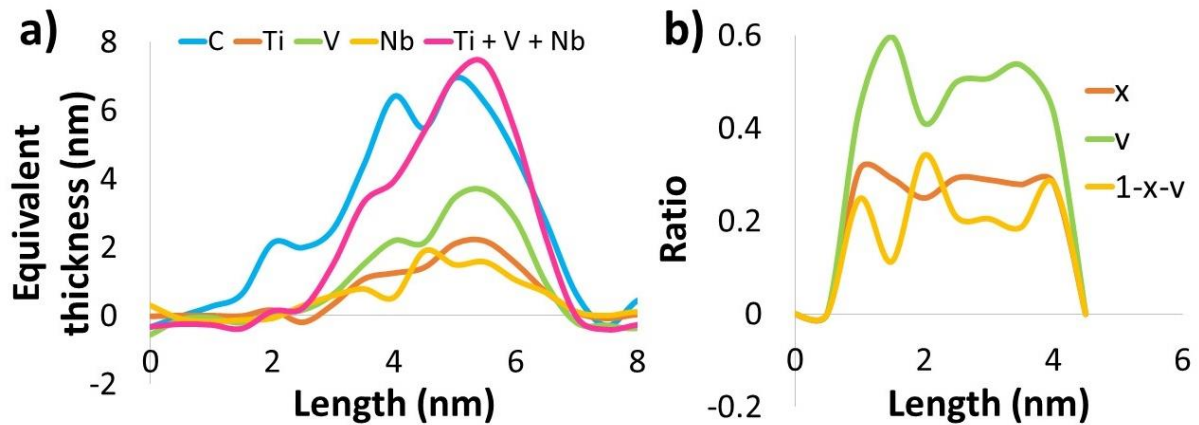


**Figure 6.11:** a) the equivalent thickness of each element in the precipitate shown by the orange arrow in Figure 6.7 and b) the values of  $x$ ,  $v$  and  $1-x-v$  in  $Ti_xV_vNb_{(1-x-v)}C_y$ .

Figure 6.11 a) shows the equivalent thicknesses of each of the elements in the precipitate across one of the axes of the precipitate. There are approximately equal amounts of titanium (orange) and niobium (yellow), with the vanadium (green) content of the precipitate being nearly double that of either of the other two metals. The sum of the equivalent thicknesses of the three metals (pink) is on average roughly the same as the amount of carbon (blue) in the precipitate, however half of the precipitate has more carbon with the other half having more metals. Figure 6.11 b) shows the values of  $x$ ,  $v$  and  $(1-x-v)$  in  $Ti_xV_vNb_{(1-x-v)}C_y$ . While the amount of titanium throughout the precipitate appears to be relatively constant, the vanadium and niobium ones vary slightly, with the amount of vanadium decreasing when that of niobium increases. This could suggest a small level of segregation between the metals in the precipitate.

#### 6.3.4. Large, manganese rich cementite particle

A large, manganese rich cementite particle was found in the CRM sample tempered for 90 minutes. Near the cementite, three circular precipitates have been found. Additionally, throughout the field a view several (Ti, V) precipitates were found. The dataset was presented before in Chapter 3 in Figure 3.8, when discussing different data processing techniques. It was clear that the composition of some of the precipitates identified was different to all the standards used so far. The manganese and titanium (identical to vanadium so only one is reproduced) from that figure is repeated here in Figure 6.12, with MnS particle indicated by an arrow on the Mn map and some edge on plate-like precipitates being indicated by an arrow on the V map. These will be discussed further on in this section.

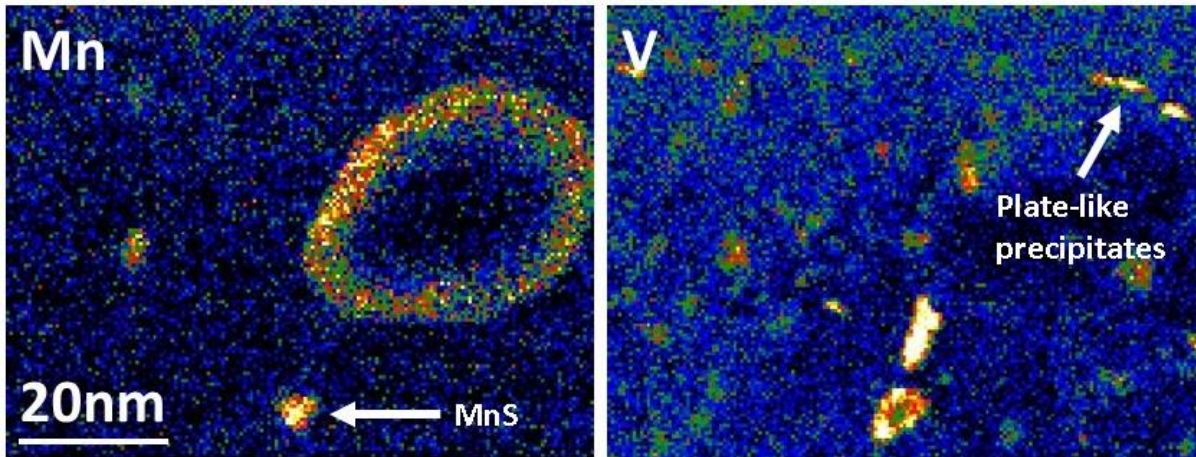


**Figure 6.12:** Manganese map of the cementite particle dataset with the MnS precipitate discussed in this section indicated with an arrow, and a vanadium map indicating some plate-like precipitates.

The composition of the smaller precipitates was uncertain, so a few MLLS fits with different sets of standards were tried. Since it was known that the cementite particle was likely to be  $(\text{Fe, Mn})_3\text{C}$ , a shape for this was extracted. However, the Fe: Mn ratio between the top of the scanned image and the bottom was quite different, so instead of thick and thin matrix shapes, spectra extracted from the top and the bottom of the dataset were used in the MLLS fit. Additionally, shapes from other elements present in the steel were included. These are chromium, phosphorus and sulphur. A shape for the O-K edge was also included to account for potential oxide. The results of the fit can be seen in Figure 6.13.

The TiC and VC coefficient maps show up the small precipitates very clearly. The NbC map suggests that there could be some Nb contribution to some of them, however when looking at the precipitate spectra this was not evident. While the signal could come from Nb, it could also have been due to data acquisition artefacts in the lower energy region of the spectra that have not been understood yet.

The three smaller, circular precipitates are clearly visible in the Cr, Mn, P and S fit coefficient maps. While there is evidence of Mn and S forming stable compounds [25], there is less evidence of Mn and P forming such compounds in steels. As such, we are confident that those three precipitates are MnS particles. The spectra extracted from one of them (bottom most one) can be seen in Figure 6.14, with the S edge labelled and clearly above the level of the background signal. On the same graph the spectrum extracted after the experimental  $\text{TiNO}_{.88}$  background was extracted from the original deconvolved spectrum image is also plotted. The Ti and V contributions from the smaller precipitates around the cementite have been extracted, as well as the  $(\text{Mn, Fe})_3\text{C}$  contribution from the cementite itself. The matrix contribution was extracted as well so there is no Fe edge in the spectrum. An edge is clearly visible at energy losses before 200eV. As was discussed before, this could correspond to elements such as S, Si or P which were present in the steel. However, MnS seems the most likely one based on previously found compounds.

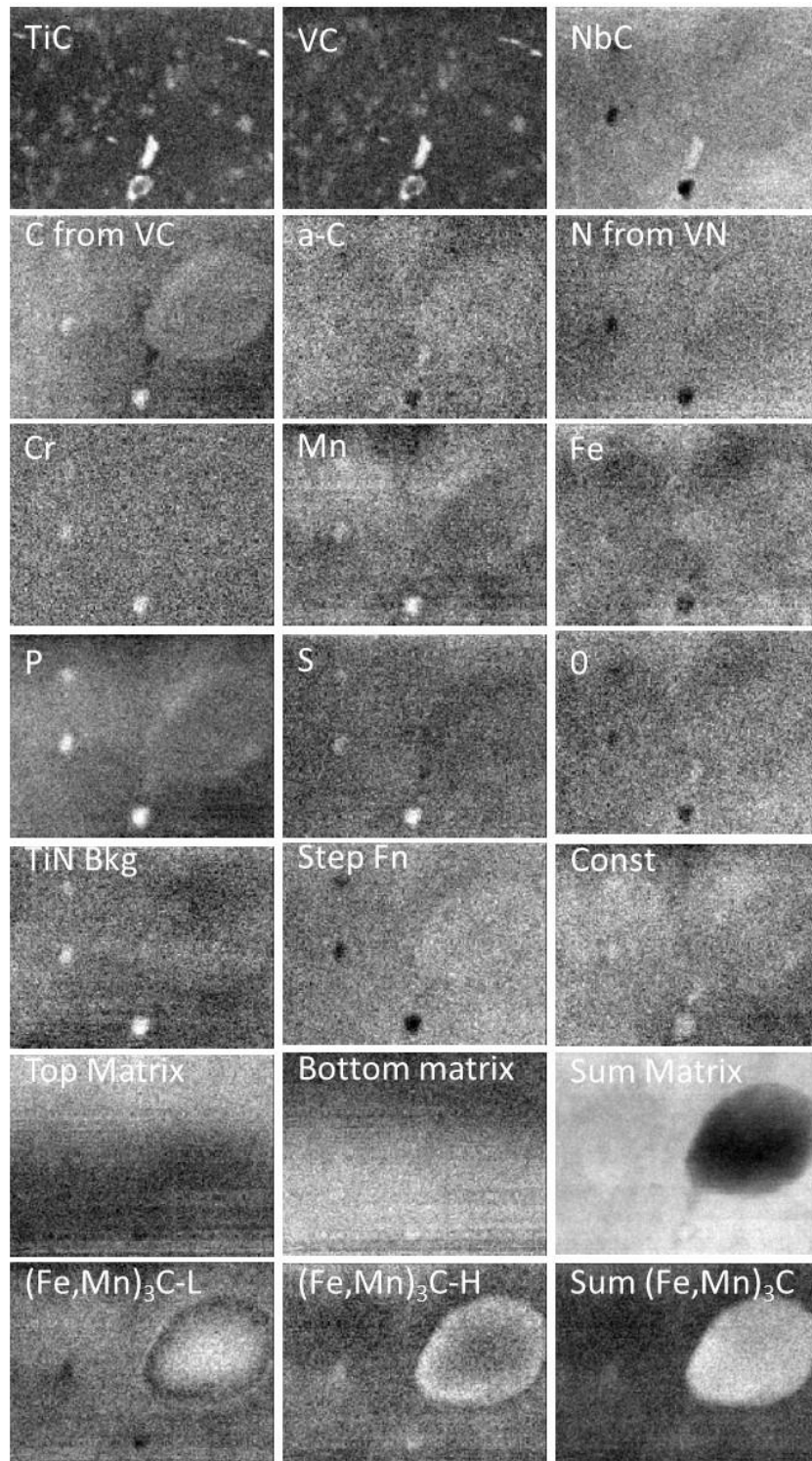


**Figure 6.13:** MLLS coefficient maps for the fit on the cementite particle and the area surrounding it. The “top matrix” contribution is a spectrum extracted from the top half of the dataset with the “bottom matrix” is a spectrum extracted from the bottom half of the dataset.

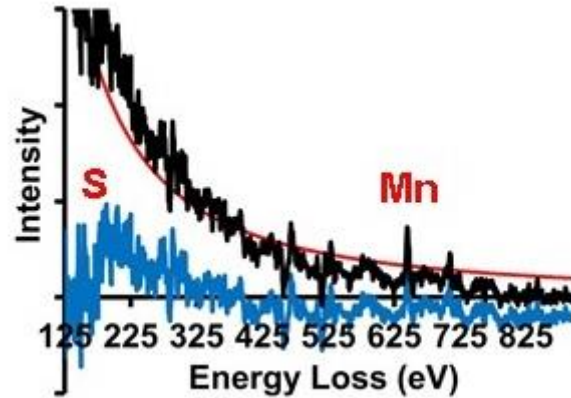


**Figure 6.14:** The extracted spectrum from one of the MnS particles surrounding the cementite, showing the Mn and S edges.

For the large cementite particle, the core/ shell structure between Fe and Mn is visible again, thus confirming the more basic analysis discussed in Chapter 3.

The exact composition of the smaller precipitates is not certain yet beyond the fact that they contain Ti and V. The research into their composition, and orientation within the matrix, is still ongoing. So far, we have seen small plate-like precipitates having formed edge-on to the direction we are seeing them from. These probably follow a Baker-Nutting orientation relationship to the matrix, if precipitated within ferrite or BCT martensite, as discussed in Chapter 1 of this thesis. The initial results from mapping these edge-on plate-like precipitates are shown in Figure 6.15, which shows the extracted spectrum (blue) with the Ti and V edges marked and clearly visible above the level of the background. The orange line represents the signal after a power law background was subtracted from the overall signal to enhance the visibility of the metal edges. However only the precipitates having formed in the thinnest matrix areas have been successfully analysed due to poor signal to noise ratio when the precipitates have formed in thicker regions of the steel. The errors on the composition of these precipitates are significantly larger than in the case of the (Ti,V)(C,N) ones discussed at the beginning of Chapter 6. This is in part due to the lack of available cross-sections for some of the elements believed to be in their composition, and partly because of their small size and lack of signal intensity above the background to make a full quantification possible at the point of writing this.

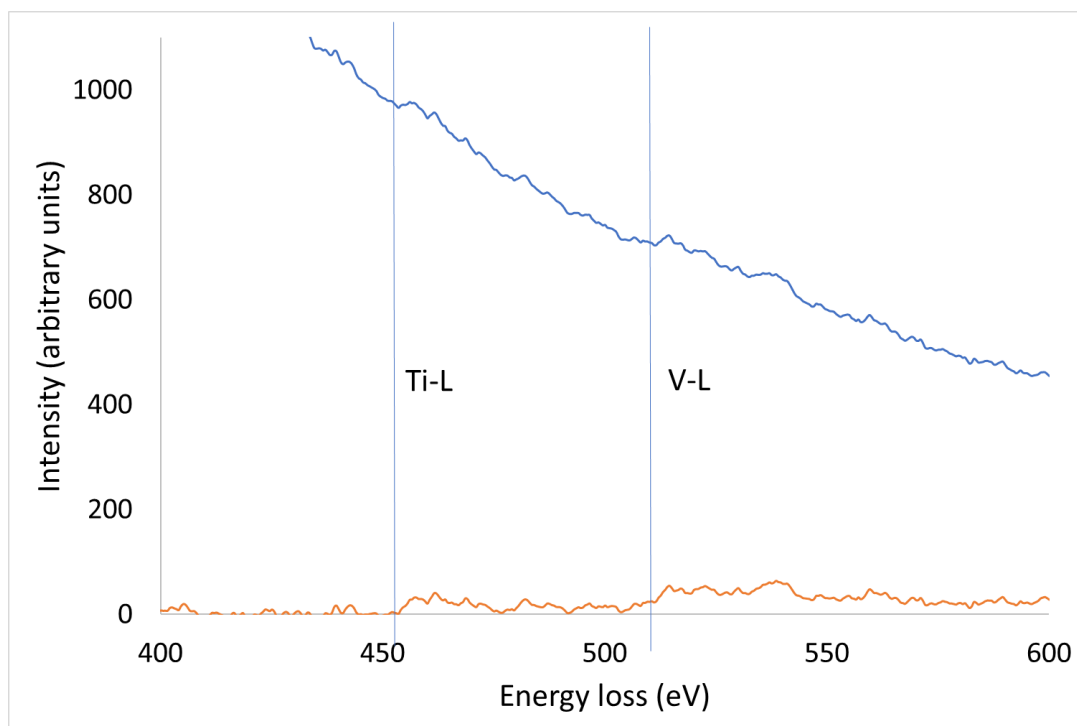


**Figure 6.15:** *Extracted spectrum from small plate-like precipitates, with the Ti and V edges marked and visible above the background signal (blue). The orange line represents the signal after a power-law background was extracted.*

## 6.4. Summary

While a few quantification methods do exist, such as fitting backgrounds before relevant edges and integrating the edge, they are not the most accurate and are highly dependent on user choice.

Multiple linear least squares (MLLS) fitting with standard shapes obtained from experimental cross-sections is a powerful tool to assess the composition of samples. However, obtaining the best fit is an iterative process and the results must be compared against the original data to find the best set of standards to be used. Still, the method is not dependent on width and positioning of background and signal windows, as the traditional quantification method is, and thus is far more accurate and easier to reproduce.

The method has been applied to a range of datasets, all precipitates having formed within a steel matrix. In the first instance, it was used to obtain the accurate composition of four (Ti, V) (C, N) precipitates formed in a high-manganese steel matrix. These precipitates were roughly circular, with a diameter of a few nm. These results have been published in 2018 [134].

The method was then applied to precipitates also containing Nb. In the first case, precipitates from the PrechMn steel containing Nb were analysed. An example of such precipitate was discussed in this chapter, where the composition is mainly NbC and nearly stoichiometric.

Then, a series of precipitates formed in a martensite tempered for 60 minutes at 600°C was analysed. The precipitates had formed alongside a grain boundary, which appears to have been later displaced. The grain boundary was found to be rich in manganese, with the precipitates being metal carbides. No nitrogen was detected in any of them, but some manganese signal could be seen in one of them.

A more complicated MLLS fit was needed in the case of the large cementite particle surrounded by smaller precipitates. Some of those precipitates were found to be manganese sulphides, with the large cementite showing Fe/Mn core/shell structure. Smaller precipitates have been found in the dataset, with some of them likely being edge-on plate-like particles and expected to follow a Baker-Nutting orientation relationship with the surrounding matrix. The exact composition of some of the smaller precipitates is not yet fully understood at the point of writing this thesis and is still a work in progress.

## Chapter 7

### Conclusions and Future work

In order to investigate the processing of titanium, vanadium and niobium microalloyed bainitic steels, and specifically to develop ways of generating rolled products with consistent properties, a project was set up under the European Commission's Research Fund for Coal and Steel. The project was led by CRM in Belgium and had partners from Spain, Germany, Belgium and the UK. The work reported in this thesis was concerned with understanding the precipitation mechanisms and chemistry of transition metal carbide precipitates in such steels, as this is critical to the macroscopic properties of the steel.

The distribution within the matrix and the chemistry of carbonitride precipitates in these steels have been studied in the Scanning Transmission Electron Microscope (STEM). This was done using Electron Energy Loss Spectroscopy (EELS) on thin cross-sections of the steel prepared using Focused Ion Beam (FIB) techniques. Firstly, the main results presented in this thesis are summarised, followed by a brief overview of some avenues for possible future work that could continue the investigations reported herein.

#### 7.1. Thesis summary

Understanding the chemistry of precipitates forming at different stages during the thermomechanical processing of steels, together with their distribution within the matrix, are of significance to the steel industry as they affects the macroscopic properties of the final steel. Nanoscale precipitate characterisation in different types of steel have been presented in this thesis, both from the current PreTiControl project and a previous project looking at precipitation in high-manganese steels (PreHiMn).

It has been demonstrated that low-loss EELS mapping is an incredibly powerful method for revealing precipitates in large areas of steel samples. The steel matrix and the titanium, vanadium and niobium carbide or carbonitride precipitates forming inside it have different chemical compositions, which leads to their EEL spectrum being different in a narrow area of the low-loss region. This was found to be useful for the mapping of particles as small as 1nm in diameter or less in large maps of hundreds of nm in dimensions. Whilst low-loss EELS has been used to identify and map different chemical phases in the past, it was not successfully carried out on such tiny particles over such large areas. When used on a series of martensitic steels tempered at 600°C (with the transition metal available for precipitation being in a ratio of Ti-10 Nb-3 V-7) for different amounts of time to assess hardness and precipitation as a function of time, it was shown that most precipitates formed have small diameters (<3nm). It was shown that the longer the steel is tempered, the larger the number of small precipitates form throughout individual grains of the matrix and this could be mapped quantitatively as number densities. Moreover, this could be correlated with changes in mechanical properties. Such small particles could not have been imaged effectively over large areas using other available methods. Larger precipitates were identified as well, but in significantly smaller

numbers. A similar trend was observed in a different composition steel (Ti-10 Nb-3 V-0), however in that case the range of diameters was narrower.

Apart from giving us access to the precipitate size distribution in different samples, our method allowed us to image them while they were still embedded in the matrix. This preserved their relationship with the steel microstructure, revealing that while many small precipitates form throughout the steel matrix, or possibly on dislocations, larger ones tend to be found on grain boundaries. These are likely to have formed earlier in the steel processing cycle taking advantage of the fact that carbon and transition metal diffuse more easily throughout boundaries than through grains.

In order to analyse the large area low-loss maps, a processing method had to be developed. This was done using pre-existing plug-ins for Digital Micrograph, such as Principal Component Analysis (PCA) and Factor Analysis available within the Multivariate Statistical Analysis (MSA) plug-in. Additionally, custom-built scripts were used, and user intervention was needed during the final processing steps.

Once precipitate-rich regions have been identified, selected precipitates were imaged using DualEELS to obtain both their low-loss and core-loss spectra. Their chemistry was then quantified using a method partially developed as part of a previous PhD and improved significantly as part of this project. Our method uses multiple linear least squares (MLLS) fitting with experimentally obtained elemental cross-sections, together with a custom-built script, to accurately quantify the composition of particles. Whilst obtaining the best fit is an iterative process, the method removes the need for subtracting backgrounds or choosing the width of edge integration windows, thus removing potential errors caused by user choice.

Four (Ti,V)(C,N) precipitates formed in a high-manganese steel were quantified. The precipitates were circular with diameters of a few nm. On average, the precipitates had more titanium than vanadium, with a significant amount of carbon but very little nitrogen which in some of the precipitates was at the level of the noise. Their thickness was measured using two different methods. Firstly, it was calculated using the sum of the partial metal thicknesses. The answer was slightly larger than the one obtained from using the mean free path  $\lambda$  and the  $t/\lambda$  map after subtracting the matrix and the amorphous carbon contributions. It is not yet understood why this difference is present, but it could be due to errors in subtracting the different contributions.

Next, the technique was used to quantify a Nb containing precipitate from the PreHiMn project. This precipitate had very little titanium and nitrogen but large amounts of carbon and niobium and was close to stoichiometry for NbC. Once the technique was tested on this Nb precipitate, particles from the current project, containing Nb, Ti and V were analysed. A group of large precipitates having formed alongside a grain boundary was imaged first. One of them was found to contain some manganese, with the boundary also being found to contain a significant concentration of manganese. Unlike the precipitates analysed before, these were found to show possible core/shell structures and segregation between metals. This observation was supported by previous literature. No conclusive evidence of nitrogen was found.

In one of the steels, a large cementite particle was observed. This again displayed some core/shell structure, in this case much clearer than the smaller precipitates mentioned previously. The edge of the particle had a higher manganese content, while the centre was more iron-rich within an overall  $(\text{Mn,Fe})_3\text{C}$  cementite composition. Around this structure, three small MnS precipitates were identified using a significantly more complex MLLS fit. In addition to the cementite and MnS precipitates, small plate-like  $(\text{V,Ti})\text{C}$  precipitates were identified throughout the field of view imaged in the dataset. Their exact composition was not quantified, but they appear to be platelet-like in morphology and to they probably follow a Baker-Nutting orientation relationship to the matrix as they are face centred cubic particles having formed inside a body centred matrix. We believe this is the case as some of them appeared circular and faint, suggested they were imaged straight down, while others were bright and appeared elliptical which suggested they were imaged edge-on.

In order to perform these MLLS fits and accurate quantifications, experimental cross-sections for each of the elements present in the precipitates need to be calculated. Another significant contribution of this project was calculating accurate experimental cross-sections for titanium, vanadium, carbon and nitrogen from DualEELS data of well-understood binary TiN, VN, TiC and VC standard samples. Additionally, preliminary cross-sections for Nb have been obtained from NbN and NbC cross-sections. These show significant differences when compared to the Hartree-Slater cross-sections that are widely used, illustrating the importance of using accurately calculated experimental cross-sections when attempting to quantify precipitates accurately. However, due to the dispersion in the spectrometer not being linear, there were mismatches between the low-loss and the high-loss part of the spectra of the Nb standards. This has been characterised and corrected for in subsequent spectrum images, however further issues with the materials (originally thought to be zirconium contamination) meant that only a provisional Nb cross-section could be calculated, and further work would be needed to reach the same degree of accuracy as for Ti and V carbides and nitrides. This means that, while the Ti and V precipitate composition has been calculated very accurately, the quantification is less accurate in the case of Nb containing precipitates.

## **7.2. Future work**

The main areas investigated in this research cover low-loss large area mapping of precipitates in steel using EELS, the accurate chemical quantification of those precipitates using DualEELS and the calculation of accurate experimental cross-sections used in the MLLS fit for quantification.

Directly related to this project on steels, the most pressing issue is to improve the quantification of niobium in precipitates. The first step towards doing that would be to obtain an accurate mean free path of high energy electrons in niobium from a needle shaped sample. With the xenon plasma FIB now being fully available, a needle shaped sample of niobium nitride should be prepared. Next, better quality spectrum images from NbN and NbC cross-section samples need to be obtained and processed. The signal in the NbN originally thought to be due to zirconium contamination needs to be better understood and extracted from the original spectrum images.

Another issue that affected the calculation of niobium cross-sections was a mismatch at the splice point between the low-loss and the high-loss spectra, as well as significant differences between the splice ratio and the time ratio of the acquired data. These were found to be partly due to non-linearity in the spectrometer dispersion and correcting for it improved the data. While the non-linearity in the spectrometer can now be corrected with a script (available in the Appendix), the cause of the non-linearity should be better understood, and the spectrometer alignments improved.

While EELS has been an excellent technique for imaging these precipitates and obtaining their distribution throughout the matrix, size and chemistry, the exact composition of the smallest precipitates has not been determined yet. So far, we know that these precipitates, often forming as plates rather than spheres, contain titanium and vanadium. Further work on quantifying these is currently being done by Prof. Alan J. Craven. This work involves finding a way to separate the individual components in the original spectrum images using MLLS fitting routines to leave only the contributions from these small precipitates. Because of significant noise in the datasets as well as other precipitates formed in the area contain MnS or  $(\text{Mn,Fe})_3\text{C}$ , separating these contributions has been more difficult. However, it is important to note how much the use of MLLS fitting to standards improves the quantification procedure and results when compared to previous methods such as background fitting or fitting using Hartree-Slater theoretical cross-sections. Differences in results due to user choice of background windows has been removed, and experimental cross-section contain far more edge information than theoretical ones did. As such, work on obtaining more experimental cross-sections from different materials should continue to expand the number of cases MLLS fitting to standards can be applied to.

Further work on quantifying and analysing small precipitates using atom probe tomography (APT) has been planned with OCAS in Belgium. APT would allow us to detect small concentrations of carbon in the matrix and image the smallest precipitates as they are forming. Additionally, it can provide a 3-dimensional view of the sample that is not possible using only EELS. As such, combining the two techniques would provide a more complete picture of the precipitation in our samples. For this APT analysis, a series of samples manufactured by OCAS have been prepared as APT needles using the xenon plasma FIB and have been shipped to Belgium at the end of 2018. APT experiments will be performed in Belgium in the near future but have not yet been done at the time of writing this thesis.

A large issue affecting the data presented in this thesis has been the quality of available detectors. The amount of noise has been an issue when trying to analyse the smallest precipitates we have imaged, with mis-matched sections on the CCD detector causing steps in the final spectrum image that had to be taken into account in further processing. These could be significantly improved if better detectors were available.

Finally, while the research presented in this thesis and the methods developed as part of it have been applied solely to precipitates in steels, the processing method could be applied to a range of other systems. Specifically, systems would have to have different phases where at least one element that exists in one phase is absent from another or have spectra different enough that they could be made as standards to be used in the MLLS fit. Examples of such

systems that are being investigated within the group include the analysis of fine precipitates of currently unknown composition found in Ti-V-Al alloys and nanoscale segregation in oxidation of precipitates in zircalloy.

## 9. References

- [1] S. . Hong, H. . Jun, K. . Kang, and C. . Park, "Evolution of precipitates in the Nb–Ti–V microalloyed HSLA steels during reheating," *Scr. Mater.*, vol. 48, no. 8, pp. 1201–1206, 2003.
- [2] J.-G. Jung, J.-S. Park, J. Kim, and Y.-K. Lee, "Carbide precipitation kinetics in austenite of a Nb–Ti–V microalloyed steel," *Mater. Sci. Eng. A*, vol. 528, no. 16–17, pp. 5529–5535, 2011.
- [3] R. (Reza) Abbaschian, L. Abbaschian, and R. E. Reed-Hill, *Physical metallurgy principles*. Cengage Learning, 2009.
- [4] M. Opiela and W. Ozgowicz, "Effects of Nb , Ti and V on recrystallization kinetics of austenite in microalloyed steels," *Journal of achievements in materials and manufacturing engineering*, vol. 55, no. 2, pp. 759-771, 2012.
- [5] S. Bao, G. Zhao, C. Yu, Q. Chang, C. Ye, and X. Mao, "Recrystallization behavior of a Nb-microalloyed steel during hot compression," *Appl. Math. Model.*, vol. 35, no. 7, pp. 3268–3275, Jul. 2011.
- [6] S. F. Medina and J. E. Mancilla, "Influence of alloying elements in solution on static recrystallization kinetics of hot deformed steels.," *ISIJ Int.*, vol. 36, no. 8, pp. 1063–1069, Aug. 1996.
- [7] J. C. Herman, B Donnay and V. Leroy, "Precipitation kinetics of microalloying additions during hot-rolling of HSLA steels", *ISIJ International*, vol 32, no. 6, pp. 779-785, 1992
- [8] B. K. Show, R. Veerababu, R. Balamuralikrishnan, and G. Malakondaiah, "Effect of vanadium and titanium modification on the microstructure and mechanical properties of a microalloyed HSLA steel," *Mater. Sci. Eng. A*, vol. 527, no. 6, pp. 1595–1604, 2010.
- [9] J. Bobynko, "Characterisation and absolute quantification of nanosized V and Nb precipitates in high manganese steel using DualEELS," University of Glasgow, 2017.
- [10] R. E. Reed-Hill, *Physical metallurgy principles*, Internatio. New York: D. Van Nostrand Company, Inc., 1964.
- [11] R. F. Mehl and W. C. Hagel, "The austenite: Pearlite reaction," *Prog. Met. Phys.*, vol. 6, pp. 74–134, 1956.
- [12] H. K. D. H. Bhadeshia, "Bainite in Steels," *Mater. Sci. Metall.*, vol. Part II Co.
- [13] H. K. D. H. Bhadeshia, *Bainite in steels - Transformations, Microstructure and Properties*, Second Edi. London, UK: ION Communications LTD, 2001.
- [14] I. Thukatani, S. Hashimoto and T. Inoue, "Effects of silicon and manganese addition on mechanical properties of high-strength hot-rolled sheet steel containing retained austenite", *ISIJ International*, vol.31, no. 9, pp. 992-1000, 1991.
- [15] S. Osamu Matsumura, Yasuharu Sakuma, Y. Ishii, J. Zha, and U. Tokiwadai Hodogaya-

- ku, "Effect of retained austenite on formability of high strength sheet steels," *ISIJ International*, vol. 32, no. 10, pp. 1110–1116, 1992.
- [16] A. M. Sherman, "Fatigue properties of high strength-low alloy steels," *Metall. Trans. A*, vol. 6A, pp. 1035–1040, 1975.
- [17] R. Kuziak, R. Kawalla, and S. Waengler, "Advanced high strength steels for automotive industry," *Arch. Civ. Mech. Eng.*, vol. 8, pp. 103–117, 2008.
- [18] H.-J. Kestenbach and J. Gallego, "On dispersion hardening of microalloyed hot strip steels by carbonitride precipitation in austenite," *Scr. Mater.*, vol. 44, pp. 791–796, 2001.
- [19] S. S. Campos, H. J. Kestenbach, and E. V. Morales, "On strengthening mechanisms in commercial Nb-Ti hot strip steels," *Metallurgical and Materials Transactions A*, vol. 32, no. 5, pp. 1245-1248, 2001.
- [20] B. Dutta, E. Valdes, and C. M. Sellars, "Mechanism and kinetics of strain induced precipitation of Nb(C, N) in austenite," *Acta Met. mater.*, vol. 40, no. 4, pp. 653–662, 1992.
- [21] B. Dutta and C. M. Sellars, "Effect of composition and process variables on Nb(C, N) precipitation in niobium microalloyed austenite," *Mater. Sci. Technol.*, vol. 3, no. 3, pp. 197–206, 1987.
- [22] R. M. Brito and H.-J. Kestenbach, "On the dispersion hardening potential of interphase precipitation in micro-alloyed niobium steel," *Journal of materials science*, vol. 16, pp. 1257-1263, 1981.
- [23] W. S. Williams, "Physics of Transition Metal Carbides\*," *Mater. Sci. Eng. A*, vol. A105/106, pp. 1–10, 1988.
- [24] T. S. Oyama, J. C. Schlatter, J. E. I. Metcalfe, and J. M. J. Lambert, "Preparation and characterisation of early transition metal carbides and nitrides," *Ind. Eng. Chem. Res.*, vol. 27, no.9, pp. 1639-1648, 1988.
- [25] S. Aminorroaya, "Effect of titanium additions to low carbon, low manganese steels on sulphide precipitation," University of Wollongong, 2008.
- [26] T. N. Baker, "Processes, microstructure and properties of vanadium microalloyed steels," *Mater. Sci. Technol.*, no. 9, pp. 1083–1107, 2009.
- [27] H. J. Goldschmidt, *Interstitial Alloys*, 1st ed. New York: Springer Science + Business Media, 1967.
- [28] P. R. Howell, R. A. Ricks, J. V Bee, and R. W. K. Honeycombe, "Precipitate orientations in isothermally transformed iron-base alloys," *Philos. Mag. A*, vol. 41, no. 2, pp. 165–175, 1980.
- [29] C. Klinkenberg, K. Hulka, and W. Bleck, "Niobium Carbide Precipitation in Microalloyed Steel," *Steel Res. Int.*, vol. 75, no. 11, pp. 744–752, 2004.

- [30] S. G. Hong, K. B. Kang, and C. G. Park, "Strain-induced precipitation of NbC in Nb and Nb-Ti microalloyed HSLA steels," *Scr. Mater.*, vol. 46, no. 2, pp. 163–168, 2002.
- [31] D. V. Wilson, "Effects of plastic deformation on carbide precipitation in steel\*," *Acta Metall.*, vol. 5, pp. 293–302, 1957.
- [32] C. Leslie, R. M. Fisher, N. Senf, and E. C. Brain, "Morphology and crystal structure of carbides precipitated from solid solution in alpha iron," *Acta Metall.*, vol. 7, pp. 632–644, 1959.
- [33] K. Yamada, K. Sato, and H. Nakamichi, "Analysis of nanometer-sized precipitates using advanced TEM," *JFE Technical Rep.*, vol. 9, 2007.
- [34] R. Okamoto, A. Borgenstam, and J. Ågren, "Interphase precipitation in niobium-microalloyed steels," *Acta Mater.*, vol. 58, no. 14, pp. 4783–4790, 2010.
- [35] M. Charleux, W. J. Poole, M. Militzer, and A. Deschamps, "Precipitation behavior and its effect on strengthening of an HSLA-Nb/Ti steel," *Metall. Mater. Trans. A*, vol. 32A, pp. 1635–1647, 2001.
- [36] S. K. Ray, S. Mishra, and O. Mohanty, "TEM study of carbide precipitation in a phosphorus-bearing low-carbon steel," *Scr. Metall.*, vol. 16, pp. 43–47, 1982.
- [37] E. A. Kenik and P. J. Maziasz, "Application of Extraction Replicas and Analytical Electron Microscopy to Precipitate Phase Studies," *Microbeam Analysis Society analytical electron microscopy meeting*, 1984.
- [38] K. Poorhaydari and D. G. Ivey, "Application of carbon extraction replicas in grain-size measurements of high-strength steels using TEM," *Mater. Charact.*, vol. 58, no. 6, pp. 544–554, 2007.
- [39] J. D. L'ecuyer, G. L'esperance, M. G. Akben, and B. Bacroix, "Precipitation behaviour of a HSLA steel containing molybdenum, aluminium and trace amounts of titanium," *Acta Met.*, vol. 35, no. 5, pp. 1149–1158, 1987.
- [40] D. B. Williams, A. J. Papworth, and M. Watanabe, "High resolution X-ray mapping in the STEM," *J. Electron Microsc. (Tokyo)*, vol. 51, no. 1, pp. 113–126, 2002.
- [41] A. J. Craven, K. He, L. A. J. Garvie, and T. N. Baker, "Complex heterogenous precipitation in titanium-niobium microalloyed Al-killed HSLA steels -I. (Ti,Nb)(C,N) particles," *Acta mater.*, vol. 48, pp. 3857–3868, 2000.
- [42] R. M. Poths, R. L. Higginson, and E. J. Palmiere, "Complex precipitation behaviour in a microalloyed plate steel," *Scr. Mater.*, vol. 44, pp. 147–151, 2001.
- [43] C. C. Ahn, *Transmission electron energy loss spectrometry in materials science and the EELS atlas*. Darnstadt, Germany: WILEY-VCH Verlag, 2004.
- [44] J. Hillier and R. F. Baker, "Microanalysis by Means of Electrons," *J. Appl. Phys.*, vol. 15, pp. 663–675, 1944.
- [45] D. B. Williams and C. B. Carter, "The Transmission Electron Microscope," in

- Transmission Electron Microscopy*, Boston, MA: Springer US, 1996, pp. 3–17.
- [46] S. Subramanian, G. Clark, K. Ly, and T. Chrasteky, “Energy-filtered transmission electron microscopy (EFTEM) of Semiconductor Devices,” *Electron. Device Fail. Anal.*, vol. 13, no. 1, pp. 20–28, 2011.
- [47] J. Verbeeck, D. Van Dyck, and G. Van Tendeloo, “Energy-filtered transmission electron microscopy: an overview,” *Spectrochim. Acta Part B At. Spectrosc.*, vol. 59, no. 10, pp. 1529–1534, 2004.
- [48] Å. Gustafson and M. Hättestrand, “Coarsening of precipitates in an advanced creep resistant 9% chromium steel—quantitative microscopy and simulations,” *Mater. Sci. Eng. A*, vol. 333, no. 1–2, pp. 279–286, 2002.
- [49] P. Hofer, H. Cerjak, and P. Warbichler, “Quantification of precipitates in a 10%Cr steel using TEM and EFTEM,” *Mater. Sci. Technol.*, vol. 16, pp. 1221-1225, 2013.
- [50] O. L. Krivanek, M. K. Kundmann, and K. Kimoto, “Spatial resolution in EFTEM elemental maps,” *J. Microsc.*, vol. 180, no. 3, pp. 277–287, 1995.
- [51] B. Schaffer, W. Grogger, G. Kothleitner, and F. Hofer, “Comparison of EFTEM and STEM EELS plasmon imaging of gold nanoparticles in a monochromated TEM.”, *Ultramicroscopy*, vol. 110, pp. 1087-1093, 2010.
- [52] C. Jeanguillaume and C. Colliex, “Spectrum-image: The next step in EELS digital acquisition and processing,” *Ultramicroscopy*, vol. 28, no. 1–4, pp. 252–257, 1989.
- [53] J. Scott *et al.*, “Near-simultaneous dual energy range EELS spectrum imaging,” *Ultramicroscopy*, vol. 108, no. 12, pp. 1586–1594, 2008.
- [54] R. F. Egerton, “Quantitative analysis of electron-energy-loss spectra,” *Ultramicroscopy*, vol. 28, no. 1–4, pp. 215–225, 1989.
- [55] F. Hofer, “Determination of inner-shell cross-sections for EELS- quantification,” *Microsc. Microanal. Microstruct.*, vol. 2, pp. 215–230, 1991.
- [56] C. Allison, W. S. Williams, and M. P. Hoffman, “Quantitative electron energy loss spectroscopy of vanadium carbide,” *Ultramicroscopy*, vol. 13, no. 3, pp. 253–263, 1984.
- [57] E. Courtois, T. Epicier, and C. Scott, “EELS study of niobium carbo-nitride nano-precipitates in ferrite,” *Micron*, vol. 37, pp. 492–502, 2006.
- [58] B. Deconlhout *et al.*, “Investigation of some selected metallurgical problems with the tomographic atom probe,” *Appl. Surf. Sci.*, vol. 76/77, pp. 145–154, 1994.
- [59] J. A. Panitz, “Imaging atom-probe mass spectroscopy,” *Prog. Surf. Sci.*, vol. 8, pp. 219–262, 1978.
- [60] M. Thuvander, M. Andersson, and K. Stiller, “Atom probe tomography investigation of lath boundary segregation and precipitation in a maraging stainless steel,” *Ultramicroscopy*, vol. 132, pp. 265–270, 2013.

- [61] M. Nöhrer, S. Zamberger, S. Primig, and H. Leitner, "Atom probe study of vanadium interphase precipitates and randomly distributed vanadium precipitates in ferrite," *Micron*, vol. 54–55, pp. 57–64, 2013.
- [62] M. Kapoor, R. O'malley, and G. B. Thompson, "Atom probe tomography study of multi-microalloyed carbide and carbo-nitride precipitates and the precipitation sequence in Nb-Ti HSLA steels," *Metall. Mater. Trans. A*, vol. 47, pp. 1984–1995, 2016.
- [63] R. Rementeria *et al.*, "Carbon concentration measurements by atom probe tomography in the ferritic phase of high-silicon steels," *Acta Mater.*, vol. 125, pp. 359–368, 2017.
- [64] A. J. Craven, M. MacKenzie, A. Cerezo, T. Godfrey, and P. H. Clifton, "Spectrum imaging and three-dimensional atom probe studies of fine particles in a vanadium micro-alloyed steel," *Mater. Sci. Technol.*, vol. 24, no. 6, pp. 641–650, 2008.
- [65] J. Melngailis, "Focused ion beam technology and applications," *J. Vac. Sci. Technol. B Microelectron. Nanom. Struct.*, vol. 5, no. 2, p. 469, 1987.
- [66] V. E. Krohn and G. R. Ringo, "Ion source of high brightness using liquid metal," *Cit. Appl. Phys. Lett.*, vol. 27, p. 479, 1975.
- [67] S. M. Kellogg *et al.*, "High throughput sample preparation and analysis using an Inductively coupled plasma (ICP) focused ion beam source," *Microsc. Microanal.*, vol. 16, p. 222, 2018.
- [68] R. Kelley *et al.*, "Xe<sup>+</sup> FIB milling and measurement of amorphous silicon damage," *Microsc. Microanal.*, vol. 19, no. 2, 2018.
- [69] T. L. Burnett *et al.*, "Large volume serial section tomography by Xe Plasma FIB dual beam microscopy," *Ultramicroscopy*, vol. 161, pp. 119–129, 2015.
- [70] M. H. F. Overwijk, "Novel scheme for the preparation of transmission electron microscopy specimens with a focused ion beam," *J. Vac. Sci. Technol. B Microelectron. Nanom. Struct.*, vol. 11, no. 6, pp. 2021, 1993.
- [71] S. Bals, W. Tirry, R. Geurts, Z. Yang, and D. Schryvers, "High-quality sample preparation by low kV FIB thinning for analytical TEM measurements," *Microsc. Microanal.*, vol. 13, pp. 80–86, 2007.
- [72] M. Schaffer, B. Schaffer, and Q. Ramasse, "Sample preparation for atomic-resolution STEM at low voltages by FIB," *Ultramicroscopy*, vol. 114, pp. 62–71, 2012.
- [73] J. P. Mccaffrey, M. W. Phaneuf, and L. D. Madsen, "Surface damage formation during ion-beam thinning of samples for transmission electron microscopy," *Ultramicroscopy*, vol. 87, pp. 97-104, 2001.
- [74] N. I. Kato, "Reducing focused ion beam damage to transmission electron microscopy samples.," *J. Electron Microsc. (Tokyo).*, vol. 53, no. 5, pp. 451–8, 2004.
- [75] B. W. Arey *et al.*, "Advantages of using Plasma FIB Over a Gallium LMIS Source,"

- Microsc. Microanal*, vol. 21, no. 0999, pp. 2015, 2001.
- [76] J. R. Michael, "Focused ion beam induced microstructural alterations: texture development, grain growth, and intermetallic formation," *Microsc. Microanal*, vol. 17, pp. 386–397, 2011.
- [77] N. S. Smith *et al.*, "High brightness inductively coupled plasma source for high current focused ion beam applications," *Cit. J. Vac. Sci. Technol. B*, vol. 24, pp. 2902, 2006.
- [78] N. S. Smith *et al.*, "Focused ion beam technology and applications," *Metrol. J. Vac. Sci. Technol. B Microelectron. Nanom. Struct. Process. Meas. Phenom.*, vol. 24, pp. 2871, 2006.
- [79] J. Jiruše, T. Hrncir, F. Lopour, M. Zadražil, A. Delobbe, and O. Salord, "Combined plasma FIB-SEM," *Microsc. Microanal.*, vol. 18, pp. 652–653, 2012.
- [80] M. K. Miller, K. F. Russell, and G. B. Thompson, "Strategies for fabricating atom probe specimens with a dual beam FIB," *Ultramicroscopy*, vol. 102, pp. 287–298, 2005.
- [81] K. Thompson, D. Lawrence, D. J. Larson, J. D. Olson, T. F. Kelly, and B. Gorman, "In situ site-specific specimen preparation for atom probe tomography," *Ultramicroscopy*, vol. 107, no. 2–3, pp. 131–139, 2007.
- [82] E. Ruska, "The development of the electron microscope and of electron microscopy," *Rev. Mod. Phys.*, vol. 59, no. 3, pp. 627–638, 1987.
- [83] A. N. Broers, "Electron Gun Using a Field Emission Source Review of Scientific Instruments," *Lanthanum Hexaboride Electron Emit. J. Appl. Phys.*, vol. 38, p. 44, 1967.
- [84] A. V. Crewe, D. N. Eggenberger, J. Wall, and L. M. Welter, "Electron gun using a field emission source," *Nanotechnol. Microelectron. Mater. Process. Meas. Phenom.*, vol. 39, no. 4, p. 5248, 1968.
- [85] S. J. Pennycook and D. E. Jesson, "High-resolution Z-contrast imaging of crystals," *Ultramicroscopy*, vol. 37, pp. 14–38, 1991.
- [86] J. M. Cowley, "Secondary electron emission in the scanning electron microscope," *A High-Resolution Scanning Transm. Electron Microsc. J. Appl. Phys.*, vol. 15, p. 20, 1969.
- [87] O. Scherzer, "The Theoretical resolution limit of the electron microscope," *J. Appl. Phys.*, vol. 20, no. 1, pp. 20–29, 1949.
- [88] M. Lentzen, "Progress in aberration-corrected high-resolution transmission electron microscopy using hardware aberration correction," *Microsc. Microanal*, vol. 12, pp. 191–205, 2006.
- [89] O. L. Krivanek *et al.*, "High-energy-resolution monochromator for aberration-corrected scanning transmission electron microscopy/electron energy-loss spectroscopy," *Philos. Trans. A. Math. Phys. Eng. Sci.*, vol. 367, no. 1903, pp. 3683–97, 2009.

- [90] I. Daberkow, K.-H. Herrmann, L. Liu, W. D. Rau, and H. Tietz, "Development and performance of a fast fibre-plate coupled CCD camera at medium energy and image processing system for electron holography," *Ultramicroscopy*, vol. 64, no. 1–4, pp. 35–48, 1996.
- [91] O. L. Krivanek *et al.*, "Vibrational spectroscopy in the electron microscope," *Nature*, vol. 514, no. 7521, pp. 209–212, 2014.
- [92] A. J. Craven and L. A. Garvie, "Electron energy loss near edge structure (ELNES) on the carbon K-edge in transition metal carbides with the rock salt structure," *Microsc. Microanal. Microstruct.*, vol. 6, pp. 89–98, 1995.
- [93] T. Manoubi, M. Tence, and C. Colliex, "Quantification of white lines in electron energy loss spectroscopy (EELS)," *Ultramicroscopy*, vol. 28, pp. 49–55, 1989.
- [94] R. F. Egerton and Z. L. Wang, "Plural-scattering deconvolution of electron energy-loss spectra recorded with an angle-limiting aperture," *Ultramicroscopy*, vol. 32, no. 2, pp. 137–147, 1990.
- [95] A. J. Craven, J. Bobynko, B. Sala, and I. Maclaren, "Accurate measurement of absolute experimental inelastic mean free paths and EELS differential cross-sections," *Ultramicroscopy*, vol. 170, 2016.
- [96] A. Gubbens *et al.*, "The GIF Quantum, a next generation post-column imaging energy filter," *Ultramicroscopy*, vol. 110, no. 8, pp. 962–970, 2010.
- [97] J. Bobynko, I. MacLaren, and A. J. Craven, "Spectrum imaging of complex nanostructures using DualEELS: I. digital extraction replicas," *Ultramicroscopy*, vol. 149, pp. 9–20, 2015.
- [98] G. Lucas, P. Burdet, M. Cantoni, and C. Hébert, "Multivariate statistical analysis as a tool for the segmentation of 3D spectral data," *Micron*, pp. 49–56, 2013.
- [99] M. Bosman, M. Watanabe, D. T. L. Alexander, and V. J. Keast, "Mapping chemical and bonding information using multivariate analysis of electron energy-loss spectrum images," *Ultramicroscopy*, vol. 106, pp. 1024–1032, 2006.
- [100] J. Spiegelberg and J. Ruzs, "Can we use PCA to detect small signals in noisy data?," *Ultramicroscopy*, vol. 172, pp. 40–46, 2017.
- [101] S. Lichtert and J. Verbeeck, "Statistical consequences of applying a PCA noise filter on EELS spectrum images," *Ultramicroscopy*, vol. 125, pp. 35–42, 2013.
- [102] P. J. Thomas and P. A. Midgley, "Image-spectroscopy-II. The removal of plural scattering from extended energy-filtered series by Fourier deconvolution," 2001.
- [103] B. G. Williams, "Electron energy-loss spectroscopy," *Prog. Solid State Chem.*, vol. 17, no. 2, pp. 87–143, 1987.
- [104] M. Tence, M. Quartuccio, and C. Colliex, "PEELS compositional profiling and mapping at nanometer spatial resolution," *Ultramicroscopy*, vol. 58, pp. 42–54, 1995.

- [105] A. J. Craven, B. Sala, J. Bobynko, and I. MacLaren, "Spectrum imaging of complex nanostructures using DualEELS: II. Absolute quantification using standards," *Ultramicroscopy*, vol. 186, pp. 66–81, 2018.
- [106] J. A. Hunt, M. M. Disko, S. K. Behal, and R. D. Leapman, "Electron energy-loss chemical imaging of polymer phases," *Ultramicroscopy*, vol. 58, pp. 55–64, 1995.
- [107] S. S. Hansen, J. B. Vander Sande, and M. Cohen, "Niobium carbonitride precipitation and austenite recrystallization in hot-rolled microalloyed steels," *Metall. Trans. A*, vol. 11, no. 3, pp. 387–402, 1980.
- [108] J. A. Wilson and A. J. Craven, "Improving the analysis of small precipitates in HSLA steels using a plasma cleaner and ELNES," *Ultramicroscopy*, vol. 94, pp. 197–207, 2003.
- [109] M. K. Miller and E. A. Kenik, "Atom probe tomography: a technique for nanoscale characterization," *Microsc. Microanal.*, vol. 10, pp. 336–341, 2004.
- [110] F. Hofer, W. Grogger, P. Warbichler, and I. Papst, "Quantitative energy-filtering transmission electron microscopy (EFTEM)," *Mikrochim. A*, vol. 132, pp. 273–288, 2000.
- [111] P. Warbichler, F. Hofer, P. Hofer, and E. Letofsky, "On the application of energy-filtering TEM in materials science: III. Precipitates in steel," *Micron*, vol. 29, no. 1, pp. 63–72, 1998.
- [112] M. Hättestrand and H. O. Andrén, "Evaluation of particle size distributions of precipitates in a 9% chromium steel using energy filtered transmission electron microscopy," *Micron*, vol. 32, pp. 789–797, 2001.
- [113] E. M. Linares, C. A. P. Leite, L. F. Valadares, C. A. Silva, C. A. Rezende, and F. Galembeck, "Molecular mapping by low-energy-loss-energy-filtered transmission electron microscopy imaging," *Anal. Chem.*, vol. 81, no. 6, pp. 2317–2324, 2009.
- [114] L. F. Valadares, F. do Carmo Braganca, C. A. da Silva, C. A. P. Leite, and F. Galembeck, "Low-energy loss EFTEM imaging of thick particles and aggregates," *J. Colloid Interphase Sci.*, vol. 309, pp. 140–148, 2007.
- [115] K. J. Annand, I. MacLaren, and M. Gass, "Utilising DualEELS to probe the nanoscale mechanisms of the corrosion of Zircaloy-4 in 350 °C pressurised water," *J. Nucl. Mater.*, vol. 465, pp. 390–399, 2015.
- [116] H. W. Yen, C. Y. Chen, T. Y. Wang, C. Y. Huang, and J. R. Yang, "Orientation relationship transition of nanometre sized interphase precipitated TiC carbides in Ti bearing steel," *Mater. Sci. Technol.*, vol. 26, no. 4, pp. 421–430, 2010.
- [117] R. F. Egerton and S. C. Cheng, "Measurement of local thickness by electron energy-loss spectroscopy," *Ultramicroscopy*, vol. 21, pp. 231–244, 1987.
- [118] C. E. I. C. Ohlund, E. Schlangen, and S. Erik Offerman, "The kinetics of softening and microstructure evolution of martensite in Fe–C–Mn steel during tempering at

- 300 °C.," *Mater. Sci. Eng. A*, vol. 560, pp. 351–357, 2013.
- [119] R. F. Egerton, "Quantitative Analysis of Energy-Loss Data," in *Electron Energy-Loss Spectroscopy in the Electron Microscope*, Boston, MA: Springer US, 2011, pp. 231–291.
- [120] R. D. Leapman, P. Rez, and D. F. Mayers, "K, L, and M shell generalized oscillator strengths and ionization cross sections for fast electron collisions," *J. Chem. Phys.*, vol. 72, no. 2, pp. 1232–1243, 1980.
- [121] R. F. Egerton, "Oscillator-strength parameterization of inner-shell cross sections," *Ultramicroscopy*, vol. 50, no. 1, pp. 13–28, 1993.
- [122] D. Rez and P. Rez, "The contribution of discrete transitions to integrated inner shell ionisation cross sections," *Microsc. Microanal.*, vol. 3, pp. 433–442, 1992.
- [123] R. F. Egerton, "Inner-Shell Energies and Edge Shapes," in *Electron Energy-Loss Spectroscopy in the Electron Microscope*, Boston, MA: Springer US, 2011, pp. 423–426.
- [124] G. Kothleitner, W. Grogger, M. Dienstleder, and F. Hofer, "Linking TEM analytical spectroscopies for an assumptionless compositional analysis," *Microsc. Microanal.*, vol. 20, pp. 678–686, 2014.
- [125] B. G. Mendis, M. Mackenzie, and A. J. Craven, "A new analytical method for characterising the bonding environment at rough interfaces in high-k gate stacks using electron energy loss spectroscopy," *Ultramicroscopy*, vol. 110, pp. 105–117, 2010.
- [126] K. Iakoubovskii, K. Mitsuishi, Y. Nakayama, and K. Furuya, "Thickness measurements with electron energy loss spectroscopy," *Microsc. Res. Tech.*, vol. 71, no. 8, pp. 626–631, 2008.
- [127] J. Bobynko, "Characterisation and absolute quantification of nanosized V and Nb precipitates in high manganese steel using DualEELS," University of Glasgow, 2017.
- [128] M. K. Miller and K. F. Russell, "Atom probe specimen preparation with a dual beam FIB" *19th International Vacuum Nanoelectronics Conference*, 2006, pp. 147–148.
- [129] H. J. Goldschmidt, *Interstitial Alloys*. Boston, MA: Elsevier Science, 2013.
- [130] W. Lengauer *et al.*, "Solid state properties of group IVb carbonitrides," 1995.
- [131] J. Billingham, P. S. Bell, and M. H. Lewis, "Vacancy short-range order in substoichiometric transition metal carbides and nitrides with the NaCl structure. I. Electron diffraction studies of short-range ordered compounds," *Acta Crystallogr. Sect. A*, vol. 28, no. 6, pp. 602–606, 1972.
- [132] M. MacKenzie, A. J. Craven, and C. L. Collins, "Nanoanalysis of very fine VN precipitates in steel," *Scripta Materialia*, vol. 54, pp. 1-5, 2006.
- [133] J. Wilson and A. Craven, "Improving the analysis of small precipitates in HSLA steels

- using a plasma cleaner and ELNES," *Ultramicroscopy*, vol. 94, no. 3–4, pp. 197–207, 2003.
- [134] A. J. Craven, B. Sala, J. Bobynko, and I. MaLaren, "Spectrum imaging of complex nanostructures using DualEELS: II. Absolute quantification using standards," *Ultramicroscopy*, vol. 186, pp. 66–81, 2018.
- [135] A. . Craven, K. He, L. A. . Garvie, and T. . Baker, "Complex heterogeneous precipitation in titanium–niobium microalloyed Al-killed HSLA steels—I. (Ti,Nb)(C,N) particles," *Acta Mater.*, vol. 48, no. 15, pp. 3857–3868, 2000.
- [136] Research Fund for Coal and Steel, "Precipitation in high manganese steels (PrecHiMn)," Brussels, 2014.

## Appendix

### 1 – Script to characterise the non-linearity in spectrometer dispersion (by Dr. B. Schaffer)

```
////////////////////////////////////
```

```
// (c) 2018 B.Schaffer, Gatan //
```

```
////////////////////////////////////
```

```
// This script will create a "sweep" ZLP stack
```

```
// in a DEELS acquisition and follows procedures
```

```
// described by A.Craven, Glasgow University.
```

```
////////////////////////////////////
```

```
// Version 05.04.2018: Added time measurement of experiment.
```

```
// Version 26.03.2018: The following changes have been made following testing:
```

```
// -the function Main has changed name to  
CallZLPSweep to avoid potential
```

```
// conflict with other scripts.
```

```
// -When carrying out doShiftToRightCCDRange,  
the value eV to shift
```

```
// has been corrected to be calculated by  
multiplying by, instead of
```

```
// dividing by, the dispersion.
```

```
// -The variable dispVal has been declared as a  
global variable so that
```

```
// it can also be used inside  
HandleDataValueChangedAction to determine
```

```
// when the end of the dispersion range has been  
reached to terminate
```

```
// the experiment.
```

```
// -Result statements have been commented out in  
HandleDataValueChangedAction
```

```

//                                to reduce computation time during high-speed
spectrometer reads.

//                                -The variables maxX1, maxY1, maxX2, maxY2 in
the CallZLPSweep function are

//                                now      declared      before      the
doPerformChannel200Setup conditional statement, to

//                                prevent the variables being declared twice.

//                                -An OKDialog box is called after running
doShiftToRightCCDRange. This prevents

//                                an issue where the max functions on the
following lines read the position of

//                                the ZLP before it is actually shifted.

//                                -The value of variable DTMax has been adjusted
to 2000 to conform to our specs.

//                                -Additional Tags have been added to the images
to keep track of the channel step

//                                and also the right hand buffer size.

// Version 12.01.2018:      First draft, coded and tested on GMS 3.3 with Faux System

//                                Don't expect it to run out-of-the box, in
particular for GMS 2.

//                                No "cleanup" or finishing of tags etc.

////////////////////////////////////

// Instructions:

//      Set up DualEELS live view, i.e. have a running EELS spectroscopy view

//      with low-loss and high-loss both set to exposures that the ZLP does not
saturate.

//      ( Don't use auto-exposure to avoid changes during series acquisition. )

//      Use the dispersion and readout-settings of your choice. The script will

//      just use whatever is in the running VIEW.

```

```

//          Set the drift-tube (shift between LL and HL ) to 0 V.
//          Set EnergyLoss (prism) to 0 V.
//          Align ZLP (with prism "align" or by automatic routine) to have ZLP at channel
200
//          With the view running, start the script.
//          Select Low-Loss and High-Loss View and specify settings, in particular
//          - The StepSize (in channels or eV) the ZLP should be moved in each step
//          - How many update-frames should be "skipped" after a drift-tube
change.
//          This should account for settling time and will need to be
empirical.
//          A dialog will indicate that the acquisition can start (OK button)
//          During acquisition, don't mess with the UI and leave it alone.
//          If it needs to be interrupted, keep SHIFT and CTRL pressed until a dialog
appears
//          and the results window prints that the script ended (and the ListenerObject
has been destroyed.)
//          "Hardcoded" parameters in the script are described below.
////////////////////////////////////
//          NO WARRANTY OF ANY SORTS. USE AT YOUR OWN PERIL.
////////////////////////////////////
number TRUE = 1
number FALSE = 0
number prismDelay_ms = 500
// ms waiting time after setting a prism value
number kFlipAdjust = 1
// use -1 if Energy-Adjust uses flipped sign (GMS 2 vs GMS 3.3 ? Not sure, needs testing )
// For GMS 3.3 using a positive Adjust value shifts the ZLP to the right (higher loss).

```

```

number kRightChannelLimit = 10

// Where to place the initial ZLP counted from right edge, value in channels.

number DTmax = 2000

// Maximum value (eV) the drift-tube can be set. Is it 1000 V ?

number doPerformChannel200Setup = TRUE

// If true, performs step where offset,align and drift-tube are set to 0. Then checks if

// ZLP maximum is (close to) channel 200 in both cases. If not: Align your system that it is

// there for those values, i.e. use align and "nullify" it once the alignment is done.

number doShiftToRightCCDRange = TRUE

// If true, places the ZLP at wanted initial position on the right hand side of the CCD.

// If set to false (and the above also set to false) the script should be started after manually

// setting the system to have the ZLP at wanted position.

number dispVal

//declaring this as global so it can be read in the listener function

number StartTick, EndTick

// Measure experiment time

class CViewListener

{

    number eIID1, srcImgID1, dstImgID1

    number srcImgID2, dstImgID2

    number nSkip, nHit, bStarted, nPos, nCh

    number keepShiftAdjust

    number dEV

    ~CViewListener( object self ) { Result( "\n ListenerObject destructed." ); OKDialog(
"Acquisition complete"); }

    object AddListener( object self, image src1, image dst1, image src2, image dst2,
number deltaEV, number skipCounter )

```

```

    {
        if ( !src1.ImageIsValid() || !dst1.ImageIsValid() ) Throw( "Invalid input images"
    )

        if ( !src2.ImageIsValid() || !dst2.ImageIsValid() ) Throw( "Invalid input images"
    )

        if ( src1.ImageGetDimensionSize(0) != dst1.ImageGetDimensionSize(0) )
Throw( "Invalid input image sizes" )

        if ( src2.ImageGetDimensionSize(0) != dst2.ImageGetDimensionSize(0) )
Throw( "Invalid input image sizes" )

        if ( skipCounter < 0 ) Throw( "Invalid skip counter" )

        keepShiftAdjust = IFGetEnergyOffset( 4 )

        string messagemap = "data_value_changed"      +
":HandleDataValueChangedAction;"

        srcImgID1 = src1.ImageGetID()
        dstImgID1 = dst1.ImageGetID()
        srcImgID2 = src2.ImageGetID()
        dstImgID2 = dst2.ImageGetID()

        nSkip = skipCounter

        nHit = 0

        bStarted = 0

        nPos = 0

        nCh = src1.ImageGetDimensionSize(0)

        dEV = deltaEV

        Debug("\n delta eV:" + deltaEV)

        Debug("\n nSkip:" + nSkip)

        elID1 = src1.ImageAddEventListener( self, messagemap )

        return self
    }

```

```

void EnableListening( object self, number doListen )
{
    bStarted = doListen
}

void RemoveListener( object self )
{
    image src1 := GetImageFromID( srcImgID1 )
    if ( src1.ImageIsValid() )
        src1.ImageRemoveEventListener( eIID1 )
    eIID1 = 0
}

void Finish( object self )
{
    if ( !bStarted ) return
    bStarted = 0
    EndTick = GetHighResTickCount()
    number elapsedTime = ( EndTick - StartTick ) / GetHighResTicksPerSecond()
    Result("\n Finishing ( resetting drift tube and shift ) - duration: " + elapsedTime
+ " sec" )

    self.RemoveListener()
    IFSetEnergyOffset( 3, 0 )
    IFSetEnergyOffset( 4, 0 )
    sleep( prismDelay_ms/1000 )
    image dst1 := GetImageFromID( dstImgID1 )
    if ( dst1.ImageIsValid() )

```

```

        {
            dst1.SetNumberNote( "Test Notes:Elapsed time (sec)",elapsedTime)
            dst1.SetStringNote( "Test Notes:Experiment end" , GetDate() + " @ " +
GetTime(1) )
            dst1.ShowImage()
        }
        image dst2 := GetImageFromID( dstImgID2 )
        if ( dst2.ImageIsValid() )
        {
            dst2.SetNumberNote( "Test Notes:Elapsed time (sec)",elapsedTime)
            dst2.SetStringNote( "Test Notes:Experiment end" , GetDate() + " @ " +
GetTime(1) )
            dst2.ShowImage()
        }
    }
}
Void HandleDataValueChangedAction(object self, number e_fl, Image img )
{
    if ( !bStarted ) return
    if ( OptionDown() && ShiftDown() )
    {
        Result("\n Aborting")
        self.Finish()
    }
    nHit++
    if ( nHit <= nSkip ) return
    nHit = 0
    image dstLL,dstHL,srcLL,srcHL

```

```

Try{
    dstLL := GetImageFromID( dstImgID1 )
    dstHL := GetImageFromID( dstImgID2 )
    srcLL = GetImageFromID( srcImgID1 )      // value copy
    srcHL = GetImageFromID( srcImgID2 )      // value copy
}
catch
{
    self.Finish()
    return
    break;
}
if ( dstLL.ImageGetDimensionSize(1) <= nPos )
{
    self.Finish()
    return
}
dstLL.slice1( 0,nPos,0, 0,nCh,1 ) = srcLL
dstHL.slice1( 0,nPos,0, 0,nCh,1 ) = srcHL
//number maxXHL,maxXLL,maxY
//max( srcLL, maxXLL, maxY )
//max( srcHL, maxXHL, maxY )
//Result("\n #"+nPos+": Maxiumum at @" + maxXLL + " vs " + maxXHL )
nPos++
// Set next shift value
if ( 0 != dEV )

```

```

        {
            number isValue = IFGetEnergyOffset( 3 )

            if ( isValue + dEV <= (DTmax * dispVal ) ) //adjusts DTMax by dispersion
to stop shift dropping of LHS of detector
                {
                    //Result( "\n\n Step #" + nPos + " changing " + dEV + " eV: " +
(isValue+dEV) + " eV" )

                    IFSetEnergyOffset( 3, isValue + dEV ) // Using driftTube
                }
            else
                {
                    Result("\n Warning: Exceeding limits. Will not set new drift tube
value." )

                    self.Finish()

                    return
                }
        }
    }
}

void CallZLPSweep()
{
    // Performing intial checks, asking the user to have
    // everything set up in advance.
    if ( !IFVerifyCommunication() )
        Throw( "No Filter System found." )

    if ( !IFIsInSpectroscopyMode() )
        Throw( "System needs to be in EELS mode" )
}

```

```

image LLview, HLview

if ( !GetTwoLabeledImagesWithPrompt( "Please select the two DEELS view images of
a currently running live View", "Select View images", "low loss", LLview, "high loss", HLview) )

    exit(0)

// Verify the two images are DEELS silblings
tagGroup LLtg = LLview.ImageGetTagGroup()
tagGroup HLtg = HLview.ImageGetTagGroup()

number doDEELS = 0

LLtg.TagGroupGetTagAsBoolean("EELS:Acquisition: Dual acquire enabled", doDEELS )
if ( !doDEELS )

    Throw( "Image '"+LLview.GetLabel()+"' is not a Dual-EELS acquisition image" )

HLtg.TagGroupGetTagAsBoolean("EELS:Acquisition: Dual acquire enabled", doDEELS )
if ( !doDEELS )

    Throw( "Image '"+HLview.GetLabel()+"' is not a Dual-EELS acquisition image" )

number isLL = 0

LLtg.TagGroupGetTagAsBoolean("EELS:Acquisition: Is dual acquire low-loss", isLL )
if ( !isLL )

    Throw( "Image '"+LLview.GetLabel()+"' is not a Dual-EELS acquisition low-loss
image" )

HLtg.TagGroupGetTagAsBoolean("EELS:Acquisition: Is dual acquire low-loss", isLL )
if ( isLL )

    Throw( "Image '"+HLview.GetLabel()+"' is not a Dual-EELS acquisition high-loss
image" )

if ( HLView.ImageGetDimensionSize(0) != LLView.ImageGetDimensionSize(0) )

    Throw( "Size mismatch of the two view images." )

if ( 1 != LLView.ImageGetDimensionSize(1) )

    Throw( "EELS View images needs to be a 1D image" )

```

```

number nChannels = LLView.ImageGetDimensionSize(0)

number nomDispVal = LLView.ImageGetDimensionScale(0)

number LLExp, HLExp

if ( !LLTg.TagGroupGetTagAsNumber( "EELS:Acquisition:Exposure (s)", LLExp ) )
    Throw( "Image "+LLview.GetLabel()+" exposure tag not found" )

if ( !HLTg.TagGroupGetTagAsNumber( "EELS:Acquisition:Exposure (s)", HLExp ) )
    Throw( "Image "+HLview.GetLabel()+" exposure tag not found" )

// Reading current setting

number apNum = IFGetActiveAperture( )

string apStr = IFGetApertureLabel( apNum )

number dispInd = IFGetActiveDispersionIndex( )

string dispStr = IFGetActiveDispersionLabel( )

dispVal = IFGetActiveDispersion( ) // [eV/ch] //this is now declared as a
global variable in line 65

if ( dispVal != nomDispVal )

    OKDialog( "WARNING: The dispersion in the image does not seem to match
the nominal dispersion." )

    number maxX1,maxY1, maxX2,maxY2

    if ( doPerformChannel200Setup )

        {

            if ( !OKCancelDialog( "Ensure DEELS view is running. Setting ZLP to channel
#200 for both views." ) )

                exit(0)

            IFSetEnergyLoss( 0 ) // Whatever is "linked" ( Prism for EELS)

            IFSetEnergyOffset( 1, 0 ) // Prisms offset ("SHIFT")

            IFSetEnergyOffset( 4, 0 ) // Prisms offset ("Align")

```

```

IFSetEnergyOffset( 3, 0 )    // Drift Tube
sleep( prismDelay_ms/1000 )

//number maxX1,maxY1, maxX2,maxY2
max( LLView, maxX1, maxY1 )
max( HLView, maxX2, maxY2 )

Result("\n ZLP positons at nominal 0 eV:")
Result("\n  low - loss : channel #" + maxX1 )
Result("\n  high - loss: channel #" + maxX2 )

if ( ( maxX1 < 190 ) || ( maxX1 > 210 ) )
    Throw( "The low-loss ZLP is not at channel 200. (" + maxX1+ ")" )
if ( ( maxX2 < 190 ) || ( maxX2 > 210 ) )
    Throw( "The high-loss ZLP is not at channel 200. (" + maxX2+ ")" )
}

if ( 0 != IFGetEnergyOffset( 3 ) )    // Drift Tube )
{
    OKDialog( "Adjusting low-loss / high-loss relative shift to 0 eV" )
    IFSetEnergyOffset( 3, 0 )    // Drift Tube
}

number store_prismAdjust = IFGetEnergyOffset( 4 )
if ( doShiftToRightCCDRange )
{
    number  eVtoShift  =  trunc(nChannels-200-kRightChannelLimit)*dispVal
//divide changed to multiple by
    if ( eVtoShift > DTmax )
    {
        OKDialog( "Using the maximum drift tube range (" +DTmax +" eV) for
shifting, but will not reach desired channel." )
    }
}

```

```

        eVToShift = DTmax
    }

    //Shifting ZLP with prism shift (using adjust)
    IFSetEnergyOffset( 4, store_prismAdjust + eVtoShift * kFlipAdjust )//  Prism
offset ("SHIFT")

    IFSetEnergyOffset( 3, 0 )    // Drift Tube
}

OKDialog("Ready?")

//number maxX1,maxY1, maxX2,maxY2
max( LLView, maxX1, maxY1 )
max( HLView, maxX2, maxY2 )

Result("\n ZLP positons at experiment start:")

Result("\n low - loss : channel #" + maxX1 )
Result("\n high - loss: channel #" + maxX2 )

number ZLPshiftStep_Ch = 5

number ZLPshiftStep_eV

if ( !GetNumber( "Wanted ZLP shift step (channels) ?", ZLPshiftStep_Ch,
ZLPshiftStep_Ch ) )

    exit(0)

ZLPshiftStep_eV = trunc(ZLPshiftStep_Ch) * dispVal

if ( !GetNumber( "Wanted ZLP shift step (eV) (now "+trunc(ZLPshiftStep_Ch)+
channels) ?", ZLPshiftStep_eV, ZLPshiftStep_eV ) )

    exit(0)

ZLPshiftStep_Ch = trunc( ZLPshiftStep_eV / dispVal )

number nSkipFrames = 0

string message = "Current exposures are ( " + LLexp + " / " + HLexp + " )\n"

message += "\n\n Skip how many frames between capture?"

```

```

message += "\n (Maybe settling time for drift tube...)"

If ( !GetNumber( message, LLex<0.01 ? 5 : 1, nSkipFrames ) )

    exit(0)

// Setting up data containers

number nSteps = trunc( maxX2 / ZLPshiftStep_Ch ) + 10

result( "\n Moving the ZLP form channel #" + maxX2 + " left until edge is reached.")

result( "\n Using step size of " + ZLPshiftStep_Ch + " channels ( " + ZLPshiftStep_eV + "
eV)." )

result( "\n Using " + nSteps + " steps maximum." )

image LLstack := LLView.ImageClone()

image HLstack := HLView.ImageClone()

LLstack.ImageResize(2,nChannels,nSteps)

LLstack.ImageSetDimensionCalibration(1,0,1,"#",0)

LLstack.SetName( "Low-loss series" )

LLstack.SetStringNote( "Meta Data:Format","Spectrum image" )

LLstack.SetStringNote( "Meta Data:Signal","EELS" )

LLstack.SetNumberNote( "Test Notes:RHS Buffer" , kRightChannelLimit )

LLstack.SetNumberNote( "Test Notes:ChStep" , ZLPshiftStep_Ch )

LLstack.SetNumberNote( "Test Notes:DTmax" , DTmax )

LLstack.SetNumberNote( "Test Notes:Ch200Setup" , doPerformChannel200Setup )

LLstack.SetNumberNote( "Test Notes:ShiftToRight" , doShiftToRightCCDRange )

LLstack.SetNumberNote( "Test Notes:dispval" , dispVal )

LLstack.SetNumberNote( "Test Notes:Skip Frames" , nSkipFrames )

LLstack.SetStringNote( "Test Notes:Experiment start" , GetDate() + " @ " + GetTime(1)
)

HLstack.ImageResize(2,nChannels,nSteps)

HLstack.ImageSetDimensionCalibration(1,0,1,"#",0)

```

```

HLStack.SetName( "High-loss series" )
HLStack.SetStringNote( "Meta Data:Format","Spectrum image" )
HLStack.SetStringNote( "Meta Data:Signal","EELS" )
HLStack.SetNumberNote( "Test Notes:RHS Buffer",kRightChannelLimit)
HLStack.SetNumberNote( "Test Notes:ChStep" , ZLPshiftStep_Ch )
HLStack.SetNumberNote( "Test Notes:DTmax" , DTmax )
HLStack.SetNumberNote( "Test Notes:Ch200Setup" , doPerformChannel200Setup )
HLStack.SetNumberNote( "Test Notes:ShiftToRight" , doShiftToRightCCDRange )
HLStack.SetNumberNote( "Test Notes:dispval" , dispVal )
HLStack.SetNumberNote( "Test Notes:Skip Frames" , nSkipFrames )
LLStack.SetStringNote( "Test Notes:Experiment start" , GetDate() + " @ " + GetTime(1)
)

LLStack.DisplayAt(300,300)
LLStack.ImageGetImageDisplay(0).ImageDisplaySetCaptionOn(1)
HLStack.DisplayAt(300,600)
HLStack.ImageGetImageDisplay(0).ImageDisplaySetCaptionOn(1)

// Attaching display listeners to view
object VObj = Alloc(CViewListener).AddListener( LLView, LLStack, HLView, HLStack,
ZLPshiftStep_eV, nSkipFrames )

OKDialog( "Start now\n\n Keep SHIFT and CTRL pressed to abort." )

StartTick = GetHighResTickCount()

VObj.EnableListening( 1 )
}

CallZLPSweep()

```

## 2 – Script to measure and correct the spectrometer dispersion non-linearity (by Mr. R. Webster)

```
// $BACKGROUND$

////////////////////////////////////

//          Dispersion Non-Linearity Processing Script

//

//          Robert Webster, April 2018

////////////////////////////////////

////////////////////////////////////

//          ANY GLOBAL PARAMETERS HERE

////////////////////////////////////

////////////////////////////////////

//          EXTRACT ZLP MAPS

////////////////////////////////////

void ZLPGauss()

{

    image LL, HL

    GetTwoLabeledImagesWithPrompt("Choose Input Images","Choose reference Low-
Loss and dispersion High-Loss images. ","Low-Loss",LL,"High-Loss",HL)

    image ref, disp

    ref:= LL.ImageClone()

    disp:= HL.ImageClone()

    number ZLPshiftStepCh = 10 //Ask what the channel step in the experiment was (this
should be implemented as a tag in future)

    taggroup acquitags

    acquitags = LL.ImageGetTagGroup()
```

```

    if(!lacquitags.TaggroupGetTagAsNumber("Test      Notes:ChStep",ZLPshiftStepCh))
if(!GetNumber("Tag not found. How many channels were stepped?", ZLPshiftStepCh,
ZLPshiftStepCh)) exit(0)

    number x, y

    ref.GetSize(x,y)

    number RHSlim = 20 //Ask what the right hand channel limit was in the experiment
(future tag).

    if(!lacquitags.TaggroupGetTagAsNumber("Test      Notes:RHS      Buffer",RHSlim))
if(!GetNumber("Tag not found. What right channel limit was used in acquisition?", RHSlim,
RHSlim)) exit(0)

    //////////////////////////////////////
//          SINGLE CHANNEL PRECISION
    //////////////////////////////////////

    image roughRefCh = ReallImage("Max Pixel Location",4,y,1)
    image roughDispCh = ReallImage("Max Pixel Location",4,y,1)

    //First, we locate the maximum pixel position in each frame and collate
//that in a single image.

    number usedCh = 0

    number i
    for(i=0;i<y;i++)
    {

        number refX, dispX, throwaway

        max(ref.slice1(0,i,0,0,x,1),refX,throwaway)

        max(disp.slice1(0,i,0,0,x,1),dispX,throwaway)

        //result("Peaks found at "+refX+" and "+dispX+"\n")

        roughRefCh.SetPixel(i,0,refX)

        roughDispCh.SetPixel(i,0,dispX)

        if(roughRefCh.GetPixel(i,0)!=0.0) usedCh++

```

```

}

//Having extracted each peak position, want to determine offsets using
//reference positions. Will allow us to calculate deviation
image deviations = Realimage("Pixel Accurate Deviations",4,usedCh,1)
for(i=0;i<usedCh;i++)
{
    if(roughRefCh.GetPixel(i,0)!=0.0)
    {
        //determine the position of the peak relative to its' reference to get
        deviation from ideal conditions
        number dev = roughDispCh.GetPixel(i,0) - roughRefCh.GetPixel(i,0) +
i*ZLPshiftStepCh
        deviations.SetPixel(i,0,dev)
    }
}

deviations.SetName("Single Pixel Deviations")
deviations.FlipHorizontal()
deviations.ImageSetDimensionScale(0,ZLPshiftStepCh)
number origin = mean(roughRefCh[0,0,1,usedCh])-(usedCh)*ZLPshiftStepCh
//changed from (x-RHSlim)-(usedCh-1)*ZLPshiftStepCh
deviations.ImageSetDimensionOrigin(0,origin)
deviations.ImageSetDimensionUnitString(0,"CCD Channels")
deviations.ImageSetIntensityUnitString("# Channel Deviation from linearity")
deviations.ShowImage()

if(!OKCancelDialog("Enhance with sub-pixel precision measurement? (Note, the maps
output by this step are centred on the rough peak position. If using maps for gaussian fit after
script ends, you will need to add the single pixel deviations to the result to obtain the correct
dispersion.")) exit(0)

```

```

////////////////////////////////////
//          SUB-PIXEL PRECISION
////////////////////////////////////

//To execute this, we need to fit a gaussian to each peak to find the centre.

//To do that, we want to shift all the peaks by the expected drift tube offset

//The measured peak positions should then characterise the deviation as before

//The window we want to slice out of the dataset will then be twice this value

number buffer = 0 // increases the window size if necessary to capture all features.

//Note, too large a buffer will result in probing outside the dataset.

number window = 2 * RHSlim + buffer

//We need to set up an image which the windowed slices will be dropped into

image subDisp = ReallImage("Extracted disp ZLPs",4,window,usedCh)

image subRef = ReallImage("Extracted ref ZLPs",4,window,usedCh)

//now we can start transferring data into this image

for(i=0;i<usedCh;i++)

{

    //The next 30 lines provide a set of checks and balances for centering the
window

    //about the rough ZLP position. Ensures that the resultant image can be
properly calibrated

    //and also that no pixels outside the image are referenced.

    number refLow = roughRefCh.GetPixel(i,0) - (window/2)

    number dispLow = roughDispCh.GetPixel(i,0) - (window/2)

    number refHigh = refLow + window

    number disphigh = dispLow + window

    number refPad = 0

    number dispPad = 0

```

```

number refSize = window
number dispSize = window
if(refLow < 0)
{
    refPad = -refLow
    refLow = 0
    refSize = window - refPad
}
if(dispLow < 0)
{
    dispPad = -dispLow
    dispLow = 0
    dispSize = window - dispPad
}
if(refHigh > x)
{
    refSize = window - (refHigh - x)
    refHigh = x
}
if(dispHigh > x)
{
    dispSize = window - (dispHigh - x)
    dispHigh = x
}

```

//Now that we have determined it is safe to pick out and move slices, it's time to do just that

```

    image dispSlice = disp.slice1(dispLow,i,0,0,dispSize,1)
    image refSlice = ref.slice1(refLow,i,0,0,refSize,1)
    subDisp[i,dispPad,i+1,dispSize+dispPad] = dispSlice
    subRef[i,refPad,i+1,refSize+refPad] = refSlice
}

```

//Now that this has been extracted, we want to set up images to have the proper calibration

```

subRef.ImageSetDimensionOrigin(0,-window/2)
subDisp.ImageSetDimensionOrigin(0,-window/2)
subRef.FlipVertical()
subDisp.FlipVertical()
subRef.ImageSetDimensionScale(1,ZLPshiftStepCh)
subRef.ImageSetDimensionOrigin(1,origin)//x-RHSlim-(usedCh-1)*ZLPshiftStepCh)
subDisp.ImageSetDimensionScale(1,ZLPshiftStepCh)
subDisp.ImageSetDimensionOrigin(1,origin)//x-RHSlim-(usedCh-1)*ZLPshiftStepCh)
subDisp.ImageSetDimensionUnitString(1,"CCD Channels")
subRef.SetName("Cropped Reference ZLPs")
subRef.SetStringNote( "Meta Data:Format","Spectrum image" )
subRef.SetStringNote( "Meta Data:Signal","EELS" )
subDisp.SetName("Cropped Dispersion ZLPs")
subDisp.SetStringNote( "Meta Data:Format","Spectrum image" )
subDisp.SetStringNote( "Meta Data:Signal","EELS" )
//subRef.ShowImage()
//subDisp.ShowImage(
image subPixDist := deviations.ImageClone()
number StartTick, EndTick

```

```

StartTick = GetHighResTickCount()

//Implement Gaussian Fit
for(i=0;i<usedCh;i++)
{
    //extract slices
    image RS, DS
    RS:=subRef.slice2(0,i,0,0>window,1,1,1,1).ImageClone()
    DS:=subDisp.slice2(0,i,0,0>window,1,1,1,1).ImageClone()
    image eR:=RS.ImageClone()
    eR=1.0
    image eD := eR.ImageClone()
    number AR, midR, widR, chisqR, convR, AD, midD, widD, chisqD, convD
    convR = 0.00001
    chisqR=1e6
    convD = convR
    chisqD = chisqR
    number DXP, RXP, hold
    number epch = RS.ImageGetDimensionScale(0)
    aR = max(RS,RXP,hold) //amplitude component
    midR = RXP - window/2//xp*scale1+origin1 //center position
    widR = 1/epch //guestimate FWHM
    aD = max(DS,DXP,hold) //amplitude component
    midD = DXP - window/2//xp*scale1+origin1 //center position
    widD = 1/epch //guestimate FWHM
    number okR = FitGaussian(RS,eR,aR,midR,widR,chisqR,convR)
    number okD = FitGaussian(DS,eD,aD,midD,widD,chisqD,convD)
}

```

```

        subPixDist[i,0] = midD - midR + deviations.GetPixel(i,0)

        number prog = round(i/usedCh*100)

        if(remainder(i,floor(usedCh/10))==0) result("ZLP fit is "+prog+"% complete\n")
    }

    subPixDist.SetName("Result of Gaussian Fits")

    subPixDist.ShowImage()

    deviations.DeleteImage()

    EndTick = GetHighResTickCount()

    number elapsedTime = ( EndTick - StartTick ) / GetHighResTicksPerSecond()

    Result("\nZLP Fit complete - duration: " + elapsedTime + " sec\n\n" )
}

////////////////////////////////////
//          RUN FITTING PROCEDURES
////////////////////////////////////

void PolyReg()
{
    //if(!OKCancelDialog("Ensure trend to be fitted is front-most image.)) exit(0)

    image data //:= GetFrontImage().ImageClone()

    GetOneImageWithPrompt("Select image containing measured nonlinearities for
fitting.", "Choose image for fitting.", data)

    image errors := data.ImageClone()

    errors = 1.0

    number chisq = 1e6

    number conv = 1e-8

    image pars:=NewImage("Poly Pars",2,6,1)

    pars = -5

```

```

image parsToFit:=NewImage("tmp",2,6,1)

parsToFit = 1

number ok = FitPolynomial(data, errors, pars, parsToFit, chisq, conv)

pars.SetName("Fit Coefficients")

pars.ShowImage()

image output:=data.ImageClone()

number i,j,scale,orig

orig = data.ImageGetDimensionOrigin(0)

scale = data.ImageGetDimensionScale(0)

for(i=0;i<output.ImageGetDimensionSize(0);i++)
{
    number outval = 0

    for(j=0;j<pars.ImageGetDimensionSize(0);j++)
        outval +=
        (((i*scale)+orig)**j)*pars.GetPixel(j,0)

    output[i,0] = outval
}

output.SetName("Fit Result")

output.ShowImage()

//DeletePersistentNote("EELSDispersion:NonLinFit")

//for(i=0;i<6;i++)

//{

//    SetPersistentNumberNote("EELSDispersion:NonLinFit:a"+i,pars.GetPixel(i,0))

//}

}

void Implement()

{

```

```
Image O_LL, O_HL, R_LL, R_HL, RCE_LL, RCE_HL, RCECI_LL, RCECI_HL, CECI_LL,
CECI_HL
```

```
Image IntensityCorrection,coeffs
```

```
Number sx,sy,sz, c5, c4, c3, c2, c1, c0,l
```

```
String NameO_LL, NameO_HL
```

```
GetThreeLabeledImagesWithPrompt("Choose Spectrum Images & Correction
Coefficients","Select SI's","Low-Loss",O_LL,"High-Loss",O_HL,"Correction
Coefficients",coeffs)
```

```
CECI_LL := O_LL.ImageClone()
```

```
CECI_HL := O_HL.ImageClone()
```

```
//Retrieve polynomial coefficients calculated in previous section
```

```
c0 = coeffs.GetPixel(0,0)
```

```
c1 = coeffs.GetPixel(1,0)
```

```
c2 = coeffs.GetPixel(2,0)
```

```
c3 = coeffs.GetPixel(3,0)
```

```
c4 = coeffs.GetPixel(4,0)
```

```
c5 = coeffs.GetPixel(5,0)
```

```
//GetPersistentNumberNote("EELSDispersion:NonLinFit:a0",c0)
```

```
//GetPersistentNumberNote("EELSDispersion:NonLinFit:a1",c1)
```

```
//GetPersistentNumberNote("EELSDispersion:NonLinFit:a2",c2)
```

```
//GetPersistentNumberNote("EELSDispersion:NonLinFit:a3",c3)
```

```
//GetPersistentNumberNote("EELSDispersion:NonLinFit:a4",c4)
```

```
//GetPersistentNumberNote("EELSDispersion:NonLinFit:a5",c5)
```

```
result("Fit Coeffs c0: "+Format(c0,"%10e")+ " c1: "+Format(c1,"%10e")+ " c2:
"+Format(c2,"%10e")+ " c3: "+Format(c3,"%10e")+ " c4: "+Format(c4,"%10e")+ " c5:
"+Format(c5,"%10e")+ "\n\n")
```

```
//Get original names of spectrum images
```

```
NameO_LL=GetName(O_LL)
```

```

NameO_HL=GetName(O_HL)

//Get dimensions of spectrum images
O_LL.Get3DSize(sx,sy,sz)

//rotate spectrum images to put dispersive direction in slice direction
R_LL = Slice3(O_LL ,sx-1, 0, 0, 2,sz, 1, 1,sy, 1, 0,sx,-1)
R_HL = Slice3(O_HL ,sx-1, 0, 0, 2,sz, 1, 1,sy, 1, 0,sx,-1)

RCE_LL = R_LL.ImageClone()
RCECI_LL = R_LL.ImageClone()
RCE_HL = R_HL.ImageClone()
RCECI_HL = R_HL.ImageClone()

//Make the intensity correction
IntensityCorrection = Slice3(R_LL,0,0,0,0,sz,1,1,sy,1,2,1,1)

//Calculate intensity correction factor according to Jacobian conversion of coordinate
systems

IntensityCorrection=5*c5*icol**4+4*c4*icol**3+3*c3*icol**2+2*c2*icol+c1+1
//(the +1 at the end is effectively bookkeeping

//apply the polynomial interpolation and subsequent intensity correction
I=0
While (I<sx)
{
    //Correct the energy
    Slice3(RCE_LL,0,0,I,0,sz,1,1,sy,1,2,1,1)=WARP(Slice3(R_LL,0,0,I,0,sz,1,1,sy,1,2,1,1),c5*
icol**5+c4*icol**4+c3*icol**3+c2*icol**2+c1*icol+c0+icol,irow)

    Slice3(RCE_HL,0,0,I,0,sz,1,1,sy,1,2,1,1)=WARP(Slice3(R_HL,0,0,I,0,sz,1,1,sy,1,2,1,1),c5
*icol**5+c4*icol**4+c3*icol**3+c2*icol**2+c1*icol+c0+icol,irow)

    //Correct the Intensity

```

```
Slice3(RCECI_LL,0,0,l,0,sz,1,1,sy,1,2,1,1)=Slice3(RCE_LL,0,0,l,0,sz,1,1,sy,1,2,1,1)*IntensityCorrection
```

```
Slice3(RCECI_HL,0,0,l,0,sz,1,1,sy,1,2,1,1)=Slice3(RCE_HL,0,0,l,0,sz,1,1,sy,1,2,1,1)*IntensityCorrection
```

```
l++
```

```
}
```

```
//undo the earlier rotation
```

```
CECI_LL = Slice3(RCECI_LL , 0, 0,sx-1, 2,sx,-1, 1,sy, 1, 0,sz, 1)
```

```
CECI_HL = Slice3(RCECI_HL , 0, 0,sx-1, 2,sx,-1, 1,sy, 1, 0,sz, 1)
```

```
CECI_LL.SetStringNote("Linearisation Coeffs:Original File Name", NameO_LL)
```

```
CECI_LL.SetNumberNote("Linearisation Coeffs:c5", c5)
```

```
CECI_LL.SetNumberNote("Linearisation Coeffs:c4", c4)
```

```
CECI_LL.SetNumberNote("Linearisation Coeffs:c3", c3)
```

```
CECI_LL.SetNumberNote("Linearisation Coeffs:c2", c2)
```

```
CECI_LL.SetNumberNote("Linearisation Coeffs:c1", c1)
```

```
CECI_LL.SetNumberNote("Linearisation Coeffs:c0", c0)
```

```
CECI_HL.SetStringNote("Linearisation Coeffs:Original File Name", NameO_HL)
```

```
CECI_HL.SetNumberNote("Linearisation Coeffs:c5", c5)
```

```
CECI_HL.SetNumberNote("Linearisation Coeffs:c4", c4)
```

```
CECI_HL.SetNumberNote("Linearisation Coeffs:c3", c3)
```

```
CECI_HL.SetNumberNote("Linearisation Coeffs:c2", c2)
```

```
CECI_HL.SetNumberNote("Linearisation Coeffs:c1", c1)
```

```
CECI_HL.SetNumberNote("Linearisation Coeffs:c0", c0)
```

```
//set image name
```

```
SetName(CECI_LL, NameO_LL+" (CorrE)(CorrI)")
```

```
SetName(CECI_HL, NameO_HL+" (CorrE)(CorrI)")
```

```
ShowImage(CECI_LL)
```

```

    ShowImage(CECI_HL)
    if(!OKCancelDialog("Save Linearised Spectrum Images?"))exit(0)
    string dir, LLname, HLname
    GetName(CECI_LL, LLname)
    GetName(CECI_HL, HLname)
    If(!GetDirectoryDialog(dir))exit(0)
    CECI_LL.SaveImage(dir+LLname+".dm3")
    CECI_HL.SaveImage(dir+HLname+".dm3")
    OKdialog("Spectrum images saved.")
}
void Main()
{
    if(OKCancelDialog("Process experimental dispersion spectrum images?")) ZLPGaus()
    if(OKCancelDialog("Proceed with 5th order polynomial fit to non-linearities?"))
PolyReg()
    if(OKCancelDialog("Use fitted nonlinearities to correct a pair of Dual-EELS SI's?"))
Implement()
}
Main()

```

### 3 – Script to quantify the precipitates using their MLLS fit coefficient maps (by Prof. A. J. Craven)

```
//Converts maps of MLLS Fit Coeficients of standards to composition maps
//With Io map and splice ratio map, get atoms per unit area
//With (VTiNb)CN cell size, it gets thickness in unit cells and absolute units.

//*****
*****

//It's very specific to the standards used in the MLLS fit and needs editing to match.

//*****
*****

// This set up for TiC98 VC83 NbC954 VN97 NbN99 C(TiC) C(VC) C(NbC) N(VN) N(NbN) C and
N are corrected for stoichiometry

//

//It should be useable whether the standards have been background subtracted or not.

//

// If not all the standards are used, dummy coefficient maps, which are set to zero can be
used.

//

//An OK dialog to give information on what's required

//This version scales the the intensities of the X/M, v, x, (1-x), y and z maps from 0 to 1 for
 $Ti_xV_vNb_{(1-x-v)}C_yN_z$ 

//THIS VERSION USES ONLY THE TiC, VC AND NbC COEFFICIENT MAPS TO CREATE THE MASK.

//THIS VERSION INCORPORATES A FILTER TO GET A BETTER MASK. IT REQUIRES A FUNCTION
TO PROVIDE THE SMOOTHING FUNCTION

//THIS FUNCTION HAS TO COME BEFORE THE MAIN SCRIPT

//THIS VERSION ADDS Ti, V, Nb, C and N THICKNESS MAPS AND PROFILES

//THIS VERSION LABELS THE LINE PLOTS

//*****
*****
```

NB

```

//          FUNCTION TO PROVIDE A SMOOTHING FILTER

//*****
*****

//This function is taken from page 52 of Bernhard Schaffer's "How to Script" e-book
Image ConvolutionKernelFilter( Image in, Image kernel, Number clipBorder )
{
    Number kx, ky, sx, sy
    GetSize(kernel,kx,ky)
    GetSize(in,sx,sy)
    if ( mod(kx,2) == 0 || mod(ky,2) == 0 )
        Throw( "Invalid kernel image. Odd dimension sizes are required." )
    if ( sx<kx || sy<ky )
        Throw( "Invalid kernel image. Kernel larger than image." )
    Number shiftX = trunc(kx/2)
    Number shiftY = trunc(ky/2)
    Image filtered = ImageClone(in) * 0
    For( Number dy = -shiftY; dy<=shiftY; dy++ )
        For( Number dx = -shiftX; dx<=shiftX; dx++ )
            filtered += in[icol+dx,irow+dy] * Sum(kernel[dx+shiftX,dy+shiftY])
    // Using Sum turns the 'single pixel image expression' into a numeric value.
    Number kSum = Sum(kernel)
    filtered /= ( kSum == 0 ) ? 1 : kSum // Set
kSum to 1 if it is 0. (no normalization)
    if ( clipBorder == 1 )
    // Sets the border pixels to zero
    {
        filtered *= (icol<shiftX) || (icol>=sx-shiftX) ? 0 : 1
    }
}

```

```

        filtered *= (irow<shiftY) || (irow>=sy-shiftY) ? 0 : 1
    }

    return filtered
}

//*****
*****

//          MAIN SCRIPT

//*****
*****

OKdialog("This script uses the MLLS coefficient maps obtained by fitting TiC98, VC83, NbC95,
TiN88, VN97 NbN99,stoichiometric C(TiC) C(VC), C(NbC), N(VN) and N(NbN) cross-sections to
a precipitate spectrum image.\n\nFor standards not used in the fit, dummy coefficient maps,
which are set to zero, can be used.\n\n The script creates maps of metal atoms/area, metal
thickness in unit cells, metal thickness in nm. Maps of v, x, (1-x-v), y, z in TixVvNb(1-x-v)CyNz.
A map of X/M in MX.\n\n It creates a mask of the precipitate position. A smooting filter is
incorporated to improve the mask. The mask is used to exclude the noise in the matrix only
region. The mask and a map of the excluded region are provided\n\nIt creates line profiles a
along a chosen vertical line in the masked maps.\n\nIt offers the option to save all the
results.")

Image TiC, VC, NbC, TiN, VN, NbN, C_TiC_only, C_VC_only, C_NbC_only, N_VN_only,
N_NbN_only, IoMap, SpliceMap

Number xTiC, xVC, xNbC, xTiN, xVN, xNbN, aTiVNbCN, Dispersion, TimeHigh, TimeLow

String NameTiC, NameVC, NameNbC, NameTiN, NameVN, NameNbN, NameC_TiC_only,
NameC_VC_only, NameC_NbC_only, NameN_VN_only, NameN_NbN_only, NameIoMap,
NameSpliceMap, FileIdentifier

//*****
*****

//          Input the data

//*****
*****

// Get the maps

```

```

GetThreeLabeledImagesWithPrompt("Select the three binary carbide maps","Enter
Data","TiC98 map", TiC,"VC83 map",VC,"NbC95 map",NbC)

GetThreeLabeledImagesWithPrompt("Select the three binary nitride maps","Enter
Data","TiN88 map", TiN,"VN97 map",VN,"NbN99 map",NbN)

GetThreeLabeledImagesWithPrompt("Select the three stoichiometric C maps","Enter
Data","Stoich C(TiC) map)", C_TiC_only,"Stoich C(VC) map)", C_VC_only,"Stoich C(NbC)
map",C_NbC_only)

GetTwoLabeledImagesWithPrompt("Select the two stoichiometric N maps","Enter
Data","Stoich N(VN) map)", N_VN_only,"Stoich N(NbN) map)", N_NbN_only)

GetTwoLabeledImagesWithPrompt("Io map, Splice map","Enter Data","Io map",
IoMap,"Splice map",SpliceMap)

//Get the substoichiometries for the standards

GetNumber("Stoichiometry TiC",0.98,xTiC)

GetNumber("Stoichiometry VC",0.83,xVC)

GetNumber("Stoichiometry NbC",0.954,xNbC)

GetNumber("Stoichiometry TiN",0.88,xTiN)

GetNumber("Stoichiometry VN",0.97,xVN)

GetNumber("Stoichiometry NbN",0.99,xNbN)

//Get the core loss and low loss acquisition times

GetNumber("Core Loss Aquisition time",40,TimeHigh)

GetNumber("Low Loss Acquistion Time",1,TimeLow)

//Get the lattice parameter of the TiNbC cell. Use linear interpolation from Goldschmidt data

GetNumber("TiVNbCN lattice parameter nm",0.44664,aTiVNbCN)

//Get the spectrum dispersion in eV/channel

GetNumber("Dispersion eV/Ch",0.5,Dispersion)

//Get the identifier to insert in the file names

GetString("Enter the identifier for the file name", "Blobby2 011",FileIdentifier)

//*****
*****

```

```

//          Get the File names

//*****
*****

NameTiC=GetName(TiC)

NameVC=GetName(VC)

NameNbC=GetName(NbC)

NameTiN=GetName(TiN)

NameVN=GetName(VN)

NameNbN=GetName(NbN)

NameC_TiC_only=GetName(C_TiC_only)

NameC_VC_only=GetName(C_VC_only)

NameC_NbC_only=GetName(C_NbC_only)

NameN_VN_only=GetName(N_VN_only)

NameN_NbN_only=GetName(N_NbN_only)

NameIoMap=GetName(IoMap)

NameSpliceMap=GetName(SpliceMap)

//*****
*****

//          Get the Scale Origin and Units

//*****
*****

Number SCx, SCy, Ox, Oy

String Unitxy

//Get the scale origin and units of TiC

GetScale(TiC,SCx,SCy)

GetOrigin(TiC,Ox,Oy)

GetUnitString( TiC,Unitxy)

```

```

//*****
*****

//  Make a mask of the precipitate

//*****
*****

//Clone TiC to preserve the tags and calibration

Image TiVNbCN :=TiC.ImageClone()

//sum TiC, VC,NbC and VN coefficients to get the signal from which to make a mask. Don't
add C-TiC-only, C-VC-only and N-VN-only as they're noisier.

TiVNbCN=TiC+VC+NbC+TiN+VN+NbN

//Name the vertical axis

ImageSetIntensityUnitString(TiVNbCN, "Sum of all MLLS Coeffs")

//Name the file

String nameTiVNbCN

nameTiVNbCN = "Sum of MLLS coefficients "+ FileIdentifier

SetName(TiVNbCN,nameTiVNbCN)

//Add the tags to the map under "Input data"

//File names

TiVNbCN.SetStringNote("Input Data:Data:01 TiC coeff map", NameTiC)

TiVNbCN.SetStringNote("Input Data:Data:01 VC coeff map", NameVC)

TiVNbCN.SetStringNote("Input Data:Data:02 NbC coeff map", NameNbC)

TiVNbCN.SetStringNote("Input Data:Data:02 TiN coeff map", NameTiN)

TiVNbCN.SetStringNote("Input Data:Data:02 VN coeff map", NameVN)

TiVNbCN.SetStringNote("Input Data:Data:02 NbN coeff map", NameNbN)

TiVNbCN.SetStringNote("Input Data:Data:03 C_TiC_only coeff map", NameC_TiC_only)

TiVNbCN.SetStringNote("Input Data:Data:03 C_VC_only coeff map", NameC_VC_only)

TiVNbCN.SetStringNote("Input Data:Data:03 C_NbC_only coeff map", NameC_NbC_only)

```

```

TiVnbcCN.SetStringNote("Input Data:Data:04 N_VN_only coeff map", NameN_VN_only)
TiVnbcCN.SetStringNote("Input Data:Data:03 N_NbN_only coeff map", NameN_NbN_only)
TiVnbcCN.SetStringNote("Input Data:Data:05 Io map", NameIoMap)
TiVnbcCN.SetStringNote("Input Data:Data:06 Splice map", NameSpliceMap)

//Parameters
TiVnbcCN.SetNumberNote("Input Data:Parameter:01 TiC stoichiometry", xTiC)
TiVnbcCN.SetNumberNote("Input Data:Parameter:01 VC stoichiometry", xVC)
TiVnbcCN.SetNumberNote("Input Data:Parameter:02 NbC stoichiometry", xNbC)
TiVnbcCN.SetNumberNote("Input Data:Parameter:02 TiN stoichiometry", xTiN)
TiVnbcCN.SetNumberNote("Input Data:Parameter:02 VN stoichiometry", xVN)
TiVnbcCN.SetNumberNote("Input Data:Parameter:02 NbN stoichiometry", xNbN)
TiVnbcCN.SetNumberNote("Input Data:Parameter:03 Core loss Acquisition Time", TimeHigh)
TiVnbcCN.SetNumberNote("Input Data:Parameter:04 Low loss Acquisition Time", TimeLow)
TiVnbcCN.SetNumberNote("Input Data:Parameter:05 TiVnbcCN Lattice Parameter nm",
aTiVnbcCN)
TiVnbcCN.SetNumberNote("Input Data:Parameter:06 Spectrum Dispersion, eV/ch",
Dispersion)

ShowImage(TiVnbcCN)

//*****
*****

//          WITHIN AN OUTER LOOP SMOOTH THE TiVCN IMAGE

//          WITHIN AN INNER LOOP SET THE THRESHOLD FOR THE MASK

//*****
*****

// Clone TiVnbcCN to get data structures for the smoothed version the mask and the excluded
region with the added tags and calibration

Image TiVnbcCNsmooth :=TiVnbcCN.ImageClone()

SetName(TiVnbcCNsmooth,"TiVnbcCNsmooth "+FileIdentifier)

```

```

Image Mask :=TiVnbcCN.ImageClone()
SetName(Mask,"Mask "+FileIdentifier)
Image Excluded :=TiVnbcCN.ImageClone()
SetName(Excluded,"Region Excluded "+ FileIdentifier)

//Set up the loop parameters
Number FlagSmooth, FlagThreshold
FlagSmooth=0
FlagThreshold=0

//Set up variables to choose a threshold for TERT and use the threshold (inner) loop below to
iterate till acceptable
Number lmax, ThresholdPerCent, ThresholdPerCentPrevious, Threshold

//Set the starting prompt value for the percentage threshold
ThresholdPerCentPrevious=4

//Set up the variables for the smoothing filter
number SizeFilter, SizeFilterPrevious

//Set the starting prompt value for the size of the filter.  Make it 5x5 as default.
SizeFilterPrevious=5

//*****
*****

// USE AN n x n ARRAY OF 1's AS A FILTER TO SMOOTH TiVCN.  n MUST BE ODD.

//*****
*****

//Run the Smoothing (outer) loop till satisfied
While (FlagSmooth ==0)
{
    //Get the size of the filter.  Initial prompt is for unfiltered.

```

GetNumber("Enter an ODD integer for the size of the filter.\n\nCombined with the threshold below, the filter size should be chosen to give a mask with zeros throughout the matrix and a precipitate size that is as large as possible.\n\nThe prompt is the last used value.",SizeFilterPrevious,SizeFilter)

```
//Remember the current filter size

SizeFilterPrevious=SizeFilter

// Generate a filter kernel of odd size populated with 1's
image FilterKernel := ReallImage("Filter",8,SizeFilter,SizeFilter)

//Populate it with 1's
FilterKernel=1

//ShowImage(FilterKernel)

//Call the filter function
TiVnbCNsmooth=ConvolutionKernelFilter(TiVnbCN,FilterKernel,1)

ShowImage(TiVnbCNsmooth)

//*****
*****

//          USE THE SMOOTHED TiVnbCN MAP TO GENERATE THE MASK

//*****
*****

//Get max value of map
Imax = Max(TiVnbCNsmooth)

//Run the Threshold loop till satisfied
While (FlagThreshold ==0)
{
    GetNumber("% of max signal to set the threshold at.\n\nThe prompt is
the last used value.",ThresholdPerCentPrevious,ThresholdPerCent)

    ThresholdPerCentPrevious=ThresholdPerCent

    Threshold=Imax*ThresholdPerCent/100
```

```

Mask = TERT(TiVNbCNsmooth>Threshold,1,0)

Excluded = (1-Mask)*TiVNbCN

ShowImage(Excluded)

ShowImage(Mask)

//GetNumber("To try another value of the threshold, enter
0"+"\\n"+"To accept the Mask, enter 1",0,Flag)

FlagThreshold = TwoButtonDialog("Is the threshold satisfactory?
YES\\n\\nIf you wish to change the smoothing filter, click YES and the option will be
provided.\\n\\nNO will allow you to try another threshold with the same smoothing filter."
,"Yes","No")

}

//GetNumber("To try another value of the threshold, enter 0"+"\\n"+"To accept the
Mask, enter 1",0,FlagSmooth)

FlagSmooth = TwoButtonDialog("Is the mask satisfactory? YES\\n\\nIf you wish to
change the smoothing filter, click NO." ,"Yes","No")

FlagThreshold=0

}

//Name the vertical axis

ImageSetIntensityUnitString(Mask, "Mask")

ImageSetIntensityUnitString(Excluded, "Sum of all MLLS Coeffs")

//Add the filter size to the tags

TiVNbCN.SetNumberNote("Input Data:Parameter:07 n for n x n filter kernel", SizeFilter)

TiVNbCNsmooth.SetNumberNote("Input Data:Parameter:07 n for n x n filter kernel",
SizeFilter)

Mask.SetNumberNote("Input Data:Parameter:07 n for n x n filter kernel", SizeFilter)

Excluded.SetNumberNote("Input Data:Parameter:07 n for n x n filter kernel", SizeFilter)

//Add the threshold percentage to the tags

TiVNbCN.SetNumberNote("Input Data:Parameter:08 Mask Threshold as % of max",
ThresholdPerCent)

```

```
TiVNbCNsmooth.SetNumberNote("Input Data:Parameter:08 Mask Threshold as % of max",  
ThresholdPerCent)
```

```
Mask.SetNumberNote("Input Data:Parameter:08 Mask Threshold as % of max",  
ThresholdPerCent)
```

```
Excluded.SetNumberNote("Input Data:Parameter:08 Mask Threshold as % of max",  
ThresholdPerCent)
```

```
//*****  
*****
```

```
// Calculate the coefficients for the metal atoms and their sum
```

```
//*****  
*****
```

```
//Calculate the total Ti
```

```
//Clone TiVNbCN to get the tags and scales
```

```
Image Ti :=TiVNbCN.ImageClone()
```

```
Ti=TiC+TiN
```

```
SetName(Ti,"Ti " + FileIdentifier)
```

```
//ShowImage(Ti)
```

```
//Calculate the total V
```

```
//Clone TiVNbCN to get the tags and scales
```

```
Image V :=TiVNbCN.ImageClone()
```

```
V= VC+VN
```

```
SetName(V,"V " + FileIdentifier)
```

```
//ShowImage(V)
```

```
//Calculate the total Nb
```

```
//Clone TiNbCN to get the tags and scales
```

```
Image Nb :=TiVNbCN.ImageClone()
```

```
Nb= NbC+NbN
```

```
SetName(Nb,"Nb " + FileIdentifier)
```

```

//ShowImage(Nb)

//Calculate total metal

//Clone TiNbCN to get the tags and scales
Image TiVNb :=TiVNbCN.ImageClone()

TiVNb=Ti+V+Nb

SetName(TiVNb,"TiVNb " + FileIdentifier)

//ShowImage(TiVNb)

//*****
*****

//Convert the sum of the metal atoms to thickness

//*****
*****

//Calculate (Ti+V+Nb) atoms/nm^2 in ppt

//Clone TiVNbCN to get the tags and scales
Image TiVNb_AtomsPerArea :=TiVNbCN.ImageClone()

//1 barn is 10E-28m2  1nm2 is 10-18nm2  Conversion factor is 1E10

//Have to divide by the dispersion in eV per channel because the cross-sections are in
barns/eV

//Have to mutiply Io by (Time Ratio)/ (Splice Ratio)

TiVNb_AtomsPerArea=TiVNb/(IoMap*TimeHigh/TimeLow/SpliceMap)/Dispersion*1E10

SetName(TiVNb_AtomsPerArea,"TiVNb_AtomsPerNm2 " + FileIdentifier)

ImageSetIntensityUnitString(TiVNb_AtomsPerArea, "Ti+V+Nb Metal Atoms/nm2")

ShowImage(TiVNb_AtomsPerArea)

//Calculate (Ti+V+Nb) thickness in ppt in unit cells

//Clone TiVNbCN to get the tags and scales
Image TiVNb_Thickness_UnitCells :=TiVNbCN.ImageClone()

//Divide by atoms/nm2 in the cell i.e 4/(cell paprameter)^2

```

```

TiVNb_Thickness_UnitCells=TiVNb_AtomsPerArea/4*aTiVNbCN*aTiVNbCN
SetName(TiVNb_Thickness_UnitCells,"Ti+V+Nb Thickness in unit cells " + FileIdentifier)
ImageSetIntensityUnitString(TiVNb_Thickness_UnitCells, "Ti+V+Nb Thickness (unit cells)")
ShowImage(TiVNb_Thickness_UnitCells)

//Calculate (Ti+V+Nb) thickness in ppt in nm
//Clone TiNbCN to get the tags and scales
Image TiVNb_Thickness_nm :=TiVNbCN.ImageClone()

//Multiply thickness in unit cells by cell size
TiVNb_Thickness_nm=TiVNb_Thickness_UnitCells*aTiVNbCN
SetName(TiVNb_Thickness_nm,"Ti+V+Nb Thickness in nm " + FileIdentifier)
ImageSetIntensityUnitString(TiVNb_Thickness_nm, "Ti+V+Nb Thickness (nm)")
ShowImage(TiVNb_Thickness_nm)

//*****
*****

//Calculate the individual non-metal signals and their sum

//*****
*****

//Calculate total C
//Clone TiVNbCN to get the tags and scales
Image C :=TiVNbCN.ImageClone()

//C in TiC, VC and NbC needs to be scaled by the stoichiometry but the Conly should be
stoichiometric

C=xTiC*TiC+xVC*VC+xNbC*NbC+C_TiC_only+C_VC_only+C_NbC_only

SetName(C,"C " + FileIdentifier)

//ShowImage(C)

//Calculate total N
//Clone TiVNbCN to get the tags and scales

```

```

Image N :=TiVNbCN.ImageClone()

//Here only stoichiometric N is involved

N=xTiN*TiN+xVN*VN+xNbN*NbN+N_VN_only+N_NbN_only

SetName(N,"N" + FileIdentifier)

//ShowImage(N)

//Calculate total non-metal

//Clone TiVNbCN to get the tags and scales

Image CN :=TiVNbCN.ImageClone()

CN=C+N

SetName(CN,"CN " + FileIdentifier)

//ShowImage(CN)

//*****
*****

//      CALCULATE THE REST OF THE ELEMENTAL THICKNESS PROFILES IN NM

//*****
*****

// Ti thickness map

Image Ti_Thickness_nm :=TiVNbCN.ImageClone()

//1 barn is 10E-28m2  1nm2 is 10-18nm2  Conversion factor is 1E10 to conver to atoms/nm2

//Have to divide by the dispersion in eV per channel because the cross-sections are in
barns/eV

//Have to mutiply Io by (Time Ratio)/ (Splice Ratio)

Ti_Thickness_nm=Ti/(IoMap*TimeHigh/TimeLow/SpliceMap)/Dispersion*1E10

//Divide by atoms/nm2 in the cell i.e 4/(cell parameter)^2

Ti_Thickness_nm=Ti_Thickness_nm/4*aTiVNbCN*aTiVNbCN

//Multiply thickness in unit cells by cell size

Ti_Thickness_nm=Ti_Thickness_nm*aTiVNbCN

```

```

SetName(Ti_Thickness_nm,"Ti_Thickness_nm " + FileIdentifier)
ImageSetIntensityUnitString(Ti_Thickness_nm, "Ti thickness (nm)")
ShowImage(Ti_Thickness_nm)

// V thickness map
Image V_Thickness_nm :=TiVNbCN.ImageClone()

//1 barn is 10E-28m2  1nm2 is 10-18nm2  Conversion factor is 1E10 to conver to atoms/nm2

//Have to divide by the dispersion in eV per channel because the cross-sections are in barns/eV

//Have to mutiPLY Io by (Time Ratio)/ (Splice Ratio)
V_Thickness_nm=V/(IoMap*TimeHigh/TimeLow/SpliceMap)/Dispersion*1E10

//Divide by atoms/nm2 in the cell i.e 4/(cell parameter)^2
V_Thickness_nm=V_Thickness_nm/4*aTiVNbCN*aTiVNbCN

//Multiply thickness in unit cells by cell size
V_Thickness_nm=V_Thickness_nm*aTiVNbCN

SetName(V_Thickness_nm,"V_Thickness_nm " + FileIdentifier)
ImageSetIntensityUnitString(V_Thickness_nm, "V thickness (nm)")
ShowImage(V_Thickness_nm)

// Nb thickness map
Image Nb_Thickness_nm :=TiVNbCN.ImageClone()

//1 barn is 10E-28m2  1nm2 is 10-18nm2  Conversion factor is 1E10 to conver to atoms/nm2

//Have to divide by the dispersion in eV per channel because the cross-sections are in barns/eV

//Have to mutiPLY Io by (Time Ratio)/ (Splice Ratio)
Nb_Thickness_nm=Nb/(IoMap*TimeHigh/TimeLow/SpliceMap)/Dispersion*1E10

//Divide by atoms/nm2 in the cell i.e 4/(cell parameter)^2
Nb_Thickness_nm=Nb_Thickness_nm/4*aTiVNbCN*aTiVNbCN

//Multiply thickness in unit cells by cell size

```

```

Nb_Thickness_nm=Nb_Thickness_nm*aTiVNbCN
SetName(Nb_Thickness_nm,"Nb_Thickness_nm " + FileIdentifier)
ImageSetIntensityUnitString(Nb_Thickness_nm, "Nb thickness (nm)")
ShowImage(Nb_Thickness_nm)

// C thickness map
Image C_Thickness_nm :=TiVNbCN.ImageClone()

//1 barn is 10E-28m2  1nm2 is 10-18nm2  Conversion factor is 1E10 to conver to atoms/nm2

//Have to divide by the dispersion in eV per channel because the cross-sections are in barns/eV

//Have to mutiply Io by (Time Ratio)/ (Splice Ratio)
C_Thickness_nm=C/(IoMap*TimeHigh/TimeLow/SpliceMap)/Dispersion*1E10

//Divide by atoms/nm2 in the cell i.e 4/(cell parameter)^2
C_Thickness_nm=C_Thickness_nm/4*aTiVNbCN*aTiVNbCN

//Multiply thickness in unit cells by cell size
C_Thickness_nm=C_Thickness_nm*aTiVNbCN
SetName(C_Thickness_nm,"C_Thickness_nm " + FileIdentifier)
ImageSetIntensityUnitString(C_Thickness_nm, "C thickness (nm)")
ShowImage(C_Thickness_nm)

// N thickness map
Image N_Thickness_nm :=TiVNbCN.ImageClone()

//1 barn is 10E-28m2  1nm2 is 10-18nm2  Conversion factor is 1E10 to conver to atoms/nm2

//Have to divide by the dispersion in eV per channel because the cross-sections are in barns/eV

//Have to mutiply Io by (Time Ratio)/ (Splice Ratio)
N_Thickness_nm=N/(IoMap*TimeHigh/TimeLow/SpliceMap)/Dispersion*1E10

//Divide by atoms/nm2 in the cell i.e 4/(cell parameter)^2
N_Thickness_nm=N_Thickness_nm/4*aTiVNbCN*aTiVNbCN

```

```

//Multiply thickness in unit cells by cell size
N_Thickness_nm=N_Thickness_nm*aTiVNbCN
SetName(N_Thickness_nm,"N_Thickness_nm " + FileIdentifier)
ImageSetIntensityUnitString(N_Thickness_nm, "N thickness (nm)")
ShowImage(N_Thickness_nm)

// C+N thickness map
Image CN_Thickness_nm :=TiVNbCN.ImageClone()

//1 barn is 10E-28m2  1nm2 is 10-18nm2  Conversion factor is 1E10 to conver to atoms/nm2

//Have to divide by the dispersion in eV per channel because the cross-sections are in barns/eV

//Have to mutiply Io by (Time Ratio)/ (Splice Ratio)
CN_Thickness_nm=CN/(IoMap*TimeHigh/TimeLow/SpliceMap)/Dispersion*1E10

//Divide by atoms/nm2 in the cell i.e 4/(cell parameter)^2
CN_Thickness_nm=CN_Thickness_nm/4*aTiVNbCN*aTiVNbCN

//Multiply thickness in unit cells by cell size
CN_Thickness_nm=CN_Thickness_nm*aTiVNbCN
SetName(CN_Thickness_nm,"CN_Thickness_nm " + FileIdentifier)
ImageSetIntensityUnitString(CN_Thickness_nm, "CN thickness (nm)")
ShowImage(CN_Thickness_nm)

//*****
*****

//          Calculate the elemental ratios

//*****
*****

//Calcuete x, v, (1-x-v) y z in TixVvNb(1-x-v)CyNz and non-metal to metal ratio and mask them

```

```

//Image Tix, Vv NbOneMinusxMinusv, Cy, Nz, XoverM, TixMask, VvMask,
NbOneMinusxMinusvMask, CyMask, NzMask, XoverMMask

string nameTix, nameVv, nameNbOneMinusxMinusv, nameCy, nameNz, nameXoverM

//Calculate x

//Clone TiVNBcCN to get the tags and scales

Image Tix :=TiVNBcCN.ImageClone()

Tix=Ti/TiVNB

nameTix="x in TixVvNb(1-x-v)CyNz " + FileIdentifier

SetName(Tix,nameTix)

ImageSetIntensityUnitString(Tix, "x in TixVvNb(1-x-v)CyNz")

//Take auto-survey intensity off and set the lower limit to 0 and and the upper limit to 1

SetSurvey(Tix,0)

SetLimits (Tix,0,1)

showimage(Tix)

//Apply the mask to the map of x to take out the noise from the matrix region

//Clone TiVCN to get the tags and scales

Image TixMask :=TiVNBcCN.ImageClone()

TixMask=Tix*Mask

nameTix="x in TixVvNb(1-x-v)CyNz MASKED " + FileIdentifier

SetName(TiXMask,nameTix)

ImageSetIntensityUnitString(TixMask, "x in TixVvNb(1-x-v)CyNz")

//Take auto-survey intensity off and set the lower limit to 0 and and the upper limit to 1

SetSurvey(TiXMask,0)

SetLimits (TiXMask,0,1)

showimage(TixMask)

//Calculate v

```

```

//Clone TiVNbCN to get the tags and scales
Image Vv :=TiVNbCN.ImageClone()
Vv=V/TiVNb
nameVv="v in TixVvNb(1-x-v)CyNz " + FileIdentifier
SetName(Vv,nameVv)
ImageSetIntensityUnitString(Vv, "v in TixVvNb(1-x-v)CyNz")
//Take auto-survey intensity off and set the lower limit to 0 and and the upper limit to 1
SetSurvey(Vv,0)
SetLimits (Vv,0,1)
showimage(Vv)
//Apply the mask to the map of x to take out the noise from the matrix region
//Clone TiVCN to get the tags and scales
Image VvMask :=TiVNbCN.ImageClone()
VvMask=Vv*Mask
nameVv="v in TixVvNb(1-x-v)CyNz MASKED " + FileIdentifier
SetName(VvMask,nameVv)
ImageSetIntensityUnitString(VvMask, "v in TixVvNb(1-x-v)CyNz")
//Take auto-survey intensity off and set the lower limit to 0 and and the upper limit to 1
SetSurvey(Vvmask,0)
SetLimits (VvMask,0,1)
showimage(VvMask)
//calculate (1-x-v)
//Clone TiNbcCN to get the tags and scales
Image NbOneMinusxMinusv :=TiVNbCN.ImageClone()
NbOneMinusxMinusv=(1-Tix-Vv)
nameNbOneMinusxMinusv="(1-x-v) in TixVvNb(1-x-v)CyNz" + FileIdentifier

```

```

SetName(NbOneMinusxMinusv,nameNbOneMinusxMinusv)
ImageSetIntensityUnitString(NbOneMinusxMinusv, "(1-x-v) in TixVvNb(1-x-v)CyNz")
//Take auto-survey intensity off and set the lower limit to 0 and and the upper limit to 1
SetSurvey(NbOneMinusxMinusv,0)
SetLimits (NbOneMinusxMinusv,0,1)
showimage(NbOneMinusxMinusv)
//Apply the mask to the map of x to take out the noise from the matrix region
//Clone TiNbCN to get the tags and scales
Image NbOneMinusxMinusvMask :=TiVNbCN.ImageClone()
NbOneMinusxMinusvMask=NbOneMinusxMinusv*Mask
nameNbOneMinusxMinusv="(1-x-v) in TixVvNb(1-x-v)CyNz MASKED " + FileIdentifier
SetName(NbOneMinusxMinusvMask,nameNbOneMinusxMinusv)
ImageSetIntensityUnitString(NbOneMinusxMinusvMask, "(1-x-v) in TixVvNb(1-x-v)CyNz")
//Take auto-survey intensity off and set the lower limit to 0 and and the upper limit to 1
SetSurvey(NbOneMinusxMinusvMask,0)
SetLimits (NbOneMinusxMinusvMask,0,1)
showimage(NbOneMinusxMinusvMask)
//Calculate y
//Clone TiVNbCN to get the tags and scales
Image Cy :=TiVNbCN.ImageClone()
Cy=C/TiVNb
nameCy="y in TixVvNb(1-x-v)CyNz " + FileIdentifier
SetName(Cy,nameCy)
ImageSetIntensityUnitString(Cy, "y in TixVvNb(1-x-v)CyNz")
//Take auto-survey intensity off and set the lower limit to 0 and and the upper limit to 1
SetSurvey(Cy,0)

```

```

SetLimits (Cy,0,1)
showimage(Cy)

//Apply the mask to the map of x to take out the noise from the matrix region

//Clone TiVNBcCN to get the tags and scales
Image CyMask :=TiVNBcCN.ImageClone()
CyMask=Cy*Mask
nameCy="y in TixVvNb(1-x-v)CyNz MASKED " + FileIdentifier
SetName(CyMask,nameCy)
ImageSetIntensityUnitString(CyMask, "y in TixVvNb(1-x-v)CyNz")
SetSurvey(CyMask,0)
SetLimits (CyMask,0,1)
showimage(CyMask)

//calcuete z

//Clone TiVNBcCN to get the tags and scales
Image Nz :=TiVNBcCN.ImageClone()
Nz=N/TiVNB
nameNz="z in TixVvNb(1-x-v)CyNz " + FileIdentifier
SetName(Nz,nameNz)
ImageSetIntensityUnitString(Nz, "z in TixVvNb(1-x-v)CyNz")
SetSurvey(Nz,0)
SetLimits (Nz,0,1)
showimage(Nz)

//Apply the mask to the map of x to take out the noise from the matrix region

//Clone TiVNBcCN to get the tags and scales
Image NzMask :=TiVNBcCN.ImageClone()
NzMask=Nz*Mask

```

```

nameNz="z in TixVvNb(1-x-v)CyNz MASKED " + FileIdentifier
SetName(NzMask,nameNz)
ImageSetIntensityUnitString(NzMask, "z in TixVvNb(1-x-v)CyNz")
SetSurvey(NzMask,0)
SetLimits (NzMask,0,1)
showimage(NzMask)
// calculate X/M
//Clone TiVNbCN to get the tags and scales
Image XoverM :=TiVNbCN.ImageClone()
XoverM=CN/TiVNb
nameXoverM="XoverM in MX " + FileIdentifier
SetName(XoverM,nameXoverM)
ImageSetIntensityUnitString(XoverM, "X/M in MX")
SetSurvey(XoverM,0)
SetLimits (XoverM,0,1)
showimage(XoverM)
//Apply the mask to the map of x to take out the noise from the matrix region
//Clone TiVNbCN to get the tags and scales
Image XoverMMask :=TiVNbCN.ImageClone()
XoverMMask=XoverM*Mask
nameXoverM="XoverM in MX MASKED " + FileIdentifier
SetName(XoverMMask,nameXoverM)
ImageSetIntensityUnitString(XoverMMask, "X/M in MX")
SetSurvey(XoverMMask,0)
SetLimits (XoverMMask,0,1)
showimage(XoverMMask)

```

```

//*****
*****

//          Calculate Line Profiles

//*****
*****

//*****
*****

//          Set up the first one and clone it for the rest

//*****
*****

Image ProfileT
Number Column, top, left, SizeX, SizeY

//Input the column for the profile
GetNumber("Select the column to be profiled",16,Column)

//Get Size of TiC
ClearSelection(TiC)
GetSelection(TiC,top,left,SizeY,SizeX)

//Set up the slicing tool

//The parameters in NewImageDataSlice are

//Dimensions of of image, Dimensions of slice, startX in image,startY in image,
//direction in slice, number of points from image, step size in imageObject Slicelt =
NewImageDataSlice(2,1,Column,0,1,SizeY,1)

Object Slicelt = NewImageDataSlice(2,1,Column,0,1,SizeY,1)

//Calculate profile of Ti+V+Nb Thickness in nm
ProfileT=TiVNb_Thickness_nm[Slicelt]

//Set name and calibration
SetName(ProfileT,"Profile Ti+V+Nb thickness in nm " + FileIdentifier)

ImageSetDimensionScale(ProfileT,0,ScX)

```

```

ImageSetDimensionOrigin(ProfileT,0,OX)
ImageSetDimensionUnitString(ProfileT,0,UnitXY)
ImageSetIntensityUnitString(ProfileT, "(Ti+V+Nb) Metal thickness (nm)")
//Add the tags to the map under "Input data"
//File names
ProfileT.SetStringNote("Input Data:Data:01 TiC coeff map", NameTiC)
ProfileT.SetStringNote("Input Data:Data:02 VC coeff map", NameVC)
ProfileT.SetStringNote("Input Data:Data:01 NbC coeff map", NameNbC)
ProfileT.SetStringNote("Input Data:Data:02 VN coeff map", NameVN)
ProfileT.SetStringNote("Input Data:Data:03 C_VC_only coeff map", NameC_VC_only)
ProfileT.SetStringNote("Input Data:Data:03 C_NbC_only coeff map", NameC_NbC_only)
ProfileT.SetStringNote("Input Data:Data:04 N_VN_only coeff map", NameN_VN_only)
ProfileT.SetStringNote("Input Data:Data:05 Io map", NameIoMap)
ProfileT.SetStringNote("Input Data:Data:06 Splice map", NameSpliceMap)
//Parameters
ProfileT.SetNumberNote("Input Data:Parameter:01 TiC stoichiometry", xTiC)
ProfileT.SetNumberNote("Input Data:Parameter:02 VC stoichiometry", xVC)
ProfileT.SetNumberNote("Input Data:Parameter:01 NbC stoichiometry", xNbC)
ProfileT.SetNumberNote("Input Data:Parameter:02 VN stoichiometry", xVN)
ProfileT.SetNumberNote("Input Data:Parameter:03 Core loss Acquisition Time", TimeHigh)
ProfileT.SetNumberNote("Input Data:Parameter:04 Low loss Acquisition Time", TimeLow)
ProfileT.SetNumberNote("Input Data:Parameter:05 TiVNbC Lattice Parameter nm",
aTiVNbCN)
ProfileT.SetNumberNote("Input Data:Parameter:06 Spectrum Dispersion, eV/ch", Dispersion)
//Also get and add the name of the map profiled
String NameDummy

```

```

NameDummy=GetName(TiVNb_Thickness_nm)
ProfileT.SetStringNote("Input Data:Data:07 Map profiled", NameDummy)
ShowImage(ProfileT)
//Add a label. THIS SHOULD BE A FUNCTION BUT I CAN'T GET IT TO WORK
//Set the variables for the lineplot labelling. These declarations are only needed at the start.
imagedisplay DISP
object SLICEID_0
//Add the foreground plot to the final plot. The next lines will be repeated for each profile
with a change of name.
DISP = ProfileT.ImageGetImageDisplay(0)
DISP.LinePlotImageDisplaySetDoAutoSurvey( 0, 0 )
SLICEID_0 = DISP.ImageDisplayGetSliceIDByIndex(0)
//Show the legend
disp.LinePlotImageDisplaySetLegendShown(1)
//Add the original label to the first slice of the final plot
disp.ImageDisplaySetSliceLabelById( sliceID_0, "(Ti+V+Nb) Thickness (nm)")
//*****
*****
//          Now do the other profiles
//*****
*****
//Calculate profile of Ti+V+Nb Thickness in unit cells
//Clone the first profile to get the calibration and tags
Image ProfileTcells :=ProfileT.ImageClone()
ProfileTcells=TiVNb_Thickness_UnitCells[Slicelt]
//Set name
SetName(ProfileTcells,"Profile Ti+V+Nb thickness in unit cells " + FileIdentifier)

```

```

ImageSetIntensityUnitString(ProfileTCells, "(Ti+V+Nb) Metal thickness (unit cells)")
NameDummy=GetName(TiVNb_Thickness_UnitCells)
ProfileTcells.SetStringNote("Input Data:Data:07 Map profiled", NameDummy)
ShowImage(ProfileTcells)

//Add the foreground plot to the final plot. The next lines will be repeated for each profile
with a change of name.

DISP = ProfileTcells.ImageGetImageDisplay(0)
DISP.LinePlotImageDisplaySetDoAutoSurvey( 0, 0 )
SLICEID_0 = DISP.ImageDisplayGetSliceIDByIndex(0)
//Show the legend
disp.LinePlotImageDisplaySetLegendShown(1)
//Add the original label to the first slice of the final plot
disp.ImageDisplaySetSliceLabelById( sliceID_0, "(Ti+V+Nb) Thickness (Unit Cells)")
//Calculate profile of the Ti Thickness in nm
//Clone the first profile to get the calibration and tags
Image ProfileTi_nm :=ProfileT.ImageClone()
ProfileTi_nm=Ti_Thickness_nm[SliceID]
//Set name
SetName(ProfileTi_nm,"Profile Ti thickness in nm " + FileIdentifier)
ImageSetIntensityUnitString(ProfileTi_nm, "Ti thickness (nm)")
NameDummy=GetName(Ti_Thickness_nm)
ProfileTi_nm.SetStringNote("Input Data:Data:07 Map profiled", NameDummy)
ShowImage(ProfileTi_nm)

//Add the foreground plot to the final plot. The next lines will be repeated for each profile
with a change of name.

DISP = ProfileTi_nm.ImageGetImageDisplay(0)
DISP.LinePlotImageDisplaySetDoAutoSurvey( 0, 0 )

```

```

SLICEID_0 = DISP.ImageDisplayGetSliceIDByIndex(0)

//Show the legend

disp.LinePlotImageDisplaySetLegendShown(1)

//Add the original label to the first slice of the final plot

disp.ImageDisplaySetSliceLabelById( sliceID_0, "Ti Thickness (nm)")

//Calculate profile of the V Thickness in nm

//Clone the first profile to get the calibration and tags

Image ProfileV_nm :=ProfileT.ImageClone()

ProfileV_nm=V_Thickness_nm[Slicelt]

//Set name

SetName(ProfileV_nm,"Profile V thickness in nm " + FileIdentifier)

ImageSetIntensityUnitString(ProfileV_nm, "V thickness (nm)")

NameDummy=GetName(V_Thickness_nm)

ProfileV_nm.SetStringNote("Input Data:Data:07 Map profiled", NameDummy)

ShowImage(ProfileV_nm)

//Add the foreground plot to the final plot.  The next lines will be repeated for each profile
with a change of name.

DISP = ProfileV_nm.ImageGetImageDisplay(0)

DISP.LinePlotImageDisplaySetDoAutoSurvey( 0, 0 )

SLICEID_0 = DISP.ImageDisplayGetSliceIDByIndex(0)

//Show the legend

disp.LinePlotImageDisplaySetLegendShown(1)

//Add the original label to the first slice of the final plot

disp.ImageDisplaySetSliceLabelById( sliceID_0, "V Thickness (nm)")

//Calculate profile of the Nb Thickness in nm

//Clone the first profile to get the calibration and tags

```

```

Image ProfileNb_nm :=ProfileT.ImageClone()
ProfileNb_nm=Nb_Thickness_nm[Slicelt]

//Set name
SetName(ProfileNb_nm,"Profile Nb thickness in nm " + FileIdentifier)

ImageSetIntensityUnitString(ProfileNb_nm, "Nb thickness (nm)")

NameDummy=GetName(Nb_thickness_nm)

ProfileNb_nm.SetStringNote("Input Data:Data:07 Map profiled", NameDummy)

ShowImage(ProfileNb_nm)

//Add the foreground plot to the final plot.  The next lines will be repeated for each profile
with a change of name.

DISP = ProfileNb_nm.ImageGetImageDisplay(0)
DISP.LinePlotImageDisplaySetDoAutoSurvey( 0, 0 )
SLICEID_0 = DISP.ImageDisplayGetSliceIDByIndex(0)

//Show the legend
disp.LinePlotImageDisplaySetLegendShown(1)

//Add the original label to the first slice of the final plot
disp.ImageDisplaySetSliceLabelById( sliceID_0, "Nb Thickness (nm)")

//Calculate profile of the C Thickness in nm

//Clone the first profile to get the calibration and tags
Image ProfileC_nm :=ProfileT.ImageClone()
ProfileC_nm=C_Thickness_nm[Slicelt]

//Set name
SetName(ProfileC_nm,"Profile C thickness in nm " + FileIdentifier)

ImageSetIntensityUnitString(ProfileC_nm, "C thickness (nm)")

NameDummy=GetName(C_thickness_nm)

ProfileC_nm.SetStringNote("Input Data:Data:07 Map profiled", NameDummy)

```

```

ShowImage(ProfileC_nm)

//Add the foreground plot to the final plot. The next lines will be repeated for each profile
with a change of name.

DISP = ProfileC_nm.ImageGetImageDisplay(0)

DISP.LinePlotImageDisplaySetDoAutoSurvey( 0, 0 )

SLICEID_0 = DISP.ImageDisplayGetSliceIDByIndex(0)

//Show the legend

disp.LinePlotImageDisplaySetLegendShown(1)

//Add the original label to the first slice of the final plot

disp.ImageDisplaySetSliceLabelById( sliceID_0, "C Thickness (nm)")

//Calculate profile of the N Thickness in nm

//Clone the first profile to get the calibration and tags

Image ProfileN_nm :=ProfileT.ImageClone()

ProfileN_nm=N_Thickness_nm[Slicelt]

//Set name

SetName(ProfileN_nm,"Profile N thickness in nm " + FileIdentifier)

ImageSetIntensityUnitString(ProfileN_nm, "N thickness (nm)")

NameDummy=GetName(N_thickness_nm)

ProfileN_nm.SetStringNote("Input Data:Data:07 Map profiled", NameDummy)

ShowImage(ProfileN_nm)

//Add the foreground plot to the final plot. The next lines will be repeated for each profile
with a change of name.

DISP = ProfileN_nm.ImageGetImageDisplay(0)

DISP.LinePlotImageDisplaySetDoAutoSurvey( 0, 0 )

SLICEID_0 = DISP.ImageDisplayGetSliceIDByIndex(0)

//Show the legend

disp.LinePlotImageDisplaySetLegendShown(1)

```

```

//Add the original label to the first slice of the final plot
disp.ImageDisplaySetSliceLabelById( sliceID_0, "N Thickness (nm)")

//Calculate profile of the C+N Thickness in nm

//Clone the first profile to get the calibration and tags
Image ProfileCN_nm :=ProfileT.ImageClone()
ProfileCN_nm=CN_Thickness_nm[Slicelt]

//Set name
SetName(ProfileCN_nm,"Profile C + N thickness in nm " + FileIdentifier)
ImageSetIntensityUnitString(ProfileCN_nm, "(C + N) thickness (nm)")
NameDummy=GetName(CN_thickness_nm)
ProfileCN_nm.SetStringNote("Input Data:Data:07 Map profiled", NameDummy)
ShowImage(ProfileCN_nm)

//Add the foreground plot to the final plot.  The next lines will be repeated for each profile
with a change of name.

DISP = ProfileCN_nm.ImageGetImageDisplay(0)
DISP.LinePlotImageDisplaySetDoAutoSurvey( 0, 0 )
SLICEID_0 = DISP.ImageDisplayGetSliceIDByIndex(0)

//Show the legend
disp.LinePlotImageDisplaySetLegendShown(1)

//Add the original label to the first slice of the final plot
disp.ImageDisplaySetSliceLabelById( sliceID_0, "(C + N) Thickness (nm)")

//Calculate profile of x from masked map

//Clone the first profile to get the calibration and tags
Image ProfileXMask :=ProfileT.ImageClone()
ProfileXMask=TiXMask[Slicelt]

//Set name

```

```

SetName(ProfileXMask,"Profile of x in TixVvNb(1-x-v)CyNz Masked " + FileIdentifier)
ImageSetIntensityUnitString(ProfileXMask, "x in TixVvNb(1-x-v)CyNz")
NameDummy=GetName(TiXMask)
ProfileXMask.SetStringNote("Input Data:Data:07 Map profiled", NameDummy)
ShowImage(ProfileXMask)

//Add the foreground plot to the final plot.  The next lines will be repeated for each profile
with a change of name.

DISP = ProfileXMask.ImageGetImageDisplay(0)
DISP.LinePlotImageDisplaySetDoAutoSurvey( 0, 0 )
SLICEID_0 = DISP.ImageDisplayGetSliceIDByIndex(0)

//Show the legend
disp.LinePlotImageDisplaySetLegendShown(1)

//Add the original label to the first slice of the final plot
disp.ImageDisplaySetSliceLabelById( sliceID_0, "x in TixVvNb(1-x-v)CyNz")

//Calculate profile of v from masked map

//Clone the first profile to get the calibration and tags
Image ProfileVMask :=ProfileT.ImageClone()
ProfileVMask=VvMask[Slicelt]

//Set name
SetName(ProfileVMask,"Profile of v in TixVvNb(1-x-v)CyNz Masked " + FileIdentifier)
ImageSetIntensityUnitString(ProfileVMask, "v in TixVvNb(1-x-v)CyNz")
NameDummy=GetName(VvMask)
ProfileVMask.SetStringNote("Input Data:Data:07 Map profiled", NameDummy)
ShowImage(ProfileVMask)

//Add the foreground plot to the final plot.  The next lines will be repeated for each profile
with a change of name.

DISP = ProfileVMask.ImageGetImageDisplay(0)

```

```

DISP.LinePlotImageDisplaySetDoAutoSurvey( 0, 0 )
SLICEID_0 = DISP.ImageDisplayGetSliceIDByIndex(0)
//Show the legend
disp.LinePlotImageDisplaySetLegendShown(1)
//Add the original label to the first slice of the final plot
disp.ImageDisplaySetSliceLabelById( sliceID_0, "v in TixVvNb(1-x-v)CyNz")
//Calculate profile of (1-x-v) from the masked map
//Clone the first profile to get the calibration and tags
Image ProfileNbOneMinusXMinusVMask :=ProfileT.ImageClone()
ProfileNbOneMinusXMinusVMask=NbOneMinusXminusVMask[Slicelt]
//Set name
SetName(ProfileNbOneMinusXMinusVMask,"Profile of (1-x-v) in TixVvNb(1-x-v)CyNz Masked
" + FileIdentifier)
ImageSetIntensityUnitString(ProfileNbOneMinusXminusVMask, "(1-x-v) in TixVvNb(1-x-
v)CyNz")
NameDummy=GetName(NbOneMinusXMinusVMask)
ProfileNbOneMinusXMinusVMask.SetStringNote("Input Data:Data:07 Map profiled",
NameDummy)
ShowImage(ProfileNbOneMinusXMinusVMask)
//Add the foreground plot to the final plot. The next lines will be repeated for each profile
with a change of name.
DISP = ProfileNboneMinusXMinusVMask.ImageGetImageDisplay(0)
DISP.LinePlotImageDisplaySetDoAutoSurvey( 0, 0 )
SLICEID_0 = DISP.ImageDisplayGetSliceIDByIndex(0)
//Show the legend
disp.LinePlotImageDisplaySetLegendShown(1)
//Add the original label to the first slice of the final plot

```

```

disp.ImageDisplaySetSliceLabelById( sliceID_0, "(1-x-v) in TixVvNb(1-x-v)CyNz")
//Calculate profile of y from the masked map
//Clone the first profile to get the calibration and tags
Image ProfileCyMask :=ProfileT.ImageClone()
ProfileCyMask=CyMask[Slicelt]
//Set name
SetName(ProfileCyMask,"Profile of y in TixVvNb(1-x-v)CyNz Masked " + FileIdentifier)
ImageSetIntensityUnitString(ProfileCyMask, "y in TixVvNb(1-x-v)CyNz")
NameDummy=GetName(CyMask)
ProfileCyMask.SetStringNote("Input Data:Data:07 Map profiled", NameDummy)
ShowImage(ProfileCyMask)
//Add the foreground plot to the final plot. The next lines will be repeated for each profile
with a change of name.
DISP = ProfileCyMask.ImageGetImageDisplay(0)
DISP.LinePlotImageDisplaySetDoAutoSurvey( 0, 0 )
SLICEID_0 = DISP.ImageDisplayGetSliceIDByIndex(0)
//Show the legend
disp.LinePlotImageDisplaySetLegendShown(1)
//Add the original label to the first slice of the final plot
disp.ImageDisplaySetSliceLabelById( sliceID_0, "y in TixVvNb(1-x-v)CyNz")
//Calculate profile of z from the masked map
//Clone the first profile to get the calibration and tags
Image ProfileNzMask :=ProfileT.ImageClone()
ProfileNzMask=NzMask[Slicelt]
//Set name
SetName(ProfileNzMask,"Profile of z in TixVvNb(1-x-v)CyNz Masked " + FileIdentifier)

```

```

ImageSetIntensityUnitString(ProfileNzMask, "z in TixVvNb(1-x-v)CyNz")
NameDummy=GetName(NzMask)
ProfileNzMask.SetStringNote("Input Data:Data:07 Map profiled", NameDummy)
ShowImage(ProfileNzMask)

//Add the foreground plot to the final plot. The next lines will be repeated for each profile
with a change of name.

DISP = ProfileNzMask.ImageGetImageDisplay(0)
DISP.LinePlotImageDisplaySetDoAutoSurvey( 0, 0 )
SLICEID_0 = DISP.ImageDisplayGetSliceIDByIndex(0)
//Show the legend
disp.LinePlotImageDisplaySetLegendShown(1)
//Add the original label to the first slice of the final plot
disp.ImageDisplaySetSliceLabelById( sliceID_0, "z in TixVvNb(1-x-v)CyNz")
//Calculate profile of X/M from the masked map
//Clone the first profile to get the calibration and tags
Image ProfileXoverMMask :=ProfileT.ImageClone()
ProfileXoverMMask=XoverMMask[Slicelt]
//Set name
SetName(ProfileXoverMMask,"Profile of XoverM Masked " + FileIdentifier)
ImageSetIntensityUnitString(ProfileXoverMMask, "X/M in MX")
NameDummy=GetName(XoverMMask)
ProfileXoverMMask.SetStringNote("Input Data:Data:07 Map profiled", NameDummy)
ShowImage(ProfileXoverMMask)

//Add the foreground plot to the final plot. The next lines will be repeated for each profile
with a change of name.

DISP = ProfileXoverMMask.ImageGetImageDisplay(0)
DISP.LinePlotImageDisplaySetDoAutoSurvey( 0, 0 )

```

```

SLICEID_0 = DISP.ImageDisplayGetSliceIDByIndex(0)

//Show the legend

disp.LinePlotImageDisplaySetLegendShown(1)

//Add the original label to the first slice of the final plot

disp.ImageDisplaySetSliceLabelById( sliceID_0, "X/M in MX")

//*****

//          Save the files to disc

//*****

// Ask if the files are to be saved. Check if the "disc" icon greys out showing that they have
been saved

//Put a YES/NO dialog box here

number legend = TwoButtonDialog("File the results?\n\nFor the first file choose/create the
folder required\n\nFor the rest just hit return to put them in the same folder\n\nBEWARE
the DISC ICON doesn't grey out even though the file has been save nor does the SAVE option
disappear from the file menu\n\nA dialog box appears at the end to show how many files
have been saved.\n\nIf it DOESN'T, check that they have been saved." , "Yes", "No")

If(Legend==0) Exit(0)

//For each image to be saved

//          Check it is valid. Drop out if it's not.

//          Get its current image name

//          Select the destination. Once the first is chosen, the rest will default to it.

//          Save the file with the current image name as the file name offered

//          For the first it's necessary to choose choose/create the folder into which the
file is saved

//          For subsequent files, this folder is automatically chosen so that only a carriage
returne is needed.

//As a precaution, the number of files saved is counted and shown at the end.

String FileName, FileName0

Number FileCount

```

```

FileCount=0

//*****
*****

//  HERE  Need to set up the save for 39 files

//*****
*****

If (!TiVnbCN.ImageIsValid()) Exit(0)

GetName(TiVnbCN, FileName0)

If (!SaveAsDialog("Please select destination", filename0, filename)) Exit(0)

//Result("\n Selected file path:"+filename+".dm3")

TiVnbCN.SaveImage(filename+".dm3")

Filecount=FileCount+1

If (!TiVnbCNsmooth.ImageIsValid()) Exit(0)

GetName(TiVnbCNsmooth, FileName0)

If (!SaveAsDialog("Please select destination", filename0, filename)) Exit(0)

//Result("\n Selected file path:"+filename+".dm3")

TiVnbCNsmooth.SaveImage(filename+".dm3")

Filecount=FileCount+1

If (!Excluded.ImageIsValid()) Exit(0)

GetName(Excluded, FileName0)

If (!SaveAsDialog("Please select destination", filename0, filename)) Exit(0)

//Result("\n Selected file path:"+filename+".dm3")

Excluded.SaveImage(filename+".dm3")

Filecount=FileCount+1

If (!Mask.ImageIsValid()) Exit(0)

GetName(Mask, FileName0)

If (!SaveAsDialog("Please select destination", filename0, filename)) Exit(0)

```

```

//Result("\n Selected file path:"+filename+".dm3")
Mask.SaveImage(filename+".dm3")
Filecount=FileCount+1
If (!TiVnb_AtomsPerArea.ImagelsValid()) Exit(0)
GetName(TiVnb_AtomsPerArea, FileName0)
If (!SaveAsDialog("Please select destination", filename0, filename)) Exit(0)
//Result("\n Selected file path:"+filename+".dm3")
TiVnb_AtomsPerArea.SaveImage(filename+".dm3")
Filecount=FileCount+1
If (!TiVnb_Thickness_UnitCells.ImagelsValid()) Exit(0)
GetName(TiVnb_Thickness_UnitCells, FileName0)
If (!SaveAsDialog("Please select destination", filename0, filename)) Exit(0)
//Result("\n Selected file path:"+filename+".dm3")
TiVnb_Thickness_UnitCells.SaveImage(filename+".dm3")
Filecount=FileCount+1
If (!TiVnb_Thickness_nm.ImagelsValid()) Exit(0)
GetName(TiVnb_Thickness_nm, FileName0)
If (!SaveAsDialog("Please select destination", filename0, filename)) Exit(0)
//Result("\n Selected file path:"+filename+".dm3")
TiVnb_Thickness_nm.SaveImage(filename+".dm3")
Filecount=FileCount+1
If (!Ti_Thickness_nm.ImagelsValid()) Exit(0)
GetName(Ti_Thickness_nm, FileName0)
If (!SaveAsDialog("Please select destination", filename0, filename)) Exit(0)
//Result("\n Selected file path:"+filename+".dm3")
Ti_Thickness_nm.SaveImage(filename+".dm3")

```

```

Filecount=FileCount+1

If (!V_Thickness_nm.ImageIsValid()) Exit(0)

GetName(V_Thickness_nm, FileName0)

If (!SaveAsDialog("Please select destination", filename0, filename)) Exit(0)

//Result("\n Selected file path:"+filename+".dm3")

V_Thickness_nm.SaveImage(filename+".dm3")

Filecount=FileCount+1

If (!Nb_Thickness_nm.ImageIsValid()) Exit(0)

GetName(Nb_Thickness_nm, FileName0)

If (!SaveAsDialog("Please select destination", filename0, filename)) Exit(0)

//Result("\n Selected file path:"+filename+".dm3")

Nb_Thickness_nm.SaveImage(filename+".dm3")

Filecount=FileCount+1

If (!C_Thickness_nm.ImageIsValid()) Exit(0)

GetName(C_Thickness_nm, FileName0)

If (!SaveAsDialog("Please select destination", filename0, filename)) Exit(0)

//Result("\n Selected file path:"+filename+".dm3")

C_Thickness_nm.SaveImage(filename+".dm3")

Filecount=FileCount+1

If (!N_Thickness_nm.ImageIsValid()) Exit(0)

GetName(N_Thickness_nm, FileName0)

If (!SaveAsDialog("Please select destination", filename0, filename)) Exit(0)

//Result("\n Selected file path:"+filename+".dm3")

N_Thickness_nm.SaveImage(filename+".dm3")

Filecount=FileCount+1

If (!CN_Thickness_nm.ImageIsValid()) Exit(0)

```

```

GetName(CN_Thickness_nm, FileName0)
If (!SaveAsDialog("Please select destination", filename0, filename)) Exit(0)
//Result("\n Selected file path:"+filename+".dm3")
CN_Thickness_nm.SaveImage(filename+".dm3")
Filecount=FileCount+1
If (!Tix.ImagelsValid()) Exit(0)
GetName(Tix, FileName0)
If (!SaveAsDialog("Please select destination", filename0, filename)) Exit(0)
//Result("\n Selected file path:"+filename+".dm3")
Tix.SaveImage(filename+".dm3")
Filecount=FileCount+1
If (!TixMask.ImagelsValid()) Exit(0)
GetName(TixMask, FileName0)
If (!SaveAsDialog("Please select destination", filename0, filename)) Exit(0)
//Result("\n Selected file path:"+filename+".dm3")
TixMask.SaveImage(filename+".dm3")
Filecount=FileCount+1
If (!Vv.ImagelsValid()) Exit(0)
GetName(Vv, FileName0)
If (!SaveAsDialog("Please select destination", filename0, filename)) Exit(0)
//Result("\n Selected file path:"+filename+".dm3")
Vv.SaveImage(filename+".dm3")
Filecount=FileCount+1
If (!VvMask.ImagelsValid()) Exit(0)
GetName(VvMask, FileName0)
If (!SaveAsDialog("Please select destination", filename0, filename)) Exit(0)

```

```

//Result("\n Selected file path:"+filename+".dm3")
VvMask.SaveImage(filename+".dm3")
Filecount=FileCount+1
If (!NbOneMinusxMinusv.ImagesValid()) Exit(0)
GetName(NbOneMinusxMinusv, FileName0)
If (!SaveAsDialog("Please select destination", filename0, filename)) Exit(0)
//Result("\n Selected file path:"+filename+".dm3")
NbOneMinusxMinusv.SaveImage(filename+".dm3")
Filecount=FileCount+1
If (!NbOneMinusxMinusvMask.ImagesValid()) Exit(0)
GetName(NbOneMinusxMinusvMask, FileName0)
If (!SaveAsDialog("Please select destination", filename0, filename)) Exit(0)
//Result("\n Selected file path:"+filename+".dm3")
NbOneMinusxMinusvMask.SaveImage(filename+".dm3")
Filecount=FileCount+1
If (!Cy.ImagesValid()) Exit(0)
GetName(Cy, FileName0)
If (!SaveAsDialog("Please select destination", filename0, filename)) Exit(0)
//Result("\n Selected file path:"+filename+".dm3")
Cy.SaveImage(filename+".dm3")
Filecount=FileCount+1
If (!CyMask.ImagesValid()) Exit(0)
GetName(CyMask, FileName0)
If (!SaveAsDialog("Please select destination", filename0, filename)) Exit(0)
//Result("\n Selected file path:"+filename+".dm3")
CyMask.SaveImage(filename+".dm3")

```

```

Filecount=FileCount+1

If (!Nz.ImgelsValid()) Exit(0)

GetName(Nz, FileName0)

If (!SaveAsDialog("Please select destination", filename0, filename)) Exit(0)

//Result("\n Selected file path:"+filename+".dm3")

Nz.SaveImage(filename+".dm3")

Filecount=FileCount+1

If (!NzMask.ImgelsValid()) Exit(0)

GetName(NzMask, FileName0)

If (!SaveAsDialog("Please select destination", filename0, filename)) Exit(0)

//Result("\n Selected file path:"+filename+".dm3")

NzMask.SaveImage(filename+".dm3")

Filecount=FileCount+1

If (!XoverM.ImgelsValid()) Exit(0)

GetName(XoverM, FileName0)

If (!SaveAsDialog("Please select destination", filename0, filename)) Exit(0)

//Result("\n Selected file path:"+filename+".dm3")

XoverM.SaveImage(filename+".dm3")

Filecount=FileCount+1

If (!XoverMMask.ImgelsValid()) Exit(0)

GetName(XoverMMask, FileName0)

If (!SaveAsDialog("Please select destination", filename0, filename)) Exit(0)

//Result("\n Selected file path:"+filename+".dm3")

XoverMMask.SaveImage(filename+".dm3")

Filecount=FileCount+1

If (!ProfileT.ImgelsValid()) Exit(0)

```

```

GetName(ProfileT, FileName0)
If (!SaveAsDialog("Please select destination", filename0, filename)) Exit(0)
//Result("\n Selected file path:"+filename+".dm3")
ProfileT.SaveImage(filename+".dm3")
Filecount=FileCount+1
If (!ProfileTcells.ImagelsValid()) Exit(0)
GetName(ProfileTcells, FileName0)
If (!SaveAsDialog("Please select destination", filename0, filename)) Exit(0)
//Result("\n Selected file path:"+filename+".dm3")
ProfileTcells.SaveImage(filename+".dm3")
Filecount=FileCount+1
If (!ProfileTi_nm.ImagelsValid()) Exit(0)
GetName(ProfileTi_nm, FileName0)
If (!SaveAsDialog("Please select destination", filename0, filename)) Exit(0)
//Result("\n Selected file path:"+filename+".dm3")
ProfileTi_nm.SaveImage(filename+".dm3")
Filecount=FileCount+1
If (!ProfileV_nm.ImagelsValid()) Exit(0)
GetName(ProfileV_nm, FileName0)
If (!SaveAsDialog("Please select destination", filename0, filename)) Exit(0)
//Result("\n Selected file path:"+filename+".dm3")
ProfileV_nm.SaveImage(filename+".dm3")
Filecount=FileCount+1
If (!ProfileNb_nm.ImagelsValid()) Exit(0)
GetName(ProfileNb_nm, FileName0)
If (!SaveAsDialog("Please select destination", filename0, filename)) Exit(0)

```

```

//Result("\n Selected file path:"+filename+".dm3")
ProfileNb_nm.SaveImage(filename+".dm3")
Filecount=FileCount+1
If (!ProfileC_nm.ImagesValid()) Exit(0)
GetName(ProfileC_nm, FileName0)
If (!SaveAsDialog("Please select destination", filename0, filename)) Exit(0)
//Result("\n Selected file path:"+filename+".dm3")
ProfileC_nm.SaveImage(filename+".dm3")
Filecount=FileCount+1
If (!ProfileN_nm.ImagesValid()) Exit(0)
GetName(ProfileN_nm, FileName0)
If (!SaveAsDialog("Please select destination", filename0, filename)) Exit(0)
//Result("\n Selected file path:"+filename+".dm3")
ProfileN_nm.SaveImage(filename+".dm3")
Filecount=FileCount+1
If (!ProfileCN_nm.ImagesValid()) Exit(0)
GetName(ProfileCN_nm, FileName0)
If (!SaveAsDialog("Please select destination", filename0, filename)) Exit(0)
//Result("\n Selected file path:"+filename+".dm3")
ProfileCN_nm.SaveImage(filename+".dm3")
Filecount=FileCount+1
If (!ProfileXMask.ImagesValid()) Exit(0)
GetName(ProfileXMask, FileName0)
If (!SaveAsDialog("Please select destination", filename0, filename)) Exit(0)
//Result("\n Selected file path:"+filename+".dm3")
ProfileXMask.SaveImage(filename+".dm3")

```

```

Filecount=FileCount+1

If (!ProfileVMask.ImageIsValid()) Exit(0)

GetName(ProfileVMask, FileName0)

If (!SaveAsDialog("Please select destination", filename0, filename)) Exit(0)

//Result("\n Selected file path:"+filename+".dm3")

ProfileVMask.SaveImage(filename+".dm3")

Filecount=FileCount+1

If (!ProfileNbOneMinusXMinusvMask.ImageIsValid()) Exit(0)

GetName(ProfileNbOneMinusXMinusvMask, FileName0)

If (!SaveAsDialog("Please select destination", filename0, filename)) Exit(0)

//Result("\n Selected file path:"+filename+".dm3")

ProfileNbOneMinusXMinusvMask.SaveImage(filename+".dm3")

Filecount=FileCount+1

If (!ProfileCyMask.ImageIsValid()) Exit(0)

GetName(ProfileCyMask, FileName0)

If (!SaveAsDialog("Please select destination", filename0, filename)) Exit(0)

//Result("\n Selected file path:"+filename+".dm3")

ProfileCyMask.SaveImage(filename+".dm3")

Filecount=FileCount+1

If (!ProfileNzMask.ImageIsValid()) Exit(0)

GetName(ProfileNzMask, FileName0)

If (!SaveAsDialog("Please select destination", filename0, filename)) Exit(0)

//Result("\n Selected file path:"+filename+".dm3")

ProfileNzMask.SaveImage(filename+".dm3")

Filecount=FileCount+1

If (!ProfileXoverMMask.ImageIsValid()) Exit(0)

```

```
GetName(ProfileXoverMMask, FileName0)

If (!SaveAsDialog("Please select destination", filename0, filename)) Exit(0)

//Result("\n Selected file path:"+filename+".dm3")

ProfileXoverMMask.SaveImage(filename+".dm3")

Filecount=FileCount+1

//*****
*****

//          Check that all the files have been saved

//*****
*****

OKdialog("There are 39 files to be saved\n\n" + FileCount+" files have been saved")
```